Universidade de Aveiro Departamento de engenharia de Materiais e Cerâmica
2016

Patrick Thierry Almeida da Rocha

Compreensão dos Mecanismos de Corrosão de Novas Ligas Biodegradáveis de Magnésio

Understanding Corrosion Mechanisms of Novel Biodegradable Magnesium Alloys

Patrick Thierry Almeida da Rocha

Understanding Corrosion Mechanisms of Novel Biodegradable Magnesium Alloys

Dissertation presented to the University of Aveiro in the fulfillment of the requirement for the awarding of the Masters in Materials Science and Engineering carried out under the supervision of Doctor Kiryl Yasakau, Post-Doc Fellowship at the University of Aveiro, and Prof. Doctor Mikhail Zheludkevich, Head of Department of the Corrosion and Surface Technology Group, at Magnesium Innovation Centre MagIC, Helmholtz-Zentrum Geesthacht.

I dedicate this work to my family and friends, who both do part of my life and always supported me…

The Board of Examiners

President

Prof. Doctor Mário Guerreiro Silva Ferreira
Full Professor from University of Aveiro, Portugal

Doutora Ana Luísa Daniel da Silva
Equivalent to Assistant Researcher, University of Aveiro, Portugal

Doutor Kiryl Yasakau
Post-Doctoral Researcher, University of Aveiro, Portugal

Acknowledgements

Firstly of all I would like to thank my supervisor, Doctor Kiryl Yasakau and Professor Mikhail Zheludkevich, for the huge opportunity to work in a exicting field. Also a great thanks for the guidance through this work and the scientific and personal support.

At the University of Aveiro, I'm thankful to all colleagues and Professors who help me to enrich my knowledge along the years. I also like to acknowledge the University of Trás os Montes e Alto Douro and all Professors and colleagues.

A huge thanks to all the scientists and engineers, staff and colleagues found in HZG, especially at MagIC. A special thanks to Carsten Blawert, Sviatlana Lamaka, Ulrich Burmester, Volker Heitmann, Gert Wiese, Daniel Hoche, among others who helped me with a substantial part of the Work. Also a great thank you to the room mates.

An Ode to my family and friends, which are so dear to me…

palavras-chave

Biomateriais, ligas de magnésio biodegradáveis, mecanismos de corrosão, fluídos corporais simulados, produtos de corrosão, eletroquímica de impedância, evolução do hidrogénio.

Resumo

A biodegradação de biomateriais em ordem a conseguir uma dissolução completa de um determinado equipamento após a realização do seu propósito, tem sido visto como uma ideia atrativa pela comunidade cientifica, devido ao elevado potencial nas melhorias a qualidade de vida do paciente e devido aos custos pós operatorios que podem ser melhorados.

O comportamento de biodegradação é consequência da elevada susceptibilidade à corrosão, inerente às ligas metálicas como o magnésio. Esta característica deve-se à instabilidade química causada pela inserção das ligas num ambiente agressivo às mesmas. Esta afirmação continua a ser verdadeira no caso em que ligas de mágnesio são introduzidas no corpo humano, em contacto com iões agressivos ao metal, presentes nos fluídos corporais.

O trabalho de investigação proposto nesta tese, tem como temática o estudo de mágnesio puro, ligas de Mg-XGd e Mg-XGd-YMn, onde o rácio estequiométrico dos elementos é X=2,5 e Y=1. As ligas usadas não se encontram comercializadas, mas existe um forte interesse no seu uso como material biodegradável devido às boas propriedades mecânicas apresentadas pelas mesmas. No entanto as taxas de corrosão necessitam de ser modeladas de forma a viabilizar o seu uso como biomaterial, e uma melhor compreensão sobre os mecanismos de corrosão podem ajudar no design de futuras ligas.

O foco deste trabalho consiste em desvendar a natureza da corrosão e devido a isso diversos fatores serão estudados, usando diferentes técnicas de caracterização i) Observar a microestrutura e os microconstituintes presentes, o seu tamanho, morfologia e composição elemental, usando para tais fins técnicas de MEV e EDS. A rugosidade e o potential Volta apresentada pelos diversos constituintes da microstrutura será levado a cabo por técnicas de MFA e SKFM.

ii) Técnicas eletroquímicas, como a eletroquímca de impedância e polarização dinâmica, serão usadas de forma a perceber o comportamento do sistemas em diversos meios eletrolíticos. Tempos longos de imersão foram realizados durante medições de Impedância eletroquímica.

iii) A composição quimica e o estudo de fases dos produtos de corrosão são realizados usando técnias de EDS e DRX, o que permite identificar os tipos de produtos preferencialmente formados durante o processo de corrosão.

iv) Uma série de outras técnicas proporcionaram uma informação mais consistente sobre o comportamento de corrosão nas ligas de mágnesio, como a evolução do hidrogénio e a observação das secções de corte.

A reprodutibilidade foi estudada usando uma amostragem em diversas técnicas. Entretanto este trabalho é baseado numa comparação qualitativa que permite entender e desvendar o porquê, como e qual o tipo de corrosão que é apresentado pelos diversos sistemas em estudo.

Os resultados obtidos pelas diversas técnias revelaram que os fenómenos de corrosão são dependentes do tipo de ambiente e das suas condições. A presença de níveis de impurezas superiores aos limites de tolerância, como o ferro, mostram que a taxa de corrosão é aumentada na presença dos mesmos, visto que aumenta a actividade catódica dos intermetálicos. O manganês como elemento de liga reduz esse efeito, diminuindo a respetiva taxa de corrosão. A formação de produtos de corrosão é dependente do pH do meio, e assim, a precipitação de compostos vai diferir com o eletrólito em uso. O sistema ternário e o magnésio puro demonstraram taxas de corrosão aproximadamente de 0,18 mm/a a 330h de imersão, imerso na solução de PBS. Estas taxas de corrosão podem ser adequadas para aplicações biomédicas.

Keywords

Biomaterials, magnesium biodegradable alloys, mechanisms of corrosion, simulated body fluids, corrosion products, eletrochemical impedance spectroscopy, hydrogen evolution.

Abstract

Biomaterials bring valuable improvements to the biomedical field. The idea behind the biodegradation behaviour of a biomaterial which can be used as an implant in the human body has attracted the attention of the scientific community, due to various benefits which may improve quality of life of injured humans.

The biodegradation behaviour of metals arises from the high susceptibility to corrosion of metallic alloys in the human body, which are in contact with aggressive ions presented by human body fluids. This especially concerns magnesium and its alloys. Magnesium alloys must comply with the requirements which are put on the biodegradable materials. Among such requirements one can name mechanical properties and controlled corrosion activity.

Investigation in this work performed on several Mg samples, including a pure magnesium (HP Mg), Mg-XGd and Mg-XGd-YMn systems with variation in stoichiometry ratio of elements, X=2 and 5 and Y=1. These are non-commercial Mg alloys which may present interest due to their potential as biodegradable materials. A tailoring of the corrosion rate is required to reduce the corrosion rate of such alloys. For that, it is incredibly wise to understand the corrosion mechanisms in different electrolytes and conditions.

To study the influence of factors which affects corrosion a series of characterization techniques were used. At first microstructure and microconstituents as intermetallics, their size, shape and elemental composition, were evaluated using SEM and EDS. Roughness and Volta potential of the different phases present in the microstructure were studied using AFM/SKFM technique, which allows to correlate the Volta potential with local corrosion of intermetallics and to observe dissolution and precipitation processes at the microscale.

Also, electrochemical measurements, such as Electrochemical Impedance Spectroscopy (EIS), potential dynamic polarization, were conducted accessing corrosion behaviour of systems in different electrolytes during short immersion times. For electrochemical characterization, in the extended time of immersion EIS was used. To obtain the corrosion rate, it was used the hydrogen evolution method.

Then corrosion products chemistry was studied using X-ray diffraction and energy dispersive spectroscopy techniques, which allow to identify the type of products formed in the different electrolytes and to correlate their formation with corrosion behaviour. Cross section analysis and identification of corrosion morphology were accessed on samples after EIS tests.

Reproducibly of measurements were ensured by studying a set of replica samples. This work is based on qualitative/qualitative comparison of results which allowed a better understanding why, how and which corrosion is present in the different systems.

The different techniques used revealed that corrosion is highly dependent on the environment and the conditions of measurements. The presence of high levels of impurities as iron induces high levels of corrosion by increasing the cathodic activity of intermetallic. Manganese as an alloying element reduces the effect of the impurities in corrosion. Corrosion products formation is pH dependent, and so, the precipitation of corrosion products compounds from different electrolytes may be beneficial or nonbeneficial to corrosion. The ternary system and the HP Magnesium demonstrate corrosion rates approximately 0.18 mm/year in PBS solution, which can be adequate for biomedical applications.

Table of Contents

List of Figures

List of Tables

LIST OF SYMBOLS

a – Pre exponential factor

A – Surface area of sample

A_A – Surface area

A^+, B^+, X^+ – Metal ions

A_0 – Current amplitude

b_a, b_c – Cathodic and anodic Tafel constant

C – Capacitance reactance

C_{dl} – Double layer capacitance

$C_{p/w}$ – Alternating Capacitance between probe and working electrode

C_R – Corrosion rate

d_{hkl} – Space between adjacent (hkl) lattice planes

Δg – Weight loss

ΔG^0 – Minimum free energy state

$\Delta V_{p/w}$ – Potential difference between probe and working electrodes

E – Electrode Potential

E_a – Activation energy

E_{an} – Corrosion potential of anode

E_{app} – Applied Potential

E_C – Corrosion potential of cathode

E_{corr} – Corrosion Potential

E_{OCP} – Open circuit Potential

E_0 – Potential amplitude

E^0 – Standard free potential

F – Faraday constant

θ – Beam incidence angle

I – Electric current

I_a – Anodic current

I_c – Cathodic current

I_g – Galvanic current

$I_{H,e}$ – Expected cathodic hydrogen rate

$I_{H,m}$ – Measured cathodic hydrogen rate

$I_{Mg,e}$ – Expected anodic magnesium dissolution rate

$I_{Mg,m}$ – Measured anodic magnesium dissolution rate

I_0 – Exchange current density

$\emptyset$ – Out of phase

$\left(\frac{\phi_w}{e}\right), \left(\frac{\phi_p}{e}\right)$ – Working electrode potential and probe electrode potential

λ – Wavelength

K – Chemical rate equilibrium constant

M_i – Immersion mass
M_0 – Initial mass
n – Number of electrons involved in electrochemical process
n_i – Moles of reactant i
N – Integral number of the Bragg diffraction order
r – Reaction rate
R – Gas constant
$R_{p(an)}$ – Polarization resistance of anode
$R_{p(C)}$ – Polarization resistance of cathode
$R_{p(an-C)}$ – Electrical resistance between anode and cathode
R_S – Electrical resistance of electrolyte
ρ – Density of sample
ρ_e – Ethanol density
ρ_{exp} – Experimental density
t – Time
T – Temperature
V_{H_2} – Volume of collected hydrogen
V_V – Volume fraction
Z, Z_i, Z_r – Impedance, Imaginary and Real part of Impedance
ω – Angular frequency
ω_{max} – Maximum phase angle
Ω – Ohm unit

ABREVIATIONS

AFM – Atomic Force Microscopy
BCC – Body-centred cubic
BMG – Biodegradable metal glass
BSE – Backscattered electron
CE – Counter electrode
EIS – Electrochemical Impedance Spectroscopy
EDS – Energy Dispersive Spectroscopy
GD-OES – Glow Discharge Optical Energy Spectroscopy
HE – Hydrogen evolution
HER – Hydrogen evolution reaction rate
MAGIC – Magnesium Innovative Center
MDL – Minimum detection limit
MIM – Monovalent Ion Model
NDE – Negative Difference Effect
PBS – Phosphate-buffered saline
PTFE – Polyteetrafluoroethylen
RE – Reference electrode
RMS – Root mean square
SCC – Stress Corrosion Crack
SE – Secondary electrons
SEM – Scanning Electron Microscopy
SKPFM – Scanning Kelvin Probe Force Microscopy
VHE – Volume Hydrogen Evolved
VPD – Volta Potential Difference
WE – Working electrode
XRD – X Ray Diffraction

Preface

The Magnesium Innovative Center (MAGIC), is a material research department, which can be found in the facilities of Helmholtz-Zentrum Geeshacht. One of the research topics is the development of functionalities which magnesium can bring to diverse applications. The applicability of magnesium found some limitations due to the inherent problem of corrosion presented by magnesium and its alloys. This work was specifically conducted in the Corrosion and Surface Technology group at MAGIC.

As an specific application and as a metal, magnesium finds use in the field of biomaterials and biodegradation. The idea behind biodegradation is to provide degradation properties to, per example, implants or materials which can be used in the human body. The selectivity of materials for those applications meet some requirements as biocompatibility, non-toxicological, adequate mechanicals properties and degradation behaviour. Therefore magnesium is seen as a suitable material since it fulfills the biocompatibility, non-toxicological requirements as element and biodegradation as a metal alloy. Others feature desirable related to magnesium is the low density and suitable mechanical properties, which are closer to the presented by the natural bone. However, some specific problems can be found related to mechanical integrity and the high reactivity to corrosion shown by magnesium in aqueous environments (specifically body fluids) leading in an increase, during these last years, in the development of research to engineering those materials.

This master thesis takes focus on the biodegradation problem present by magnesium. Specifically, it wants to understand and characterize the fundamental principles behind the biodegradation in body fluid systems. However this present to be a tremendous work, and so, it was selected solutions as simulated body fluid which mimic the inorganic salts present into the body, and to study the influence of each solution, separated electrolytes were found to be an adequate practice. Another feature of this work is that it was selected three types of alloys, one of them the reference (a HP Magnesium), Mg-Gd and Mg-Gd-Mn alloys. This two last alloys are relatively new and do not found commercialization. However, they are seen as suitable candidates to biodegradation devices since 1) the addition of Gadolinium improves mechanical properties compared to pure magnesium, 2) Manganese should “deactivate” the susceptibility of impurities to corrosion and 3) all together found adequate biocompatibility and seems to fulfil this requirement. The problem related to toxicology depends on the degradation rate since

some elements can be non-toxic at certain daily concentrations. By another way, the increase in concentration levels can bring medical complications.

To better understand the susceptibility to corrosion of those metals a series of characterization techniques were chosen, firstly, to compare qualitatively corrosion rates between the different systems in use and to try to undercover the reasons behind those rates.

The content of this thesis is divided into four main chapters. The Chapter I is the state of the art where it will introduce concepts about biomaterials and biodegradation, in the various materials which find applicability in the field, corrosion problems associate to magnesium and research, conducted in various magnesium alloys. It will present the strategy of thesis and which main characterization techniques were used.

Chapter II is focused on the experimental methodology, explaining briefly the functionalities and conditions of the principal characterization techniques used. Chapter III conducted the analysis of results obtained in a laboratory environment. Chapter IV will discuss the results, offering a deeper overview and general features of the investigation work. Topics as unusual corrosion rates, mechanisms of corrosion, improvements which can be made to work in further lines of investigations will be addressed. It finalizes with the conclusions and most important aspects found in the understanding of the mechanism of corrosion and difficulties in the conduction of the experimental work. The characterization of this chapter is done by a more introspective analysis about the master thesis dissertation in general.

Chapter I – State of art

I.1 Biomaterials and the phenomena of biodegradation

The development of science and the will of a constant improvement in the human conditions brings, sometimes, great improvements in the development of new ideas and materials. Regarding biomaterials, any substance or combination of substances (excluding drugs) which are used in a biological body in contact with body fluid, find as functions, per example, replacing or assist organic tissues. Those materials allow the improvement and/or maintenance in the quality of life of each human [1],[2]. Important to refer that materials used in devices such as surgical or dental instruments are not categorized was biomaterials [1].

The loss of function of tissue and/or body structures, by external or body internal factors, leads to the use of biomaterials, replacing or augmenting functionalities. Some requirements as to be fulfilled to use a biomaterial. The most common conditions are adequate mechanical and physical properties, suitable biocompatibility to avoid adverse tissue or body reactions, and non-toxicity/carcinogenic properties. The availability and the low coast can also present substantial role in the selection of those biomaterials [1]. The class of biomaterials is very diverse and as so polymers, metals, ceramics, and composites can be used. An overview of some basic applications of each categorical material is presented in Table I.1. Composites are not specified and found mainly use in dental implants [1]. It is important to note that the development of science brings in an every daily base new insights in biomaterials applications, where micro and nanotechnology are an important tool, per example, to mold biomaterials as self-assembly and biomimetic matrices materials. Biodegradable wireless implants can be too an example as a strange, but practical, new insight in biomaterials [3]. This is a strange world where much of creativity can be found, and a better inside can be overviewed in bibliography [4],[5].

Bioapplications that demands physical interaction with the human body leads to a careful selection of the respective biomaterial. Mechanical properties, depending on the application, are a first and demanding design parameter. Properties such as strength, toughness or ductility are important parameters in applications such as bone replacement, bone repair, metal plates for fractures, stents, dental implants, screws and staples, parts of other devices like artificial hearts, pacemakers and catheters and wireless implants among others [3],[4].

Table I.1 - Overview of materials used as biomaterials and some general applications [1], [2].

Materials	Polymers	Ceramics	Metals
Applications	• Dental implants and restorations; • Soft tissue replacement an drug delivery systems (DDS) ; • Joint replacement, sutures and blood contacting devices;	• Dental implants and restoration as bio cements; • Bio coatings on metal surfaces; • Joint and bone replacements;	• Dental implants and restorations; • Biosensors and antibacterial agents; • Joint and bone replacements; • Bone plates fracture fixation and blood contacting devices such stents;

It is introduced the Ashby chart, plotting strength vs. density properties allowing the comparison of different types of materials classes [6], which in this particular case can be used as biomaterials. Observing Figure I.1, for example, it can be observed that the natural material offers a relative lower maximize strength than metals, or more particularly magnesium alloys. Magnesium is presented as a light and low dense metal. These metal alloys are a good option when choosing biomaterial for a particular bioapplication.

Nowadays the most used metals for bio-applications are systems based on titanium, stainless steel, and cobalt-chromium-molybdenum. Several complications are related to those materials [5].

A relatively new concept is the biodegradation of biomaterials. This results in the loss and/or deterioration of mass, when exposed to biological activity/medium [7]. However, the tailoring of biodegradation can be used to beneficiate mechanical properties, regulated with the importance of environmental adequacy [7]. Almost all types of materials can experience this phenomenon (as ceramics, polymers, metals, etc.) and in the scope of the thesis author, biodegradable metals appear as metals deterioration in a biological environment (as the human body). Bio-inert and bioactivity are also properties which can found as desirable in the tailoring of biomaterials [5].

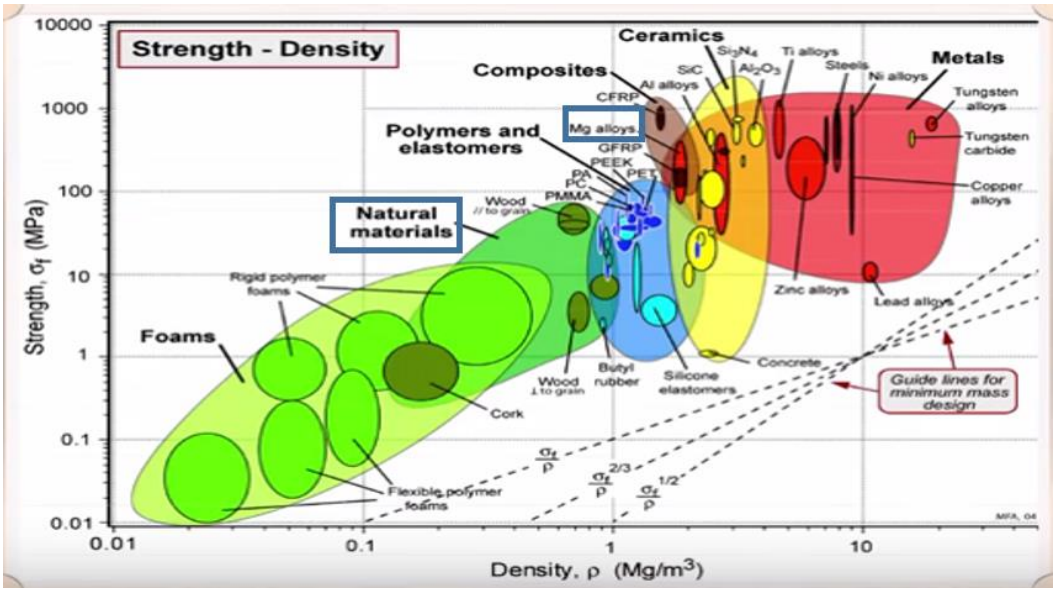

Figure I.1 - Ashby chart strength – density for selection of materials [6].

I.2 Biodegradable alloys: Magnesium as a strong candidate

In twenty century it was possible to observe a forwarding step in the use of biomaterials for medical applications. John Charnley's was one of the firsts in doing a hip replacement, using for that polytetrafluoroethylene (PTFE) and stainless steel. It was a driving time for biomedical implants and a scientific society awareness was noted in how biomaterials could help in the improvement of human physical conditions [8].

Historically, magnesium alloys only could appear due to the discovery of the element magnesium, by Joseph Black in 1755. After that, Sir Humphrey Davy managed to isolate the Mg metal by electrolytic processes, in 1808. It takes about 25 years for Michael Faraday, in this époque assistant of Sir Humphrey, to get the production of this metal with high purity degree, which allowed the commercial use with adequate mechanical and physical properties. That was possible, using electrolysis process, reducing dehydrated MgCl2, in 1833, and the industrial production was set in motion by Robert Bunsen, using the same principals in a small laboratory, which happens in 1852 [8].

Magnesium is a fairly flammable metal when in contact with air and when the specific surface area is increased. It finds its use in the initial times of his discovery, in pyrotechnical instruments, like igniting bands or wires for flashlights of the upcoming photographic industry, being these products present in the world exhibition of London in 1862 [8].

Due to the abundance of magnesium ions in the human body, Mg^{2+}, and being released in the corrosion process of magnesium alloys, the use of this element in biological systems is increasing. Furthermore, magnesium is a vital nutrient for life, and it is present in every cell type for all organisms [8]. It is also an essential element in everyday dietary and efficiently controlled in the biological systems by homeostatic mechanisms. So it can be

seen like a non-toxicological element and can be used in human body and organic systems. Maybe for those reasons, the physician Edward C. Huse saw an advantage in use Mg wires as vessels ligature to stop the bleeding of three human's patients in 1878. He reported another particularity, here Mg corrosion was slower in vivo, and the degradation time-dependent was related to the size of the Mg wire [8].

Examples of the use of magnesium alloys in biomedical applications can appear as an injured connective tissue, such as a bone fracture or a ligament rupture, that require mechanical fixation to support the tissue/bone growth. In Figure I.2 it is possible the visualization of the rising curve of healing bone strength (b) with the decreasing curve that can be related, per example, to the ideal strength and stiffness which an implant for fracture fixation should have, in respect of time. It is important to note that, at a first stage the bone doesn't have sufficient strength to allow a perfect growth, and so implant needs to carry almost all the load. That is required in the beginning when the best mechanical properties are required. With growth and healing of bone, the mechanical strength of implant can be decreased, allowing the degradation, with a determined rate, not damaging the fixation stability [9].

The appearance of biodegradable implants can provide some improvements, comparable to implants which are currently in use. These improvements, as the elimination of subsequent surgery, to remove the implant, can reduce costs for the operative treatments of injuries. Control corrosion rates it is demanded to provide specific degradation behavior and mechanical resistance, depending on the type of biomedical application. In Table 2 it can be observed some mechanical properties of current clinical biomaterials [9].

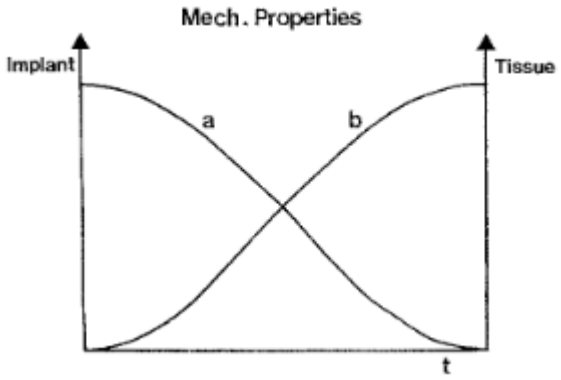

Figure I.2 - Schematic diagram of the ideal change in strength over time of a degrading implant accompanied by the healing tissue rate [9].

To design Mg alloys with adequate mechanical and corrosion properties, one need to add alloying elements. Because it is tough to eliminate impurities in pure magnesium, some alloying elements can reduce the influence of impurities on the degradation behavior of alloy. Mechanical properties also can be designed using the addition of elements in the alloy microstructure. It is important to note that magnesium presents, as the main barrier to

the use as a biodegradable biomaterial, the high reactivity to aggressive mediums and characterized by a high degradation rate (observe Figure I.3.a)). Iron provides a poor corrosion resistance to the alloy, but the addition of manganese is a way to improve this property, by forming relatively harmless intermetallic compounds. This aspect will be covered forward in this work. Toxicity is an important matter when talking about the addition of elements in biodegradable magnesium alloys [10].

Table I.2 - Physical and mechanical properties of current clinical biomaterials, some of them biodegradable alloys, and bone [11],[10],[12].

Materials	Density (g/cm^3)	Elastic moduli (GPa)	CompressiveYield stress (MPa)	Toughness ($MPa.m^{1/2}$)
Cortical bone	1,8 – 2,1	3 – 20	130 – 180	3 – 6
Magnesium	1,74 – 2,0	41 – 45	70 – 110	15 – 40
Titanium alloy	4,4 – 4,5	110 – 117	250 – 1245	55 – 115
Co-Cr alloy	8,3 – 9,2	200 – 300	450 – 900	-
Stainless Steel	7,9 – 8,1	189 – 205	170 – 1000	50 – 200
Synthetized HA	3,1	73 – 117	400 – 900	0,7

It is important to note that magnesium and its alloys have strong competition in the field of biodegradable metals. Addressing the internal competition between metals, which present better mechanical properties comparable to biodegradable polymers (Figure I.3.b)), biodegradable metal glass (BMG) and magnesium alloys can lead the front, followed by iron and its alloys. Figure I.3.b) relates compressive yield stress and Young modulus of some biodegradable materials.

Yield stress is often taken to be the stress needed to induce a specified amount of permanent strain, and it is quite low for pure magnesium, comparing to other metals (Table I.2), due to the intrinsic nature of magnesium crystal structure (hcp structure). Alloying elements or biodegradable metal glass are practical methods to bring better mechanical properties to the intrinsic structure of magnesium. In general, magnesium metal glass and his crystalline alloys present better compressive yield stress with an adequate Young modulus (closer to that of cortical bone, observed in Table I.2, as elastic moduli also known as Young modulus). Those properties are comparatively with other materials presented in the diagram (Figure I.3, as iron alloys and polymers) and even with pure magnesium [13].

Table I.2 also shows three alloys used as biomaterials. Despite the high compressive yield stress presented, which is usually a good mechanical requirement for biomedical devices, the Young modulus is too high, when comparing to the one observed by cortical bone. The relative high difference between Young modulus leads to fixation and bone interface complications. It was established in [14] that after the removal of internal metallic fixations, the residual bone remain weaker than normal, due per example,

to the adverse effect of rigid plates on bones, which leads to stress protection atrophy [14]. It is clear that mechanical adequacy always depends on the type of bio applications and per example, specific hydrogels [15], which presents a very small Young modulus comparable to other biomaterials, can found utility in drug delivery systems or soft tissue engineering, as biodegradable biomaterials. [15]

Figure I.3.a) is an adaptation of Figure I.2, and it is noted that polymers present the longer degradation behavior during the implantation time, despite current lower mechanical adequacy than biodegradable alloys. Magnesium, as stated before, is a highly reactive metal, and by consequence it's degrading very fast in an aggressive medium as body fluids, not supporting the mechanical needs during full implantation time. One can note in Figure I.3.a), that iron metals present an adequate biodegradable behavior since, after the remodeling period and fully recovery of the injury, iron-based bioimplants are fully degraded.

Iron as biodegradable metal can overview undesirable properties as the ferromagnetic nature associated to iron structures and not suitable to MRI. By other hands in vivo experiments shows that the degradation resistance is not as satisfactory as in-vitro experiments and so degradation behavior can be lower than the one represented in figure I.3a). Mechanical properties can be a lower point in the use of biodegradable Fe alloys, due to the high Young modulus presented by those alloys and observed in figure I.3.b) [16]. The recommended daily allowance of iron is about of 10 mg, much lower than magnesium, but it is an essential element presented in cells and body fluids [17].

The main problem in the applicability of magnesium alloys is the high inherent biodegradation behavior, which can be comprehended by observing figure I.3.a). As consequence resorption and high rate of hydrogen release (a product from reactions presented in magnesium corrosion) can lead to medical complications. Magnesium and alloy elements used in biodegradable metals are usually nontoxic, but resorption (high degradation rate leads the increasing concentration of alloy elements in medium, which can cause an adverse biological response) can inverse these beneficial properties. Elements usually present in the body and used in those biodegradable alloys are Mg, Zn, Ca and Mn [18]. Hydrogen release is other intrinsic problem offering by the biodegradation of Mg alloys, due to the probable cyst formation. Gas pockets, necrosis of surrounding tissues, bloodstream block, can even lead to the dead of the patient and serious problems due to the high reactivity of magnesium [18]. The in vitro hydrogen evolution rate for Mg and Mg alloys containing Mn and Zn (per example) are reported to be within tolerable limits, as <0,01 ml/cm2/day [18]. The recommended daily allowance for magnesium incorporation into body fluids is about 400 mg. Zinc is also reported to fulfill biocompatibility requirements, with an allowance recommendation of 40 mg per day [17].

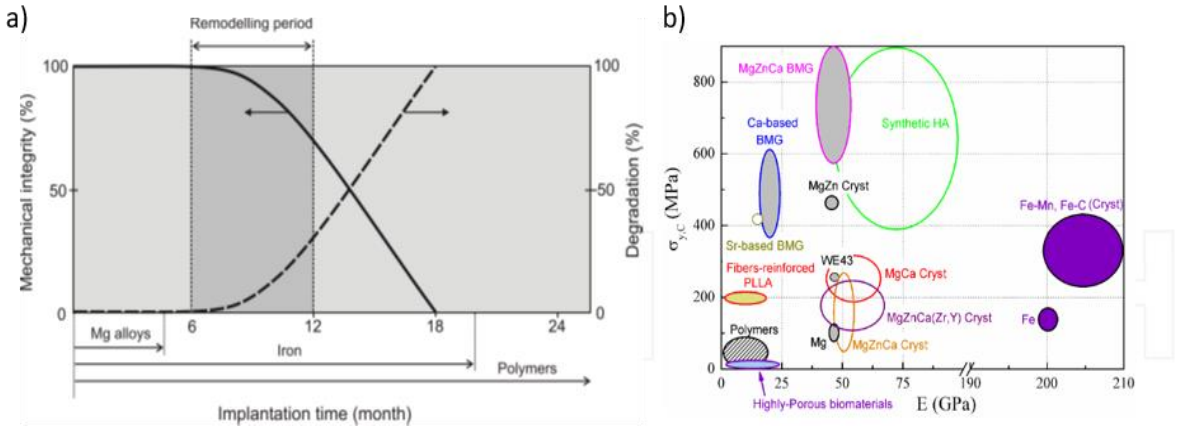

Figure I.3 - Illustration a) ideal behaviour between degradation vs mechanical integrity for biodegradable biomaterials, b) young modulus vs tensile compressive stress of diverse classes of biodegradable biomaterials [13].

I.3 Corrosion in magnesium

When the subject is corrosion it is important to find a definition for this phenomenon. When the subject is corrosion, it is important to find a definition for this phenomenon. It is wise to understand that corrosion affects all the branches of materials known, like ceramics, polymers and metals, among others. In literature it's possible to find a definition that well defines corrosion: "Corrosion is the deterioration of a substance (by electrochemical or chemical interactions) or its properties because it's reaction with the environment" [19].

The definition supported on the concept of degradation does not describe all the phenomena associated with corrosion, particularly those concerning of metals. An example of this particularity is the formation of an oxide layer on the surface of materials, in certain environments, which in particular cases prevents or retards the metal degradation, i.e. it affects the corrosion rate. It is necessary to understand that corrosion is mainly an interfacial reaction that occurs between the material and its environment, in which the material oxidize, and the environmental species (for example H_2O, O2) reduce.

In corrosion science, metallic corrosion represents a critical subject, especially when in contact or exposed to aggressive media, such as moisture and aqueous environments. Beside that corrosion plays a significant role in economy, and his prevention or correction is critical for society and all kind of materials [20]. Metal corrosion is characterized by the invertibility of electrochemical reactions (redox), occurring under a difference in potential and under the presence of an oxidizing agent. Metal oxidation will remove atoms from metal structure to the environment, which are ionized due to the loss of charge for an oxidizing agent, occurring reduction of the oxidizing agent. The electronic exchange between this two agents, from an electrode (the electric conductor) to an

electrolyte (ionic conductor) is the cause of the electrochemistry and metal corrosion can be seen as an electrochemical system.

Magnesium and its alloys are very active due to the presence of magnesium elements, inducing a poor corrosion resistance in aqueous solutions. To understand the corrosion of metallic species the 2nd Principle of Thermodynamics can be cited, which essentially, states that: "the matter tends towards a maximum state of disorder" and two systems in contact will share the energy until reaching an energetic equilibrium. Chemical potential (or free energy) tends to be decreased to get a state of minimum energy. For that, atoms on the surface of a metal tend to leave the crystal lattice when in contact with a more stable medium, originating corrosion [20]. That is a real problem in engineering applications of magnesium and its alloys, and frequently it is used passive protection, coating the surface against reactive mediums. In the application of biodegradable alloys, the problem becomes tricky since the corrosion is preferential, but it is necessary to slow down the rate of corrosion, because of loss of mechanical by the biodevices and other complications addressed in section I.1 and I.2. It is important to refer the inability of magnesium to establish and/or maintain protective surfaces films, which contributes to a low corrosion resistance of Magnesium and Magnesium alloys. Surface films formed on Magnesium surface under ambient air or aqueous conditions, typically consists of mixtures of MgO or $Mg(OH)_2$. Those films can provide adequate protection depending on environment, but the vulnerability to disruption by salts specimens decrease the protection effect [21]

Corrosion of magnesium in aqueous solutions, like water, proceeds according to the following reactions (Eq. 1 - 5), leading to the formation of gaseous hydrogen and magnesium hydroxide as main products. The magnesium hydroxide produced can work as a quasi-passive film when deposited on the metal surface [22], providing some corrosion protection to the bulk material. The balancing cathodic reaction results in an increase of pH, which favors the precipitation of $Mg(OH)_2$, which can stabilize the passive film. With time, the cathodic reaction leads to an alkalization of the solution, owing to the balance between the anodic (oxidation) and cathodic (reduction) partial reactions. Therefore, the overall reaction results in a pH increase. It must be mentioned that hydrogen evolves during the response according to the partial cathodic reaction [23].

$Mg\ (s) \rightarrow Mg^{2+} + 2e^-$	(anodic partial reaction)	(I.1)
$2H^+ + 2e^- \rightarrow\ H_2(g)$	(cathodic partial reaction)	(I.2)
$2H_2O_{(aq)} + 2\ e^- \rightarrow H_2(g) + 2OH^-$	(cathodic reaction)	(I.3)
$Mg^{2+} + 2OH^- \rightarrow\ Mg(OH)_2$	(product formation)	(I.4)
$Mg\ \ + 2H_2O_{(aq)} \rightarrow Mg(OH)_2 + H_2(g)$	(overall reaction)	(I.5)

I.3.1 Thermodynamics of Corrosion

In an electrochemical cell, the anode is always the site of oxidation, independent of is polarity.

Faraday's law, which tells us that a charge transfer occurring at a specific time, given by equation I.6, will measure the current value associated with those process, relating the charge transfer and the mass of products formed:

$$I = n.F\frac{dn_i}{dt} \qquad \text{Equation (I.6)}$$

, where I is the electric current in amperes, dn_i/dt represents the rate of reaction in mols/s, F is the Faraday constant (96.485 C/mol) and n the non-dimensional charge number representing the stoichiometric coefficient of the electrons in the equation for electrode reaction [24].

By this, it is easily understood that corrosion rate can be characterized by a weight loss, or by measuring the current between electrolyte/electrode in a defined area (current density), as examples. Usually corrosion rate it is a measurable quantity by a mass loss unit per surface per time.

Progressing with corrosion, the formation of corrosion products (see partial anodic reaction I.1 and overall reaction I.5), which can be formed by dissolved anions and cations, can lead to compacted and/or porous films formation. Acidic environment usually has affinity not to form precipitates. The solubility of products of corrosion in a closed environment will determine the preponderance to occur precipitation at the metal surface. At neutral or basic conditions (and sometimes in acidic environments) it's possible that non-soluble compounds (with low solubility constant) are formed, and so precipitation of corrosion products at metal surface form a surface layer, which can slow down corrosion rate but hardly stopping it down [22].

Oxide films are an example of corrosion products that offer corrosion resistance and are considered a compact film, which is formed on the surface, protecting the metal to corrode. Usually is a very thin layer in the order of nanometres and is intrinsic to metals. As such it is always important to understand how the corrosion rate can be affected by properties of corrosion products, which can change over time if new compounds are precipitating and changing structural properties. The changes on properties can offer problems as accelerated corrosion over time and to well understand the reaction mechanisms it is important to conduct experiments over long immersion times, to evaluate the performance affectation by the deposition of corrosion products.

The corrosion rate of metals is mainly determined by the reactivity of the metal-environmental interface. And so chemical and physical characterization of interface and

electrochemical behavior at certain environment should be done, to understand well corrosion of metals [24].

Chemical equilibrium, corresponds to the minimum free energy state, and spontaneous reactions always undergo to the minimum free energy state, and so:

$$\Delta G^0 = -RT \ln(K) \quad \text{(I.7)}$$

, where ΔG^0 is the standard Gibbs free energy, R the universal gas constant, T the temperature and K the chemical rate equilibrium constant. The same goes for an electrochemical reaction, but the standard free energy it is given by:

$$\Delta G^0 = -nFE^0 \quad \text{(I.8)}$$

,where E^0 is the standard free potential, and some values are addressed in Table I.3, which is also understudied as the equilibrium potential of a cell reaction. An electrochemical cell includes two half–cell reactions between an electrode/electrolyte, and the equilibrium potential of an electrode is the difference in the electric potential between metal and solution, at equilibrium. Electrochemical characterization techniques usually measure potentials, but what is measured is the potential differences between two electrodes, since the electrode potential cannot be measured in an absolute manner. It is necessary to create a reference electrode, and the so-called standard hydrogen electrode (SHE) is chosen as a standard reference electrode. By convention, the SHE is in respect to 1 atm pressure and 298 K of temperature. The electrochemical series of standard potentials can be observed in Table I.3 for different half-cell reactions.

If the same metal species have more than one oxidation state, the potential equilibrium in respect to metal is referred to the oxidation state which is less noble [25]. Electromotive Series was constructed under very restrictive conditions and in general, is reproducibility is not practical. The use of different electrolytes may also change the relative potentials of different materials. Galvanic series appears as another possible series based on real solutions, determining the nobility of metals and semi-metals, and both series are in good agreement.

Some exceptions can are found in the Electromotive Series. In a 3% NaCl water solution titanium develop a cohesive and adherent oxide layer, which shields the surface from corrosion and transforms is potential from negative (anodic) for positive (cathodic), making it the most corrosion-resistant structural metal known until today, becoming in metal with a higher potential than silver. Interpreting the Electromotive Series (the same interpretation is valid for Galvanic series), negative potentials denote an active potential, and the lower this value is, a more reactive metal to corrosion can be observed. One should not occur without the other and due to the coupled between anodic and cathodic reactions, a cathodic reaction with a nobler (more positive) potential has to be possible in that system

for corrosion to progress spontaneously. Another particularity occurs in the presence of complexing agents, which replaces water molecules in the hydration of a dissolved ion metals. Those ligands change the stoichiometry of the dissolution reaction of metal, leading in general to a lower standard potential. The ion Cl^- is an example of a complexing agent. It is possible to measure the equilibrium constant of a complex formation between an ion Mn^+ and the dissolved complexing agent, using Nernst equations [26].

Table I.3 - The Electromotive Series adapted from [26] for some elements. Potentials are relative to SHE reference, at 25ºC, 1 atm of pressure for gas phases, ion concentration of 1 mol and the solid phases are pure.

	Electrode reaction	Standard Potential, E^0 (V)
Noble Metals	$Au^{3+} + 3e^- \rightarrow Au$	1,50
	$Pt^{2+} + 2e^- \rightarrow Pt$	1,20
	$Ag^+ + e^- \rightarrow Ag$	0,799
	$Cu^{2+} + 2e^- \rightarrow Cu$	0,37
Reference	$H^+ + e^- \rightarrow H_2$	0
Active Metals	$Ni^{2+} + 2e^- \rightarrow Ni$	-0,250
	$Fe^{2+} + 2e^- \rightarrow Fe$	-0,440
	$Zn^{2+} + 2e^- \rightarrow Zn$	-0,763
	$Mn^{2+} + 2e^- \rightarrow Mn$	-1,185
	$Ti^{2+} + 2e^- \rightarrow Ti$	-1,63
	$Al^{3+} + 3e^- \rightarrow Al$	-1,66
	$Gd^{3+} + 3e^- \rightarrow Gd$	-2,279
	$Dy^{3+} + 3e^- \rightarrow Dy$	-2,295
	$Mg^{2+} + 2e^- \rightarrow Mg$	-2,37
	$Na^+ + e^- \rightarrow Na$	-2,71
	$Ca^{2+} + 2e^- \rightarrow Ca$	-2,76
	$K^+ + e^- \rightarrow K$	-2,92
	$Li^+ + e^- \rightarrow Li\ (s)$	-3,05

POURBAIX DIAGRAMS

The potential – pH diagrams, also called Pourbaix diagrams, relates the dependency of the reversible potential of an electrode reaction with pH in water and is very useful in engineering applications. Through Nernst equation, it is possible to calculate the values of potential. Pourbaix diagram represents all the standard chemical potentials (y-axis of

Figure I.4) possible and the domains stability of oxides, ions, and other species into solution, achieved at a certain pH (x-axis of Figure I.4).

One can be seen three types of lines, plotted in the diagram. The vertical lines represent reactions which occur independently of potential and are characterized by pure redox reactions. Horizontal lines are pH independent and represent charge transfer reactions, which involves only electrons and reduced and oxidized species. The slope lines are pH and potential dependent and represent reactions involving electrons and ions. Those lines distinguish three typical domains, the passive domain (occurring due to the formation of an oxide and/or hydroxide layer), the immunity domain, where metal do not corrode, and the active corrosion domain where anodic dissolution of metal occurs. The reactions of water decomposition are represented, and they play the role of partial cathodic reaction (reaction I.2) since the oxidation of magnesium reduces water, and the stability domain in which magnesium is stable is below to the stability domain of water [27]. The potential of Magnesium is very active, and under this conditions, the Pourbaix diagram of water shows liberation of hydrogen and alkalinization of electrolyte (Figure I.4.a)).

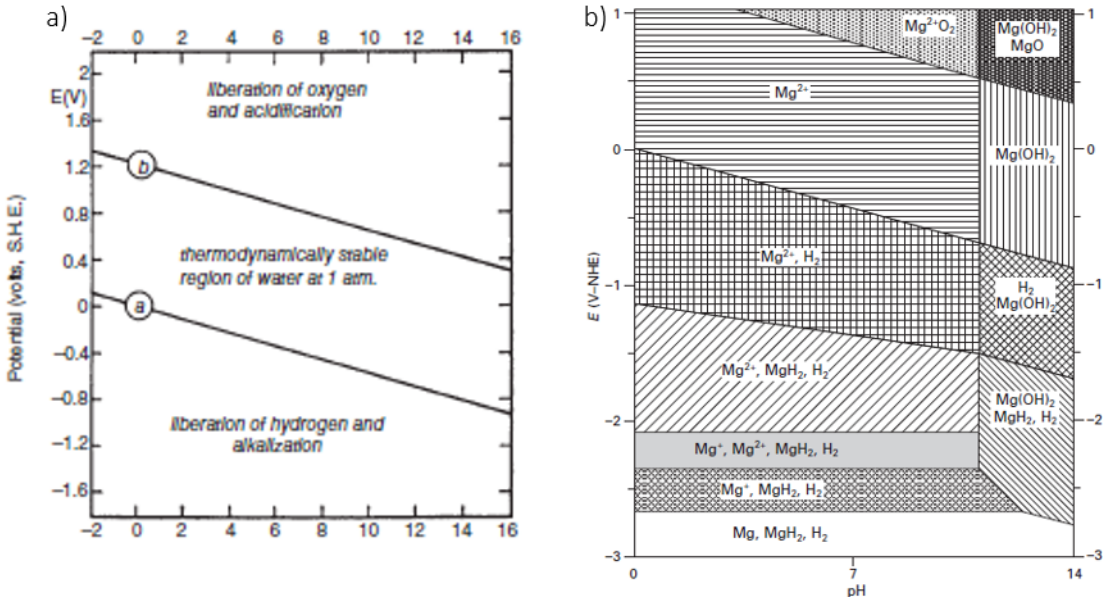

Figure I.4 - Pourbaix Diagram (T=25 °C) of a) water, showing the hydrogen line in a, below which hydrogen is evolved, the oxygen line in b, above which oxygen is evolved and the stable region of water (do not react) in between line a and b, b) magnesium showing the range of corrosion (in between vertical and horizontal line), passivation(after the vertical line) and immunity (below the first horizontal line counting from top of graphic) [28], [22].

Reactivity of magnesium in water can undergo many possible reactions and so Pourbaix diagram for magnesium it is shown in Figure I.4.b). This diagram takes into account the most probable compounds formation and it can be seen that the passive regions limited by the vertical line can underline different corrosion products. The corrosion domain potential vs pH is large and the immunity domain very narrow, undergoing to

values of potential (below -2.5 V) well below of the magnesium standard potential. A high alkaline passive domain is observed after 10.5/11 of pH. The main products of the magnesium oxidation are shown in the respective regions and are magnesium ions, oxides, and hydroxides. For the stable region of water and the active region of magnesium, only Mg2+ are resulting from magnesium oxidation.

While Mg dissolves below a pH value of approximately 10.5 (depending on the ionic concentration), it forms a passive $Mg(OH)_2$ film at higher pH values, as shown in the Pourbaix diagram (Figure I.4.b)). The blood pH is around 7.3 – 7.4 since it presents buffer inorganic salts, and consequently the magnesium is actively dissolved because of is high reactivity appetence and extremely low standard potential. Those consequences lead to a high susceptibility of Mg and its alloys to galvanic corrosion, and it is a serious matter in Mg technology for diverse applications [22].

Pourbaix diagram can only predict the thermodynamic behavior of metals in water, and nothing tells about the kinetic of corrosion, which plays a significant role in the magnesium corrosion. For body fluids, it is possible that passive products as $Mg(OH)_2$ are not forming during magnesium corrosion process, and although they are water based solutions, their chemical nature can affect the standard potential vs pH domains and the respective product formation. Another particularity of Pourbaix diagram is that it assumes all the substances formed are uniform. A pH gradient can originate during Mg corrosion between the metal surface (local pH) and bulk solution, due to the high reactivity of magnesium, affecting the stability of compounds formation. Another particularity is that it's not taking into account the presence of other aggressive species (as Cl^-) in the solution, which can change passivity range of formation for higher values of pH [22].

I.4 Types of Corrosion and Particularities of Magnesium and it's Alloys

Corrosion is characterized by different types and it is highly dependent on chemical composition and microstructural features of metals. In this subchapter, it will be presented certain kinds of corrosion and some specifications of magnesium. At the end of the subchapter the Negative Difference Effect, phenomena intrinsic to Magnesium and Magnesium alloys will be explained and referred the primary mechanisms proposed behind this effect.

I.4.1 Uniform corrosion

If metal alloy presents a relative uniform microstructure, being not possible to distinguish between a cathode or anode site, the entire surface of metal acts simultaneously as cathode or anode. The uniform microstructure can lead to uniform corrosion. The anodic dissolution present in this type of corrosion leads to a uniform loss of material distributed to the entire surface exposed to the corrosion medium. During dissolution, the metal atom leaves the structure and goes as an ion of valence into the solution with the evolution of

hydrogen. At pH 7 and above the cathodic reaction supports the formation of OH- and H2 (g). Acidic environments are characterized by hydrogen reduction, without formation of Hydroxyl groups, and so the formation of oxides/hydroxides passive films can be compromised. The metal phase is an electric conductor, and so it supports the transfer of charge and the occurrence of the processes are separated in sites, on the metal surface. The uniform corrosion is characterized in such a way that this distance is in few atom diameters. Those sites are changing over time, and uniform corrosion goes further. Oxygen dissolution can affect the formation of products and will not be addressed since it does not play a significant role in the scope of thesis [29].

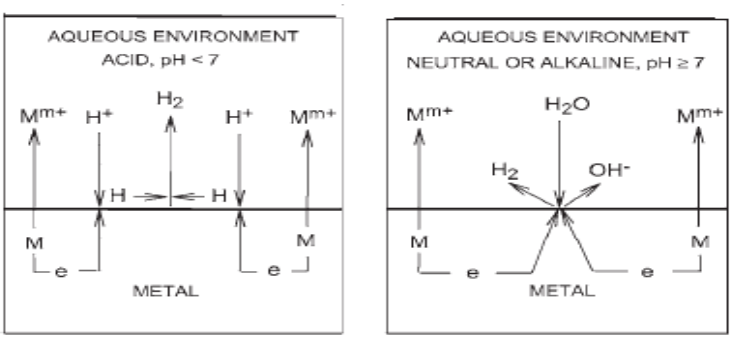

Figure I.5 - A schematic illustration of the uniform corrosion mechanism, with pH dependency [29].

I.4.2 Galvanic corrosion

The difference in this type of corrosion is referred to a dissimilar metal corrosion. The difference in standard potential between two different metals, electrically connected and exposed to the same electrolyte, undergoes to an equilibrium in potential difference which leads to the dissolution of the less noble metal and cathodic protection of the noblest one. It is so possible to distinguish between two types of galvanic corrosion. The external galvanic corrosion, which can occur with the coupling of two different metals, or internal galvanic corrosion, which is a result of the intrinsic microstructure of metal. Regarding the thematic of this work, the last one will be addressed.

It can occur like a severe localized attack to the anodic phase. Impurities elements like Fe, Ni or Cu are present in pure magnesium, defining structural characteristics and bring the corrosion to internal galvanic corrosion. They have a detrimental effect on corrosion performance of Mg even when present in only small amounts. Micro-galvanic cells are resulting from the formation of impure phases, due to the low solubility of impurities in Mg, offering a consequent low hydrogen overvoltage. A way to strike this problem is, during alloy production, use high purity material to keep the impurities at low levels, below a tolerance limit. The secondary phases present in Magnesium alloys can also act as micro – cathodes leading to the dissolution of the Mg matrix adjacent to them. However, it is rarely that alloying elements (as Zn, Cd) cause higher damage than the impurity elements due to their higher hydrogen overvoltage, and that will lower potential

difference between anodic and cathodic regions in the alloy (in respect to magnesium). It is important to note that several factors can increase the susceptibility of metals to galvanic corrosion. Those factors can be high conductivity of the medium, the large potential difference between anode and cathode, the low polarizability of anode and cathode, large area ratio of cathode to anode and a small distance from anode to the cathode [30],[31]. The common galvanic effect can be explained by the following relationship [32]:

$$I_g = (E_c - E_{an})/(R_{p(an)} + R_{p(C)} + R_s + R_{p(an-C)}) \quad \text{(I.9)}$$

, where I_g represents the galvanic current, E_c and E_{an} indicate the corrosion potential of the cathode and anode, respectively, the $R_{p(c)}$ is the polarization resistance of the cathode, $R_{p(an-c)}$ is the electrical resistance between the anode and cathode (which normally can be negligible if the two electrodes are in direct electrical contact), $R_{p(an)}$ is the anodic polarization resistance and R_s is the electrical resistance of the electrolyte.

Regarding these affirmations and the electrochemical properties, the best candidate for a biodegradable implant would be high purity Mg alloys. However, this is not necessarily true because HP Mg does not meet the mechanical requirements and so it is an undesirable approach. Another form of cathodic activity can undergo at the grain boundaries regions, where the grain interior regions can support anodic activity. Hence, corrosion does not propagate along the grain boundaries, but take place in the matrix close to the grain boundaries and eventually leads to undercutting and grain fallout. This concept is controversial [33], because some reports a fine microstructure to have more grain boundaries, which can act as corrosion barriers and increase the corrosion resistance. It is important to consider the processing route, because of microstructural changes, such as the phase distribution or dislocation density, also affect the degradation behavior. Dislocations, for example, are said to locally decrease the equilibrium potential leading to accelerated dissolution [33].

I.4.3 Pitting corrosion

It is a type of localized corrosion that leads to corrosion gradients at the surface of the metal (which should present a passive layer) and formation of pits. These pits are the occurrence of relatively small active anode places, which loss atoms from the structure, promotes a pit with a certain depth. The as like hole depth can express a pitting factor, and the ratio between deepest pit and the average metal penetration can be determined by the weight loss of sample. An approach to this method is represented in Figure I.6. Aggressive anions can play a significant role in this type of corrosion and cavities usually are in order of tens of micrometers. An oxidizing agent such as oxygen and/or ferric ions can also induce pit behavior. Another particularity is the anode/cathode surface ratio, where dissolution inside the pit can increase if the surface ratio is small [27].

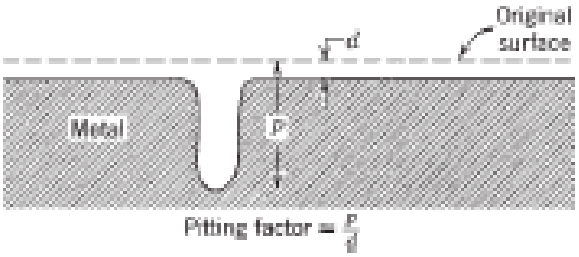

Figure I.6 - Pitting corrosion mechanism [27].

In magnesium, stable pits can be formed at adjacent faults to an intermetallic fraction presenting cathodic behavior, which occurs due to the breakdown of a supposed passive surface films [16]. Low passivation alloys or heterogeneous electrolytes also can show this type of corrosion.

A mechanism of pit initiation is proposed [24] and is known as anodic de-passivation. It is characterized by the penetration of aggressive anions such as chloride into the passive film, which could exchange positions in the crystal lattice of the passive film with O^{2-}. This effect could increase the electrical conductivity of film and/or the formation of soluble compounds (as per example magnesium chloride compounds) leading those two factors to the breakdown of the passive film.

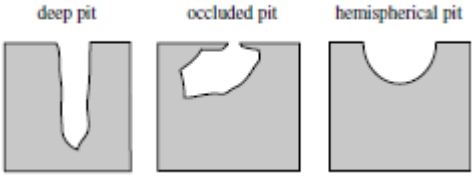

Figure I.7 - Different morphologies of pits [24].

Pits can present different morphologies as observed in Figure I.7. Those are the main pits morphology, which can show deep narrow spots exhibiting crystalline attack, occluded pits which can grow under corrosion products layer or hemispheric pits with a large corroded surface.

In magnesium, corrosion can occur at preferred crystallographic planes. In [34] it was observed that a crystallographic dependence for pitting susceptibility of Mg single crystals could happen, with the basal plane of Mg (0001) exhibiting the lower resistance to localized corrosion [35].

I.4.4 Crevice corrosion

The occurrence of this In stagnant electrolytes, it is prone to occur crevice corrosion. The occurrence of this type of corrosion usually starts what metal/alloy surfaces holes, lap joint under bolts or at crevices, as examples. The mechanisms behind crevice

corrosion are related to oxygen depletion (gradient in concentration of inside and outside crevice) and acidification inside a crevice, which is characteristic, particularly, for high passivity metals [27],[35].

Magnesium metals do not usually present crevice corrosion since the galvanic effect is mainly a consequence of hydrogen evolution and not oxygen reduction. But in practice, crevice corrosion can be observed in magnesium alloys, but due to the accumulation of moisture, or when the crevice section is exposed to a solution for a longer time than the outside section. In those case, the mechanism behind crevice corrosion is not oxygen depletion and consequent acidification [22].

I.4.5 Filiform corrosion

It is a localized type of attack that undergoes in coated metal surface [27], as per example for magnesium alloys, where a passive hydroxide/oxide magnesium layer is present [22]. It can be seen as tunnel structures forming under a passive film formed on the metal surface. Pitting and uniform corrosion is possible to occur at the same time as filiform corrosion is present. The morphology of filiform corrosion can be observed as randomly distributed thread-like filaments [35]. It is interesting to note that in a passive state, localized attacks are more frequent to occur than at an active state [16] and so filiform and pit corrosion can occur. Other factors which affect localized attacks are the weak conductivity of electrolyte and the relatively small area ratios between anode/cathode [35]

This type of corrosion can initiate in NaCl solutions as well as pitting corrosion. Filiform can initiates and evolve its morphology projected from the pit, appearing as a like semi-cylindrical filament structure. Also, the development of filiform corrosion can lead to pits, developing from the morphological filament. It is observed this type of corrosion in some uncoated bare extruded magnesium alloys, which can indicates the presence of naturally formed high resistant oxide films. It is stated that this kind of corrosion is accompanied with a voluminous gas evolution at the front head of filiform [22]. The ionic diffusion, which can be observed by electrochemical means of chloride ions, can be behind this corrosion phenomena in magnesium [22].

An example of filiform corrosion can be observed in an AZ91D Mg alloy in alkaline chloride solutions. An anodic dissolution characterizes the different stages and at the same time by the “growth, absorption and desorption of hydrogen bubbles, the development of pitting corrosion and the possible inhibiting process by protective MgH_2 film”, stated in [22]. Chloride attack can lead to this type of corrosion.

I.4.6 Stress Corrosion cracking

Induced tensile/residual stress and environment of corrosion affect this type of corrosion, and failure appears to be brittle if under SCC. The tensile/residual stress comes

from manufacturing processes that can induce deformation (as in welding processes, specifically in heated affected zones).

Stress corrosion cracking can appear as transgranular or intergranular if the origin od corrosion is related to mechanical stress of structure. This corrosion can occur from the first minutes of time exposition or during many years follow in stressed metals [27].

The initiation of SCC starts from the exposure of metal in an appropriate environment, followed by a stress crack initiation and ending in is propagation. Metallurgical, mechanical and environmental are preponderant factors to control this type of corrosion [27].

Specifically for magnesium, the susceptibility to this corrosion is higher to Mg-Al alloys, increasing with Al concentration. It is also observed in Mg-Zn alloys, and free Al and Zn magnesium alloys should present increased resistance to stress crack corrosion. Environments that can induce this type of corrosion in magnesium alloys are deionized water, seawater, urban industrial, coastal areas and many others, with the dissolved oxygen playing an important role in the acceleration of the SCC. In magnesium, the SCC is usually transgranular [27], where secondary and/or branching cracks, often initiate in pits. Hydrogen embrittlement is seen as a preponderant factor which affects SCC [27],[36]. It is important to perform periodic inspections to prevent this type of corrosion.

I.4.7 Intergranular corrosion

Intergranular corrosion, also known as intercrystalline corrosion, is a localized type of attack along/at the anodic grain boundaries in a metal microstructure, where inside areas of grains acts like a cathode, to support an electrochemical reaction. The dissolution of grain boundaries leads to the formation of deep sites, which can works to the loss of mechanical integrity of the full structure [27]. Grain boundaries can provide a nucleation site for phase precipitation from unstable solid solution. The precipitation of constituents in grain boundaries, as carbides, is usual to occur in stainless steels and if occurring, is called sensitization, and the susceptibility to intergranular corrosion increases [35].

If precipitation constituents are concentrate in grain boundaries and are anodic in respect to adjacent matrix (undepleted solid solution), intergranular corrosion can occurs. But chemical composition gradients can originate solution depletion zones, in between precipitates and matrix. If depletion zone is cathodic in respect to precipitate, case represented in Figure I.8, and under anodic dissolution of boundaries phase, metal ions A^+ and B^+ are released to the medium and X^+ suffer reduction at metal surface. A particular case of previous one can occur when precipitates are discontinuous structures along the grain boundaries. In Figure I.8.b) it is possible to observe this particular case and localized attack occur at this regions. The results in the microstructure of the cathodic deplected zone in Figure I.8.a) is a continuous defect type of crevice [29].

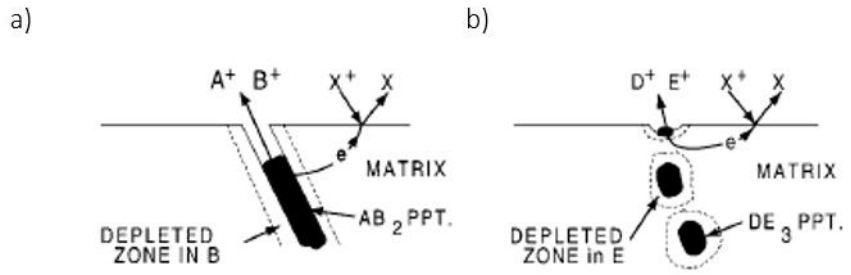

Figure I.8 - Illustration of a intergranular type of corrosion in which grain boundaries phases are anodic in respect to depletion zone and matrix, a) continues phase structure b) discontinues phase structure [29].

Figure I.9 shows another case where depletion zones are anodic in respect to grain boundaries and/or undepleted zones (matrix). In both cases matrix and/or precipitates in grain boundaries are supporting cathodic activity. If the precipitate structure is continuous the depleted zone is excavated and the defect structure it is introduced near grain boundaries. This effect can be observed in Figure I.9.a). The Figure I.9.b) shows a particular case where a discontinuous phase structure it is seen. In this case undermined particles (which acts as cathodes) are released into the medium due to the dissolution of depleted zones. In both cases, the reduction of specie X^+ is occurring at the metal surface. Depleted zones can be seen as enrichment zones of the element forming boundaries grain precipitates when compared to the matrix. Alterations in solid solution (matrix) inside the grain is frequent to occur if anodic to the depleted zone. In both this cases localized attack are observed, and large local corrosion rates are noted mainly due to the large cathode/ anode area ratios [26],[29].

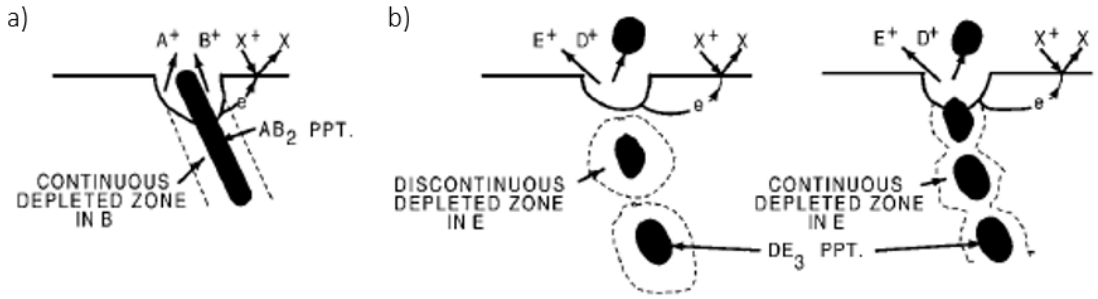

Figure I.9 - Illustration of a intergranular type of corrosion in which grain boundaries phases are cathodic in respect to depletion zone and/or matrix, a) continues phase structure b) discontinues phase structure [29].

Due to the low standard potential of magnesium, usually, alpha matrix (magnesium matrix) works as an anode and intermetallic, and/or the precipitates works as a cathode. Intergranular corrosion is not frequent to occur in magnesium and its alloys. By another hand, interdendritic corrosion takes place in cast metals, which progresses along preferentially paths between dendritic formations [26].

About a critical chloride concentration, exfoliation can occur, particularly in unalloyed Mg, considered as a type of intergranular attack and is not observe in Mg alloys. This process is characterized by a preferential attack at certain crystallographic planes. Swelling is a result of this localized attack, and is caused due to an apparent delamination of magnesium crystals intercalated with corrosion products. Further in time, the corrosion attack can lead to the disintegration of partially whole grains, leaving behind large irregular pits shapes [36].

I.4.8 The Negative Difference Effect in Magnesium and it's Alloys

The Negative Difference Effect is related to the corrosion of magnesium. Partial cathodic reaction (reaction I.2) during corrosion release hydrogen gas and the anodic reaction (reaction I.1) is responsible for the dissolution of magnesium ions into solution. This is true but, under certain circumstances, it is noted an increase of the hydrogen evolution reaction rate (HER) during anodic reactions, so a cathodic product is formed during the anodic reaction. The NDE can be observed under polarization measurements, where a nobler applied potential is accompanied by hydrogen evolution release [37].

Figure I.10 represent a Tafel kinetic plot, in which anodic and cathodic potential-current lines are highlight by I_a and I_c, respectively. The intersection of both lines leads to the I_o at E_{corr}. Tafel theory says that when applied a nobler potential, E_{app}, the rate of anodic half reaction I_a, should follow the $I_{Mg,e}$ direction [37]. At the same time the cathodic half reaction should decrease along the curve I_c until reaching the $I_{H,e}$ position.

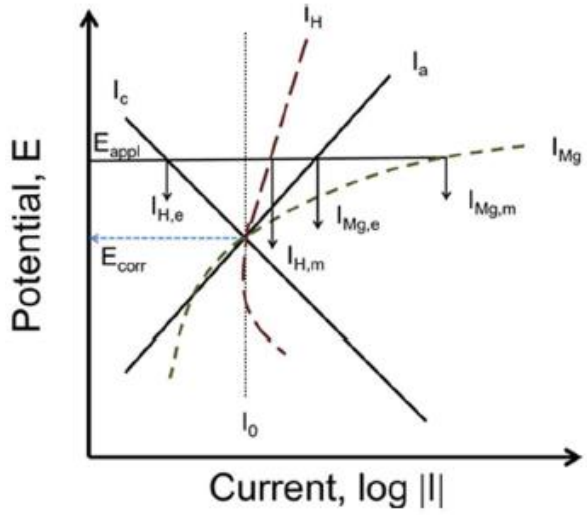

Figure I.10 - Illustration of the NDE under applied potential (Tafel kinetic plot) showing differences in the Tafel theory in magnesium [37].

The statement before was telling the expected behavior, but instead when applied a more positive potential E_{app} in respect to E_{corr}, the rate of cathodic reaction follows the direction of the dashed line I_H, until reach $I_{H,m}$. Meanwhile, anodic reaction current for

magnesium increases fast and follows the dashed line I_{Mg}, until reach $I_{Mg,m}$. The $I_{H,m}$ is higher in current than $I_{H,e}$ so an increase in the HER rate is noted during anodic polarization. The negative difference is in respect to I_o. By another hand, the anodic current for magnesium follows at higher rates than the expected by an anodic potential-current line. So it is possible to state that Faraday's law is not fulfilled. Over decades scientists are trying to deal with this phenomena, and different mechanisms have been proposed by the scientific community, which will be now addressed.

The partially protective film

Under anodic polarization, current is flowing in between the metal surface and electrolyte. NDE is a direct result of the breakdown of the passivity [37] and pits formation occurs. Associate to this phenomena could be related the adsorption of aggressive ions, like chloride, instead of OH^-. Also, the creation of pits could support a cathodic reaction inside the pit, and so the increase of potential, which leads to more pits formation, increasing hydrogen release under anodic polarization [38]. Figure I.11 represent this effect where it can be observed the formation of passive films as $Mg(OH)_2$ and MgO [39], [40] and posteriori local attack of passive film. However there is no direct evidence that the film is partially protective and Parrault [41] criticized this mechanism, since it is not explaining the corrosion potential of magnesium under neutral or acidic solutions.

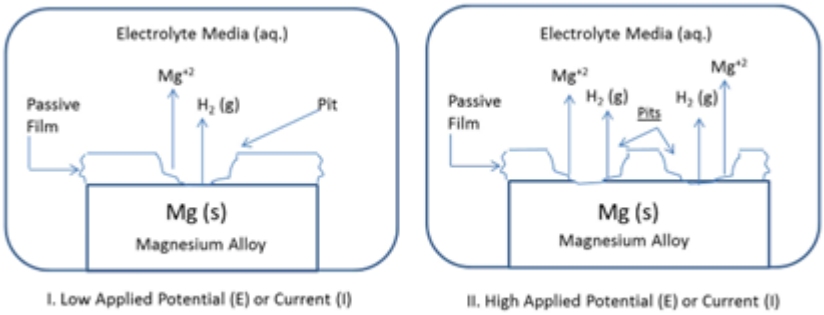

Figure I.11 - Illustration of the partial protective film under low and high applied potential and current [42].

Undermined particles

Another possibility of the appearance of a NDE during anodic polarization it is appointed to the undermining and removal of secondary phases which acts as a cathode [43], [41]. The particles undergo accelerated local corrosion at the particle boundaries by galvanic corrosion. This behavior usually leads to higher corrosion rate performed by weight loss than electrochemical dissolution.

Monovalent Mg Ion

A transient monovalent magnesium ion can be evolved during anodic reaction:

$$Mg\ (s) \rightarrow Mg^{+} + e^{-} \quad \text{(I.10)}$$

,the calculated valence of Mg^{+} is reported in between a range of 1.33 to 1.66 and can be found in literature [27], and by the following equation hydrogen gas is been releasing, during anodic dissolution:

$$Mg^{+} + 2H^{+} \rightarrow 2Mg^{2+} + H_2(g) \quad \text{(I.11)}$$

Figure I.12 shows a schematic of this reaction. It was reported in [28], that between a range of -0,5 to -2 mA/cm^2 it was occurred a drop in the anodic current density to almost zero value [42].

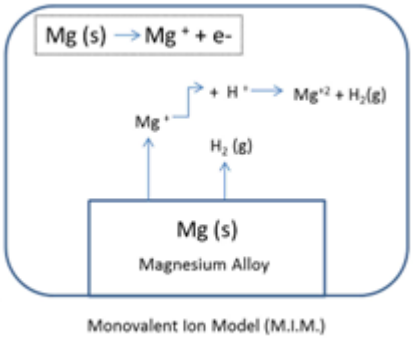

Figure I.12 - Illustration of the Monovalent Ion Model (MIM) [42].

MgH_2 formation

Another explanation is the formation of this compound, which can be observed in the Pourbaix diagram (section I.3.1). The reduction of the respective hydride:

$$Mg^{+} + 2H^{+} + 2e^{-} \rightarrow MgH_2 \quad \text{(I.12)}$$

This compound is not stable with water and reacts releasing hydrogen gas:

$$MgH_2 + H_2O \rightarrow Mg^{2+} + 2OH^{-} + 2H_2(g) \quad \text{(I.13)}$$

Equation I.13 is a cathodic reaction and so the consequent increase of anodic dissolution should decrease the HER rate and this compound formation [44], contradicting NDE.

Re-deposition of the iron impurities based on Heyrovsky mechanism

Impurities related to magnesium microstructure can influence HER during anodic polarization under two mechanisms, proposed in [45]. The re-deposition of metallic iron at

the corrosion forefront and subsequent cathodic Heyrovsky reaction of water reduction could lead to extensive hydrogen evolution under anodic polarization. The following reactions helps into the explanation:

$$H_2O + e^- \leftrightarrow H_a + OH^- \quad \text{(I.14)}$$

$$2H_2O + H_a + e^- \leftrightarrow H_2(g) + OH^- \quad \text{(I.15)}$$

Reaction I.14 shows the chemical desorption described by Tafel-Volmer mechanisms and reaction I.15 shows the electrochemical desorption process of Heyrovsky reaction, which occurs at much faster kinetics than the previous one [45]. Heyrovsky reaction can be seen as an electrode alkaline electrolysis and can cause exposition of iron impurities due to a cathodic surface activity, increasing the HER reaction under anodic polarization. It is likely, that Mg dissolution and undermining mechanism around freshly re-deposited Fe film leads to its detachment followed by dissolution, reduction and another re-deposition process [45].

Almost all the mechanisms depending on factors as film protective rupture, diffusion of active species on magnesium surface, dissolution of the exposed surface, nucleation and growth of the protective film on the bare surface and localized conductivity and pH.

I.5 Factors Affecting Corrosion in Metal and Magnesium Alloys

There are two main factors which affect the rate of corrosion of metal: the environment and the physical metallurgy. For that, it is important to identify the primary variables which can induce corrosion and characterized them.

I.5.1 Material structure and microstructural effects

Like it as mentioned before, every material has a particular corrosion potential, and so metallic alloys present specific corrosion potentials and rate of corrosion. Microstructural effects in corrosion mainly depend on the type of metallurgy conditions that affects the microstructure in different ways, and so the corrosion rate is expected to vary between alloys with the same chemical composition but subject to different metallurgical conditions. Different type of elements can be added to magnesium, and these elements usually play different roles in altering alloy's properties. Corrosion resistance is one of the desirable properties, and some alloying elements can increase the corrosion resistance, as per example, decreasing activity of the impurities like iron, by forming a new, less reactive phase or changing the chemical composition of the current phase, making them also less reactive.

Protective oxide films and the development of adherent and insoluble corrosion products provide protective barriers to the metal surface from further dissolution, and it is

important to characterize them. However, after prolonged exposure to aqueous environments, corrosion processes will result in metal dissolution. Properties like grain size, the type of intermetallic, and quantity and quality of phases are the main variables, which can hugely affect the corrosion rates of an alloy in a particular environment [46].

I.5.1.1 Intermetallic/phase formation

Intermetallic compounds which mostly arise from metal alloying, are forming during solidification of a liquid phase. It was already exposed some cases during the explanation of corrosion types, where it is possible to acknowledge the influence of such components in corrosion. Limited solubility of metals in Magnesium results in the development of secondary phase particles, which precipitate after the solubility limit was achieved. Secondary phases are characterized by specific electrochemical properties, which when in contact with a surrounding metal matrix gives rise to a localization corrosion. This phenomenon is well known in magnesium alloys [47],[48], and the localized corrosion is largely driven by the so-called "micro galvanic coupling" between those microstructural constituents. Mostly due to the intrinsic low potential of pure magnesium, the α-Mg phase assumes the anodic reaction site. An exception noted to date is the Mg-Ca alloys, where the Mg2Ca phase dissolves preferentially to the α-Mg matrix. It is interesting to refer that during localized corrosion, the anodic dissolution is supported by a cathodic reaction occurring upon "more noble" secondary phases that are polarized cathodically at the potential of the bulk alloy.

The SKPFM is a useful technique to evaluate the Volta Potential and to understand the micro galvanic relationships of intermetallic phases. Some values of Volta Potential of different intermetallic phases can be observed in Table I.4 (those values can suffer changes, strongly depending on chemical composition and environmental conditions).

Table I.4 - Estimated Volta Potential values (mV) for specific intermetallics, in respect to a specific alloy, found in reference.

Intermetallic phase	Volta Potential (mV)	Parent Alloy	
Al-Gd	90	AM50GdA	[49]
Al-Mn	257	AZ80	[50]
Al-Mn-Fe	262	Mg-Al-Ca	[51]
Al-Mn-Gd	200	AZ91DGdA	[48]
Mg-Ca	-100	Mg calcium alloy	[52]
Mg-La	50	Mg lanthanum alloy	[52]
Mg-Si	96	AZ80	[53]
Mg-Y	50	Mg yttrium alloy	[52]
Zr-Zn-Fe	180	ZE41 as cast	[47]
All depletion zone near Al-Mn phase	-72	AZ91D	[54]

The values of Volta Potential find in Table I.4 are in respect to Magnesium Matrix, which also can undergo different values in respect to the solubility of alloy elements, chemical composition and environmental conditions.

I.5.1.2 Grain size

Grain size is strongly affected by casting procedure and entropy conditions can influence not only the physical properties of the alloys but also its corrosion performance. Specifically, the decreasing of the size of magnesium grains has frequently been reported to reduce corrosion rates. These phenomena have been observed in alloys such AZ31, AZ91, ZK60 and rare earth containing systems [55]. The beneficial effect of the reduction of grain size arises from the formation of a better passive layer, an improvement in the protection capabilities of the β-phase network, and a reduction in cracking of the corrosion product layer. Once again this is not as linear as could be since some reports said that a decrease in grain size could lead to an increase in corrosion rate [48]. For sure the grain size is not the only characteristic affecting the corrosion rate but also the elemental distribution can provide some substantial changes in corrosion rates of Mg alloys. For example, a higher Al content in the inside regions of Mg grains in Mg-Al alloys can increase the corrosion resistance of the grain [56], but can also initiate grain boundary corrosion. However, it is evident from the available literature that, besides grain size, other microstructural factors affects phenomenon as micro galvanic coupling, already explain in the previous work. It is possible to claim that while grain size will affect anodic kinetics, alloying elements can control cathodic kinetics [46]

I.5.1.3 Metal as impurities

Metal impurities are different from alloy elements since their presence in microstructure it is not desirable and/or recommended. At certain concentrations, it can even be detrimental to the corrosion properties of magnesium alloys. Per example, it was found in [57] that concentrations up to 0.02 wt% of Fe, Ni, Cu and Co can induce a high increment in the corrosion rate and be severely deleterious to alloy. By other way elements as Al, Sn, Cd, Mn, Si and Na shows relatively small influence on the corrosion rate up to a concentration of 5wt%, and can even be beneficial at certain concentrations [58]. Other metal elements which can affect the corrosion rate at relatively moderate levels are Ag, Ca and Zn. It can be used as alloy elements beneficial, and relatively inert elements to corrosion.

Silicon found an interesting particularity since this metal is not detrimental as iron or other elements to corrosion of magnesium and so can be used as an alloy element. However, in [59] it is stated that Mg-containing Si impurities can present high corrosion rate due to the precipitation of Si-rich particles containing iron. This phenomenon can occur even at low ppm level, influencing the solidification behavior of Fe phase,

promoting the formation and growth of Fe particles that contain silicon. A third element can be used to reduce the tolerance limit of Fe, as Al or Mn [60].

When a certain impurity initiates a high effect in corrosion rate, the cathodic impurity can goes undermined and removed or finish to be covered by corrosion film [57]. Other studies confirmed that the most critical factor in the corrosion rate is the purity of magnesium [61]. In figure I.13 it is possible to observe the relations of certain impurities with the corrosion rate, with a special focus for iron, which is the main impurity in magnesium alloys [62],[62]. The tolerance limit for Cu, Fe and Ni are 0.1 %, 0.005%, and 0.0005 wt%, respectively. Certain alloys have an increase in the tolerance limit, as per example the AZ91, which increase the respective tolerance limit of previous elements for 900, 20 and 12 ppm, respectively [63]. Below the tolerance limit corrosion rate should be between acceptable values of corrosion (uniform corrosion).

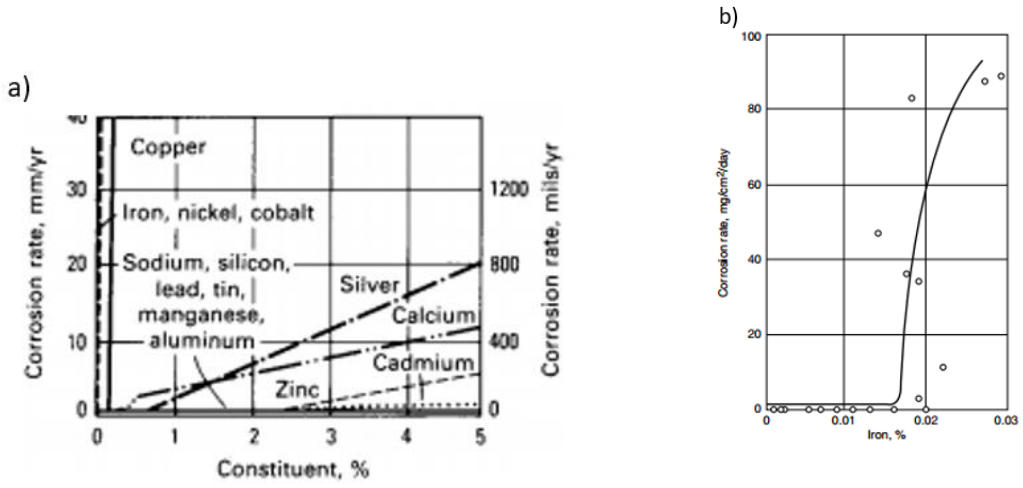

Figure I.13 - In illustration a) the effect of alloying elements and contaminant metals on the corrosion rate of magnesium, immersion in a 3% NaCl solution, b) Iron content effect in corrosion rate and the respective tolerance limit for commercially pure magnesium, immersed in a 3wt% NaCl solution [62].

Heavy metal contaminations as the ones stated before (impurities or fasteners), can induce pitting attack or galvanic corrosion, which are two types of localized attacks to the magnesium matrix [62]. Their low solid solubility induces precipitation of intermetallic compounds which acts as active cathodes in respect to magnesium matrix [59]. Effect of composition, size and distribution of impure intermetallic plays an important role into corrosion, as so the cooling rate conditions [58]. Those impurities have as origin different sources. Per example, they could come from melting tools as crucibles, copper from raw aluminum, while nickel can arise from stainless steel tools used in foundry [59]. Many times it is important to use cleaners in foundry and control chemical composition of the alloy to fulfill the tolerance limit for impurities. It is important to distinguish different types of pure magnesium, as commercially pure (CP Mg) and highly pure magnesium (HP Mg). The CP Mg are usually pure magnesium systems with a content of iron impurities

above the tolerance limit (figure I.13) of Iron for Mg (tolerance to corrosion). By another way, HP Mg is known to have content of iron below the tolerance limit. Figure I.14 shows the dependency of corrosion rate (which increase with increasing of hydrogen evolution, a feature to characterize corrosion in magnesium) where CP Mg shows a higher corrosion rate than HP Mg. Many times it is important to use cleaner in foundry and control chemical composition of the alloy to fulfill the tolerance limit for impurities [64].

The tolerance limit of Iron for Magnesium can be observed in Figure I.13. This value is in respect to the eutectic composition of Mg-Fe diagram (0.018 wt%) which can be consulted in [64]. When this content is over past the Fe in magnesium overcomes from a metastable state to form a well-defined BCC structure, which could be responsible for higher corrosion rates [64]. However, it was also noted low corrosion rates to casting magnesium containing less than 180 ppm of Fe [64].

Ultra-pure magnesium is another relatively new definition used to characterize pure magnesium and magnesium alloys with iron content less than 2ppm. The UP Mg arise from the addition of a certain amount of Zr into the molten Mg. The Zr addition leads to thermodynamic reactions, and $FeZr_x$ particles are formed. By density, these particles can settle into the bottom of the melt. The addition of alloying elements as Gd and Dy to UP Mg can improve corrosion rate even more by originating stainless Mg after to dissolve the alloying element into solid solution [61].

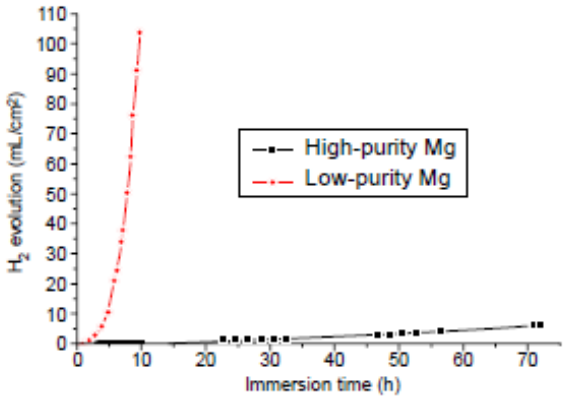

Figure I.14 - Illustration of corrosion rate dependent of hydrogen evolution with respect to immersion time. Representation of a low purity magnesium, also known as commercially magnesium with a 280 ppm and a highly pure magnesium with 45 ppm iron concentration [61].

I.5.2 Environmental Factors

In environmental conditions there are four factors that predominantly determine the rate of corrosion attack: the availability of oxygen, the type and concentration of dissolved salts in the system, pH and temperature of the environment. Oxygen usually plays a significant role in atmospheric corrosion [65], but in biodegradation of magnesium alloys it

seems to not be a key issue [23] [62], and so it will not be described in the following sections.

I.5.2.1 pH Evolution

In the pH evolution, the type of medium will play a substantial role in the characteristics of the resulting products of corrosion. Under certain conditions of potential and pH, the interaction between a metal and electrolyte form protective films in a process known as passivation. In the presence of more hostile conditions (per example acidic environment), active process of corrosion will occur. The main tool that is used to predict reactivity in the system affected by electrochemical and environmental conditions is the Pourbaix diagrams, which give us the potential-pH diagram (this subject was already addressed in section I.3.1). It is possible to predict the stability of the system and products for metal at a given pH solution and equilibrium conditions [66]. An example of a Pourbaix diagram can be seen in Figure I.4, for Mg immersed in water with a NaCl concentration of 3%. More complex corrosion environments, i.e., blood serum, may impact corrosion susceptibility of Mg alloys in a different way compared to a simple water – Mg system. For the scope of this work, some simulated body fluid and is affectation in biodegradation of magnesium alloys will be taken into account.

I.5.2.2 Chloride Ion Concentration

It has been noted that the corrosion of magnesium in water forms a hydroxide (OH^-) layer on the surface of the material. The chloride ion concentration plays a significant role in corrosion. If the corrosive medium contains any chlorides with concentrations above 30 mmol/L, the hydroxide film formed during immersion can be converted to magnesium chloride ($MgCl_2$) rather than magnesium hydroxide (observe equation I.16) [62] [49]. In the case of biological fluids where chloride concentrations are approximately 150 mmol/L, surface pitting corrosion can occur and be severe. It is important to refer that types of corrosion evidenced on the surface of metal alloys are depending upon the electrolytic medium in which the corrosion of the material is taking place.

$$Mg(OH)_2 + 2Cl^- \rightarrow MgCl_2 + 2OH^- \quad \text{(I.16)}$$

The Magnesium chloride is a very soluble compound due to the relatively high constant of solubility, and so when precipitating it can be easily dissolved, increasing the Cl^- and interrupting film formation of other compounds.

I.5.2.3 Temperature

Temperature it is also known to affect the rate of reaction as demonstrated by the Arrhenius equation:

$$r = A\, e^{-Ea/RT} \quad \text{(I.17)}$$

,where r is the reaction rate, A is the pre-exponential factor, E_a is the activation energy, R is the gas constant, and T is the temperature. Aqueous environments can have different temperatures due to geographic location, water flow and small deviations of concentration and chemical composition. According to Equation I.17, an increase in temperature increases the chemical reaction rate. The rate of corrosion tends to increase with rising temperatures, partially as a result of increased ionization and mobility of the reactants [67]. Temperature conditions in laboratory experiments are taken into account. Is possible to study the difference in corrosion rates, between environment temperatures, approximately 25°C and body fluid temperature, around 37°C specifically speaking about biodegradable alloys studies. In this work a room temperature will be considered, and it will not take into account the affectation of temperature in corrosion. Further insights can be observed in reference [68], [69].

I.6 The role of alloying in corrosion of biodegradable magnesium alloys

A wide range of elements have been tried as alloying additions to Mg to improve its mechanical and corrosion properties and, as a requirement, it is used elements that do not cause significant cytotoxicity at low concentration and, as so, can be acceptable in bioapplications. The more common alloying elements are described in this sub-chapter. When selecting an alloying element, its influence on the corrosion properties of the alloys must be taken into consideration. There is a notion in the literature that due to galvanic coupling, no alloy can attain equivalent corrosion rates to pure Mg which contains no potential localized cathodes [70].

I.6.1 Mn

The adding of Manganese in alloying is mostly to improve the corrosion resistance by converting iron into relatively harmless intermetallic compounds. It was found [58] two main mechanisms of deactivation of iron impurities by Mn addition. One is the formation during melting of intermetallic compounds which settle to the bottom of the melt, lowering the iron content of the alloy. The other mechanism known is the encapsulation of Iron particles which remain in the metal during solidification, making the iron compounds less active as micro galvanic cathode [71]. However slightly increases in the yield strength can be achieved [72].

The concentration of Mn should be less than 0,8 µg/L in blood serum. Like an essential trace element, it plays a fundamental role in the metabolic cycle of lipids, amino acids, and carbohydrates. This element also influences the immunity system, bone growth, blood clotting, cellular energy regulation and neurotransmitter synthesis. The high concentrations of Mn could induce neurotoxicity [72].

.

I.6.2 Zn

It The Zinc element plays a very similar role to the Al, when added into Mg alloys. It can strengthen the alloy and improve tensile strength, and can also improve corrosion resistance. However, the amount of addition of Zn is limited, since, for example, in Mg-Al alloys more than 2 wt% can lead to the alloy embrittlement and weaker the mechanical properties [73].

From another hand, the increasing of Zn content in Mg alloy can increase the corrosion rate. That possibly happens by becoming enriched at the surface of the alloy during corrosion. The presence of Zn within the β-phase of Mg alloys has also been reported to make the β-phase a stronger cathode [73].

Zinc it is also a trace element in the human body and its normal level in blood serum is 12,4 – 17,4 µmol/L. It is a cofactor for specific enzymes in bone and cartilage and is essential for the immunity system. However, high concentrations of Zn can lead to neurotoxicity [10].

I.6.3 Ca

Calcium also contributes to the solid solution and precipitation strengthening in Mg alloys. It can act as a grain refining agent, contributing to grain boundaries strengthening. However, large amounts can induce problems in Mg alloys, like the hot tearing. The normal serum level in blood is around 0,919 – 0,993 mg/L and can help in the regeneration of bone. It is the most abundant mineral in the human body (1 – 1.1 kg), which is mainly stored in the bone and teeth's [74].

I.6.4 Li

Lithium is a very defining element since it is the only element that can induce a change in the lattice structure of Mg from hexagonal close packed (hcp) to body-centred cubic (bcc) [74]. It can be used to lift up the ductility and formability of Mg alloys, but not the strengthening of them. It was found that Li can improve resistance corrosion of a Mg-Li-Al-Re alloy. That happens because Li shifts the pH of solution for a pH higher than 11,5 (Pourbaix Diagram figure I.4.b)), which is a stabilized region of Mg(OH)2, deposition of a film on the surface of metal. However, the in vivo alkalization is a hazard to the human body [74].

The reference values of the content in the blood serum in the human body are 2 – 4 ng/g. Lithium compounds are used for the treatment of psychiatric disorders. However, it is possible to induce overdosage by Li, which leads to physical problems to kidneys and lungs, causing potential congenital disabilities on children's [74].

I.6.5 Zr

Zirconium can enhance the yield strength through Hall-Petch strengthening and is an effective grain refining agent in Mg alloys.[74]

In vivo zirconium displays excellent biocompatibility, not being seen any evidence of carcinogenicity or mutagenicity in the physical body. In vitro, the presence of Zr exhibits a low ionic cytotoxicity. It presents an excellent resistance to corrosion, and an osteocompatibility equals or higher than those offered by titanium alloys [75].

I.6.6 RE

The RE can reduce Fe cathodic activity by forming RE-Fe phases which present less cathodic activity than Fe to Mg. The RE are considered grain refiners elements, like the zirconium element [76].

Rare earth elements are a set of seventeen elements in the periodic table, specifically the fifteen lanthanides plus scandium and yttrium. For applications in Mg alloys, RE can be divided into two major groups. Firstly, the group that has a large solid solubility in Mg, and comprises the Y, Gd, Tb, Dy, Ho, Er, Tm, Yb and Lu elements. The second group presents only limited solid solubility in Mg alloys, and the elements that make up this group are the Nd, La, Ce, Pr, Sm and Eu [10].

The purpose of using elements in Mg alloys is to improve mechanical and corrosion resistive properties. The addition of some RE elements can provide solution and precipitation strengthening, by keeping some of RE in solid solution, and by precipitating intermetallic phases, improving the high temperature creeping resistance (which not find biodegradable application) of Mg alloys. Various RE-doped Mg alloys such as Mg – 8Y, Mg – 10 Gd and LAE 442 are proposed as implant materials, and so, biomaterials [77],[78].

The RE elements with low solid solubility, shows a higher influence on cell reactions than those RE with high solid solubility, excepting the Eu element. Among the RE with high solid solubility (Y, Gd and Dy), the presence of yttrium into the body it is positively regarded as with enables the macrophages cells. By another hand, cellular reaction to Gd and Dy was comparably low, with a slight advantage for Dy [79].

Mg alloys are rarely binary systems and are formed as ternary, quaternary systems where the alloying elements can have synergistic effects on structural and corrosion properties. Figure I.15 shows the solid solubility limits with increasing temperature for magnesium. In bioapplications, temperature does not play a significant role, since

physiological temperature is around the 37°C. But a trend follows for high to room temperature with decreasing solubility of RE in magnesium alloys with decreasing temperature.

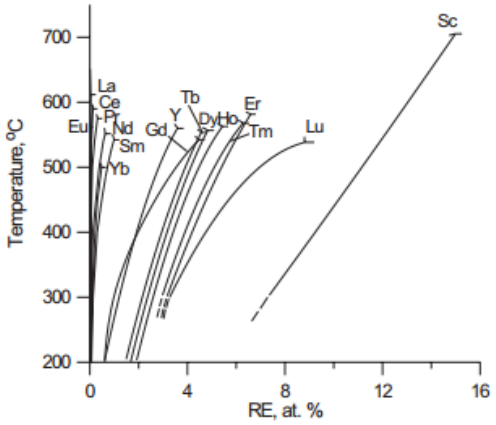

Figure I.15 - Solubility of the RE metals in magnesium [80].

I.6.7 The Mg – Gd phase diagram and some particularities

The Mg –Gd phase diagram presented it is proposed in [81]. A full range diagram can be found in [82] and the phase diagram of Mg-Gd it is presented to better understand further investigation done in this work. One peritectic binary compound can be identified in the PD, the Mg5gd. In the full phase diagram plus three peritectically formed compounds appear, the Mg3Gd, Mg2Gd and MgGd, precipitating a single solid phase without lamellar structure. In figure I.16 it is possible to observe a significant solubility of approximately 23 wt% or 4.6 at% [83] at the eutectic temperature and the formation of the intermetallic phase Mg5Gd. The dashed line represents the solidus line and at is left it is presented the domain of the Mg with gadolinium in solid solution [81]. Another alloy will be studied further in this work, characterized by the addition of Mn into a binary Mg-Gd alloy. A full ternary system of Mg – Gd – Mn were not found in the literature. However in [84] a study about thermodynamic calculations in this ternary system can be found. This investigation state that no ternary phase was found at T=500°C. The solvus line which separates the homogeneous solid solution and the Mg+Mg5Gd phase determines the solid solubility limit in which gadolinium is in solid solution. The range of this line had suffered changes over time, and a better understand can be consulted in reference [81].

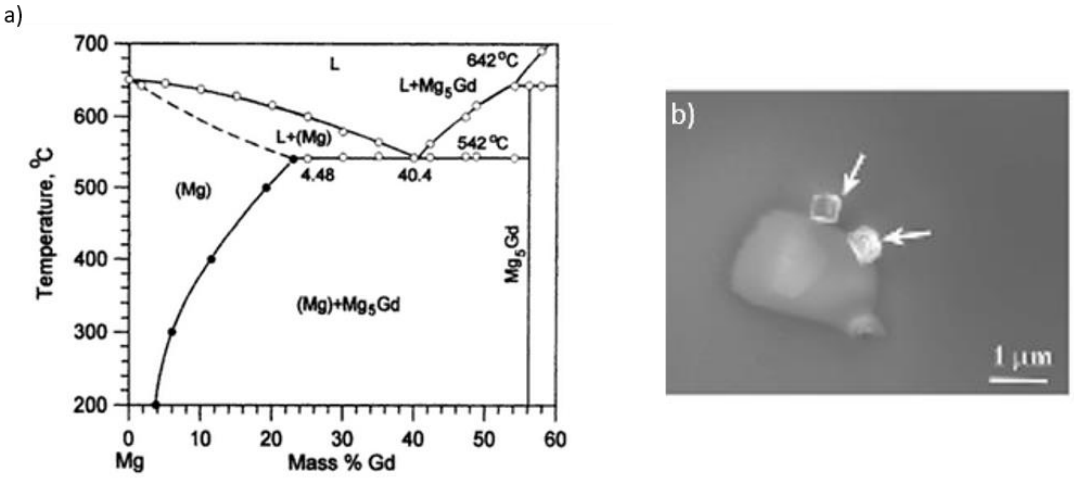

Figure I.16 - Illustration in a) phase diagram of binary alloy Mg – Gd [81] and b) a DyH_2 located near a Mg-XDy phase founded in Mg-20Dy casting alloy [85].

It is possible to found unexpected Mg-RE based metal alloys, precipitates with cubic morphology and designated as an RE-cuboid phase [83]. This intermetallic is an RE hydride with fcc phase, which was found with the help of an electron energy loss spectroscopy analysis [83]. Different proposals were stated in the literature about the possible formation of the intermetallic since the Mg – RE phase diagram usually do not show this phase, as is possible to observe in Figure I.16.a)(phase diagram of Mg-Gd) and Figure I.16.b) (SEM picture of a DyH_2 intermetallic). One of this proposals is that GdH_2 is generated during melting or nucleated during solidification (with the rate of solidification affecting the formation of this particles) and the casting atmosphere plays a significant role due to reactions with the melt [83]. Another propose found in the literature is the appearance of those particles during the sample preparation at room temperature when hydrogen-containing sources, such water, are used [60]. The content or RE present in magnesium alloy affects also the amount of REH_2 present in the microstructure of alloy.

The phase diagram of Mg-Dy is very similar of the one Mg-Gd, and so it is also not expected the formation of DyH_2 compounds.

I.7 Studies on existing biodegradable Mg-Alloys

I.7.1 Mg – Ca alloys

Mg-Ca alloys are being investigated since Ca element can contribute with improved mechanical properties and is a nontoxic element, as stated before. The ultimate tensile strength and elongation of the as-cast Mg-1Ca alloy are 71.4 MPa and 1.87 %. These parameters are, improved to 166.7 MPa and 3% after hot rolling, and to 239 MPa and 10.6% after hot extrusion. During the in vivo implantations, the pins of Mg 1 wt% Ca alloy gradually degraded within 90 days and showed a corrosion rate of 1,27 mm/y. Krause et al. [86] investigated the initial mechanical strength and the degradation behavior with

the associated changes in mechanical properties of Mg0,8Ca, LAE442 and WE43 alloys for osteosynthesis implants. They saw that Mg0,8Ca showed the least initial strength and the highest loss in volume after 6 months, and conclude that its use as a load bearing degradable implant material seems to be limited [86].

I.7.2 Mg – Zn alloys

Zhang et al, studied Mg 6 wt.% Zn alloy, which exhibited tensile strength approximately 279.5 MPa and elongation 18.8 % after solid solution treatment and hot working [87]. This alloy was implanted into the femoral shaft of rabbits, presenting a degradation rate in vivo of about 2.32 mm/y with newly formed bone surrounding the implant. Zhang et al. optimized the Zn content of Mg-XZn-1Mn alloys to 1 wt.% based on their mechanical and corrosion properties. The extruded Mg-1Zn-1Mn alloy, with a tensile strength of 280 MPa and an elongation of 22 %, was implanted into the femoral of a rat. Post-operation examination after 18 weeks showed that around 54% of the implant was left [88]. In general Mg-Zn alloys show good potential for medical applications.

I.7.3 Mg – RE alloys

The Mg-RE alloys were used in clinical cases recently. In the first clinical treatment reported in [89], 20 patients were treated with absorbable Mg stents (3.0-mm-diameter, 15-mm-length, containing Mg>90 % and RE) for suboptimal angioplasty. No major or minor amputation was necessary for any of the patients, yielding a limb salvage rate of 100 % . Another case is shown in [90], in a 6-month randomized study on 60 patients (74 lesions), using stents that degraded too rapidly, resulting in the occurrence of restenosis within 6 months [90]. The Mg alloy stent was also used to sustain perfusion of a long segment re-coarctation in a new-born. Due to a rapid degradation process, the stented vessel returned to its previous course and a second stent was implanted. Despite the two stents were used in the new-born, pathological Mg levels in serum were not detected [90]. It is necessary to modify and/or re-design the stents so that a prolonged degradation time can be achieved. For that it is substantially important to investigate the corrosion properties in different novel Mg alloys, despite that clinical studies confirm the possibility of Mg alloys as implants, it is necessary to improve corrosion and/or mechanical properties of biodegradable Mg alloys.

I.8 Aim and Outlines of Thesis

It is significant the advances noted in the use of biomedical devices like implants, or stents, and in nowadays, the will of a constant improvement in medicine is the driving force to investigate novel biodegradable magnesium alloys. For sure, other types of alloys can be used for this kind of application, but magnesium element is one of the best

candidates because of is low toxicity and adequate mechanical properties. However, biodegradable alloys show some problems in this kind of applications. They present high rates of corrosion, and sometimes uncontrolled hydrogen liberation, which can lead to medical complications. Specifically, magnesium is a high active element and in high pure magnesium alloys, impurities can degrade behavior, working as cathodes to the matrix. The addition of elements in alloys can help to improve corrosion behavior, but also mechanical properties. It is of most importance the right choose of elements, considering toxicological properties, and other factors, which can prejudice over to increment the quality of magnesium alloy as a biomaterial. There are a substantial number of alloys to study and improve as so the information about their properties in bioapplications, and improve the understanding of mechanisms behind biodegradation.

The scope of this work is to study and characterize the corrosion behavior and characterize the microstructure of Mg alloys, specifically Mg-Gd and Mg-Gd-Mn systems, and compare them with pure Mg. Major aspects of study for this work will concern the following points:

- Effects of alloying elements such as Gd and Mn on Mg-alloys microstructure and corrosion resistance. The influence of secondary elements concentrations on alloy's properties will be studied.
- Effects of different simulated body fluid environments and the affectation of chemical composition in the corrosion properties of the selected Mg alloys. The conditions will include NaCl solution (0.147 M), Ringer solution and PBS solution. It is important to characterize the corrosion medium, and a set of appropriate techniques will be used for this purpose, present in the next chapters.

To describe the corrosion behavior of Mg alloys different electrochemical methods will be used:

- Classical corrosion immersion tests in various types of corrosion environment, giving an answer on general corrosion of the Mg alloys samples. Those methods are electrochemical impedance spectroscopy (EIS), DC-polarization and H2 evolution.

The relevant methodologies that will be used to characterize the effects of microstructure on corrosion in novel biodegradable Mg alloys are:

- Scanning Electron Microscopy (SEM), which will be performed to characterize phases, shapes, and their distributions. These techniques will provide information about surface microstructure and localized corrosion attacks;
- Atomic Force Microscopy or specifically Kelvin Probe Force Microscopy (a semi-contact type of AFM), will be used to evaluate topography and Volta Potential of a sample surface. It gives the information about the composition and electronic properties of metallic phases at local scale on the surface. It will be used in conjunction with immersion tests and Electron microscopy measurements;

Chemical analysis of alloys submitted to corrosion tests will be done to identify the composition of the products of corrosion:

- XRD: X-ray Diffractions will be used to get a qualitative analysis of the phases present in Mg alloys;
- Glow discharge optical energy spectroscopy, GDOES, which can reveal the presence of elements with depth, helping to characterize corrosion products;
- Energy Dispersive Spectroscopy (EDS) will be used to identify changes in elemental composition;

With this, it is expected to get a better overview of the mechanisms of corrosion of those Mg alloys in different solutions (in vitro tests), which contains inorganic salts presented by body fluids, as calcium carbonates and sodium phosphates. The constant learning about the techniques in use and the science behind this phenomenon's, as so the laboratory experience and self-learning, are the most important objectives found in the dissertation work.

Chapter II – Experimental Methodology and Materials

II.1 Materials and Solutions

Materials and solutions have to be prepared for this investigation and experimental work to study corrosion and electrochemical phenomena. A set of experiments were designed and used to characterize properties and to understand corrosion behavior of different systems. It will be described briefly the techniques and the conditions parameters utilized for the various characterization methods. The ability to make a proper interpretation of results can come from a precise explanation of techniques used on this work.

II.1.1 Alloys in use

A binary Three Mg and Mg alloy systems were used for the experimental work. A binary system consisting of Mg and Gd elements, where Gd acts like an alloying element, with two different wt% content, namely Mg2Gd and Mg5Gd (2 wt% and 5 wt% respectively). In addition, two ternary systems consisting of Mg, Gd and Mn elements were studied, namely Mg5Gd1Mn and Mg2Gd1Mn, where Mn was added (1 wt%) in the form of a master alloy (Mg-Mn). A high reference purity (HP) Mg was additionally used in this work. In the manufacture of these alloys, an electrical resistance furnace was used and alloy elements were put into solution when a molten state of magnesium was achieved. In Figure I.1 it is represented a regular beam cast used in this work and the casting ingot presented dimensions, respectively of, 1.8 cm in diameter and 20 cm in length. The preparation of all alloys was performed at HZG. Table II.1 and II.2 shows the nominal composition of a pure Mg and Mg - Gd system. Chemical composition was performed by inductively coupled plasma atomic emission spectroscopy.

Table II.1 – Average experimental composition of a HP Mg, N=3.

Alloy/ Composition (%)	**Fe**	**Cu**	**Ni**	**Al**	**Ca**	**Mn**	**Si**	**Zn**	**Mg**
Pure Mg	0,0054	0,0002	0,0002	0,0128	0,0049	0,0195	0,0398	0,0019	balance

The analysis of Table II.1 allows the observation of a relatively higher concentration of impurities as Mn, Al, and Si. The Iron content limits are well below the tolerance limit of Fe in Magnesium (I.5.1.3), and so it will be addressed as a Highly Pure Magnesium. Binary system present a high concentration of iron impurities that can be

observed in Table I.2. For the ternary system, an additional of 1 wt% Mn was used in the composition. It is important to refer that inductively coupled plasma atomic emission spectroscopy could reveal some mismatch in the identification of a proper content to Gd.

Table II.2 – Average experimental composition of Mg – Gd systems, N=3.

Alloy/Composition(%)	Fe	Gd	Mg
Mg 2Gd	0,024	1,94	Balance
Mg 5Gd	0,032	4,99	Balance

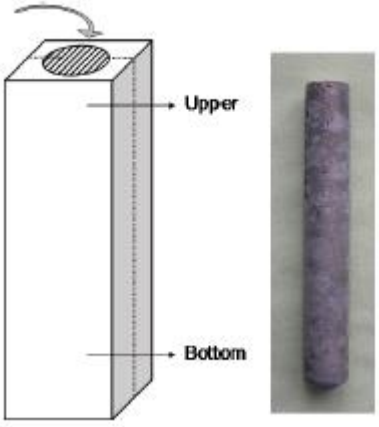

Figure II.1 - Illustration of a typical cast mould and cast rod ingot used in this work.

II.1.2 Solutions

Yufeng Zheng in his work [91] present general solutions used to mimic physiological body fluids. Ringers and Phosphate Buffered Saline (PBS) solutions are also typical electrolytes used in vitro studies [92] [93] [94] [95] [96] [97] [98]. In Table II.3 it is presented the chemical composition of electrolytes utilized in this work and compared with a Human Blood Plasma, regarding the concentration of inorganic salts.

Table II.3 - Chemical composition of solutions used in this work and of the Human blood plasma [68].

Solutions	Inorganic ion concentration (mM) of solutions							
	Na^+	Cl^-	Ca^{2+}	Mg^{2+}	SO_4^{2-}	K^+	HCO_3^-	HPO_4^{2-}
Standard	145.4	145.4	---			---	---	---
Ringers	147.8	151.7	1.8			2.7	2.4	---
PBS	147	139.8	---			2.7	---	11.3
Blood Plasma	142.0	103.0	2.5	1.5	0.5	5.0	27.0	1.0

Reagents were dissolved in deionized water, one by one, using a stirring magnet to agitate solution and accelerate dissolution. The correction and measurement of pH were done at the last step of solution preparation, using a pH meter. To correct pH acid/base (HCl/NaOH) solutions (0.01 mM) were used. Starting pH of the solution was, for the 0.9 wt% NaCl of 7.2 ±0.1, for Ringers 7.4 ±0.1 and PBS 7.4 ±0.1. Ionic conductivity also was recorded.

II.2 Metallographic preparation

Metallographic preparation techniques were used to look into the microstructure, as well as surface preparation of alloys before performing corrosion tests. That requires the use of grinding and polishing machines, etching, etc. This preparation, when done in a properly way allows the observation, using microscopic techniques, of the microstructure constituents. A brief description of methods used for sample surface preparation will be done in next subchapters. The metallographic preparation was done in the Metallographic Lab of the MagIC department at HZG.

II.2.1 Grinding

Samples were sectioned before grinding into geometries of 1.8 cm and 0.5 cm for electrochemical measurements, and 1cm and 0.4 cm for hydrogen evolution measurements. For metallographic purposes, SiC coated abrasive grinding papers are a common abrasive. It is available different paper grades, ranging from coarse 60 grit to very fine 4000 grit size. Specifically for soft materials, it is not necessary to start the process with a very coarse grade since it can be applied large deformation on the surface. By other hand problems can appear in the breakdown of the SiC particles, if it is started the process with a too fine grade paper [99].

To rectify this problem and due to the softness of magnesium, a starting grade of 320P was chosen. Post categories used were 500, 800, 1200 and 2500 P SiC papers. In the last grinding steep, alumina was used to allow to get a finer grinding. The grinding wheel velocity of rotation was maintained at 150 rpm and was water cooled. A steady load hand pressure to hold a sample in the grinding process was used, with the surface of sample parallel to the sheet paper surface. One minute was used in each grade steep and 10 minutes to the last grade paper (using alumina stone in the last 5 minutes of grinding preparation).

For electrochemical and hydrogen evolution measurements, samples were prepared until grade P1200 without using alumina stone.

Between each grading steep the surface of samples was rinsed in water. After using the last grade, a posteriori ethanol rinsing step was done.

II.2.3 Polishing

In this procedure, it was used a Black CHEM 2 polishing pad, which is a porometric polymer pad, mounted on a flat plate. An alcohol based cooling agent was used. The polishing process was started with a coarse aqueous diamond suspension of 3um size and use a further 1um size diamond suspension, both steps with a duration of 5 min. On the final stage OPC free water was used to remove micro scratches which came from the last polishing step. Between each step, the samples were quickly rinsed in water, followed by rinsing in ethanol and exposed to hot air to dry the surface. All these processes used a hand steady load pressure to hold the samples of the polishing cloth, using 80 rpm rotation velocity. In the last polishing step only ethanol was used to rinsing the metal surface.

II.2.4 Chemical etching

A conventional chemical etching used in HZG was used to reveal grain boundaries and provide contrast on Mg surface. The etching chemical composition is composed of distillate water (30 – 40 mL), acetic acid (6.5 – 7 mL), ethanol (140 mL) and picric acid (24 – 40g). Samples were immersed in solution during 3 to 5 s, cleaned with ethanol and dried in hot air.

II.2.5 Cross-section sample preparation

Cross section of samples was prepared to study corrosion layer formation and visualize interface damage. The cross section was mounted using an Emotec 30 cold epoxy resin. Samples were placed in circular foams, filled with a polymer solution. The resin was allowed to dry at room temperature. A brief grinding and polishing processes were done, as stated before.

II.3 Characterization techniques

A set of characterization techniques were used in this work, as Electrochemical Impedance Spectroscopy, Hydrogen Evolution measurements, Potentiodynamic Polarization, Scanning Electron Microscopy, among others. A brief description of techniques and conditions used will be done in this subchapter.

II.3.1 Electrochemical Measurements

It was used a computer-controlled potentiostat Gill AC, observed in Figure II.2, to perform electrochemical measurements. All Electrochemical tests were performed in a set of stirred electrolytes: 0,9 wt% NaCl, Ringer's and PBS solutions at 23 ± 0.5 °C. A group of three electrodes and an electrochemical cell (around 350 mL of capacity) were used in techniques such Potentiodynamic Polarization (PDP) and Electrochemical Impedance Spectroscopy (EIS) (in open circuit potential, OCP). It is represented in figure II.2 the

working electrode (WE, 1.52 cm2 of exposed area, which uses a rubber ring to isolate the exposed area) that is placed between the cell hole, establishing contact with an electrolyte and a conductive copper piece of metal. A saturated Ag/AgCl electrode was used as reference represented by RE in Figure II.2, and a platinum mesh (AE in Figure II.2) as a counter electrode. Times of immersion are specified for each technique on next subchapters. All measurements were done in triplicate to verify reproducibility.

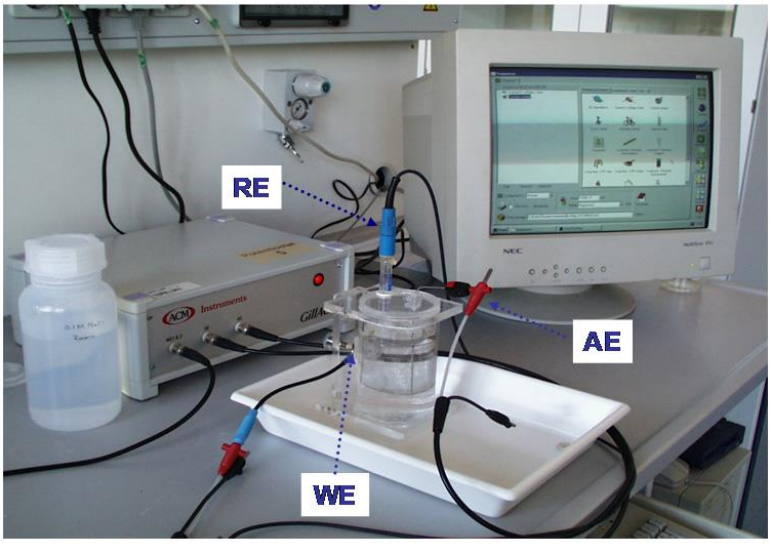

Figure II.2 - Illustrative scheme of an electrochemical station and respective components, used on this work.

II.3.1.1 Potentiodynamic Polarization (PDP)

The electrochemical cell used on PDP (potentiodynamic polarization) is composed of a set of three electrodes, the working electrode (WE), counter (CE) and a reference electrode (RE), as stated in section II.3.1. A potentiostat is used to control a DC voltage signal, applied to a working electrode (WE), which allows the measurement of a transient current response flowing through the WE and CE. A scheme of an electrochemical cell and system utilized can be seen in figure II.2. This technique is destructive since it changes properties of a surface sample due to the high potential amplitudes applied on WE.

Small steps of potential are used during this process and usually it present scans over a large range, typically from -0,5 to 1,5V and back to -0,5 versus the OCP. For the applied potential a current response it's measured, with a particular magnitude and direction, providing information about the type of reaction (anodic/cathodic) is occurring between the electrolyte and the sample. The direction and extent of the current provide information about what kind of results (anodic/chatodic) that occur between the electrolyte and the sample.

OCP (Open circuit potential)

The OCP is a technique that measures the potential difference (also known as steady state potential) between the working and reference electrodes when there is no current or potential existing in the cell. If net current is zero (the current produced by the anode are all consumed in the cathode), the anodic current (Ia) = - cathodic current (Ic), and steady state can occur at this point. However, equilibrium could not occur, since zero net currents can arise through a balancing of different reactions [24] and so corrosion is a non-equilibrium process that may take place at steady state. It can be monitored, by recording the change in potential over time. If the rate of corrosion does not changes with time the system achieved steady state. At beginning a rapid variation of potential it is expected both further with time, the metal/solution interface approach to a steady state (or a quasi-steady state), decreasing the variation of potential over time. Criteria for steady state conditions can be changes of less than 5 mV in E_corr over a range of 10 minutes [24].

Corrosion Potential

Corrosion potential, represented by Ecorr, it is a "mixed" potential determined by the kinetic and thermodynamics of reaction. Kinetics give indication about when and how fast the reaction is going and thermodynamics says if it is possible to occur. This property is described in Tafel diagram as the interception of the anodic and cathodic lines.

Breakdown and Passivation Potential

The observation of PDP plots allows identifying passivation potential (if present) as the starting potential where a sudden increase of current density is happening. Passivation potential is characterized by a "saturation" current density, where polarization curve almost exhibits a straight vertical line in respect to the possible axis. Breakdown potential usually occurs after passivation and, when a sudden increase in current density it is observed.

The intrinsic nature of a spontaneous corrosion reaction is characterized by a dependency of the cathodic and anodic reaction. At a respective corrosion potential, a corrosion current is generated, and it's current it is the result of the cathodic and anodic current, and so:

$$I_a = -I_c = I_{corr} \qquad \text{Equation (II.1)}$$

,where Ia is the anodic current, Ic the cathodic current and Icorr the corrosion current. It is not possible to measure the Icorr directly, so it has to be estimated since the cathodic reaction consumes all current. A method to determine Icorr is the Tafel extrapolation where the anodic and

cathodic curves are fitted into straight lines, and the interception of both origins the Icorr. Cathodic and anodic current can be derived from Tafel equation:

$$I = I_0 e^{\frac{2.303}{b}(E-Eocp)} \qquad \text{Equation (II.2)}$$

,where I_0 is the exchanged current at equilibrium (reaction dependent constant), I is the measured current, b the reaction Tafel constant, E the electrode potential and E_{OCP} corrosion potential. Equation II.2 described a generic Tafel equation that can be applied for each half cell reaction, assuming that the current rates are controlled by kinetics only (activation polarization), and so it comes the Buttler – Volmer equation:

$$I = I_0 \left(e^{\frac{2.303}{b_a}(E-E_{OCP})} - e^{-\frac{2.303}{b_c}(E-E_{OCP})} \right) \qquad \text{Equation (II.3)}$$

,where b_a and b_c are, respectively, the anodic and cathodic Tafel constant in V/decade of current. An illustration of Equation II.3 can be observed in figure II.3.a). Two conditions can be applied to equation II.3, one when a potential is must higher than Ecorr, and then the first term of equation dominates and gives origin to a straight line with slope equal to the anodic Tafel constant. Near the condition that is given by (II.1), and due to the mixed potential, the Ecorr is somewhere near the Eocp for both electrode processes and the exchange current is the corrosion current. So at this point it is possible to obtain the Icorr and respective Ecorr by the interception of the two straight lines (Tafel extrapolation, see figure II.3.b)).

Extrapolation of Tafel Slopes

The i_{corr} can be estimated by extrapolating the anodic and cathodic branch of the polarization curves, resulting from the mixed potential theory. Under the corrosion potential (or rest potential) the rate of the two reactions are identical and is known as the corrosion current density. This is possible with the assumption of conservation of charge under the rest potential, where the reduction reactions must consume all the electrons produced in oxidation reactions. It is known as a steady state reaction domain since the rate of reactions is constant. An interpretation of Evans Diagram allows to use Tafel extrapolation (illustration in figure II.3.b)) in polarization curves and estimate the corrosion current, but with certain conditions [100], [20]:

- The extrapolation of anodic and cathodic branch from polarization curves, should be done at potential well away from the E_{corr} , where the domain of each potential is well established and the applied current density is virtually equal to the current density estimation branch. The limit to starts a Tafel extrapolation should be at least from ±50 mV in respect to OCP.

- The interception of both extrapolated curves at the E_{corr} indicates the i_{corr}, where both anodic and cathodic reaction rates are constant and identical;
- Corrosion rate can be calculated by transforming Faraday's law and using the Tafel extrapolated i_{corr}, when the sample is under an uniform corrosion, and so the units come in mm/year;
- At least one of the branches from polarization curves should exhibit Tafel, i.e linear behavior on semi logarithmic scale, along one decade in respect to current density. Anodic polarization branches are often not used in magnesium (due to NDE phenomena) since they do not present linear regions, and cathodic extrapolation is enough to estimate the i_{corr};

Diffusion control, pitting phenomena and Ohmic losses are some of the characteristics which can lead to a wrong interpretation and estimation of the i_{corr}, as, per example, the presence of electroactive species [100]. The Corrosion rate it is not presented and calculated in this work due to several criticism and non-correlation with other methods were demonstrated in several works [101], [102]. However, an interpretation of Potentiodynamic Polarization curves and estimation of i_{corr} can help to reveal several features of the electrochemical systems.

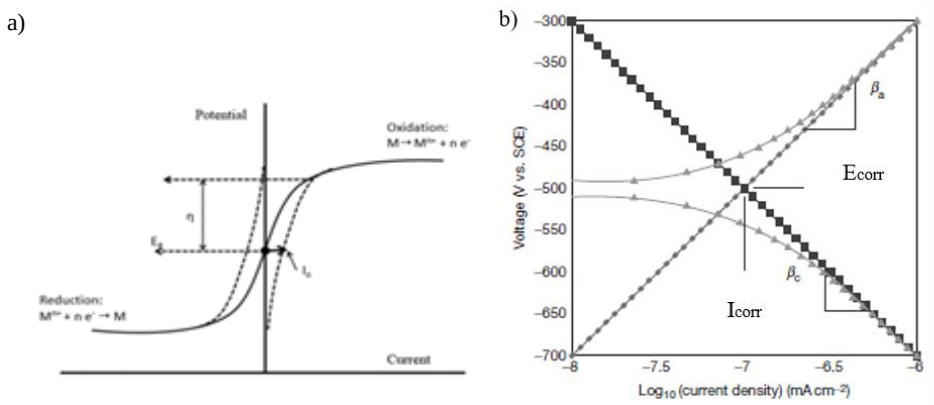

Figure II.3 - Illustration of a) Representation of dependence between electric current and voltage obtained from the equation of Butler-Volmer [24]. b) Evans diagram and representation of Tafel extrapolation of anodic and cathodic slopes [5].

CONDITIONS

The Potentiodynamic Polarisation measurements were started at -150 mV about OCP. The scan rate was 0.2 mV/s and the test was finish when a current limit of 5 mA/cm2 was reached.

The tests were performed in 0.9 wt% NaCl, Ringer's and PBS solution. When applied a potential the test shows a sweep from a certain voltage below the OCP to a certain voltage above the OCP, thereby polarizing the working electrode. The current

measured during the polarization scan gives an indication of the corrosion properties of the sample in question. Alloys used in this experimental technique were HP Mg, Mg2Gd, Mg5Gd, Mg5Gd1Mn and Mg2Gd1Mn.

II.3.1.2- Electrochemical Impedance Spectroscopy

Electrochemical Impedance Spectroscopy is a general technique used to study electrochemical systems. In this work, it is used mainly to characterize corrosion processes and identify corrosion mechanisms, as also dynamic mechanisms that occur in those processes. It enables the understanding of electrochemical system behavior and the role of corrosion products formation in corrosion systems. It allows measuring a broad range of frequencies obtaining a large range of information about the electrochemical system, by electrical means, as the capacitance of the Helmholtz double layer and resistance of an oxide or corrosion products deposition in the metal surface. Besides that, this technique present more functionalities depending on the application in use.

By analogy with the studies of electrical, it is possible to ascribe a transfer function, as the ration between the imposed input potential and the measure output potential, and named as Electrochemical Impedance. It is possible to observe in figure II.4 this balance, therefore necessary to impose a potential disturbance to the system and to measure the own current response.

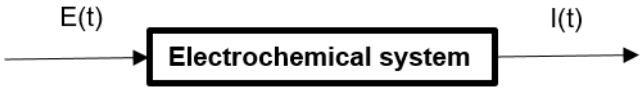

Figure II.4 - Illustration of an input and output in electrochemical impedance systems.

E(t) and I(t) are function depending on the application of a AC disturbance, as it can be seen by the periodic function bellow:

$$E(t) = E_0 * \sin(wt) \longrightarrow I(t) = I_0 * \sin(wt + \emptyset)$$

The electrical perturbation of the system is an applied potential (it a frequency of f=w/2π and amplitude E_0) with a measurable response of amplitude I_0 and out of phase of ∅. The electrical Impedance tell us:

$$E(w) = Z(w) * \mathrm{I(w)} \qquad \text{Equation (II.4)}$$

,with E(w) and I(w) the Fourier Transformations in the frequency domain (w), in respect to current I(t) and potential E(t). And so the electrical impedance can be seen as the complex ratio of the voltage to the current in altering current. It is so equated to the resistance of an AC circuit since the impedance in a DC circuit is zero. The resistance can be seen as the impedance at phase angle equal to zero. It is so a complex number, which can be written in an algebraic and geometric way:

$$Z(w) = |Z(w)|e^{(j\emptyset(w))}$$ Equation (II.5)

and

$$Z(w) = Z_r(w) + j.Z_i(w)$$ Equation (II.6)

,with $|Z(w)|$ the modulus of impedance, $Z_r(w)$ the real part of impedance and $Z_i(w)$ the imaginary part of impedance. Some precaution have to be taken into account to assure that the system in study is stationary and the current response is $I(t) = f(E)$ is linear under all disturbance range. This imposes that the amplitude of perturbation E(0) should be sufficiently low, with values in range of 10 to 5 mV. The measured current occurs in between the counter and working electrode, which represent an average of all the phenomena occurring in the surface of the working electrode.

The representation of the Electrochemical Impedance measurements can be done using different plots. The Nyquist plot, which can be observed in Figure II.5, is a Cartesian representation of the Z_r and Z_i. This division allows the identification of three primary values, which are, the polarization resistance (R_p), uncompensated resistance (R_s – resistance of solution) and maximum phase angle (ω_{max}). The R_p value can be found when looking the interception of Nyquist curve with real axis at low frequencies, minus the solution resistance, at high frequencies. The capacitance of double layer (Cdl) can be fitted from the maximum point of the Nyquist curves on the imaginary axis. It is so possible to simulate an equivalent circuit inherent to a Nyquist plot. However in complex electrochemical systems, where the impedance values and frequencies of the electrode processes span several orders of magnitude, the correct interpretation of Nyquist plot can become difficult [103].

Another second method to interpret EIS measurements is the Bode magnitude and phase angle Plot (polar coordination representation), which will be used in this work for EIS analysis. As seen in Figure II.5, the magnitude plot is given in function of the log of |Z| and the log of frequency. It is also possible to find the C_{dl} using Bode Plot. With phase angle interpretation, which is a function of phase angle with the log of frequency, the ω_{max} founds relation to the frequency where the magnitude of the phase angle is of greatest value.

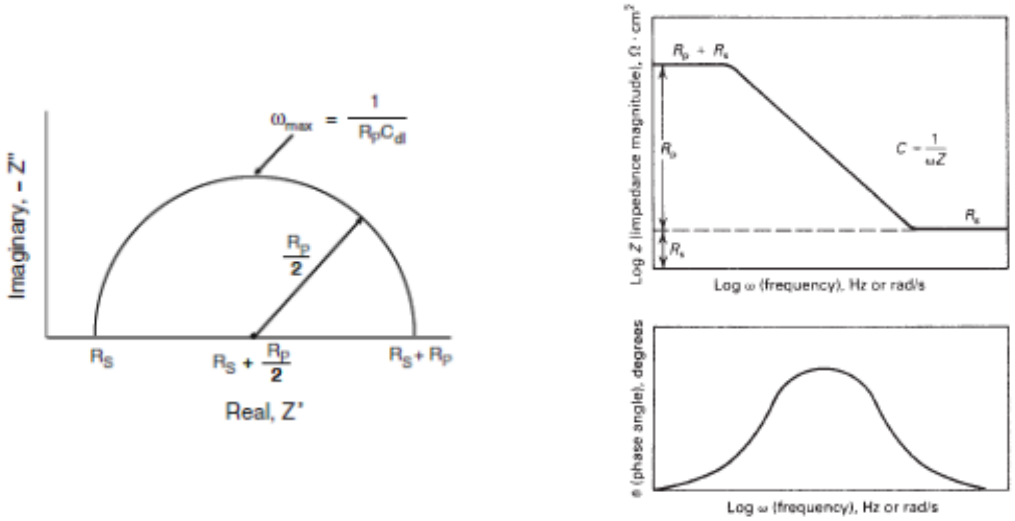

Figure II.5 - Illustration of a ideal Nyquist Diagram in the right of the figure. In the left of the figure and above the Bodes Magnitude Plot and bellow representation of a Phase Angle Plot [100].

The maximum in the phase angle is referred to the absolute value since phase angle values are usually negative and for that reason, the YY axis is represented inverted. Often, the amount of ω_{max} in Bode Phase Pot do not correlate with the value from the Nyquist Plot. The equation to calculate C_{dl} from Bode Plots is [100]:

$$C_{dl} = (\omega_{máx} * R_p)^{-1} * (1 + R_p/R_s)^{1/2} \qquad \text{Equation (II.7)}$$

CONDITIONS

Electrochemical impedance spectroscopy (EIS) measurements were performed setting up the equipment in the frequency range between 0.01 and 30000 Hz with an amplitude of ± 10 mV rms. Impedance measurements were performed after different exposure periods of 1, 3, 6, 12, 24. Longer time measurements were recorded in all 24 hours until 216 hours of immersion (for HP Mg and Mg5Gd1Mn immersed in 0.9 wt% NaCl solution) and 336 hours of immersion (for Mg2Gd1Mn immersed n 0.9 wt%NaCl, Ringers and PBS solution and HP Mg immersed in Ringers and PBS solution). The EIS in Binary system were performed only during 24 hours of immersion in the 0.9 wt% NaCl solution.

II.3.2 X-Ray Diffraction - XRD

The x-rays are characterized by a range of wavelengths between the 0.1 and 10 Å and are electromagnetic waves. The lattice constants of crystals are of the same order of magnitude, and so it is very useful the analysis of crystal structure using x-rays [104].

This type of radiation is produced when any electrically charged particle, usually electrons, of sufficient kinetic energy is rapidly decelerated. The production of x-rays radiation is produced in an X-ray tube, which contains a source of electrons and two metal electrodes. The particles are redirected to the anode due to the high voltage that is maintained across the electrodes. Due to an impact with a target, x radiation is produced in all directions [105].

The generated rays, which come from the target, are a mixture of different wavelengths that depends on the tube voltage [105]. The radiation represented by such curves is called continuous, white or bremsstrahlung, which means ‘breaking radiation,' once it appears due to the electrons deceleration.

When the voltage on an x-ray tube is raised above a certain critical value (characteristic of the target x-ray metal), sharp intensity maxima appear at certain wavelengths, superimposed on the rest of the spectrum [104]. The peaks are called characteristic peaks and are very narrow. These lines may be defined as K, L, M, etc lines, as they increase in wavelength. Although only the K lines are useful in x-ray diffraction, because the longer wavelengths are easily absorbed [104]. Though there are several lines in the K set, only the three strongest are usually observed$K_{\alpha^1}, K_{\alpha^2}$ and K_{β^1}.

A geometric relation determines the angular distribution of the intense peaks from a diffraction pattern of a crystalline structure and is given by the Braggs law [106]:

$$2d.sin\theta = n.\lambda \qquad \text{Equation (II.8)}$$

The path difference between two rays is 2dsinϴ, where θ is the angle between the incident ray and the crystallographic plane. For interfering constructively, the path difference is an integral number of wavelengths. The integral number is the order of the Bragg reflection. The physical process is schematically shown in Figure II.6. Usually, the detection of diffracted beam is acquired by a moving detector in a goniometer, which counts the fraction of diffracted x–ray at certain angles position, producing peaks in relative intensity (counts per second), versus the diffraction angle (2θ) [106].

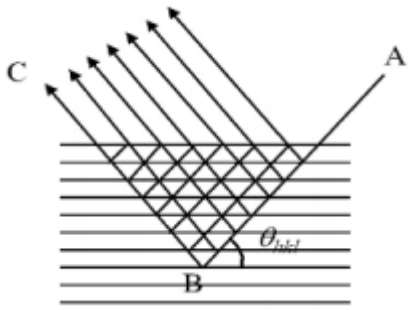

Figure II.6 - Constructive interference of an x-ray and a crystalline structure. A) X-ray source, B) Atom located at a crystallographic plane, C) Constructive interference [105].

CONDITIONS

These studies were carried, as stated before, to identify bulk crystallographic phases on microstructure of HP Mg, Mg2Gd, Mg5Gd, Mg5Gd1Mn, and Mg2Gd1Mn. At *Helmholtz Zentrum Geesthacht*, a Bruker diffractometers used an x-ray source of Cu-K_α radiation (λ = 0.15406 nm) operating at a potential of 40kV and 40 mA of current, during measurements. The sweeping angles had a range 20 to 90°2Θ, with an increment of 0,025°2Θ at room temperature. Samples were previous grinded with 1200 grade, cleaned with deionized water and ethanol, used hot steam air to dry the surface.

The peaks presented in diffractograms were identified in software and compared against the NIST Powder Diffraction Database files (PDF) from the International Centre of Data Diffraction.

II.3.3 Density analysis of samples

The density of samples was determined by using the principle of Archimedes. Archimedes principle states that a displaced volume of fluid caused by the immersion of a sample it is equal to the volume of the sample [107]. The volume of the suspended object relates to the apparent mass divided by the density of the liquid of immersion [107]. It is well understood by observing the equation II.9, that experimental density (or Archimedes density) is proportional to: the initial mass of sample (M) multiplied by the density of a known fluid (ρ_e, absolute ethanol was used due to high reactivity of magnesium with water), divided per the difference of the initial and immersed mass (M_w).

$$\rho_{exp} = \frac{M.\rho_e}{M - M_w} \qquad \text{Equation (II.9)}$$

CONDITIONS

A Sartorius LA 230S electronic analytical and precision balance was used to evaluate experimental density (ρ exp). Calibration was done adjusting temperature, pressure and liquid fluid density utilized in the experiment. Initial mass is recorded and it is adjusted the liquid mass, for the calculation of the immersed mass. The Sartorius balance calculates the following values.

II.3.4 Scanning Electron Microscopy (SEM) / Energy dispersive spectroscopy

SE MODE

From Figure II.7 it is observed that SE (secondary electrons) results from the first scatterings electrons. The secondary electrons are defined as a result of inelastic scattering, and they are a group of low energy electrons (below 50eV) [108],[109]. The ratio of number of SE (SEEC) leaving the surface is higher at low energy beam or higher incident angle beam. SE detector only measures the secondary electrons from the respective interaction volume and preferential those near the surface. Resolution is higher in this mode since the interaction volume is lower and is determined by beam energy. This mode is very sensitive to topography and is an excellent method to analyze the surface of materials [108].

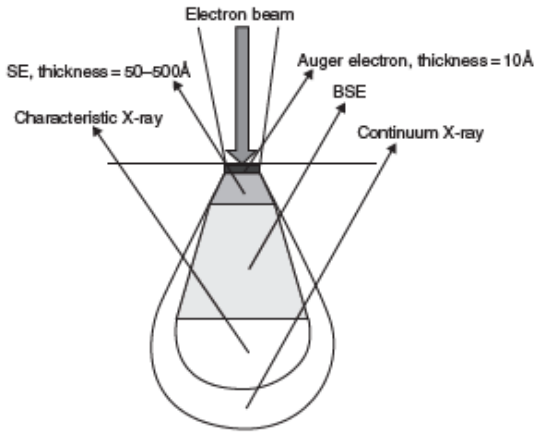

Figure II.7 - Representation of interaction volumes for electronic beam with a material and the secondary radiation produced from those interactions [108].

BSE MODE

Backscattered electrons can also be detected to create an image. In Figure II.4 it is possible to identify the BSE volume of interaction. The backscattered electrons signal have higher energy than 50 eV and comes from mainly elastic scatterings [109]. The volume

(and depth) of the interaction zone increases with an increase of beam energy or a decreasing in the atomic number of the elements in the material. Since the volume of interaction is higher than the one observed in SE mode, the resolution decrease when comparing the image of SE (1 nm). If the specimen atomic number increases, elastic interactions increase too, and a higher signal on BSE is detected. This effect can create contrast in the image, allowing composition information and at the same place topographical information too [108].

EDS MODE

This mode of detection was also used for this work to analyze the elemental composition of the microstructure. Energy dispersive spectroscopy detectors can be found copulated with BSE and SE detectors in SEM. Usually, they are made of a solid state semiconductor of Si(Li). Energy dispersive spectrometer is a microanalysis, where it is detected a specific energy or wavelength of atomic elements.

When a high electronic energy beam strikes an electron from an inner shell of an atom, this one can be removed from his original position. The free space originated by the remove of electron ionizes the atom. This excited state needs to quickly return to the normal state by refilling the vacancy with an outer shell electron. The exchange of electrons will create a difference in energy (corresponding to the characteristic x-ray) between outer an inner shell and generate an X-ray photon [110] that can be detected.

The utilization of EDS tool as a microanalysis method has to take into account the sensitive factor to low weight concentration measurements. A minimum detection limit (MDL) ranges between 0,1 wt% to less than 1wt%. If the detection is above to values of 10wt%, the element can be defined as a major. If values are between 1wt% and 10wt% inclusive, it is a minor, and for values below 1wt%, it is a trace value [109]. EDS is a nondestructive technique, and the sample preparation requirements are minimal [110].

Qualitative analysis allows the identification of elements in a given sample. If the wt% concentration is held above the MDL, it can be recognized the presence of this element. For values below MDL, it should be stated that the attendance of this element is at concentrations lower that the MDL. Background counts should be removed before the analysis of spectrum.

Elemental line profiles and dot maps use EDS detectors to represent a graphical illustration of the elemental composition, used for qualitative analysis. In dot mapping, the peak-to-background ratio is poor, with limits approximately 2-5 wt% [75].

II.3.5 Hydrogen Evolution Tests

The overall corrosion reaction of magnesium in aqueous solution is:

$$Mg\ (s) + 2H_2O\ (aq) \leftrightarrow Mg\ (OH)_2\ (s) + H_2\ (g) \uparrow \qquad \text{Equation (II.10)}$$

With this reaction, one mole of dissolved Mg generates one mole of hydrogen gas (1 ml H2 (g) = 0.001083 g dissolved Mg) and this relation is possible to observe in the Equation II.11. The experimental setup adjusted for this technique collects hydrogen gas that ascends into a column fulfill with solution and store it in the upper part of a graduated burette (100 mL and 50 mL eudiometer were used with the respective resolution of 0,2 and 0,1 mL), above the line column of the solution. The increasing pressure of the air above this line, due to hydrogen volume accumulation, leads to a depression of the solution column, and the reading of this depression in the eudiometer, measures the volume of hydrogen release at a certain time (close system). Before starting the experiment, the gas pressure inside the Eudiometer tube has to be adjusted with respect to the outside atmospheric pressure. This adjustment can be achieved by regulating the meniscus of solution inside the tube to the water level marked outside the tube.

Fishing line assembly specimens were used to perform hydrogen evolution (illustration of a typical set up can be observed in Figure II.8) to keep all surfaces of the sample exposed to media. A funnel was placed above the specimen allowing the ascending hydrogen bubbles to be collected by the eudiometer (a rubber stopper sealed the connection between the funnel and the eudiometer). Beakers used to support the solution and samples had a volume of 500 mL and 20 mL of resolution.

Conversion of the total amount of collected hydrogen into mass at a certain time is followed by the relation [111],[112], [113]:

$$\Delta g = 0{,}001083 * V_{H_2} \qquad \text{Equation (II.11)}$$

,where Δg is weight loss in g and V_{H_2} is the volume (in mL) of collected hydrogen.

The average volume and corrosion rate regarding the hydrogen evolution was calculated as average values of triplicate hydrogen evolution tests. The triplicate measurements for each criteria condition was made to ensure reproducibility of results. The following equation was used to access values of CR:

$$C_R = \frac{8{,}76*10^4*\Delta g}{A*t*\rho} \qquad \text{Equation (II.12)}$$

,where A is surface area exposed of samples in cm^2, t is the time in hours corresponding at specific a Δg and ρ is the density of alloys in g/cm^3.

Figure II.8 - Illustration of a typical fishing line specimen under HE measurements. This method was used in the investigation work and the image is adapted from [114].

CONDITIONS

All the measurements were performed at room temperature (23 ± 1 °C) and using different solutions referred in II.1.2. The sample surface preparation was described in II.2, as also the dimensions of samples used on Hydrogen Evolution. The starting pH was controlled and the procedure explained in II.1.2. Due to the high reactivity of Mg – Gd alloys, the experiment was stopped after 30 hours. All the other systems were run during 360 hours of immersion. Measurements were conducted at static conditions, which not affects the stability of the suspended sample, with an aspect ratio of 170 ml: 1cm^2, which is a high value, adopted due to the non-renewed solution method. The pH and conductivity were measured before and after measurements and can be consulted in section III.3.2.

II.3.6 Atomic Force Microscopy (AFM)/ Scanning Kelvin Probe Force Microscopy (SKFM)

The AFM and SKFM were used as methods of investigation to evaluate the electrochemical nature of localized zone on the metallic alloy surface, which could contribute to a better understanding of the localized mechanisms present in the corrosion processes.

THE AFM AND TOPOGRAPHY

Those two techniques are included in a vast field of Scanning Probe Microscopy. The development of SPM in 1982 (by G. Binning and Rohrer at IBM) allowed the discovery of AFM which is an instrumental technique that permits the measurement of the surface topography of different materials with sub-nanometer resolution.

The sample surface is scanned by a sharp tip of a cantilever structure. The physical forces between the tip and the scanned surface lead to a deflection of the cantilever. This deflection is measured by a laser beam, which is appointed to the position of the cantilever and reflected, captured by a photodetector, which reads the information about the orientation of the primary structure. A piezoelectric scanner provides a feedback mechanism, and guarantee that the tip maintains the same height to the surface, with a constant tip-sample interaction forces. The piezoelectric can move along the x,y and z positions. The x and y positions are responsible for the scanning of the sample surface and the movement in z-directions controls the force between the tip and the sample. A resulting map (x,y,z) presents the topography of the sample surface. Mechanical contact force, van der Walls forces, magnetic forces, chemical bonding, electrostatic forces and chemical bonding are all type of interaction forces between tip and surface sample [115].

It exists three main modes for AFM operations, which are known as Contact Mode AFM, Tapping Mode AFM, and Non-Contact Mode AFM. The one use in this investigation was Tapping Mode for topography measurements.

THE SKPFM AND VOLTA POTENTIAL

The mapping of the Volta Potential difference (also known as contact potential difference) along a surface can be acceded using SKPFM, under a non-destructive way. It interacts with electrical forces between metal surface and the cantilever tip, observing the working function of surfaces at atomic or molecular scales. The probe and the specimen (which acts as a working electrode) are put in parallel, as two conductors, and the vibrating capacitor method allows to measure the electron work function. The distance between those two conductors is varying, resulting from the vertical vibration of tip, creating an alternating current (I_t), which is defined by an alternating Capacitance (C_p) and the potential difference between working electrode (Φ_w/e) and the probe (Φ_p/e), $\Delta V_{p/w}$ [116]:

$$I(t) = \Delta V_{p/w} * (dC_{p/w}/dt) \qquad \text{Equation (II.13)}$$

,and the equation for the potential difference between working and probe:

$$\Delta V_{p/w} = (\Phi_w - \Phi_p)/e \qquad \text{Equation (II.14)}$$

The potential of the probe(Φ_p/e) is calibrated against a reference, which is kept constant during measurements and the working function it is obtained(Φ_w). The work function, in SKPFM, can be probed using two different operational modes, single pass mode and dual pass mode. In this work the dual pass mode was used, where a first pass is performed, in which the topography of the specimen is recorded. In the second pass the data recorded is used to lift the probe at a specific distance from the specimen surface, and so the potential is measured at a constant distance between the probe and working

electrode (sample surface). During the second pass, the probe oscillates due to the applied AC voltage, and the potential of the sample is then measured [117].

The Figure II.9 shows a typical set up of an SKPFM components circuit. The piezo drive component is off during the second pass, and so the feedback loop that controls the vertical piezo-element is open. A DC bias potential and an oscillating AC potential (with a frequency equal to the resonant frequency of the cantilever free vibrations) are applied to the tip. The AC voltage applied is necessary to produce an alternating electrical force between the tip and the sample. The second feedback loop is responsible for adjusting DC potential to nullify the vibration amplitude of the cantilever and hence the electrostatic force. The Volta potential map of the sample measured in respect to the tip is obtained by the recorded of bias voltage. It is so necessary to repeat this procedure for each line along the slow scan axis to create the Volta potential map.

This technique is very useful for corrosion science since it allows the possibility to distinguish surface zones which present different electrochemical nature, however under some limitations [115]. A conductive cantilever was used, with a platinum tip to the scanner the metal surface.

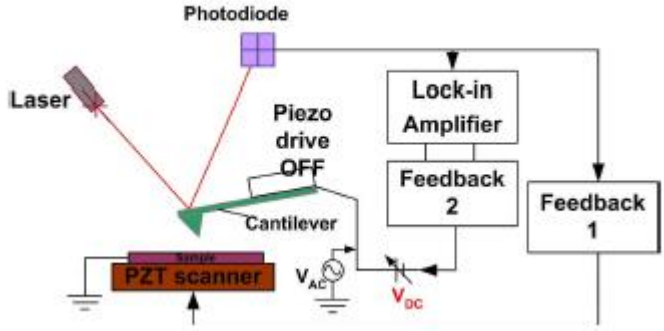

Figure II.9 - Illustration of a SKPFM circuit, with main components [115].

CONDITIONS

A commercial Atomic Force Microscope (AFM), Digital Instruments NanoScope III system with an Extender electronic module, was used for AFM and scanning Kelvin probe force microscopy (SKPFM) measurements. The AFM operated in lift mode with two pass scans. The lift scan height was 100 nm. Drive amplitude in interleaves control for the second pass scan was 5000 mV. For all measurements, silicon probes covered with PtCr layers were used.

II.3.7 Glow Discharge – Optical Spectroscopy (GDOES)

The Glow Discharge Optical Spectroscopy found application to corrosion in the way that it can be used to investigate and characterize properties of coatings or corrosion products deposited on the metal surface. It allows a rapid elemental depth profiling at low vacuum. It is also applicable to conductive and non-conductive substrates. This technique can be applied to analyse thick and thin films [118].

GDOES is characterized by the use of vacuum vessel filled with a low-pressure argon. A voltage is applied across two electrodes, a copper tube working as an anode and the sample, which is connected to a cathode. During the experiment, the sample works as the cathode himself. An O-Ring of relatively soft material is used to seal the sample surface from the outside atmosphere. The electrical field leads (usually applied by a Radio frequency device) to electrical breakdown of the gas, creating an ionic plasma. The specimen surface is consequently eroded (or etched) by ions which are sputtered from the cathode into the plasma leading to optical emission following excitation. Each optical emission of an element have a characteristic wavelength that is quantified (by an optical spectrometer), and so the concentration of each element is obtained. In qualitative analysis, it is counted the intensity of each element. The quantitative analysis requires a sample control to perform calibration of GDOES set up. A scheme of a typical Grimm design set up used in GDOES can by observed in Figure II.10 [119].

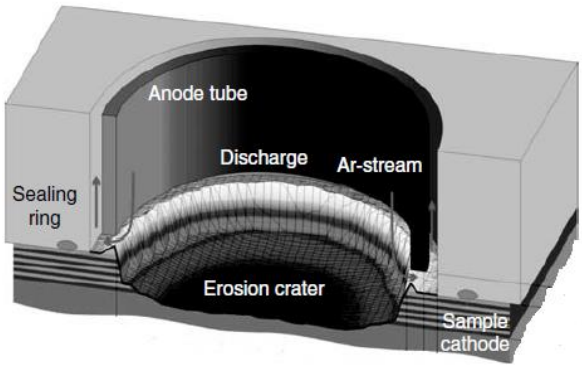

Figure II.10 - Grimm design of a GDOES set up, after cathodic sputtering of sample surface [119].

In this work, it was used a qualitative depth profile analysis. It is possible to observe in a qualitative depth profile changes in the elements intensity with respect to the sputtering time. An overlay of elemental intensity line allows a comparison in between elements. A typical qualitative line profile can be observed in Figure II.11.

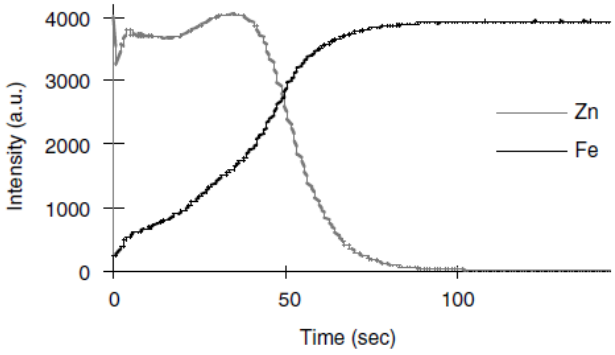

Figure II.11 - Qualitative line profile of a GDOES measurements, representing the intensity concentration for two measured elements, Zn and Fe, in function of the sputtering time [119].

Some artifacts can occur in this technique. In qualitative measurements, the variation in the sputtering rate affects the depth profile, which can become not linear with the time scale. This artifact is common near the interface of layers, where the roughness of interface also plays a significant role, influencing the intensity line profile. Since the emission intensity is proportional to the sputtering rate, the variation of sputtering rate can cause a distortion in the apparent concentrations and intensities, which is more noted at the interface between layers. This type of distortion can disappear with an accurate quantification. Another known artifact which can occur during GDOES is a preferential sputtering, originated by a coarse microstructure and the presence of different phases. This artifact could lead to a mismatch of the concentration profiles [119].

CONDITIONS

GDOES depth profile analysis of the corrosion products was done using a HORIBA GD-Profiler 2 with a copper anode of 4 mm in diameter. Argon sputtering of the sample surface occurred at a pressure of 900 Pa and power of 10 W.

CHAPTER III – Analysis of Results

III.1 Characterization of Alloys before immersion

This subchapter is characterized by a previous characterization of metal alloys, before immersion tests. Experimental density, XRD, and microstructure characterization are the main topics addressed.

III.1.1 Density and XRD measurements

Finding out the density of materials working alloys is a good practice in engineering and science, which can assure reproducibility of the production process of alloys. For more, in this work, density plays an important role, since it is a desired property intrinsic to magnesium alloys. Experimental density was calculated using Archimedes principle experiment.

Table III.1 - Experimental density from alloys in study, calculated using the Archimedes Principle.

Density(g/cm^3)	HP Mg	Mg2Gd	Mg5Gd	Mg2Gd1Mn	Mg5Gd1Mn
Archimedes density	1.737±0	1.760±0.003	1.782±0.013	1.764±0.001	1.7975±0.003

The experimental density represented in Table III.1 shows an excellent agreement between the experimental density of HP Mg and the theoretical density of pure magnesium. The increase of Gd content increases the density of binary system, which was expected due to the high molecular weight presented by gadolinium. The addition of manganese further increase the binary Mg2Gd density and a similar trend is observed to the ternary alloy Mg5Gd1Mn. The densities of elements are respectively for Mn, Gd and Mg 7.21, 7.90 and 1.738 g/cm2 [120]. It is possible to observe that small amounts of alloying elements did not show significant changes in the density with respect to Pure Magnesium.

The analysis of XRD patterns present in Figure III.1 allows the qualitative identification of the dominant crystallographic phase present in the microstructure of as-cast alloys Mg-Gd, Mg-Gd-Mn and HP Mg.

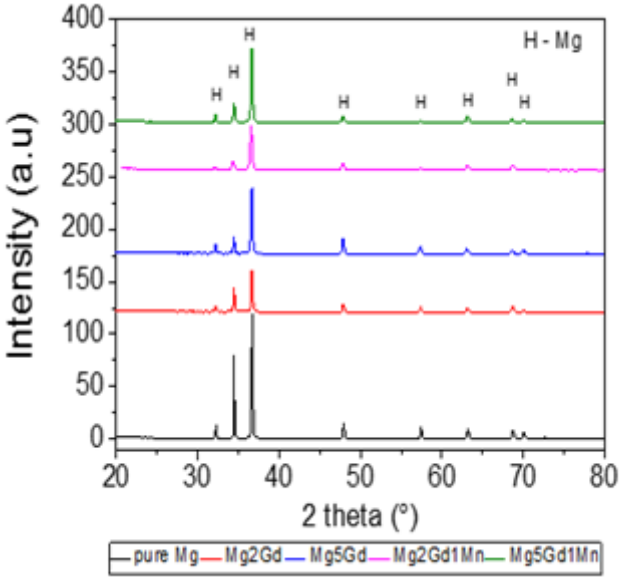

Figure III.1 - The XRD patterns of bulk Mg alloys used in this work.

The X-ray patterns and the observation of the reflection peaks confirmed the formation of hexagonal Mg (for comparison, the observations corresponding to Mg hexagonal phase with space group P63/mmc according to the JCPDS database card no. 04-007-3847). However, no identification of secondary phases, as the Mg5Gd phase was observed. Low-resolution XRD and/or relative similar peaks position between those two phases could explain this effect. It was observed in [121] a similar trend, where the identification of Mg5Gd phase was possible in the Mg10Gd alloy, but not in the Mg5Gd and Mg2Gd alloy.

III.1.2 Microstructure evaluation

The characterization of microstructure allows identifying microconstituents using complemental EDS analysis. At the same time, grain morphology can be revealed as other intrinsic features connected to the cast metals. For this purpose, the main techniques used in this subchapter are Optical Microscopy, Scanning Electron Microscopy and Energy Dispersive Spectroscopy.

III.1.2.1 Optical microstructure

Figure III.2 reveals the grain size and structure of an etched surface for pure magnesium, Mg-Gd and Mg-Gd-Mn alloy systems, and at the same time the surface of an unetched Mg5Gd alloy. The observation of Figure III.2.a) allows the identification of a columnar (or elongated) grain type structure, with the growth of the crystal in the cooling direction of casting (arrow direction). The grains present length size in the order of

millimeters size. The calculation of a reliable statistical size of grain found difficulties due to the large grain size characteristic of those cast metals and as so it is not presented.

Figure III.2.b) shows the grain morphology of the Mg2Gd alloy. Similarities with grain morphology of the HP Mg can be observed. However, a shorter size of grains in length and larger in width can be identified, which can indicate a beginning of a grain transformation. The microstructure of Mg5Gd depicted in Figure III.2.c) shows a different morphology of grains when compared with the previous systems. Those grains appear with an equiaxed morphology and relatively smaller in size, which can indicate a complete grain transformation for the Mg5Gd alloy.

Ternary systems Mg2Gd1Mn (Figure III.2.d)) and Mg5Gd1Mn (Figure III.2.e)) also undergo a grain transformation, but morphologies of grains are slightly different from the binary system. The optical micrograph of Mg2Gd1Mn in Figure III.2.d) shows two main grain structures, an outer columnar grain growth in the cooling direction and an inner large equiaxed grain, which can indicate grain growth in opposition to the direction of heat flow [122]. This formation at inner regions can indicate the presence of a lower cooling rate at the limit of grain transformation, which can be related to gradients in chemical composition [123]. Figure III.2.e) shows a complete transformation of the columnar grains into coarse equiaxed grains.

The appearance of segregation zones (of alloy elements) localized along as like dendritic arms is a feature off as cast metals [123], and the same feature is present in the metal alloys worked in this investigation (observe micrograph in Figure III.2.f)). Alloying elements are responsible for the formation of segregation zones (solute rejection) caused by a relatively wide temperature span between liquidus and solidus line [122]. The addition of certain alloy elements can also induce the precipitation of intermetallics. The microstructure of all alloys will be better addressed in the next subchapter.

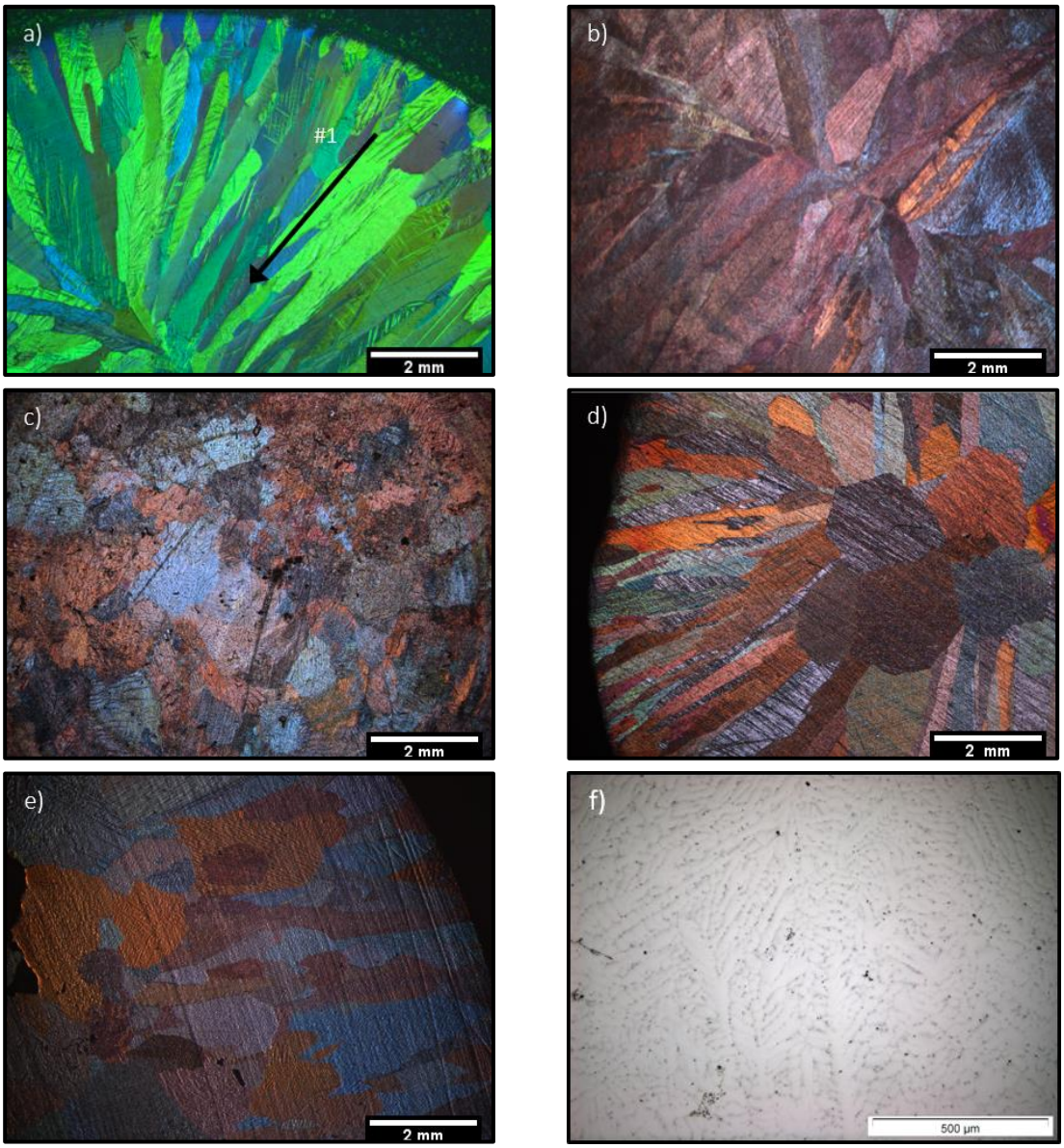

Figure III.2 - Optical micrographs revelling grains structure of etched surface: a) pure magnesium, b) Mg2Gd, c)Mg5Gd, d)Mg2Gd1Mn and e)Mg5Gd1Mn, and unetched surface f) Mg5Gd.

III.1.2.2 Electron microscopy and microstructure characterization

The BSE pictures reveal a contrast between a dark matrix and brighter zones, which can be related to the formation of segregations during solidification. A relatively large grain size was identified in the previous section for all alloys, and segregations are appearing inside the grains at interdendritic formations. The as like dendritic arm seems to be an enrichment zone of segregated alloying elements (with respect to the matrix). This can be observed in Figure III.3. The volume fraction of brighter zones seems to increase with the increase of Gd content when comparing Figure III.3.a) and b). A similar behavior seems to occur with the ternary alloys, depicted in Figure III.3.c) and d), respectively, Mg2Gd1Mn and Mg5Gd1Mn.

It was used the ImageJ software to access the measurement of the volume fraction, which is proportional to the surface area by the relation VV=AA. This relation can be found in stereological projection methods [124]. Threshold and brightness/contrast adjustment allowed to get a measurement of the phase fraction, respectively, For Figure III.2.a), b), c) and d) and are respectively 2.615%, 5.196%, 1.138% and 3.771%, which confirm the previous statements. Due to the presence of segregation zones, it is hard to calculate a reliable estimation of the volume phase fraction, and so those values are under a qualitatively base analysis.

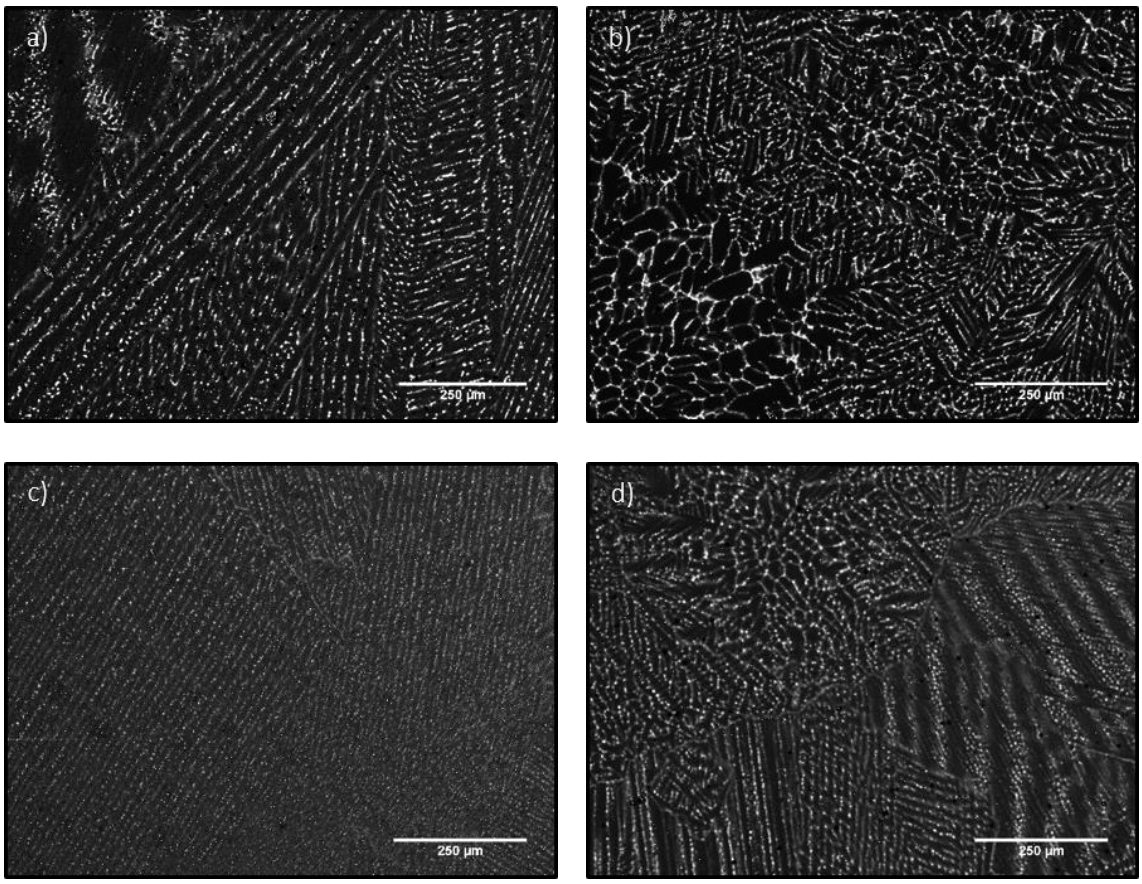

Figure III.3 - Overview of microstructure (BSE images) of as cast a) Mg2Gd, b) Mg5Gd, c) Mg2Gd1Mn and d) Mg5Gd1Mn.

III.1.2.2.1 Microstructure characterization of binary alloys

The binary alloys used in this work were prepared with concentrations of 2 and 5wt% of Gd, as stated in section II.1. Gadolinium shows a substantial solubility in magnesium of 4.3 at% at the eutectic temperature. When solubility limit is reached, Gd precipitate in the Mg5Gd phase.

A typical microstructure of the as-cast Mg2Gd is shown in Figure III.3.a) and III.4. The BSE mode image shows a dark matrix, brighter zones (which are presenting with a grey coloration) in a string-like formation, relatively small white dots dispersed in the

matrix and cluster formation of white particles. The increased magnification micrograph of a white cluster formation is illustrated in Figure III.4.b) and III.4.c). The respective EDS point analysis (selected zones represented by #) of the elemental composition (in at %) of specific elements highlighted in Figure III.4 are represented in Table III.2.

The Mg matrix analysis is appointed by spot #4 and shows gadolinium dissolved into the solid solution of the α-Mg, and by the MDL factor, it is possible to identify its presence as a trace element. The analysis of other zones depicted in Figure III.4.b) shows detection of Fluor, and is concentration ca be found in the darker like string structure, along with oxygen, which can indicate, and by BSE contrast, the presence of a non-metallic oxidized inclusion. Probably this string formation is dirty from casting, and Fluor can come from the reaction of liquid metal with foundry atmosphere.

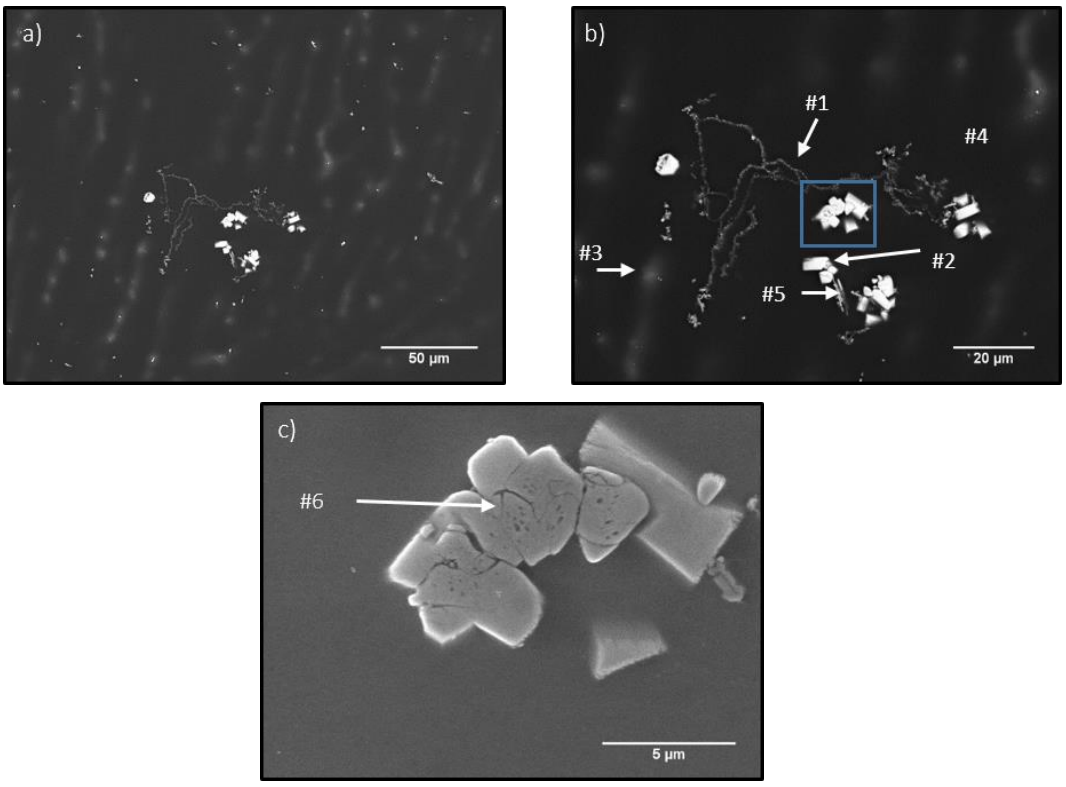

Figure III.4 - Micrographs of the microstructure of an Mg 2Gd alloy, a) BSE figure at a certain scale and b) BSE figure of a magnified zone from Figure III.4.a) and c) SE micrograph of a selected spot in Figure III.4.b), represented by the blue square.

The representative spot #2 shows the elemental composition of a fairly large square intermetallic (which shows morphological similarities with a cuboid structure). This particle seems to present a relatively large atomic concentration of gadolinium and it is possible to argue (applying the MDL factor) that it is a major element in the structure of this intermetallic. Observing the elemental maps in Figure III.5, the elemental distribution of magnesium was decreased at those areas, comparatively to the magnesium matrix and brighter zones. Instead, Table III.2 shows a relatively high concentration of Magnesium in

spot #2 which can be related to the interaction volume of beam penetration with the surrounded areas (magnesium matrix). It is also observed in Table III.2 a relatively large amount of Si element at this point, which was not detected in magnesium matrix and brighter zones. Another particularity is the detection of iron concentration in spot #5, accompanied by silicon and gadolinium. A brighter zone identified by #3 shows an increase in gadolinium content when comparing to the magnesium matrix. It is also observed in Figure III.4.c) an intermetallic and the respective elemental composition it is represented by spot #6 in Table III.2. The white's fairly large particles present a higher concentration of alloy and impurity elements in respect with other micro constituents. Silicon and iron are probably impurities in the microstructure.

Table III.2 - EDS analysis of some micro constituents highlighted in Figure III.4.b) and c).

Analysis	Elements (at%)					
	F	**Fe**	**Gd**	**Mg**	**O**	**Si**
#1	5.072	---	1.219	84.515	8.948	0.246
#2	---	---	17.888	69.434	1.620	11.058
#3	---	---	2.251	97.446	0.303	---
#4	---	---	0.182	98.386	1.432	---
#5	---	5.188	5.282	79.524	4.420	5.586
#6	---	---	31.839	26.198	4.961	37.002

Figure III.5 shows the elemental distribution for the alloys elements, Si, O and F. The represented map allows to identify different structures as the possible oxidized structure in the presence of Fluor and a relatively large white intermetallics as concentrated zones in gadolinium and silicon (possible a Gd_x Si_y H_z intermetallic). Also, it was identified small intermetallics with a high concentration of gadolinium and brighter zones (segregation zones), which are rich in gadolinium than the matrix. Iron elemental distribution was not presented since its concentration was only detected in this specific place. It is not clear the appearance of a stable morphology of the eutectic Mg5Gd phase, which can be in a phase transition or present at very low concentration. Segregation zones are brighter zones with increased concentration of gadolinium with respect to magnesium matrix.

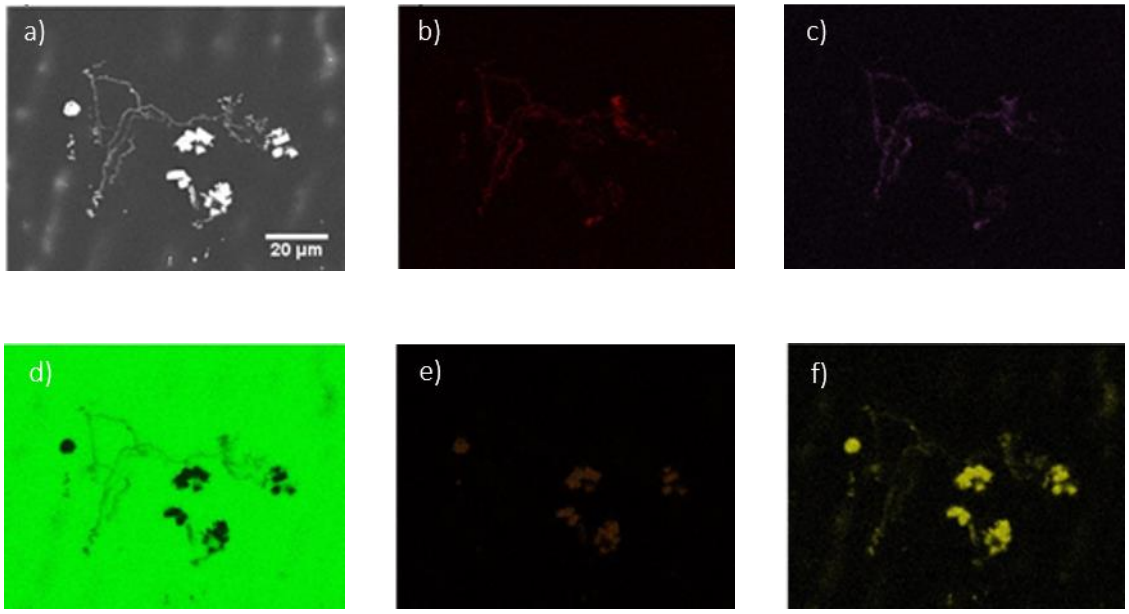

Figure III.5 – Illustration of a) SE micrograph of the Mg2Gd. Elemental maps of the microstructure for b) Oxygen, c) Fluor, d) Magnesium, e) Silicon and f) Gadolinium.

In Figure III.6 it is represented a microstructure of the as-cast Mg5Gd. Compared with the previous microstructure analysis, a clearly eutectic formation it is observed. The fraction of this phase seems to be larger which corroborates the previous volume phase fraction calculation stated in III.1.2.2. It is possible to observe in Figure III.6.b) a network of the supposed Mg5Gd phase, formed along the segregation zones. In figure III.6.c) and d) it is possible to observe other microconstituents. Figure III.6.c) shows the presence of a well-defined square intermetallic near the probably Mg5Gd phase. By another hand Figure III.6.d) shows a similar intermetallic observed in the previous figure with a high content of impurities (Si and Fe), and the elemental composition can be consulted in Table III.3.

The respective elemental composition of the selected zones represented by # in Figure III.6 is presented in Table III.3, which allows the identification of the different microconstituents. Point #1 accounts for the composition of a white planar zone, with a Mg/Gd ratio near 7.3 at%, which can indicate the presence of a Mg5Gd phase. The elemental composition of this compound was measured in different places along the network and showed almost no deviation in elemental composition. In point #2 it is possible to observe an enrichment zone in gadolinium localized in segregation zones.

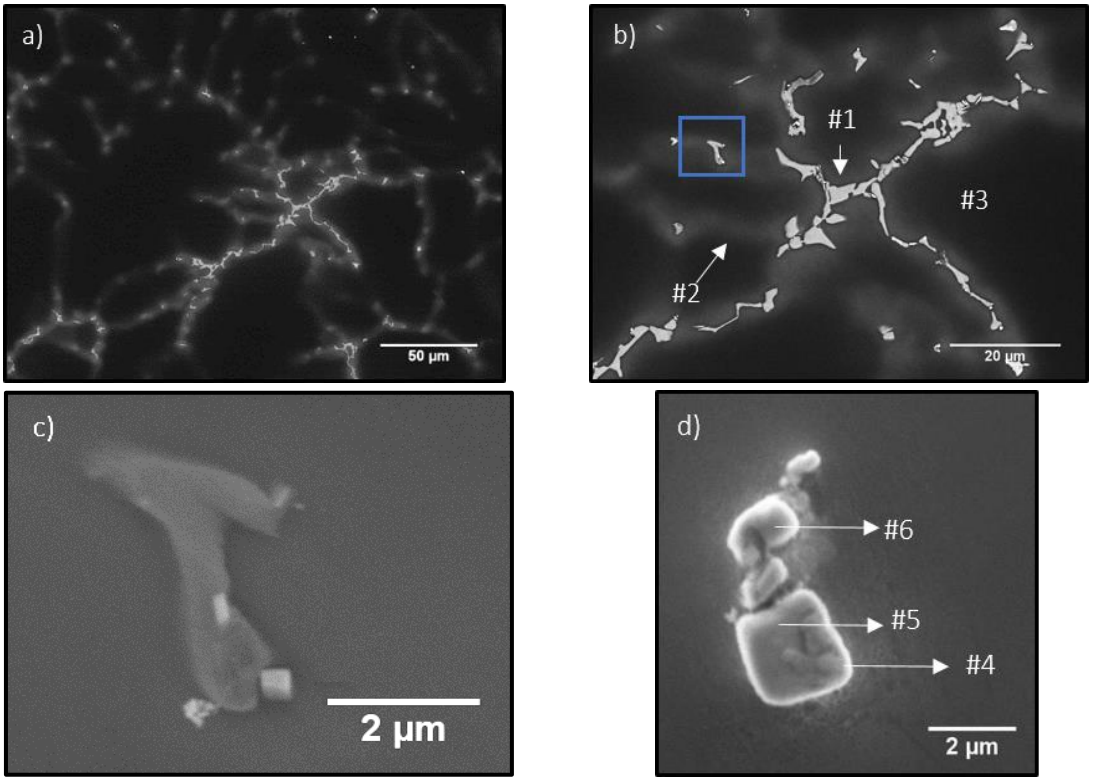

Figure III.6 - BSE micrograph of Mg5Gd microstructure, a) network of micro constituents and b) magnification of the III.6.a) zone. SE micrograph of c) intermetallic highlighted in figure III.5.b) by the blue square, d) high magnification of a similar cuboid intermetallic, found in Mg5Gd.

This enrichment zones are brighter than the matrix and present higher content (when comparing composition with point #3, the Mg matrix) of gadolinium. The elemental composition depicted in Table III.3 shows a higher concentration of gadolinium, silicon and iron in the type of structure observed in figure III.6.d), which by MDL factor, are majors elements of this microconstituent.

Table III.3 - EDS analysis showing the elemental composition of specific zones represented in Figure III.6.b) and d).

Analysis	Elements (at%)				
	Gd	Mg	O	Si	Fe
#1	11.873	87.694	0.433	---	---
#2	3.463	95.757	0.780	---	---
#3	0.384	98.489	1.127	---	---
#4	9.358	42.926	8.040	23.474	16.202
#5	14.233	12.331	7.186	37.371	28.879
#6	8.574	59.581	4.319	11.299	16.227

The elemental map analysis in Figure III.7 allows visualizing the distribution of elements in the microstructure of the Mg5Gd alloy. It is clearly observed that those grey

phases are gadolinium-based (possibly the Mg5Gd phase by interpretation of the phase diagram in figure I.16.a) in section I.6.7) and brighter areas, which are appearing in Figure III.6 are segregation zones, richer in gadolinium in respect to magnesium matrix. The presence of impurity elements was not observed in the Mg5Gd phase and segregation zones. The MDL factor can attribute gadolinium as a minor element in segregation zones and Gadolinium is presented as a rejected solute from a supposed Mg-Gd phase. In spite of the clean zones observed in Figure III.6a) and b), some dirty zones were found in the microstructure of Mg5Gd. A particle with a high amount of Iron and Silicon can be observed in Figure III.5.d) with the presence of main elements in is composition as Si, Fe and Gd. This intermetallic seems to present a heterogeneous elemental composition, and it is possible to be an intermetallic of the family of Gd_x Fe_y Si_z H_w.

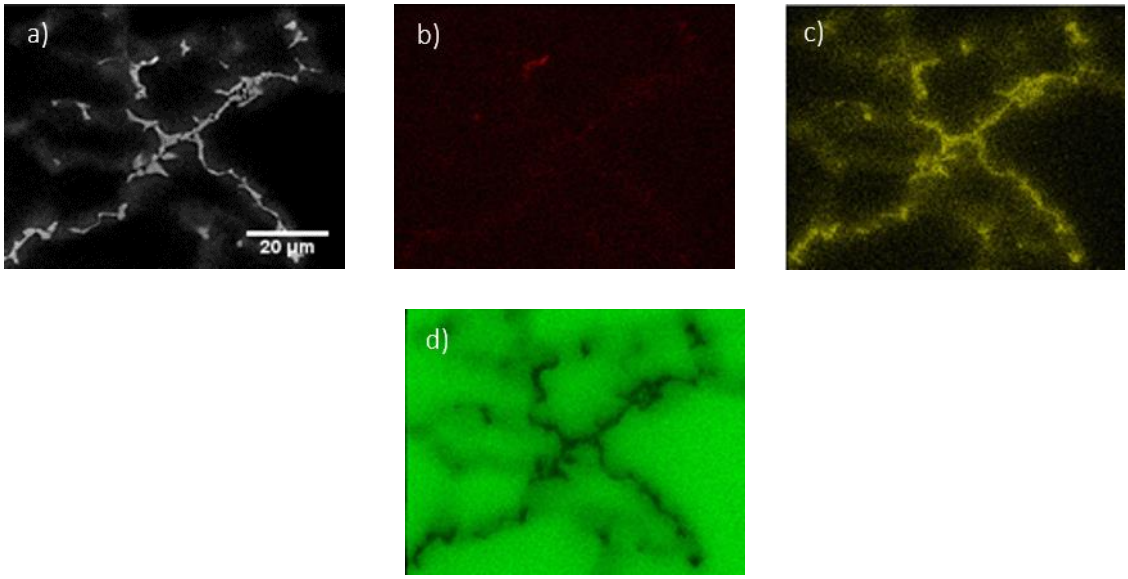

Figure III.7 - Elemental map of the main elements identified in microstructure of Mg5Gd, a) SE micrograph, b) Oxygen c) Gadolinium and d) Magnesium.

III.1.2.2.2 Microstructure characterization of ternary system

An alloy element was added into the microstructure of Mg – Gd alloys to increase the performance of corrosion since manganese is known to deactivate the strong micro galvanic effect promoted by the presence of Iron precipitates compounds (look into Section I.5.1.3 for a more detailed information). Figure III.8 shows a relatively high magnification of the microstructure of Mg2Gd1Mn. The addition of Mn into the alloy do not seem to bring significant modifications in the morphology of micro constituents. However, particles with increased concentration of Mn can be observed in spot #4 (consulted the table III.4 and Figure III.8.a)). Brighter zones are observed as previously stated and white particles dispersed in brighter zones and matrix also can be identified. A magnification of

representative zones like the one represented by the blue square in Figure III.8.a) shows highly defined cuboid intermetallics.

Table III.4 shows the elemental composition of selected areas described in Figure III.8.a). Point #1 and #2 depicted enrichment zones of gadolinium. However, point #2 have a relatively small gadolinium concentration, which can attribute a trace presence by MDL factor. Point #3 and #4 are concentrated zone of Gd as it shows the EDS point analysis in Table III.4 and seems to be accompanied by an increase in Si and Mn when comparing with previous numerical analysis. However, point #4 shows a relatively higher amount of Si and Mn than point #3. The point #5 represents an elemental analysis of the magnesium matrix and shows solubility of Mn and Gd into magnesium solid solution.

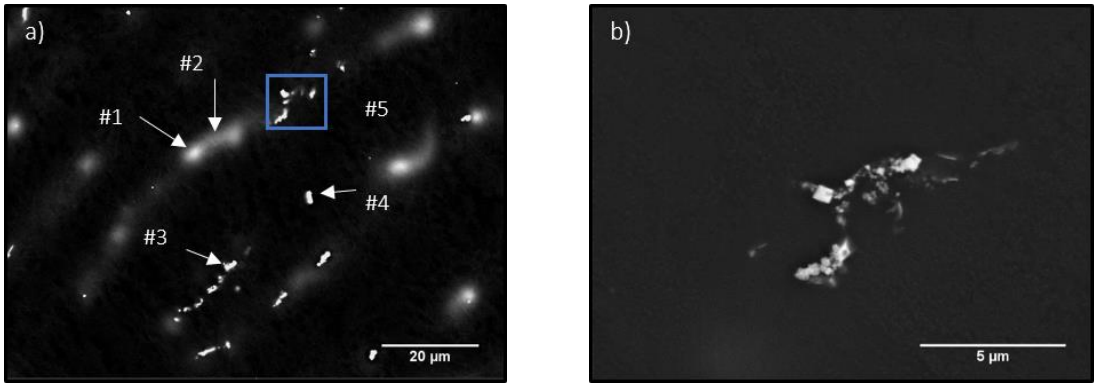

Figure III.8 - Illustration of the microstructure of an Mg2Gd1Mn alloy, a) a relative low magnification zone, b) a high magnification of a typical zone highlighted by the blue square in Figure III.8.a).

It is possible to attribute to white particles, observing the elemental composition in Table III.4, a higher concentration of the alloy element manganese as well as a higher concentration of the impurity silicon. However the discrepancy in the concentration of Mn and Si between point #3 and #4, which can indicate the presence of a different type of intermetallic, or differences in size of intermetallics.

Table III.4 - Elemental composition from selected zones representing micro constituents observed in Figure III.8, for a Mg2Gd1Mn alloy.

Analysis	Elements (at%)				
	Gd	Mg	O	Si	Mn
#1	1.040	98.344	0.254	---	0.363
#2	0.698	98.638	0.30	---	0.364
#3	0.613	96,704	0.910	0.995	0.778
#4	1.387	90.787	1.755	3.250	2.821
#5	0.064	98.646	0.869	---	0.421

The elemental map in Figure III.9 shows the distribution of elements in a cluster of intermetallic, observed in Figure III.8.b). It is clearly noted a higher concentration of Gd in the square intermetallic with respect to magnesium matrix, accompanied with manganese and silicon. By comparison, this kind of morphology seems to be similar to the one represented by #3 in Figure III.8.a). The concentration of oxygen in this zones is not clearly defined by the elemental map (Figure III.9.b)). The concentration of Si seems to relatively small when compared with previous microstructures of previous alloys.

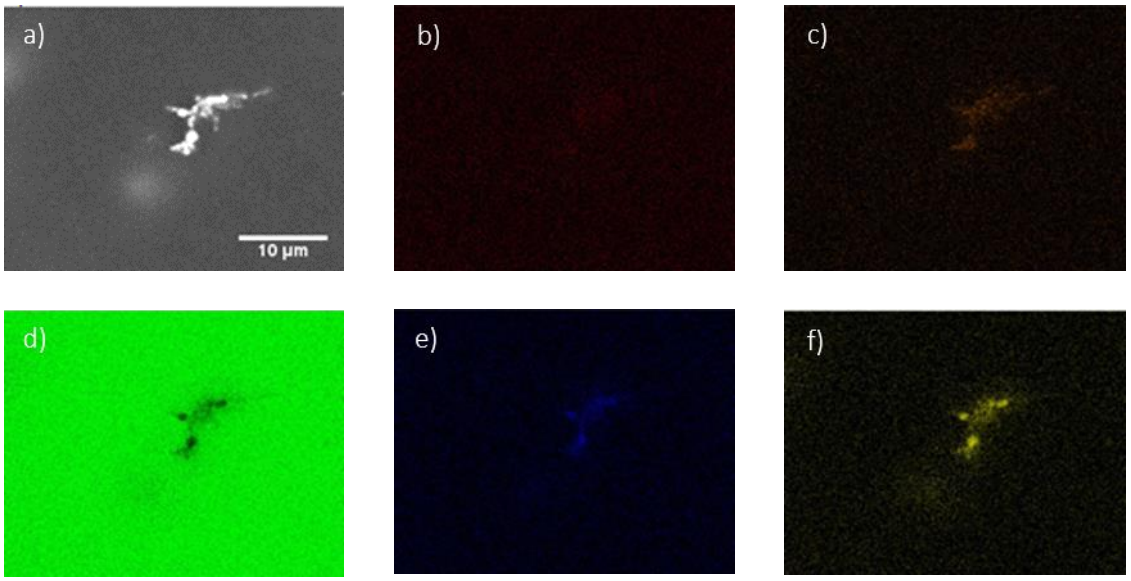

Figure III.9 – Illustration of the elemental map of the Figure III.8.b), showing a) SE micrograph of a cluster formation of intermetallics. Map elements of b) Oxygen, c) Silicon, d) Magnesium, e) Manganese, f) Gadolinium.

The increased amount of Gd added to the alloy Mg5Gd1Mn seems to bring a higher fraction of intermetallic, which can be observed in Figure III.10. Particles with morphology like filament can be found in Figure III.10, marked by the point #2. Brighter zones continue to appear and are selected by point #3 and #4. Point #6 and #1 shows particles with different morphologies. Figure III.10.b) shows a cluster of particles in the microstructure of Mg5Gd1Mn and the own elemental map analysis is presented in Figure III.11. It is also showing particles with different morphologies, highlighted by various blues squares.

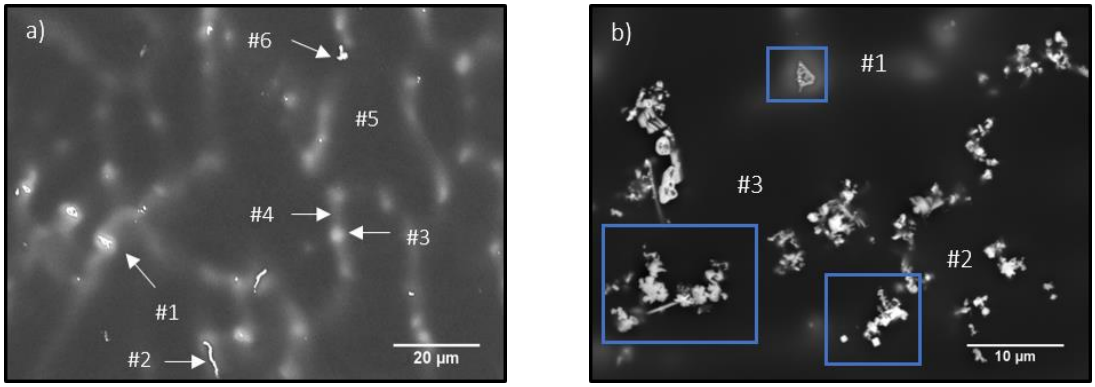

Figure III.10 – Illustration a) and b) shows micrographs of the Mg5gd1Mn microstructure at different magnifications.

The elemental map observed in Figure III.11 shows a distribution of elements of the microstructure found in Figure III.10.b). Manganese is well dissolved in secondary phases but an increase of is content in white particles can be observed. Particles of type #3 (Figure III.10.b)) seems to present a trend between the growth of Si and Mn, which can be observed in Figure III.11. It was also found gadolinium in higher concentrations in those particles, with respect to matrix and brighter zones.

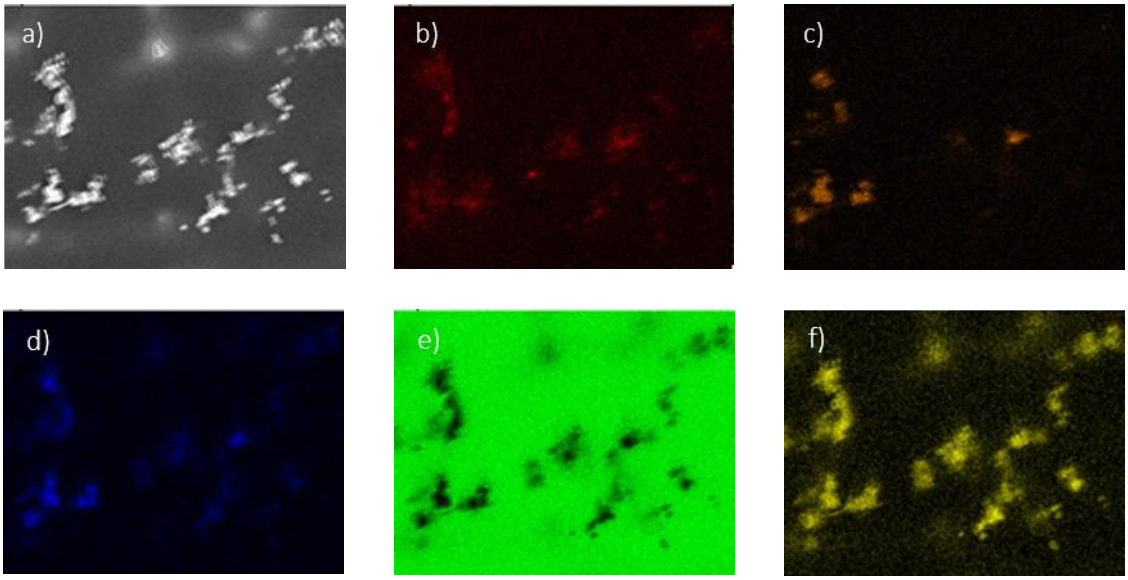

Figure III.11 - Elemental maps from a cluster formation of intermetallics found in the microstructure of an Mg5Gd1Mn alloy, a) SE micrograph, b) Oxygen, c) Gadolinium, d) Magnesium, e) Silicon and f) Manganese.

Particles of type #1 (Figure III.10b)) are accompanied by a slight decrease in concentration of Mg element in respect to magnesium matrix and segregation zones. Segregation zones and grey structure represented by point #1, #3 and #4 in Figure III.10.a) and #1 in Figure III.10.b) also present higher concentration of Gd in respect to magnesium

matrix. Mn seems to be uniformly distributed along the matrix, segregations and Mg5Gd phase. But the magnesium signal detected by EDS detector shows a relatively higher amount of magnesium in this zones when compared to white particles. The silicon element was not detected in traceable amounts at this zones, which is corroborate by elemental composition analysis in Table III.5. The grey particles can be a Mg5Gd phase with Mn dissolved into the structure.

The Figure III.12 shows a magnification of intermetallic represented in Figure III.10.b) by the selected blue areas, and the EDS point analysis can be observed in Table III.5. In Figure III.12.a) it is seen a cuboid-type of intermetallic rich in Gd when comparing with the matrix. In the Figure III.12.b) it can be observed particles with angular edges and "flower" type of morphology. Enrichment in Si and Mn it is observed when compared with the cuboid intermetallic. Iron was also detected in the structure of those intermetallics (Figure III.12.b)).

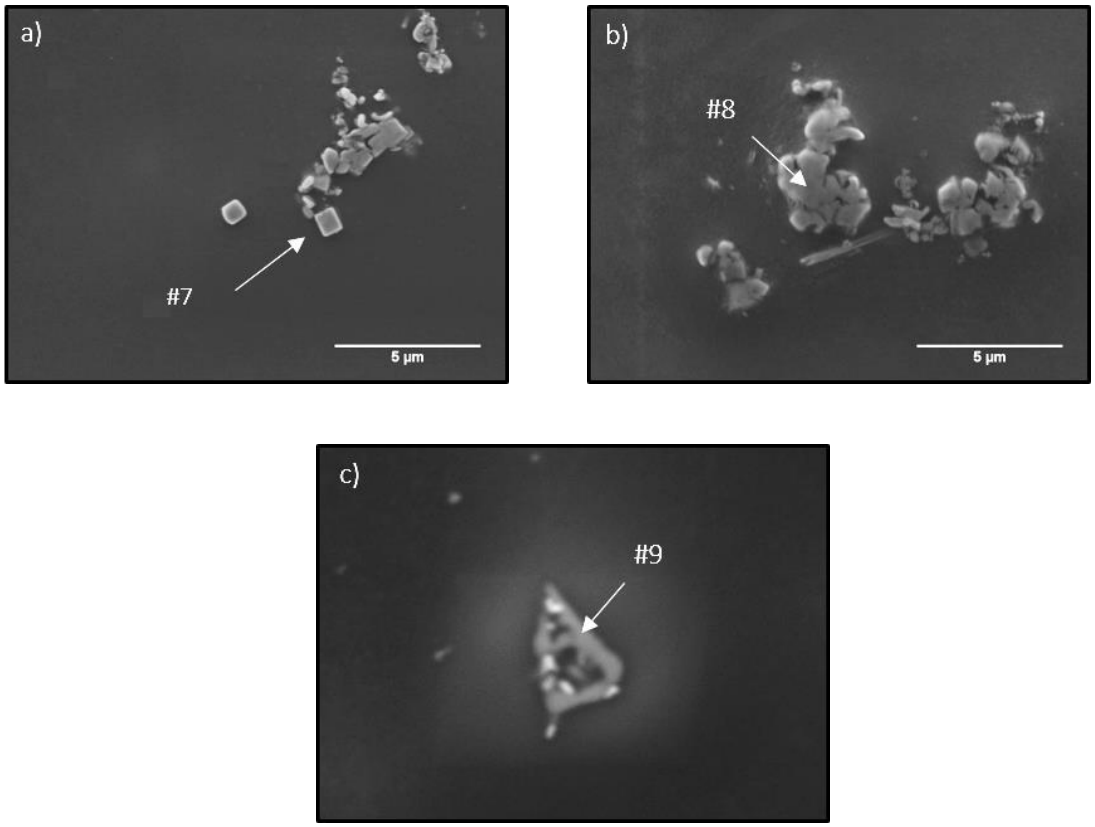

Figure III.12 - SE micrograph of different particles found in the microstructure of Mg5Gd1Mn. Those SE micrographs are from intermetallic highlighted in Figure III.10.b) and appointed by blue squares, respectively a) square #2, b) square #3 and c) square #1.

Figure III.12.c) shows a similar intermetallic phase observed in Figure.III.5.c), where smaller as like cuboid intermetallics are located in the surroundings and inside of this phase. The elemental composition shows an increase in gadolinium in respect to the

matrix and a reduced amount of Mn in respect to intermetallics described previously. No impurity as silicon was detected in is structure.

The presence of gadolinium is higher in the enrichment zones of Mg5Gd1Mn than in the enrichment zones observed in Mg2Gd1Mn, and so the Gd content increases (see Table III.4 and 5). These zones also show dissolved manganese in relative similar amounts which can indicate that solubility in these zones does not depend on the gadolinium addition. The concentration values of Mn in segregation and matrix are relatively similar in both Mg2Gd1Mn and Mg5Gd1Mn, and the same do not occur with gadolinium. Manganese in segregations and matrix is observed as a trace element in respect to MDL factor.

Intermetallic of type #6 and #8 (in the respective Figure III.10.a) and III.12.b)) seems to present higher concentration of the alloying elements as well as impurity element Si, and a similar trend it is found in intermetallic represented by #4 (Figure III.8.a)) in the microstructure of Mg2Gd1Mn.

The as like cuboid intermetallic appears relatively cleaner (less amount of Si) in the ternary system when comparing the previous as like cuboids appearing in the binary system, which present a higher amount of impure elements, due to higher Si and Fe content in their microstructure. However, a better statistical analysis to EDS should be addressed to verify the trend of impurities in cuboid structures.

The atomic concentration and the elemental maps also demonstrate that Mg in EDS analysis is probably detected from the surrounded matrix and this particle maybe do not have Mg in their composition.

Figure III.12.c) shows what it seems to be a Mg5Gd phase since similarities are presented in morphology and BSE contrast with the metallic compound represented in Figure III.6.c). However traceable Mn it is found in the elemental composition which can be dissolved in the solid phase of the precipitate since is concentration is under trace values, in respect with MDL. No silicon was found in those structures.

Iron as an impurity was detected in the microstructure of the intermetallic of type #8 (observe Figure III.12.b)). However, the atomic concentration is well bellowed of that detected in binary systems. Insoluble secondary intermetallic phases were detected in all microstructures. Binary alloys present a dominant cuboid shape type of intermetallic, which can appear dirty in impurities as Si and Fe, however, this could be not a trend to all cuboid intermetallic presented in binary alloys. Enrichment zones of gadolinium and the possible Mg5Gd phase are relatively clean, and their fraction increases with the addition of Gd, in both systems (ternary and binary alloys).

Table III.5 - Elemental composition evaluated by EDS point analysis from different places observed in microstructure presented in Figure III.10.a) and III.12.

Analysis	Elements (at %)					
	Gd	**Mg**	**O**	**Si**	**Mn**	**Fe**
#1	1.46	97.577	0.626	---	0.337	---
#2	3.438	94.784	0.925	---	0.853	---
#3	1.999	96.997	0.579	---	0.425	---
#4	1.414	97.824	0.398	---	0.364	---
#5	0.363	98.222	0.975	---	0.440	---
#6	3.943	86.62	5.198	2.101	2.138	---
#7	14.17	78.680	6.867	0.163	0.285	---
#8	3.939	66.251	13.20	8.88	6.218	1.504
#9	6.294	92.396	0.550	---	0.760	---

III.2 Short immersion time characterization

In this subchapter techniques such as AFM/SKPFM, SEM, polarization and EIS were used for studying the alloys systems during short immersion time, immersed in different electrolytes. The short immersion time is corresponding to around 24 hours of immersion.

III.2.1 AFM/SKPFM Measurements

Atomic force microscopy measurements were conducted on Mg5Gd and Mg5Gd1Mn alloys in a 0,9 wt% NaCl solution to examine local corrosion behaviour of intermetallic. Differences in topography over time can be attributed to local corrosion attack. On the other hand, Volta Potential Difference (VDP) can be attributed to the cathodic/anodic response activity of the surface of different micro constituents. The measurements were carried at an initial time without immersion of sample, at 10 minutes of immersion and 180 minutes of immersion for both systems.

The colour range for topography goes from black to a minimal surface height and white colour for maximum height. At the same time and for the VDP, the colour bar follows the same principle as the topographic colour bar, where brighter regions in the colour map can be identified with a nobler potential with respect to darker areas which present a lower Volta potential.

The surface of Mg5Gd displays a relatively flat topography with phases protruding from the surface, which can be observed in Figure III.14.a). The topographic differences are due to different mechanical properties (hardness) between the various micro constituents presented in the microstructure. In zones #1 and #2 it can be identified rich gadolinium intermetallics with, probably, an increase of Si (and occasionally iron) impurities. By another hand, those intermetallics are located near or inside of a Mg5Gd

phase and/or segregation zone. Zone #3 identifies gadolinium enrichment zones and perhaps the presence of a Mg5Gd phase.

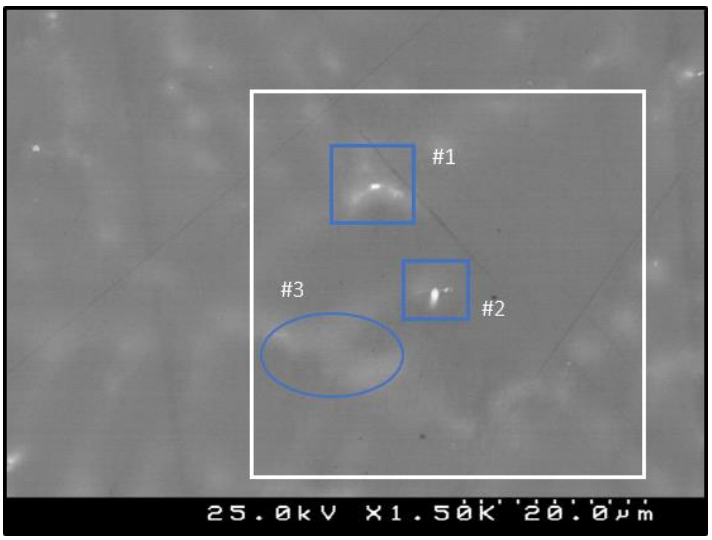

Figure III.13 - SE micrograph of an Mg5Gd alloy before immersion in a 0.9 wt% NaCl solution.

VDP color map (Figure III.14.b)) shows that segregation zones (which are gadolinium enriched) have a lower Volta Potential in respect to magnesium matrix (at an initial stage). By other hand zone #1 and #2 appears with a nobler Volta potential with respect to the matrix. It is possible to attribute to particles like GdH_2 a higher Volta potential which can be due to the presence of relatively large levels of impurities or due to the intrinsic chemical composition of this intermetallic (high presence of Gd and H), or both.

After 10 minutes of immersion in the 0.9 wt% NaCl electrolyte the topographic map in Figure III.14.c) shows an increase in height from a few decades of nano to micrometers size from previous zones #1 and #2 appointed in Figure III.13. Other areas are appearing with an increase of height, and the Figure III.13 do not allow to identify this zones correctly. However zone #2 seems to present a stronger micro galvanic coupling since deeper zones are appearing in the surrounds of the intermetallic. This possibly occurs due to an anodic dissolution of the surrounded atoms, at a high rate. Other possible cathodes can be identified by observing the Figure III.14.c), since an increase of the topographic level of the surface can be detected.

The zone identified in spot #2 during the first 3 hours of immersion seems to reach high cathodic activity, due to the increase of topography in respect to the matrix, supporting a strong cathode behavior (micro galvanic coupling, which increase anodic dissolution of surrounded areas and water reduction promoting the formation of corrosion compounds near cathodic sites). A spreading of the VDP near strong cathodes can indicate small re-deposition of metallic species (possibly iron), but topography (in Figure III.14 c) and e)) it is not sensitive to this deposition (of the spreading areas). This spreading effect

also was recorded in the Figure III.14.d) at 10 minutes of immersion. The initial low potential of the supposed Mg5Gd phase and/or segregations with respect to magnesium matrix could be an indication of dissolution of those phases. Such aspect does not seem to occur since topographic do not show significant changes in height. It is possible that those phases/segregations do not participate in corrosion at 3 hours of immersion.

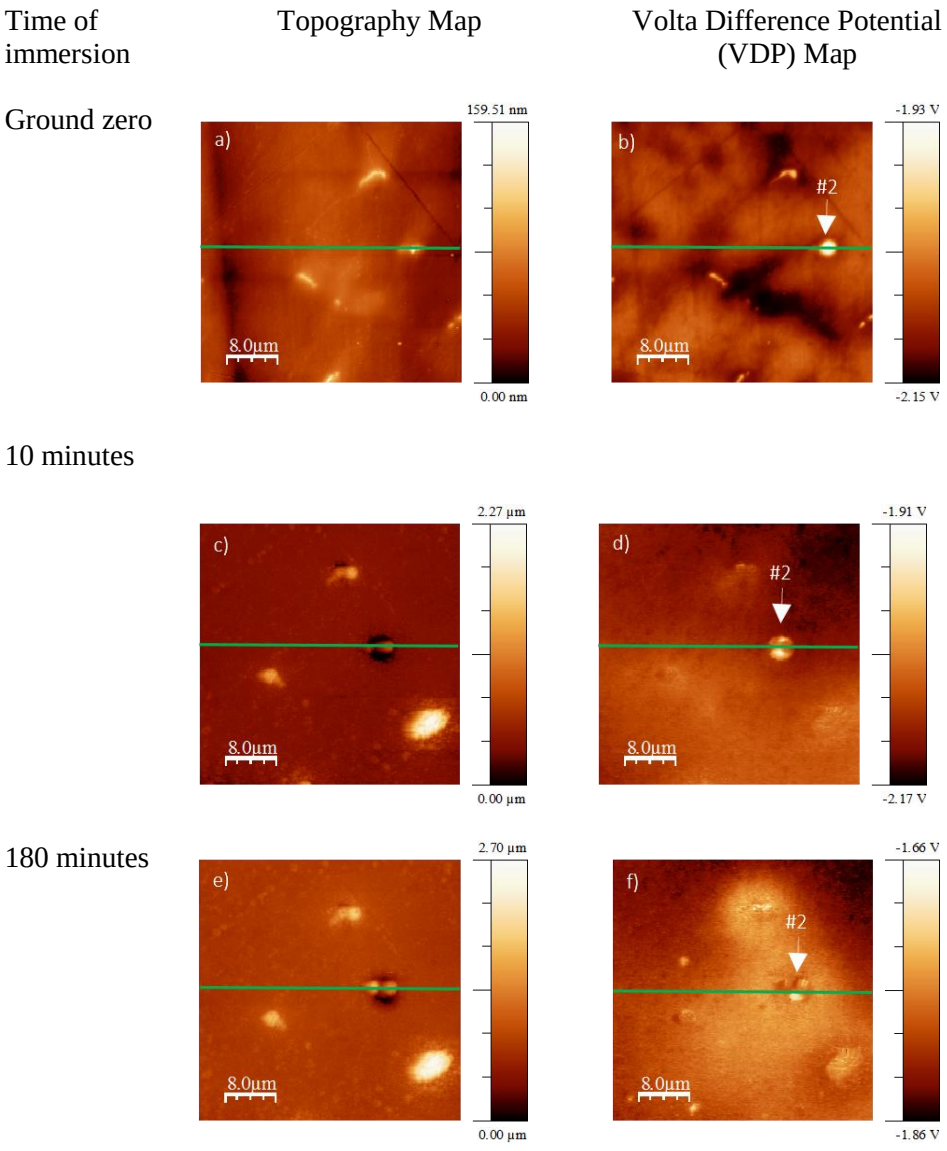

Figure III.14 - AFM/SKPFM characterization of the Mg5Gd immersed in a 0.9 wt% NaCl solution, a) Topography map at zero time of immersion, b) VDP map at zero time of immersion, c) Topography at 10 minutes of immersion, d) VDP map at 10 minutes of immersion, e) Topography map at 180 minutes of immersion and f) VDP map at 180 minutes of immersion.

The observation of the line profile (Figure III.15), which corresponds to the green line outlined in Figure III.14 can better explain what is occurring at zone #2, which by SEM interpretation it could be a possible GdH2 particle (cuboid intermetallic). The

topographic line depicted in Figure III.15.b) at zero minutes of immersion, shows a slight increase of topographic which starts at 25 um with respect to the scan distance. This feature is accompanied by an increase in the Volta potential line, reaching a maximum value of Volta Potential at around 27.5 um. This increase in potential it is not linear, and a local maximum can be observed before to reach the global maximum of VDP line profile. A cluster of cuboid particles or differences in chemical composition of the cuboid intermetallic could explain this behavior.

At 10 minutes of immersion, the topographic line (Figure III.15) start to increase, near 25um of the scan distance. VPD line is accompanying this increase (observe Figure III.15), reaching a maximum at around 27.5 um. However the value of VPD is lower than the VPD at an initial stage, maybe do to the deposition of corrosion products at those places. This effect could be explained because cathodic reaction produces hydroxyl groups (OH-) according to reaction I.3, and it is possible the precipitation of corrosion compounds at the top or near those phases. This maximum in VPD at 10 minutes of immersion do not correspond to the maximum in surface height line, but to a smaller height point. Before to reach this global maximum (topographic line), a local maximum it is observed at approximately 26 um (Figure III.15)). It is possible that two cuboid particles are coexisting (since the initial VPD line seems to distinguish two different potentials), interconnected by magnesium matrix and/or segregated zones. The small distance between them can lead to a strong galvanic coupling (particles working as cathodes), resulting in a strong dissolution in the space between them (anodic dissolution). This effect could explain the appearance of dark zones in Figure III.14.c) (surrounding #2).

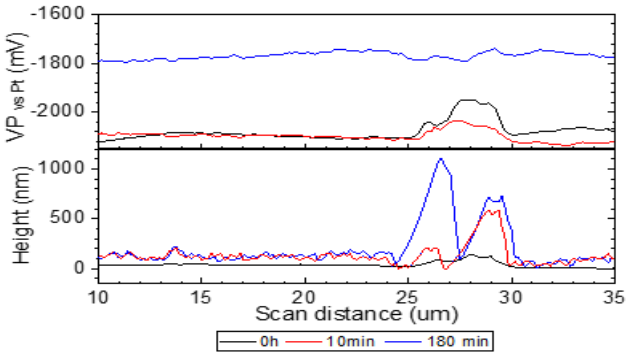

Figure III.15 - Line profiles from a green outlined line which can be observed in figure III.14. In the bottom of the figure it is represented the surface height line profile and in the top the VPD line profile.

The strong potential presented by the maximum Volta potential at initial stages could lead to a high release of hydrogen gas which does not allow the deposition of corrosion products. Particle chemical deviation also could be responsible for this effect.

At 180 minutes a similar behavior it is observed but the surface height at #2 (Figure III.14) increases even more (and also enlarges is horizontal size), which, again, could indicate cathodic effect noted at those places, and so corrosion products deposition is occurring. The overall Volta potential shift to higher values due to probably the spreading effect of VPD observe in Figure III.14.f), which could be attributed to metal redeposition. This decrease of VPD seems to be a result of the ennoblement of the metal surface The VPD line in between the values of 25 and 30 um seems to homogenize the VPD, which could be due to the formation of a semi-protective corrosion layer, at this time.

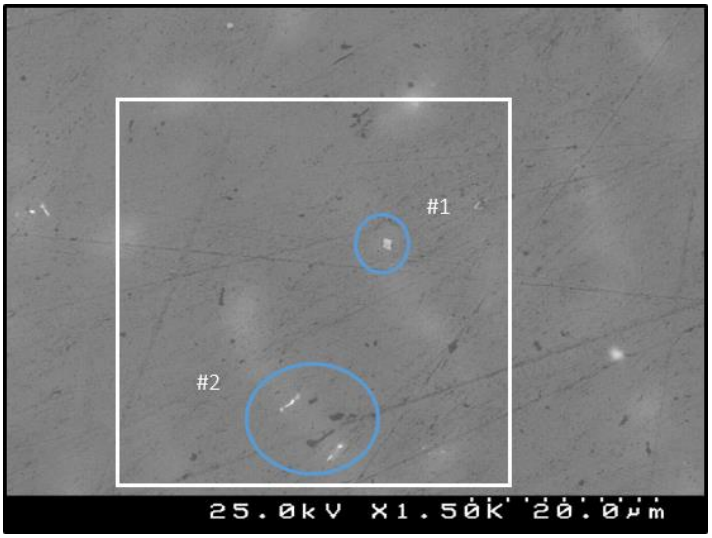

Figure III.16 - SE micrograph of an Mg5gd1Mn alloy before immersion in a 0.9 wt% NaCl solution.

Figure III.16 shows an SE picture of the microstructure of Mg5Gd1Mn. It is possible to identify different zones marked by #1 and #2. Zone #1 is representing a possible cuboid particle (which in the ternary system seems to be cleaner in impurities), and #2 is representing segregation zones (which are richer in Gd in respect to the matrix). The segregation zone seems to contain intermetallics of the type #1 depicted in Figure III.10.a) (probably Mg5Gd phase with Mn dissolved in this phase).

By observing Figure III.16 and III.17.b), it is possible to denote that segregation zones are more homogeneous in VPD than the previous system (Mg5Gd alloy), at zero minutes of immersion. At the same time, topography map appears relatively homogeneous. A unique characteristic is observed in zone #1, where it is shown a strong Volta Potential signal surrounded by a decrease of Volta Potential, making a type of halo structure. Some artefacts can be observed in Figure 17.a), b) and d), which probably are scratches on top of the metal surface, and can come from metallographic preparation. Perhaps zone #1 is showing a cuboid-type of intermetallic, which is cleaner in impurities, with respect to binary systems. The previous microstructure analysis showed Mn dissolved in magnesium matrix, segregations and even in cuboid particles, which can be the reason for a more homogeneous VPD when comparing Mg5Gd alloy.

At 10 minutes the particles represented by zones #1 and #2 have an increase of the amplitude of VPD in respect to surrounded areas and Mg matrix (due to the lower Volta Potential of the matrix). However topography maps in Figure III.17.c) do not show an increase in surface height, with respect to those places. Further increase of time of immersion to 180 minutes shows deep zones (represented by dark zones) surrounding particle #1, when no significant changes occur to the other micro constituents (observe Figure III.17.e)), with respect to topography.

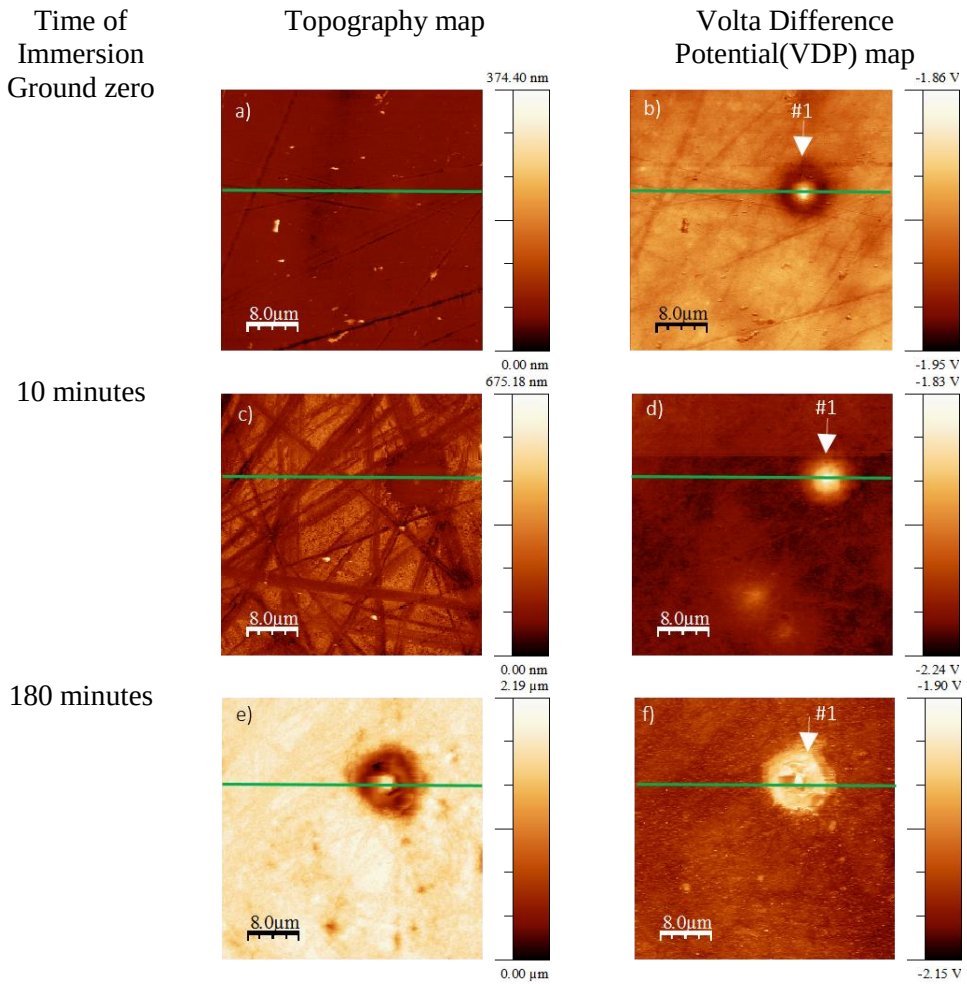

Figure III.17 - AFM/SKPFM characterization of the Mg5Gd1Mn immersed in a 0.9 wt% NaCl solution, a) Topography at zero time of immersion, b) VDP maps at zero time of immersion, c) Topography at 10 minutes of immersion, d) VDP maps at 10 minutes of immersion, e) Topography at 180 minutes of immersion and f) VDP map at 180 minutes of immersion.

The VPD map for this time of immersion shows a spreading effect for this particular place (zone #1 Figure III.17) and do not denote significant changes to other micro constituents. This feature can be observed in figure III.17.f). A better understanding can be achieved if observed the line profile outlined in Figure III.18.

The particle #1 (Figure III.17) clearly shows a higher Volta Potential with respect to the magnesium matrix observed by the increase of Potential of the VPD line. The difference of amplitude appears to be lower than the one represented by Figure III.15 at the same time of immersion. The corresponding increase of time of immersion to 10 minutes, increased the difference amplitude between the global maximum of VPD and the respective magnesium matrix since the supposed magnesium matrix experienced a shift to lower values of Volta Potential (this feature can be observed in Figure III.18.a). Watching Figure III.18, the topographic line does not show any response to this shift in VPD values, since no significant differences were noted from 0 to 10 minutes of immersion, and so no cathodic activity can be attributed to this particle.

It is possible to observe at 180 minutes of immersion, the appearance of deeper zones (probably an indication of pit formation) in the surrounding of the particle #1. This phenomenon can be observed in Figure III.17.e) by the appearance of a hole structure and in the topographic line found in Figure III.18, where deeper zones can be localized in the surrounds of the particle #1. Another feature is the overall increase in the Volta Potential from magnesium matrix and possible other micro constituents, with respect to the 10 minutes of immersion, and a decrease of the global maximum in Volta potential line. However a third strange behavior it is observed where the possible bottom of the pit it is showing an increase in potential since the VPD line shows an increase of Potential at those places. At the same time, no corrosion products are being deposited on the surface since the relative surface height is not increased. The non-deposition of corrosion products could be explained by a low local increase of pH and so the preferential precipitation of Mg $(OH)_2$ could not occur at this stage. The increase in potential in the depth of the pit could somehow reveal an under intermetallic, which was probed because of the anodic dissolution. However, those are assumptions, and further investigation should be taken into account.

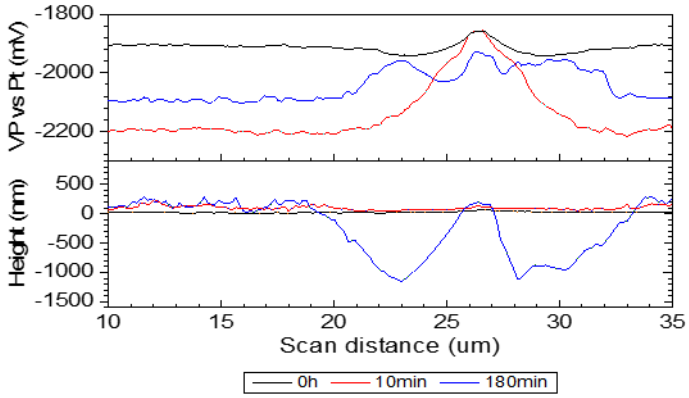

Figure III.18 - Line profiles from an outline line which can be observed in figure III.17 at green. In bottom of figure the surface height line profile and in the top the VDP line profile.

III.2.2 SEM observations

The surface of Mg5Gd was observed by SEM after immersion and AFM/SKPFM measurement and is represented in Figure III.19. The increase of Mg and O peaks found in EDS spectrum (Figure III.19.b)) allows stating that structures in zone #1 (and other structures in the same figure which is appearing with white coloration) are possible Mg(OH)2 deposited in/or at near places to the cathodes. In the other way, a strong galvanic coupling between intermetallic (rich in impurities which could increase the relative potential of phase) leads to a higher dissolution and the formation of a structure like a pit. Corrosion initiation seems to occur near intermetallic type #1 (EDS show increase in Si and Gd, indicates a possible cuboid intermetallic). The cavities surrounding this intermetallic were promoted by a possible cathodic overpotential, as shown in Figure III.14, leading to propagation of corrosion.

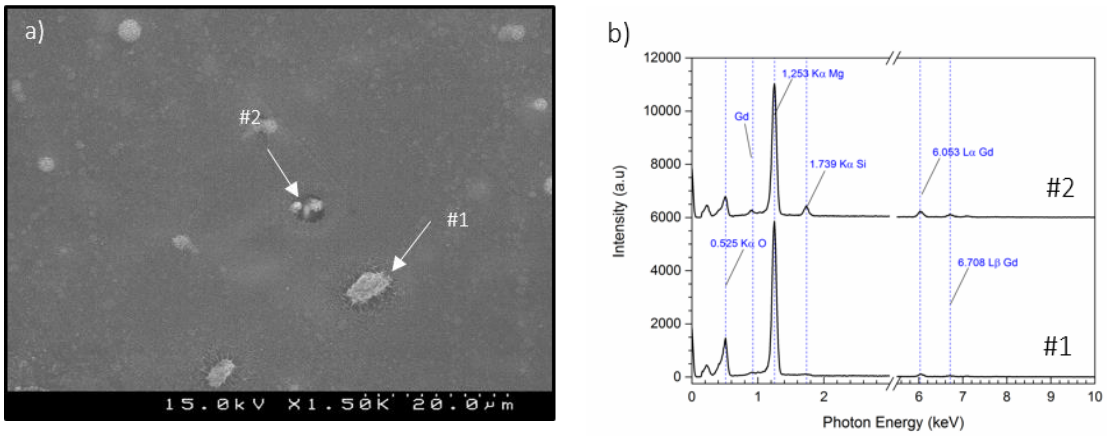

Figure III.19 - The illustration is representing in a) morphology of surface after 3 hours of immersion in a 0.9 wt% NaCl for Mg5Gd, b) EDS spectrum performed in zone #1 and #2.

Figure III.20 shows the morphology of the surface of Mg5Gd1Mn after 3 hours of immersion in a 0.9 wt% NaCl. The probed place is with respect to the surface presented in Figure III.16 and 17. It is possible to observe a supposed pit formation surrounding the white particle, which is in agreeing with Topographic and VPD maps found in Figure III.17, at three hours of immersion. The typical EDS spectrum represented in Figure III.20.b) shows a relatively high presence of Gd at those zones, which can corroborate the presence of an intermetallic. Zone #2 do not show a significant increase in O peak, which can indicate no deposition of corrosion products near those type of particles.

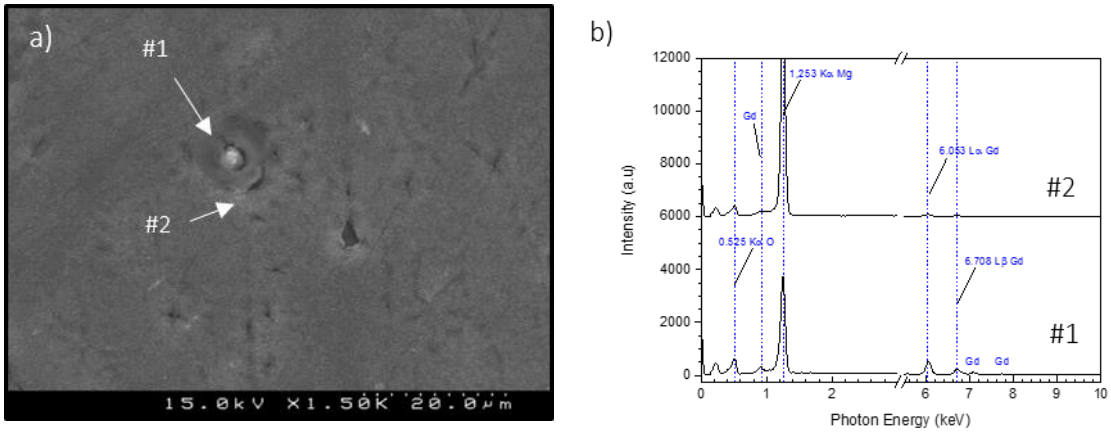

Figure III.20 - The illustration is representing in a) the morphology of surface after 3 hours of immersion in a 0.9 wt% NaCl for Mg5Gd1Mn, b) EDS spectrum of the zone #1 and #2 represented in figure III.20.a).

III.2.3 Potentiodynamic Polarization

Physiological body are dynamic, aggressive environments containing proteins, dissolved oxygen and various ions in solution. Body fluids parameters as the concentration of chlorides, pH and the temperature can present large impact on corrosion behavior of metals, as the buffered effect present by them.

Due to the focus on degradable metals for bio-applications, it was necessary to use standard aqueous solutions which simulate the ionic concentration of human blood (body fluids). In this work simulated inorganic salts solutions were used, putting aside the organic compounds interactions and temperature control. To better understand the influence of different components, it was used solutions with less complexity that allow getting a better view on the impact of various compounds on the passivity of Mg alloys.

The Figure III.21 and 22 show the resulting polarized curves. In the y-axis, it is observed the applied potential, with respect to the Ag/AgCl standard potential, while the x-axis displays the resulting current density, which was measured during polarization. All polarization measurements were started at a potential of -0,150 V versus the OCP. The linearity of the cathodic branch corresponds to hydrogen evolution and Mg $(OH)_2$ film formation, which are characteristic of cathodic reactions. Reduction of hydrogen, producing H_2 (g), consumes electrons and should be a limiting process at potentials lower than recorded in OCP.

A surface layer can form a barrier between the magnesium alloy surface and the solution, preventing the contact between the metal surface and solution. It is possible to observe a semi-passive behavior in the polarization curve of Mg2gd1Mn showed in Figure III.22.b). For Mg5Gd1Mn the same can be observed but with a less strong effect. The barrier effect can increase resistivity, slowing down the current density with the growing potential, under anodic polarization. This is understood as a significant increase of

potential and a limiting current density. However, the breakdown of the semi-protective layer further increases current density.

Figure III.21.b), can give an indication that protective film can work better to passivation than other alloys at this time of immersion. However comparing current densities in Table III.6 it is observed that HP Mg alloys present the lower current density, follow by Mg2Gd1Mn, Mg5Gd1Mn, Mg2Gd and Mg5Gd, in a 0.9 wt% NaCl solution. Regarding corrosion, this can mean an increase in corrosion through the same direction. Also, the breakdown of the passive film can explain an increase in I_{corr} and subsequent increases in corrosion rate (the relation between both variable I_{corr} and CR can be described by the Faraday law, observed in equation I.6). The I_{corr} is measured using Tafel extrapolation of the linear cathodic branch.

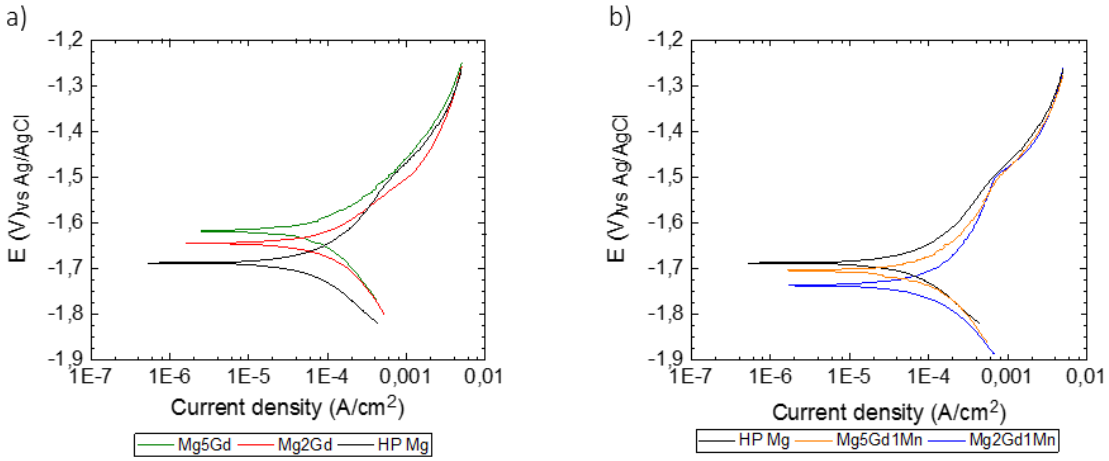

Figure III.21 - Polarization curves of working alloys during one hour of immersion in a 0.9 wt% NaCl solution. In a) Polarization curves for Mg5Gd, Mg2Gd and HP Mg, in b) Polarization curves for HP Mg, Mg5Gd1Mn and Mg2Gd1Mn.

Binary alloys present the higher corrosion current, and HP Mg has the lower corrosion current. The presence of gadolinium and impurities brings nobler potential to the binary alloys when comparing with HP Mg. The addition of Manganese to the binary system brings lower potential with respect to the reference. In Table III.6 it is observed that the increasing amount of Gd leads to higher values of the estimated I_{corr}, which can be related to higher values of corrosion rate for Mg5Gd, followed by Mg2Gd. The respective average values of I_{corr} and E_{corr} can be observed in Table III.6.

Table III.6 - Illustration of the values for the Corrosion Current density (Icorr) and Corrosion Potential, estimated using Tafel extrapolation. Those values are in respect to the first hour of immersion in a 0.9 wt% NaCl solution.

Alloys	Ecorr (V)	Icorr (uA/cm^2)
HP Mg	-1,689± 0,022	55,5± (2,4)
Mg2Gd	-1,655 ± 0,011	120± (2,9)
Mg5Gd	-1,611± 0,01	142,9± (1,1)
Mg2Gd1Mn	-1.750±0,009	85,4± (4,6)
Mg5Gd1Mn	-1.705± 0,003	106,7± (2,7)

Ringer's solution as an electrolyte brings the addition of carbonates into solution. A similar behaviour in Potentiodynamic Polarization curves (PP), in comparison with the Mg2Gd, Mg2Gd1Mn and HP Mg, can be observed in Figure III.23.a). A particularity is that E_{corr} decreases for all systems, but Mg2Gd still presenting the nobler E_{corr} and the reference the lower E_{corr} and the same trend is observed for I_{corr} in Table III.7. The passivation behaviour also changes for HP Mg since the anodic curve seems to suffer a higher variation of potential under a small increase of current density. A more pronounced passivation for Mg2Gd1Mn (in respect with the previous electrolyte) can be observed in Figure III.22.a).

The effect of phosphate buffered saline solution in Potentiodynamic Polarization curves can be noted in the Figure III.22.b), conducted for HP Mg, Mg2Gd and Mg2Gd1Mn. One can observe that passivating behaviour is becoming more defined in those systems. For Mg2Gd1Mn the current density shows passivation at lower values when comparing the previous electrolytes.

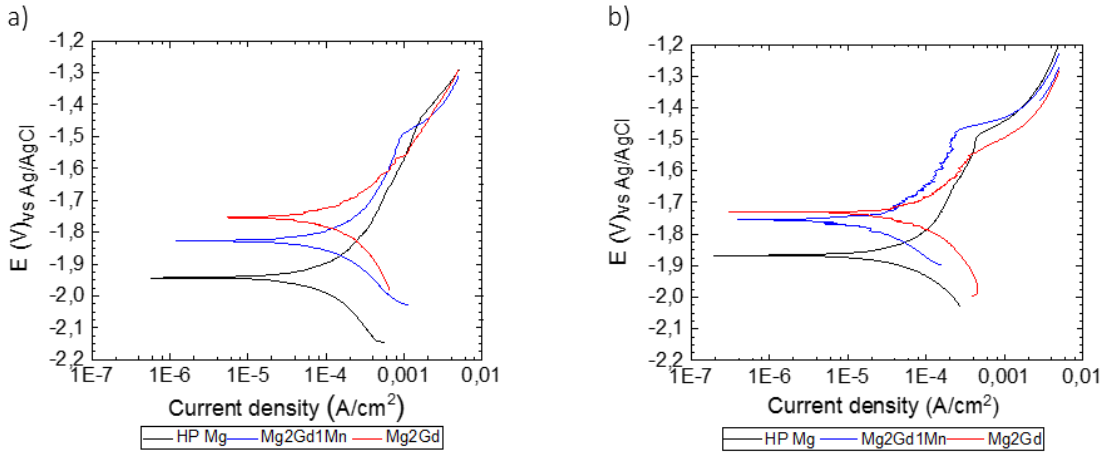

Figure III.22 - Polarization curves of Mg2Gd, Mg2Gd1Mn and HP Mg alloys during one hour of immersion in a) Ringers solution and b) PBS Solution.

The HP Mg and the binary system show a more defined passivation of the anodic curve at higher values of current density when comparing Mg2Gd1Mn.

Table III.7 shows the respective Corrosion Potential (E_{corr}) and Current Density Potential (I_{corr}) estimated by Tafel extrapolation of the polarization curves. The direct relation of I_{corr} with Corrosion Rate access by Faraday's. The direct relation of I_{corr} with Corrosion Rate access by Faraday's Law allows saying that the higher values of I_{corr} should present higher values of Corrosion Rate. In this sense a similar trend it is noted when comparing the previous electrolyte, however, samples exhibit higher corrosion rate, growing in the follow direction, respectively, HPMg, Mg2Gd1Mn, Mg5Gd1Mn, Mg2Gd and Mg5Gd.

Table III.7 - Illustration of the values for the Corrosion Current density (Icorr) and Corrosion Potential, estimated using tafel extrapolation. Those values are in respect to the first hour of immersion in a Ringer's solution.

Alloys	Ecorr (V)	Icorr (uA/cm^2)
HP Mg	-1,911±0,031	82,5± (11,1)
Mg2Gd	-1,749 ±0,015	191,1± (16)
Mg2Gd1Mn	-1,824± 0,002	104,8± (1,7)

One can see in Table III.8 that corrosion current is decreased for all samples in comparison with previous electrolytes, and so, as it is expected, corrosion rate should be lower. The binary system still presents the higher I_{corr} in respect to HP Mg and Mg2Gd1Mn. The improvement in I_{corr} can be related to the formation of stable phosphate compounds in an early stage since passivation is increased.

Table III.8 - Illustration of the values for the Corrosion Current density (Icorr) and Corrosion Potential, estimated using Tafel extrapolation. Those values are in respect to the first hour of immersion in a PBS solution.

Alloys	Ecorr (V)	Icorr (uA/cm^2)
HP Mg	-1,861±0,005	32,7± (4,3)
Mg2Gd	-1,7 ±0,030	101,3± (4,1)
Mg2Gd1Mn	-1,793± 0,041	34,1± (11)

III.2.4 EIS measurements

Corrosion products film, according to their homogeneity and stability can provide resistance to the charge transfer. It is easily understood that the higher is the impedance presented by a surface protective layer, the higher it will be the corrosion resistance of the same alloy.

It is important to mention than the more heterogeneous is the microstructure of alloys the more difficult it is to formulate equivalent circuit's models for the impedance spectrum, due to the complexity of electrochemical process at the metal/solution interface. The fact that different mechanisms of corrosion (like localized and uniform corrosion) can

occur at the same time it is complicated by film formation which increases the difficulty of interpretations of impedance spectra's.

To better understand corrosion behaviour of the alloys and impact of possible corrosion protecting layers on the metal surface the values of modulus of impedance were collected at 0.01 Hz. It is possible at this frequency to compare the differences demonstrated by each Mg alloy system.

Highly Pure Magnesium

Figure III.23.a) shows Bode plots and phase angles of HP Mg immersed in a 0,9 wt% NaCl solution during the first 24 hours at room temperature. Absolute impedance values at low frequencies (0.01 Hz) increase from 1000 to 2200 ($\Omega.cm^2$) in the first 6 hours. A breakdown in modulus of impedance appears during the next 6 hours and at 12 hours this value decreases to 982 $\Omega.cm^2$. At 24 hours of immersion, the value of modulus of impedance is 1307 $\Omega.cm^2$.

Absolute impedance does not stabilize during the first 24 hours of immersion. This may indicate localized corrosion attack and breakdown of passive protection film on the metal surface.

The analysis of Bode and phase angle plots for HP Mg immersed in Ringer's solution, which is represented in Figure III.23.b), shows some changes of spectrums. Contrary to the previous electrochemical system, no breakdown is occurring during the 24 hours of immersion.

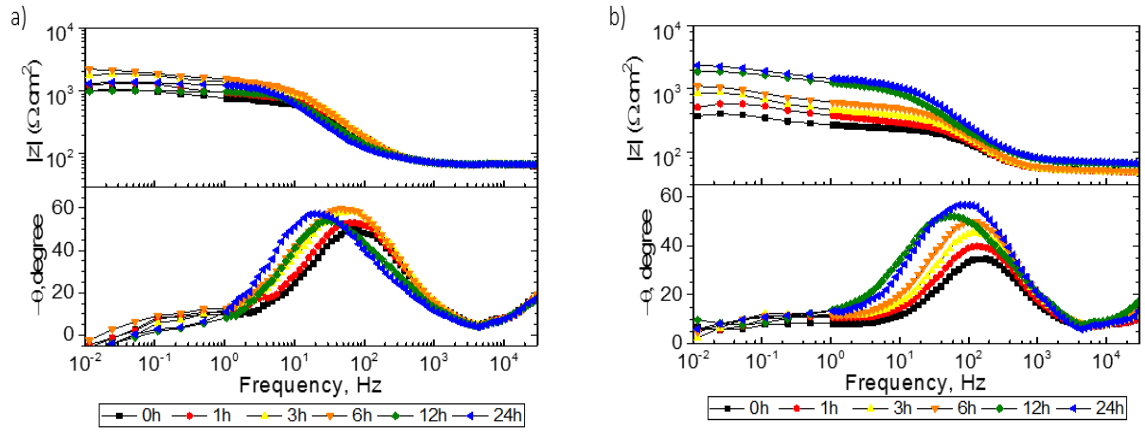

Figure III.23 - a) Bode plot represented in the upper figure and phase angle plot represented in bottom of the figure, for HP Mg in a 0,9 wt% NaCl solution during the first 24 hours of immersion b) Bode and phase angle plots for HP Mg immersed in Ringers solution, during the first 24 hours of immersion.

After 6 hours of immersion impedance value continuously grows from 372 $\Omega.cm^2$ at the time of immersion to 1094 $\Omega.cm^2$. In the next six hours of immersion the value recorded is 1885 $\Omega.cm^2$ and for the 24 hours, a value of modulus of impedance of 2371 $\Omega.cm^2$ is achieved. For what is possible to state by the differences between the previous

electrolytes is that calcium carbonates bring an improvement to the surface layer, may be due to a preferential formation of carbonates on the metal surface which block the ingress of chlorides. It is noted a slight increase in solution resistance comparing with the previous electrolyte.

The addition of phosphates to the solution shows a similar behaviour as the Ringers solution, but the value of modulus of impedance at 24 hours is lower (1631 Ω.cm^2). The starting value of impedance is 546 Ω.cm^2, at six hours of immersion 990 Ω.cm^2 and twelve is 1230 Ω.cm^2. Nevertheless, the solution resistance does not seem to be affected during this first 24 hours of immersion. Those observations can be observed in Figure III.24.

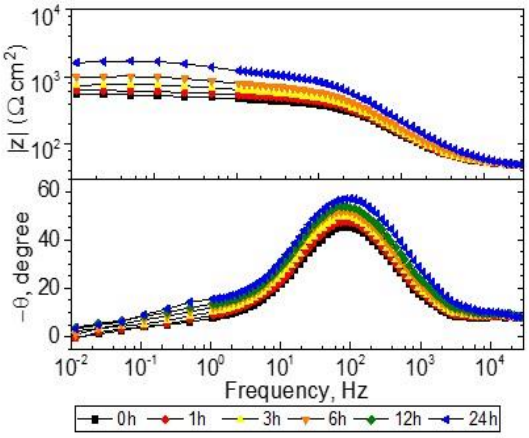

Figure III.24 - Bode plot in upper part of figure and phase angle plot representation in bottom of the figure for the HP Mg alloy immersed in PBS solution during the first 24 hours.

Binary Alloys

The initial value of modulus of impedance for Mg2Gd is 392 Ω.cm^2 and in the first hour a slight increase is noted, to 556 Ω.cm^2. In the next five hours the value of impedance is decreased to 133 Ω.cm^2, at twelve hours is 98 Ω cm^2 and at 24 hours the value of $|Z|$ is 90 Ω.cm^2 (Figure III.25.a)).The measurements were stopped due to the high corrosion activity. It is possible that an initial passive oxide/hydroxide film is quickly damaged thus losing the protective properties.

Mg5Gd alloy shows a similar behaviour but with differences registered in the first hours of immersion. At the time of immersion, the modulus of impedance was measured and the value was 136 Ω.cm^2. At six, twelve and twenty-four hours of immersion the respective values are, 100, 102 and 108 Ω.cm^2. This can be observed in Figure III.25.

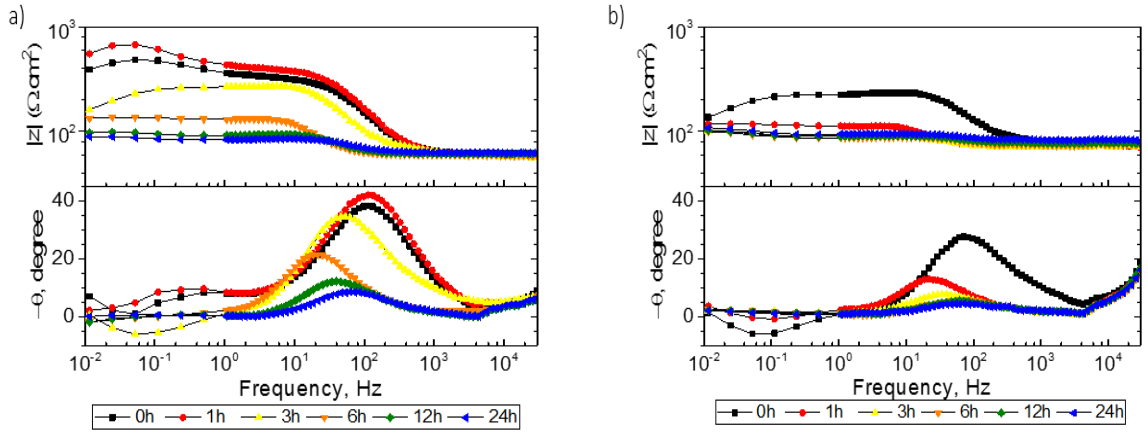

Figure III.25 - Bode and phase plots for a) Mg2Gd alloy and c) Mg5Gd alloy, both immersed in a 0.9 wt% NaCl solution during 24 hours.

Ternary Alloys

The addition of Mn element to alloy structure changes corrosion behavior when compared to binary systems and HP Mg (in a 0.9 wt% NaCl solution). Modulus of impedance at low frequencies is different. The Mg2Gd1Mn alloy Bode and phase angle plots are represented in Figure III.26.a) and the initial value of modulus of impedance is 446 Ω.cm^2. During the first twenty-four hours of immersion, it is possible to observe a continuous growth in value of $|Z|$ reaching 2306 Ω.cm^2, at twenty-four hours. For six and twelve hours the values of impedance are respectively, 1475 Ω.cm^2 and 1910 Ω.cm^2.

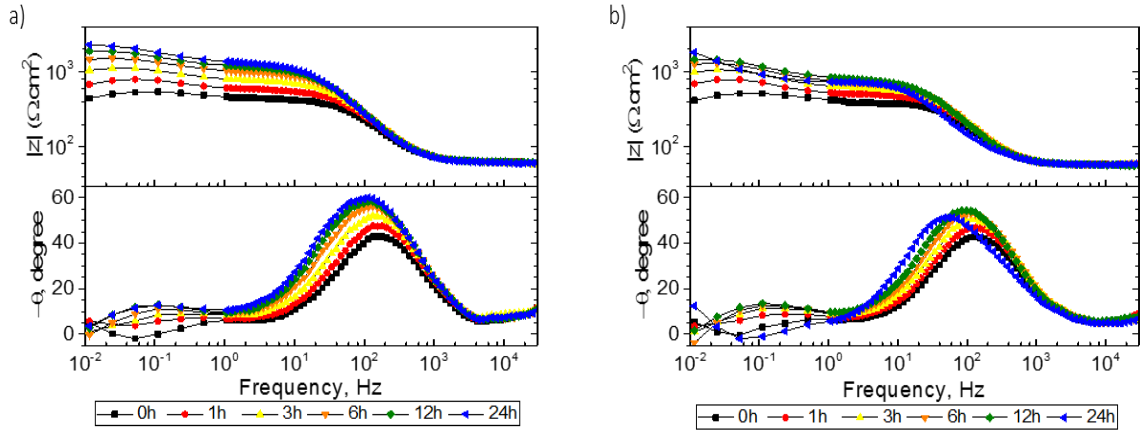

Figure III.26 - Bode and phase angle plots for ternary system immersed in 0,9 wt% NaCl solution during 24 hours. The representation of systems in a) the Mg2Gd1Mn alloy and b) the Mg5Gd1Mn alloy.

Analysing Mg5Gd1Mn system (Figure III.26.b) the initial value of $|Z|$ is 416 Ω.cm^2 and at twenty-four hours is recorded a point value of 1821 Ω.cm^2. During the six and twelve hours measurements the respective values recorded are 1277 and 1480 Ω.cm^2.

It is possible to observe in Figure III.27.a) the measurements of impedance in Mg2Gd1Mn alloy immersed in Ringer's and PBS solution. The initial value for impedance modulus is of 396 Ω cm^2, in Ringer's solution, and at six, twelve and twenty four hours the measured values are respectively, 922, 1248 and 1834 Ω cm^2. Comparing with the 0,9 wt% NaCl solution a slower increase in $|Z|$ seems to occur.

A similar behavior is recorded in PBS electrolyte (Figure III.27). It is measured an initial value of $|Z|$ of about 720 Ω cm^2. For the six, twelve and twenty-four hours the values of modulus of impedance are, respectively, 1120, 1253 and 1336 Ω cm^2. It appears that at this time the evolution of impedance value is lower compared with a 0.9 wt% NaCl solution.

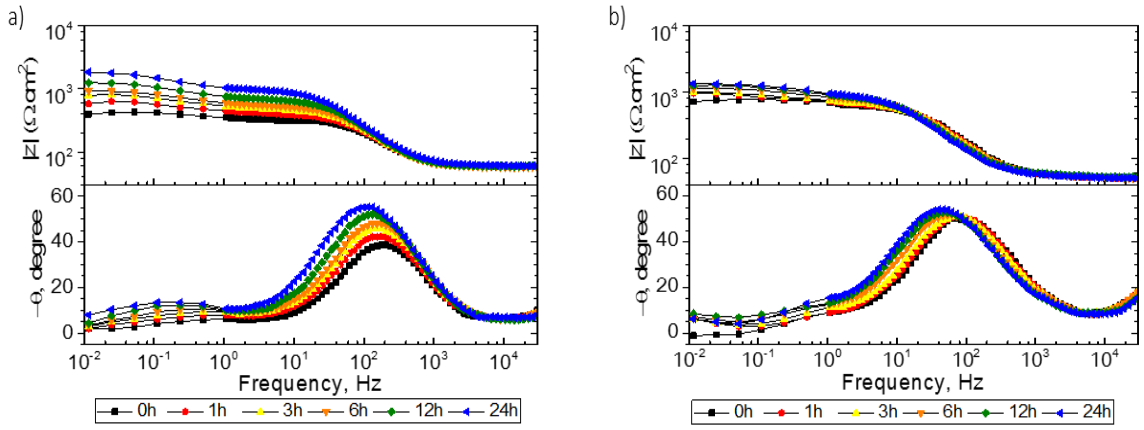

Figure III.27 - Bode and phase angle plots of Mg2Gd1Mn alloy immersed in a) a Ringers solution and b) PBS solution, during the first 24 hours of immersion.

The first 24 hours of Immersion

Ternary system Mg2Gd1Mn shows increasing $|Z|$ values for all electrolytes. However, impedance modulus is higher in NaCl solution for this alloy. The buffering effect of carbonates and phosphates (this last more pronounced) can explain this behaviour since an increased rate of deposition of corrosion products can be achieved in the 0.9 wt% NaCl electrolyte.

If a comparison is made between HP Mg and Mg2Gd1Mn in the 0.9 wt% NaCl solution, Mg2Gd1Mn seems to bring some increase in $|Z|$ values around 12 hours of immersion. When comparing Ringers and PBS electrolyte, the behaviour appears change, and some intermediate compound formation with the alloy elements could explain this fact.

A general conclusion is that a passive oxide/hydroxide layer can offer initial protection to alloys. Breakdown of the passive layer can induce corrosion in the HP Mg, decreasing the impedance value. Moreover, Mg2Gd1Mn at 24 hours seems to present a better protective behaviour when comparing with HP Mg and Mg5Gd1Mn systems. It is

well noted the lack of corrosion resistance offered by the binary system, in part due to the relatively high amount of impurities. Mg2Gd system shows initially passive behaviour and then high corrosion activity. Those observations can be observed in Figure III.28.

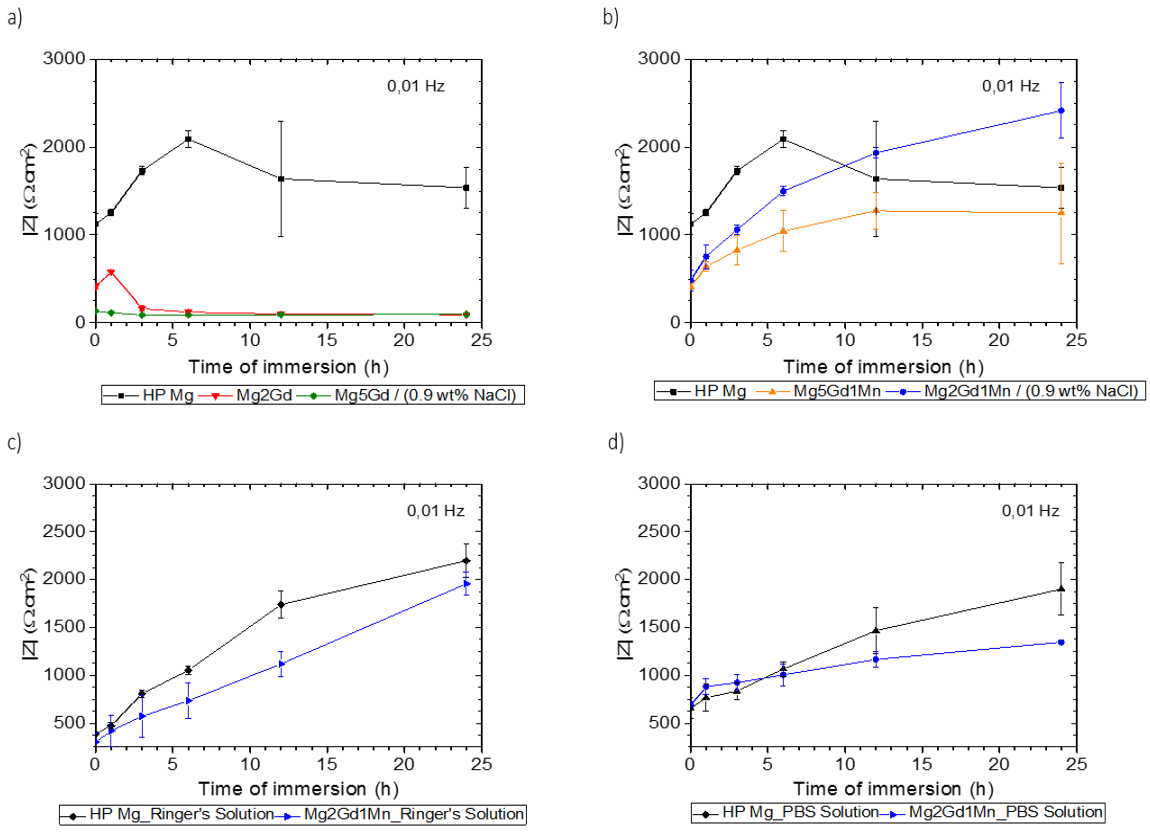

Figure III.28 - Comparison of the impedance modulus values during the first 24 hours of immersion, at 0.01 Hz and the respective reproducibility of experiments between a) Mg5Gd, Mg2Gd and HP Mg in the 0.9 wt% NaCl Solution, b) HP MG, Mg5Gd1Mn and Mg2Gd1Mn in the 0.9 wt% NaCl Solution, c) HP Mg and Mg2Gd1Mn in the Ringer's Solution, d) HP Mg and Mg2Gd1Mn in the PBS Solution.

III.3 Long immersion time characterization

This is long term immersion tests and the exposition to the solution were done during 336 hours, except HP Mg and Mg5Gd1Mn, which were immersed in a 0.9 wt% NaCl, during 216 hours.

III.3.1 EIS measurements

Highly Pure Magnesium

At 24 hours of immersion the value of modulus of impedance is 1308 Ω.cm^2, for the 0.9 wt% NaCl electrolyte. A representation of the Bode and phase angle plots can be observed in Figure III.29.a). Impedance values at the 96 hours increase up to 4189 Ω.cm^2.

During the further time of immersion (192h), it is possible to note a slight increase in values of $|Z|$ till 4660 Ω.cm^2. At 216 hours the modulus of impedance suffer a decrease in value to 3818 Ω.cm^2.

Comparing the effect of Ringers Electrolyte with the 0.9 wt% NaCl electrolyte on HP Mg, the impedance values at twenty four hours starts from higher values of $|Z|$ approximately 2371 Ω.cm^2 (Figure III.29.b)). An increase of this value is noted for the next 24 hours, until reach 3851 Ω.cm^2. At 96h of immersion, a breakdown in the value of modulus of impedance occurs lowering its value to 1582 Ω.cm^2. At 336 hours the $|Z|$ value is 1933 Ω.cm^2.

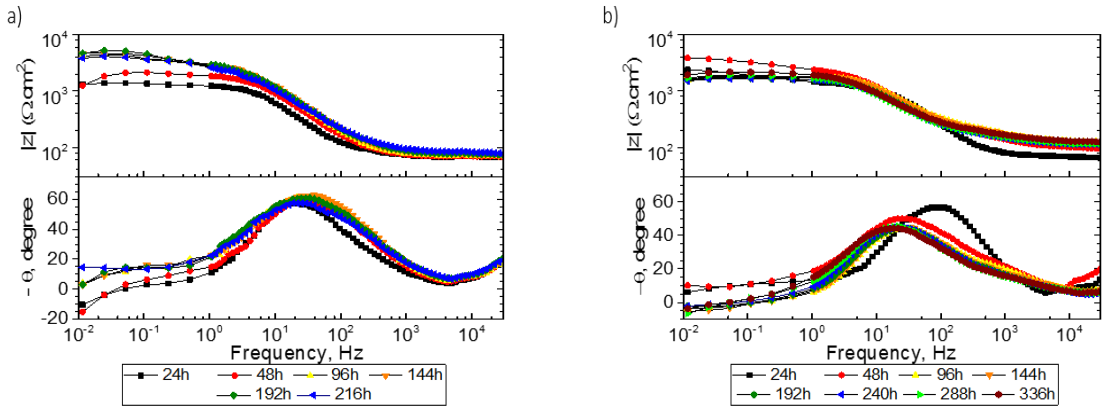

Figure III.29 - Bode and phase angle plots for HP Mg immersed in a) 0.9 wt% NaCl during 216h and b) Ringers solution during 336h.

In Figure III.30 it is observed the Bode and phase angle for HP Mg immersed in PBS. In those measurements, it is important to mention that a quick increase of modulus of impedance value from 1631 Ω.cm^2 to 8202 Ω.cm^2 from the 24 hours to 144 hours is observed. The impedance value continuous to grow until 13994 Ω.cm^2. The continuous growth can be related to the formation of stable phosphorous corrosion products layer.

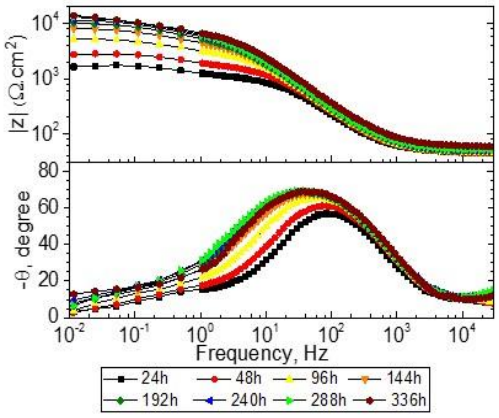

Figure III.30 - Bode and phase angle plots for HP Mg immersed in a PBS solution during 336 hours.

Ternary Alloys

Mg5Gd1Mn sample immersed in a 0.9 wt% NaCl electrolyte, shows the modulus of impedance at 24 hours stopped at 1821 Ω.cm^2 (Figure III.31.a)). In the further measured hours, impedance goes down to 806 Ω.cm^2, 691 Ω.cm^2, 558 Ω.cm^2, respectively for the 48, 144 and 216 h of immersion.

Mg2Gd1Mn alloy immersed in a 0.9 wt% NaCl solution presents at 24 hours a $|Z|$ value of 2306 Ω.cm^2 (Figure III.31.b). During immersion an increase in impedance values to 3529 Ω.cm^2 occurs, at 144h. A continuous growth of impedance can be observed in Figures III.31.b) and at final immersion time (336 hours) the measured point is 4467 Ω.cm^2.

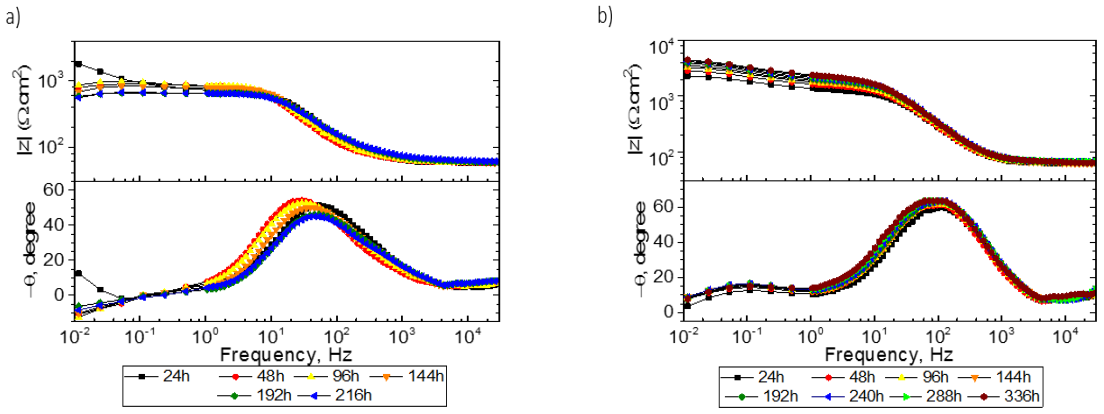

Figure III.31 - Bode and phase angle plots for a 0,9 wt% NaCl solution, a) Mg5Gd1Mn immersed during 216 h and b) Mg2Gd1Mn immersed during 336h.

Bode plots (represented in Figure III.32.a)) for Mg2Gd1Mn immersed in Ringer's solution shows a whole new behaviour. At 24 hours and low frequency values (0.01 Hz), the modulus of impedance was 1834 Ω.cm^2. The value of |Z| at others point measurements, i.e. 96, 240 and 288 hours are 968, 719 and 544 Ω.cm2 respectively. At 336 hours of immersion, the modulus of impedance value is 573 Ω.cm^2.

In PBS the Bode plots can be observed in figure III.32.b). At 24 hours the value of modulus of impedance (at low frequency 0.01 Hz) is 1336 Ω.cm^2. Impedance continuously increases until the 240 hours and $|Z|$ value is 8616 Ω cm^2. At the end of the experiment the $|Z|$ value is 6174 Ω.cm^2.

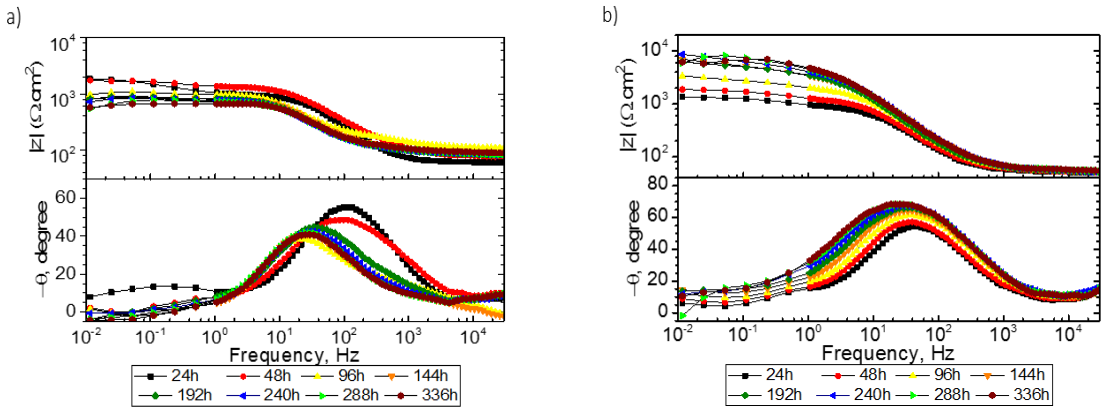

Figure III.32 - Bode and phase angle plots for Mg2Gd1Mn immersed during 336 h in a) Ringers solution and b) PBS.

Long term impedance of Alloys

Ternary system Mg2Gd1Mn shows a small amplitude increase of $|Z|$ values along the immersion time of the 0.9 wt% NaCl solution (Figure III.33) and deviation of mean value seems to be quite narrow. In PBS and until 180 h of immersion the increased amplitude of $|Z|$ is higher (Figure III.33) than the 0.9 wt% NaCl solution, correlating a more protective/resistive layer formation to corrosion. However, some localized breakdown seems to occur (and so deviation of mean value also increase). Despite that phenomena, the values of $|Z|$ continues higher than the 0.9 wt% NaCl solution. This could be addressed to stirring conditions and some intermediate compounds formation, or experimental artefact where OCP is changing during the EIS measurements. In Ringer's solution, the corrosion layer presents a much lower $|Z|$ indicating a more corrosive system.

HP Mg also present low values of $|Z|$ in Ringer's solution, and so lower resistance of the semi-protective corrosion layer. However a difference it is observed in PBS, where after 180 hours the amplitude of $|Z|$ continues to grow and do not present a breakdown of protective film formation (Figure III.33). In the 0.9 wt% NaCl solution the corrosion layer experienced a significant increase of amplitude of $|Z|$ at around 50 hours of immersion. However, a reverse seems to occur after 180 hours of immersion.

Ternary system Mg5Gd1Mn presented a small value of $|Z|$ along all immersion time in the 0.9 wt% NaCl solution. One can be noted that carbonates do not seem to beneficiate the resistance of the formation of corrosion compounds at long immersion time and for Mg2Gd1Mn and HP Mg. Probably stirring conditions could be behind those effects, influencing the pH value and precipitation rates. However, the probable precipitation of phosphates compounds seems to beneficiate the resistance of corrosion layer at long immersion time, for both systems. In Figure III.33 it is possible to observe those particularities.

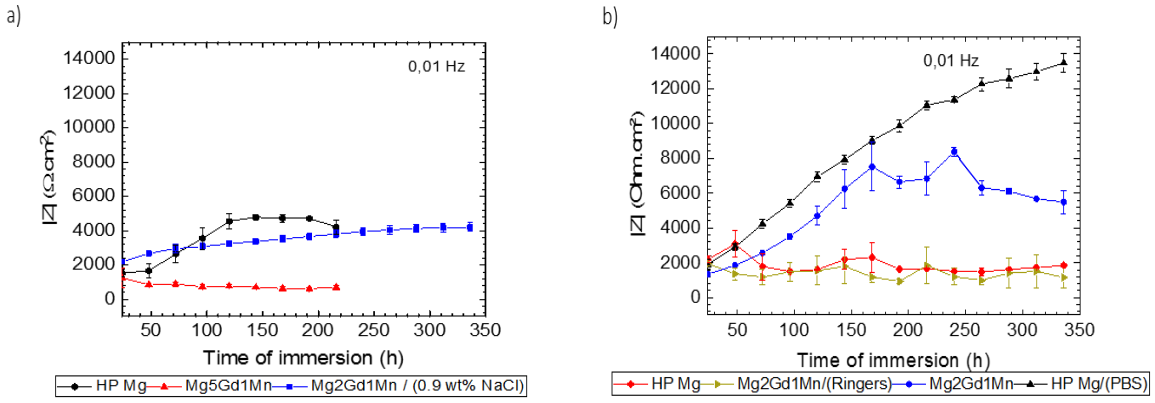

Figure III.33 - Comparison of the impedance modulus values during the follow hours until 336 hours of immersion, at 0.01 Hz and the respective reproducibility of experiments between a) electrochemical systems in a 0.9 wt% NaCl solution, b) Mg2gd1Mn and HP Mg in Ringers and PBS solution.

III.3.2 Hydrogen evolution measurements

The complexity of electrochemical EIS fitting does not allow, in this work, the calculation of Rp and subsequent corrosion rate. In this next section, it will be presented the VHE (Volume of Hydrogen Evolved) in function of time and the consequent Corrosion Rate (CR) plots for each immersion condition. Also, it is referred the rate of hydrogen evolution, which allows a better understanding about the dynamic of the VHE.

Binary Alloys

The extent of hydrogen evolution is a quantitative indicator of the rate of corrosion used to characterize magnesium and its alloys. The observation of Figure III.34 shows that binary systems present a significant corrosion rate, and at approximately eight hours is value for Mg2Gd and Mg5Gd are, respectively, 19.28 mm/y and 103.98 mm/y. At the end of experiments (about 32 hours of immersion), the corrosion rate for Mg2Gd is 77.96 mm/y and for Mg5Gd is 169.67 mm/y. One is noted that binary system Mg2Gd seems to present a relative linear behaviour on this scale, by other hand Mg5Gd after to present a rapid hydrogen release appears to experience a decrease in the same at approximately 7 hours of immersion. This effect can be related to some experimental error due to the high rate of corrosion and the eudiometer capacity. Another explanation could be linked to a high corrosion product deposition and the respective increase of the thickness of corrosion layer, which could bring some protection to the metal surface. However it is well noted that Mg5Gd presents a higher corrosion rate in all measured points, comparatively to Mg2Gd, and as a result, a higher extent of his evolved volume of hydrogen it is observed in Figure III.34.a).

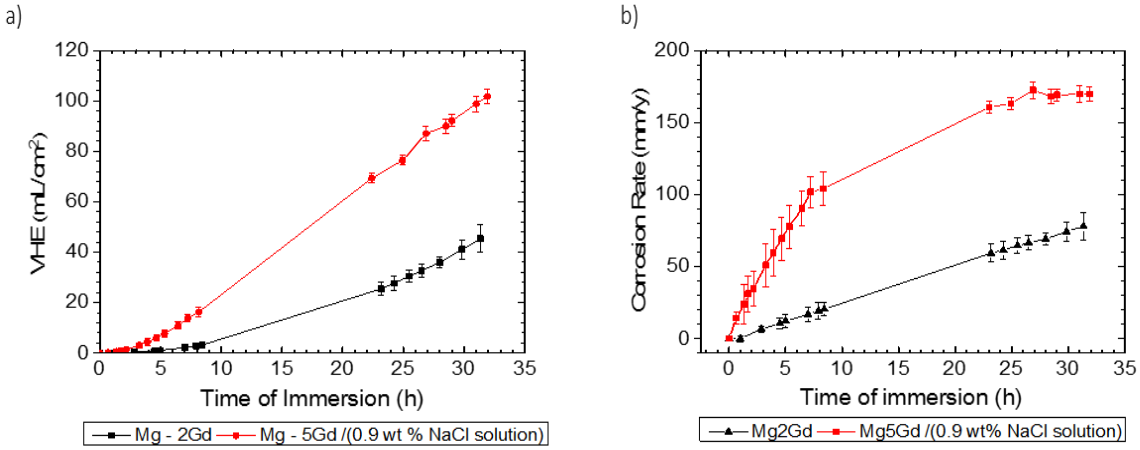

Figure III.34 - Illustration of a) Volume of Hydrogen Evolved for Mg2Gd and Mg5Gd, b) Corrosion Rate over time for Mg2Gd and Mg5Gd. Both alloys were immersed in a 0.9 wt% NaCl solution.

Ternary Alloys and HP Mg

The VHE as a function of time is represented in Figure 35 for HP Mg and ternary system. The time range of immersion of the experiment, which is 360 hours of immersion, was divided into four selected zones, to facilitate the interpretation of results. Zone I and zone IV are representing 30 hours of immersion, one in respect to the first 30 hours and the other to the last 30 hours of immersion, respectively. Zone II and III have the same amplitude in time with which one corresponding to 150 hours of immersion, and obviously, zone II comes first in order than zone III. The slopes of curves for each system and each zone was calculated, and the values are represented in Table III.10. Linear interpolation was done to calculate points in between measurements, if necessary.

One can be seen, when studying the 0.9 wt% NaCl electrolyte that the mean behaviour of HP Mg seems to be the one who presents the higher volume of Hydrogen evolution during the immersion time. The ternary system Mg5gd1Mn follows it and in last comes the Mg2gd1Mn that presents a smoother rate of hydrogen evolution. Analysing Figure III.35.b), the electrolyte was changed to Ringer's solution bringing the sodium carbonate, calcium chloride and potassium chloride into the solution. For this condition, the Hydrogen release rate tells us that Mg2Gd1Mn and HP Mg follows approximately equal in hydrogen release during almost 200 hours of immersion, with a relatively slower rate of hydrogen release for Mg2Gd1Mn. At this time a reverse in behaviour is noted and Mg2gd1Mn goes to higher values of rate of hydrogen than HP Mg, experiencing an acceleration in the Hydrogen release.

Phosphate buffered solution brings the sodium and potassium phosphates into solution. Observing figure III.35.c). The hydrogen evolution rate values are significantly reduced, presenting maximum values of around 1.2 mL/cm2 in the full-time scale, what is slower when comparing 0.9 wt% NaCl solution (around 16 mL/cm2) or Ringers (around 10 mL/cm2). HP Mg and Mg2Gd1Mn present a similar Hydrogen release over time, with a

slight increase for Mg2Gd1Mn. This release seems to be more irregular for the ternary system than HP Mg, due to oscillations during measurements.

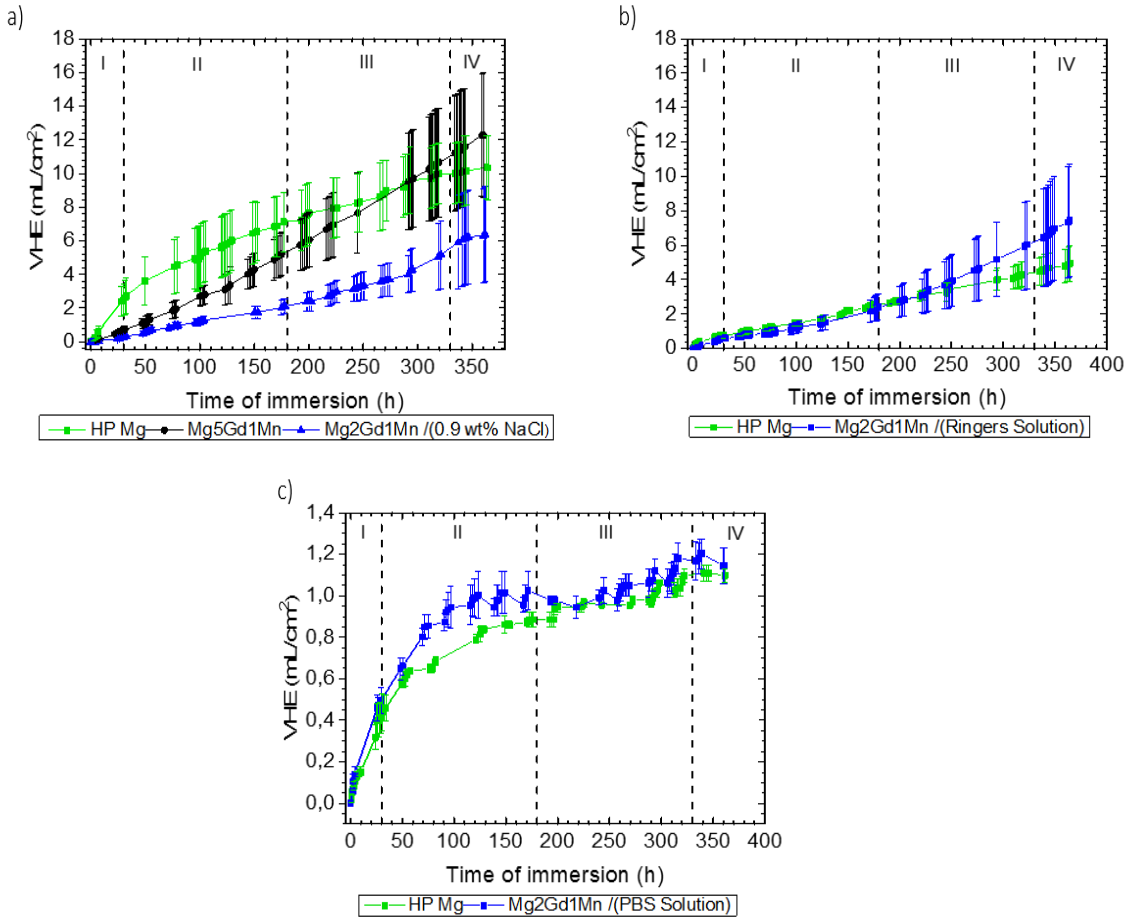

Figure III.35 - Volume of Hydrogen Evolved over time for a) Ternary Alloys and HP Mg immersed in a 0.9 wt% NaCl solution, b) Mg2Gd1Mn and HP Mg immersed in Ringer's Solution and c) Mg2Gd1Mn and HP Mg immersed in PBS Solution. All measurements were conducted during 360 hours of immersion.

As said before, Table III.9 can relate the rate of hydrogen release per hour. For the 0.9 wt% NaCl electrolyte, both ternary alloys present an increase over time of the rate of hydrogen release. This means that probably cathodic activity and hydrogen gas formation is higher in zone IV (and at a long time of immersion) than in zone I (and so short time of immersion). Mg2Gd1Mn presents a lower rate of hydrogen release than Mg5Gd1Mn, and so, in the overall time of immersion, Mg2Gd1Mn releases less hydrogen than Mg5Gd1Mn. The increase rate of volume of Hydrogen evolved at long immersion times can be related to the breakdown of the semi-protective layer, composed of corrosion products.

Observing the behaviour of the rate of hydrogen evolution release for HP Mg in the zone I (for the 0.9 wt% NaCl and Ringers), it is significantly higher than the other two alloys, presenting lower rate than the ternary system in zone III and IV, and so in the long immersion times. This can be due to an improvement of the passive characteristic of protective oxide/hydroxide film. In PBS HP Mg presents a lower rate of hydrogen release

in the zone I when comparing the Mg2gd1Mn. The following zones show a similar trend between both metals.

Table III.9 - Values of rate of Hydrogen evolution release for the three electrolytes in study and for the different systems, catalogued in different zones time dependent. Those values were calculated using the slope of curves.

Electrolyte	Material	(H_2 ml/cm^2 per hour)				Total
		I	II	III	IV	
0,9 wt% NaCl	**HP Mg**	0,104	0,032	0,020	0,015	0,171
	Mg2Gd1Mn	0,009	0,014	0,023	0,025	0,071
	Mg5Gd1Mn	0,024	0,031	0,038	0,041	0,134
Ringers	**HP Mg**	0,021	0,014	0,011	0,012	0,058
	Mg2Gd1Mn	0,019	0,012	0,025	0,035	0,091
PBS	**HP Mg**	0,0143	0,005	0,0012	0,0005	0,021
	Mg2Gd1Mn	0,0166	0,007	0,0011	0,0009	0,0255

Corrosion rate

To interpret corrosion rate it is important to understand that the same was calculated using equation II.12, and it is dependent on the volume of hydrogen evolved (which is transformed in grams), which depends on sample area as sample density and time. It is thus possible to access an instantaneous corrosion rate and observe the dynamic of its behaviour.

Figure III.36.a) shows the HP Mg and ternary systems CR behaviour in 0.9 wt% NaCl solution. HP Mg presents an initial high corrosion rate when comparing with the other systems, and it is largely reduced, for the following zones. Corrosion rate increases for both ternary system, and somehow it stabilizes at lower values than HP Mg changing at slow rates in the different zones. Mg2Gd1Mn seems to experience a brief decrease in corrosion rate, increasing again at the end of zone I. Corrosion rate for HP Mg during the zone III and IV decrease until some stabilization is achieved at the end of immersion.

Figure III.36.b) compares the behaviour of Mg2Gd1Mn and HP Mg in Ringer's solution. It tells that HP Mg present large corrosion rate values in the zone I (which applies to the previous electrolyte too). The same happens in Mg2Gd1Mn but the amplitude is not so high, and it decreases rapidly even while it continues in the zone I, as HP Mg in ringers solution.

After that HP Mg seems to present a similar behaviour when compared to 0.9 wt% NaCl but with lower values in CR. In respect to Mg2Gd1Mn, the corrosion rate appears to be higher than in 0.9 wt% NaCl solution, in all accounted zones.

For PBS solution, the phosphates bring lower corrosion rates at long immersion time (zone II, III and IV). However, in the zone I, it is possible to experience corrosion rate

relatively high for both alloys and in all zones HP Mg presents lower CR values than Mg2Gd1Mn. It is well noted the stability and protection ability that phosphates bring to the corrosion products deposit layer.

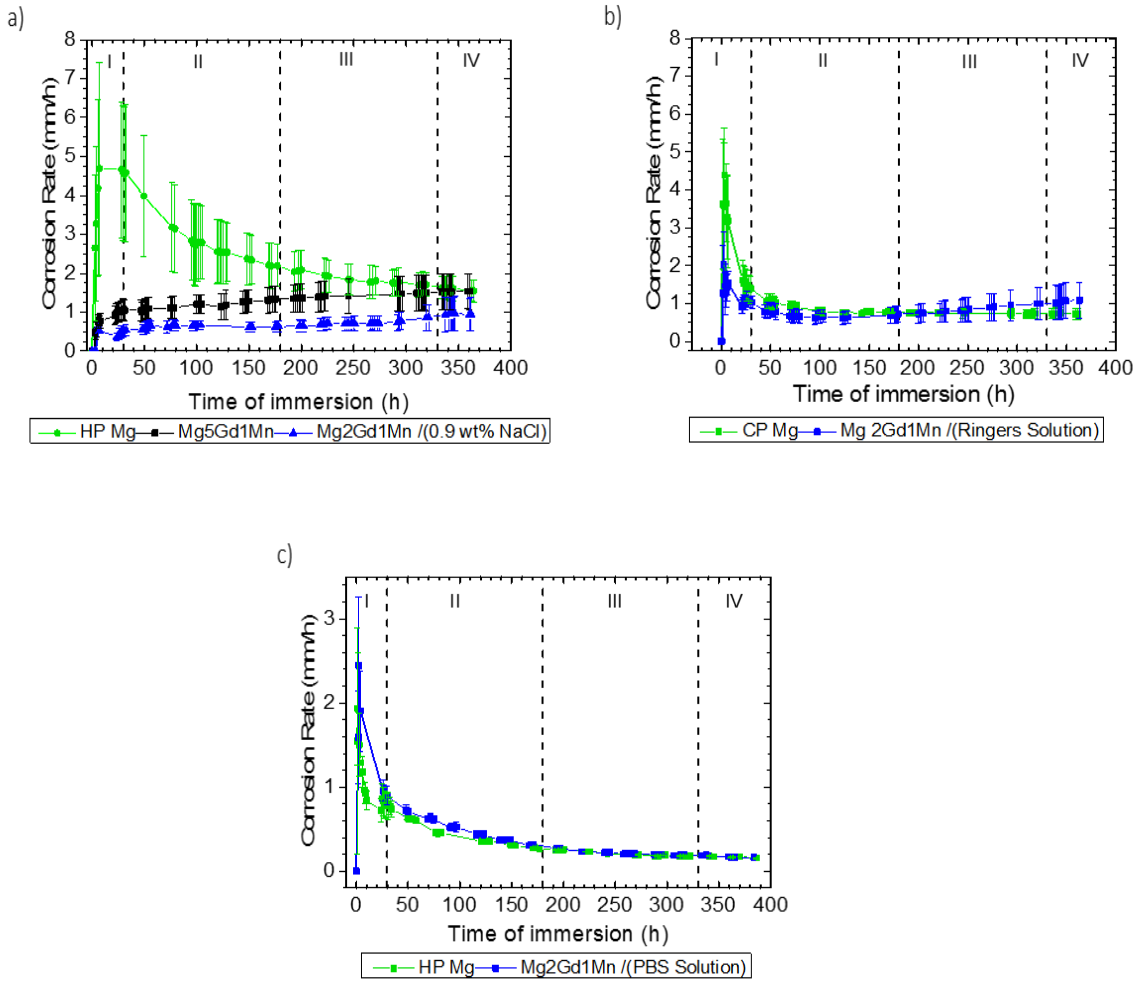

Figure III.36 - Corrosion Rate over time for ternary systems and HP Mg immersed during 360 h in a) a 0,9 wt% NaCl Solution b) Ringer's Solution and c) PBS Solution.

The average of CR separated per zone is presented in Table III.10. The values show that the highly corrosive electrolyte is the 0.9 wt% NaCl solution for HP Mg. By another hand, Ringer's solution do not seem so protective to Mg2Gd1Mn but improves the protectiveness of HP Mg. HP Mg present higher corrosion rates than Mg5Gd1Mn and this one higher CR than Mg2Gd1Mn, in 0.9 wt% NaCl solution. An exception occurs between HP Mg and Mg5Gd1Mn in zone IV were a slight reverse seems to happen. Another particularity is the increase in corrosion rate observed in the ternary system in all zones. It is possible to observe that some systems show a decrease in corrosion rate during all the immersion time. This pattern can be found for HP Mg in all electrolytes and Mg2Gd1Mn in PBS solution.

Table III.10 - Values of the corrosion rate for three electrolytes in study and for the different alloys, catalogued in different dependent zones.

Electrolyte	Material	Accumulative CR (mm/y)			
		I	II	III	IV
0,9 wt% NaCl	**HP Mg**	3,029	2,768	1,841	1,597
	Mg2Gd1Mn	0,33	0,624	0,722	0,982
	Mg5Gd1Mn	0,669	1,185	1,394	1,524
Ringers	**HP Mg**	2,389	0,867	0,745	0,733
	Mg2Gd1Mn	1,094	0,722	0,843	1,058
PBS	**HP Mg**	0,997	0,438	0,207	0,171
	Mg2Gd1Mn	1,204	0,468	0,211	0,180

pH measurements after immersion

The bulk pH for all solutions was recorded at the end of experiments and presented in Table III.11. It is possible to observe the pH values after immersion tests as the ionic conductivity. One can be noted that the high variations in pH between samples in the 0.9 wt% NaCl electrolyte occurs in the binary system with an increased pH comparing with other systems (each was recorded during 31 hours). Instead, ternary and reference samples were measured during 360 hours. The Ionic conductivity of the NaCl solution used in ternary alloys and reference is much higher when compared binary alloys. The long immersion can lead to a higher concentration of ionic species in solution.

Table III.11 - Bulk pH and ionic conductivity of the electrolyte, after HE measurements. Average of samples used.

Electrolyte	Material	pH	σ_i(mS/cm)
0,9 wt% NaCl	HP Mg	9,67±0,101	19,92±0,108
	Mg2Gd1Mn	9,40±0,127	21,45±0,271
	Mg5Gd1Mn	9,56±0,057	24,46±0,102
	Mg2Gd	10,43±0,030	16,43±0,020
	Mg5Gd	10,48±0,035	16,69±0,065
Ringers	HP Mg	9,17±0,114	21,30±0,223
	Mg2Gd1Mn	9,56±0,103	19,98±0,439
PBS	HP Mg	7,57±0,054	19,92±0,127
	Mg2Gd1Mn	7,47±0,008	20,97±0,741

A similar behavior of ionic conductivity is observed in the Ringer and PBS solution. The variation of bulk pH does not change so much when compared Ringers and NaCl solution. But in PBS the bulk pH after the measurements is much lower than in the others two electrolytes. Again, and follow the same pattern as stated in EIS measurements, the addition of phosphates to electrolyte can be behind these buffering effect.

III.4 Corrosion products: Identification and morphology

Corrosion phenomena seriously affected surface of samples used to perform immersion tests. The two main techniques of immersion used to study corrosion interactions was Hydrogen evolution tests and EIS measurements.

On this section it was used a set of techniques in order to identify/study precipitated corrosion products. Optical inspection is often a way to start when the subject is corrosion. It was carried optical inspection in the corroded surface of EIS and HE samples, also to the cross section of samples that present worst resistive behaviour in EIS measurements.

SEM observation of the corroded surface allows to look to the morphology and identify damage on samples. With this technique it is possible to identify porosity, observe crystalline morphology, etc. Using EDS detector it is possible to qualitatively observe the elements present in the surface of the corroded samples.

Preparation of cross section of corroded samples allows to observe how corrosion affected the metal surface, and the metal/corroded layer interface can give good indications about mechanisms of corrosion. By other hand GDOES allows to qualitatively identify the presence of the main elements and their variation with the increasing depth of corrosion layer. Those analysis were done in EIS samples.

III.4.1 Optical observations of EIS and HE samples

EIS Samples

Figure III.37 allows the observation the corroded surface of samples immersed in the 0.9 wt% NaCl solution (the respective immersion times are identified in the caption of the Figures). The Figure a) and b), presents high deposition of corrosion products, and the corroded surface appears to be similar between both alloys. Observing Figure III.25 and III.28.a) it is possible to see that those samples (Mg2gd and Mg5Gd, respectively) presents the lower |Z| and at 24 hours the value of |Z| is around 100 $\Omega.cm^2$. Those corrosion products deposited on the metal surface seem to be volumetric with low porosity and low density. The corroded surface of Mg5Gd1Mn appears to be quite damage, which can explain the low modulus of |Z|, after 216 hours of immersion in comparison with Mg2Gd1Mn and HP Mg. At the same time, Mg2Gd1Mn and HP Mg seems to presence a quite uniform and stable corroded layer.

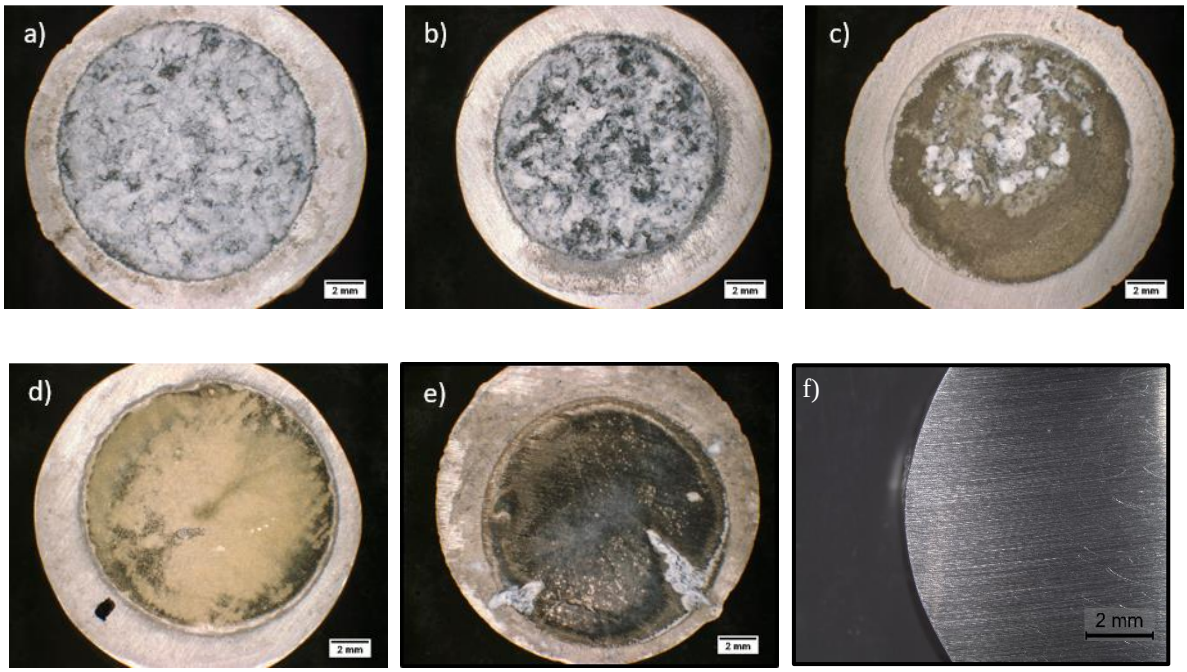

Figure III.37 - Corroded surface of EIS samples immersed in a 0.9 wt% NaCl solution, a) Mg2Gd and 24 hours of immersion, b) Mg5gd and 24 hours of immersion, c) Mg5Gd1Mn and 216 hours of immersion, d) Mg2Gd1Mn and 336 hours of immersion and e) HP Mg and 216 hours of immersion. Figure f) shows a non-corroded surface of a magnesium alloy

EIS measurements were performed in the HP Mg and Mg2Gd1Mn, since both presence adequate resistive behaviour in the 0.9 wt% NaCl solution. Figure III.38 shows the corroded surface after immersion in Ringer's Solution. The surface of samples appears relatively degraded, with a non-uniform deposition of white salts in the corroded surface. Figure III.32 a), III.33.b) and III.29.b) allows to observe that those samples present a relatively low modulus of impedance |Z| in comparison with the previous electrolyte.

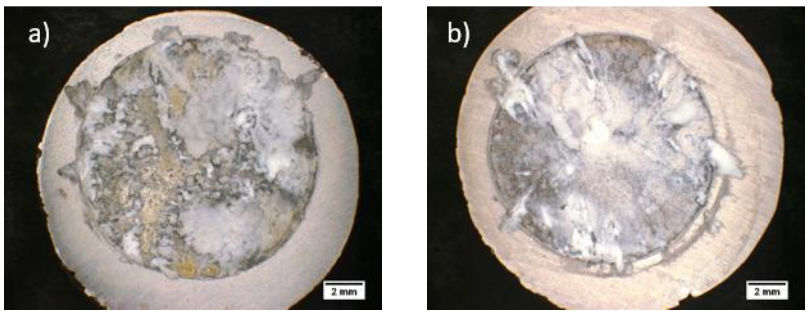

Figure III.38 - Corroded surface of immersed samples in Ringers solution after perform EIS measurements: surface of a) Mg2Gd1Mn and b) CP Mg. Both immersed during 336 hours.

The relatively high degradation of the corroded surface could be behind of this phenomena. Figure III.37.f) shows a non-corroded surface of a magnesium alloy. The corroded surface of PBS Solution samples seems to be quite uniform, as also the surface of

the 0.9 wt% NaCl solution. PBS brings higher values of |Z| at long immersion times. However, Mg2Gd1Mn experienced some breakdown of the corroded layer, which can be observed in Figure III.33.b) and III.34.b). At this point, it is important to refer that the mechanisms of degradation tightly depends on the electrolyte composition and perhaps on the stirring conditions. Film formation will be studied in detail in the next chapters.

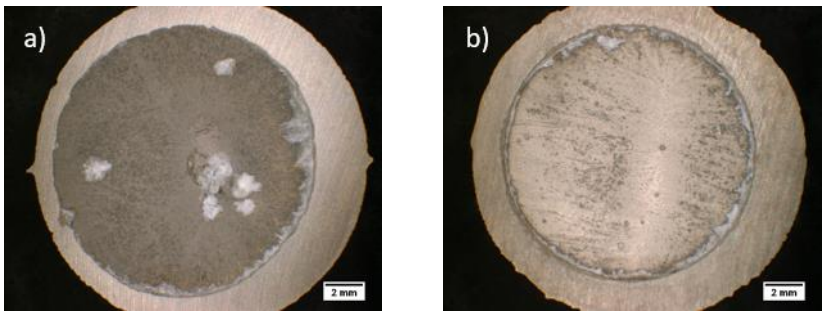

Figure III.39 - Corroded surface after immersion in PBS solution for EIS samples, a) Mg2Gd1Mn and b) CP Mg. Both immersed during 336 hours.

Cross section samples of EIS measurements

Further, cross-sectional studies were performed in the Mg2gd1Mn and HP Mg immersed in 0.9 wt% NaCl solution and PBS solution, for EIS measurements. To better understand how the worst performed EIS samples look like, the corroded interface was recorded by Optical Microscopy. It is possible at this scale to observe different characteristic of each sample. Per example binary alloys observed in Figure III.40.a) and b) and after 24 hours of immersion, presents a highly degradation metal surface, probably due to the presence of metal impurities, which activates micro galvanic coupling between the different microconstituents.

By other hand Figure III.40.e) shows the metal interface of Mg5Gd1Mn. It is possible to observe large pits formations (hole type structures), indicating localized corrosion. Those pits could be characterized as hemispheric pits (see section 1.4.3). It is known that Mn reduces the effect of impurities as Fe when added into the microstructure. However, some intermetallic was found in the microstructure of Mg5Gd1Mn which present Iron content, however in lower amounts than in binary system. The one place tracked could be not significant, but after look at the metal interface, it is probably the cause of this effect.

The observation of Figure III.40.c) and d) allows to identify some pit formation of Mg2Gd1Mn and HP Mg in Ringer's Solution. Those pits seem to present a characteristic morphology presented by occluded pits (Section I.4.3). Those features are probably due to localized chloride attack, which leads to localized breakdown of semi-protective corrosion

layer, leading to localize corrosion. It is justifiable that all those samples present relatively small values of |Z| at long immersion time.

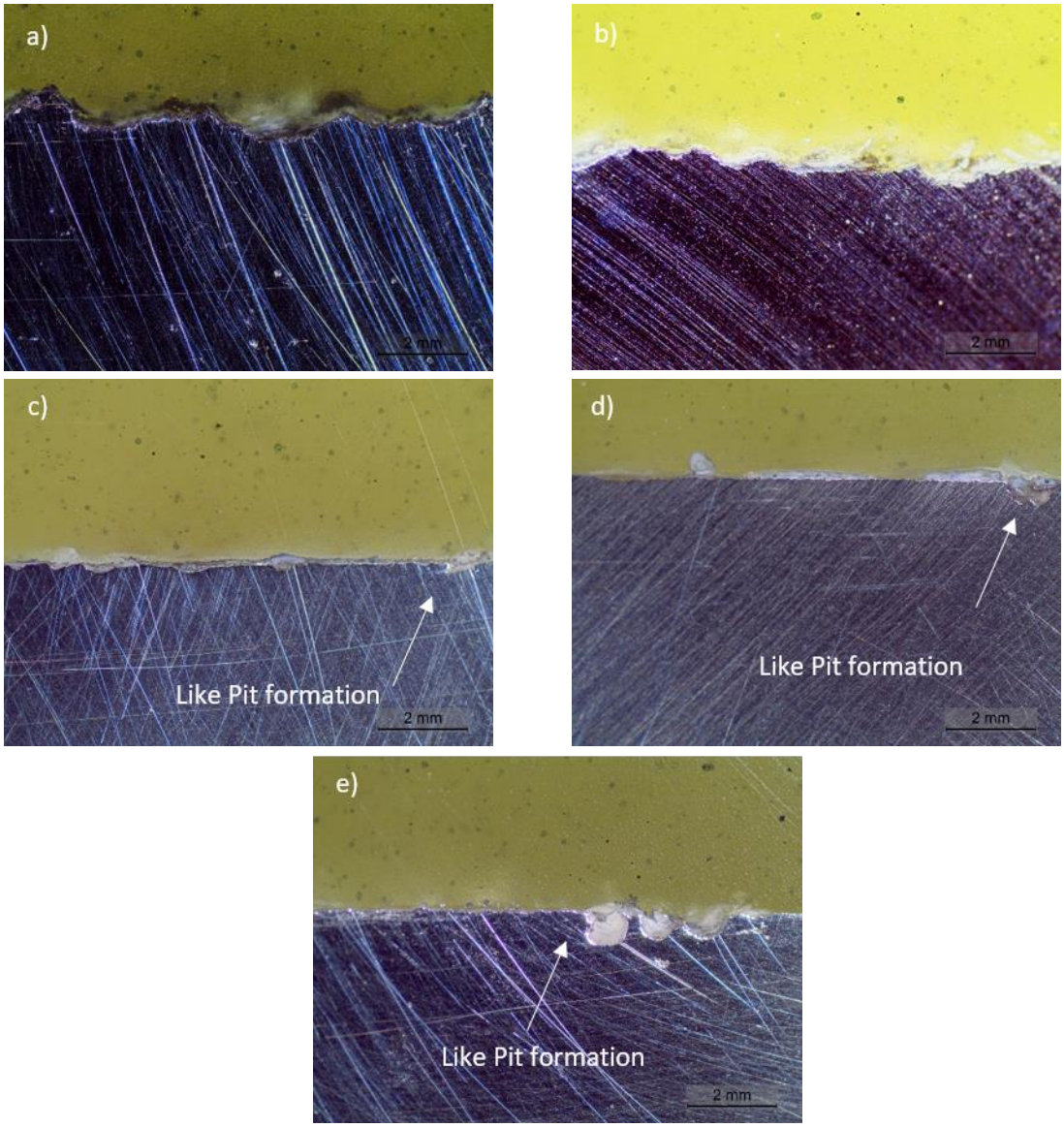

Figure III.40 - Cross section of the EIS samples which presented relatively low |Z| values, a) Mg5Gd and b) Mg2Gd, immersed during 24 hours in the 0.9 wt% NaCl Solution. c) Mg2Gd1Mn and b) HP Mg, immersed in Ringer's Solution during 336 hours. e) Mg5Gd1Mn immersed in the 0.9 wt% NaCl Solution during 216 hours.

Hydrogen Evolution Samples

The corroded surface of samples used in hydrogen evolution tests was observed under macroscopic observations, and samples are illustrated in the following Figures. It is possible to see that a highly corroded surface characterizes binary systems after 33 hours of immersion. A relatively similar corrosion layer for EIS samples is deposited around the surface of binary alloys (HE samples for binary alloys represented in Figure III.41 a) and

b)). Those samples experienced a relatively high corrosion rate. The Mg5Gd1Mn present some breakdown of corrosion layer (maybe due to localized attack) (as observed in EIS sample Figure III.37.c)), which can be seen in the Figure III.41.c). Degradation of corrosion surface of Mg5Gd1Mn seems to undergo at long immersion times since Mg5Gd1Mn showed accelerated corrosion rate at those times of immersion. By another hand, HP Mg suffers relatively high corrosion rates at short immersion time and so the degradation of the surface can occur at the initial stage of corrosion. After that HP Mg experienced a slowing down in the corrosion rate (observe Figure 36). The Mg2Gd1Mn presents a relatively uniform corrosion layer, due to the small values of corrosion rate shown in all the time of immersion.

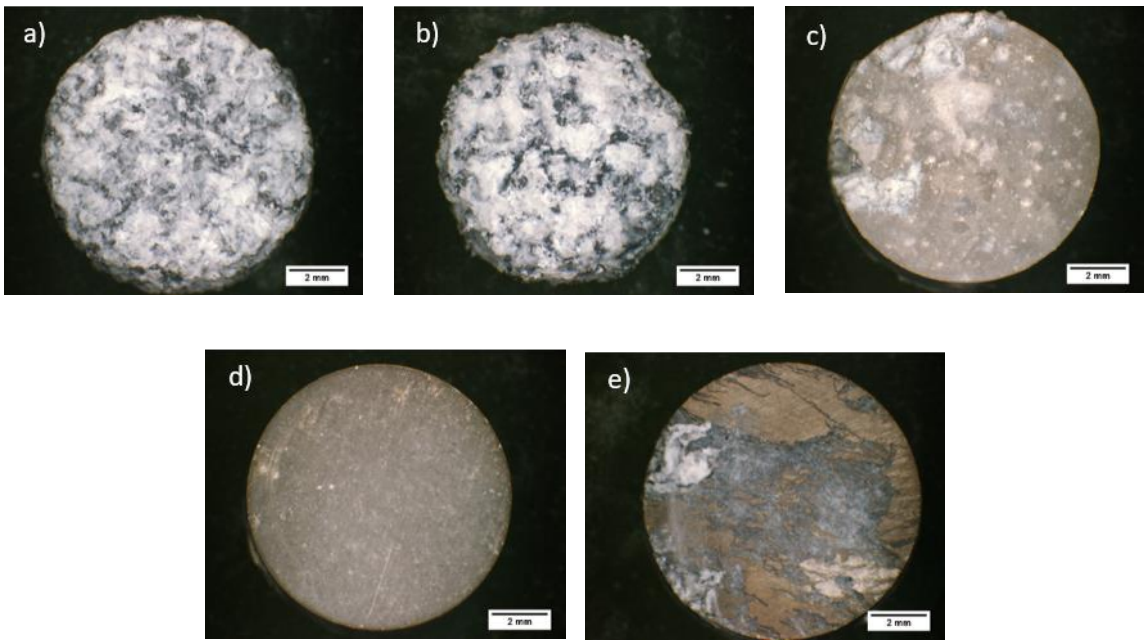

Figure III.41 - Corroded surface of HE samples in the 0.9 wt% NaCl solution, a) Mg2Gd and 33 h of immersion, b) Mg5Gd and 33 hours of immersion, c) Mg5Gd1Mn and 360 hours of immersion, d) Mg2gd1Mn and 360 hours of immersion and HP Mg and 360 hours of immersion

Figure III.42 shows the corroded surface of Mg2Gd1Mn and HP Mg immersed in the Ringer's Solution. It seems to present a quite uniform corrosion layer, due to the low corrosion rates experienced by both alloys at long immersion time (observe figure III.36).

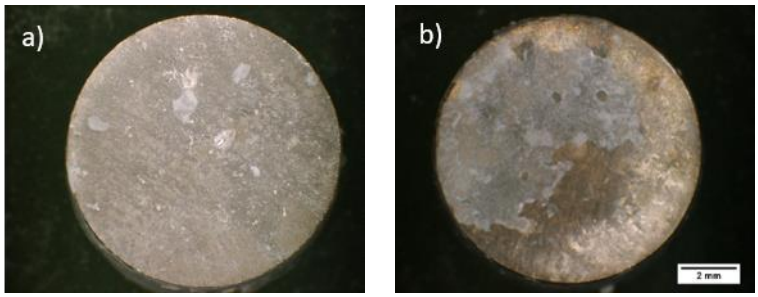

Figure III.42 - Corroded surface of HE samples immersed in Ringer's Solution, a) Mg2gd1Mn immersed during 360 hours, b) HP Mg immersed during 360 hours.

In Figure III.43 it is possible to observe the corroded surface of Mg2Gd1Mn and HP Mg immersed in PBS Solution. The Figure III.36, shows lower corrosion rates for those samples, and in fact this electrolyte seems to be the one who achieves more protective behaviour to corrosion. Observing the Figure below the corrosion layer seems to be quite uniform for both samples.

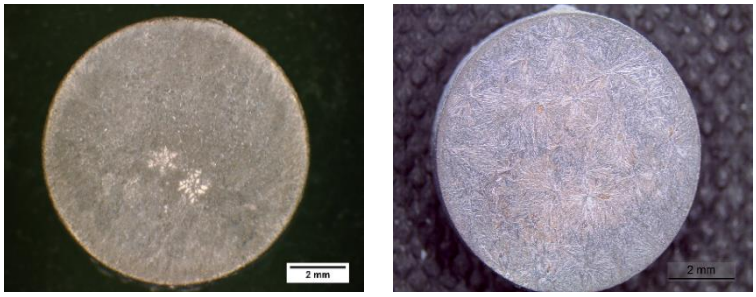

Figure III.43 - Corroded surface of HE samples immersed in PBS Solution, a) Mg2gd1Mn immersed during 360 hours, b) HP Mg immersed during 360 hours.

III.4.2 SEM observations of the morphology of corrosion products

The corrosion phenomena seriously affect the surface of samples used to perform immersion tests. Morphology of samples performed in EIS measurements was studied to get information about the corroded surface.

In this section, it was used a SEM to observe the corroded surface and to identify the main morphological features. The use of EDS allows the identification of the presence of elements in the film formation, qualitatively.

Substrate interferences between the electronic beam used by EDS, and atoms in the surrounded areas of a spot/area analysis, can affect the intensity of signal peaks. The characteristic carbon peaks have a Kα energy of 0.277 keV and due to the deposition of a carbon layer on the top of samples to reduce charge effect in SEM observation, those peaks are not analysed in the further EDS spectrums, but it is possible to observe the presence of those peaks.

III.4.2.1 Morphology of the corroded surface in HP Mg

The reference system (a pure magnesium metal) was used in this study to compare the electrochemical behaviour with other systems. Highly Pure Mg was put in contact with three electrolytes employed in this study, a 0.9 wt% NaCl solution, Ringer's and PBS solution. It is possible to note, looking into the electrochemical results that mechanisms of corrosion are changing when modified the immersion solutions and so differences in corroded morphology of the surface of samples are expected.

HP Mg immersed in 0.9 wt% NaCl solution

A mud-crack pattern is revealed by SE picture in Figure III.44 a) and b). Formation of cracks can be related to the drying process after immersion, were sudden dehydration of surface could induce tension on the structure and surface shrinkage (release of hydroxyl groups (OH^-), possibly causing tension forces in the surface). The mud crack pattern seems to be relatively flat and homogeneous but at higher magnification (Figure III.44.b)), it is possible to see different sizes in mud patterns plateaus and cracks. It is also possible to distinguish white round spherical particles (represented by spot #2 on Figure III.44.b)) and an exfoliation pattern on the surface of mud plateaus.

Observing the EDS selected-area (Figure III.44.c)) it is possible to verify that spot #2 present a higher intensity peak of oxygen, with respect to spot #1. This can indicate that the white particle is probably a $Mg(OH)_2$ particle deposited in the top of the corrosion layer. It was detected small peaks of Si and Cl in corrosion matrix (spot #1) which can indicate the presence of trace amount of those elements. The relatively high presence of O and Mg can reveal the possible presence of Brucite as the main corrosion product deposited on the surface. However, the matrix (spot #1) presents a weak signal of O, which can indicate a relatively thin corrosion layer deposited on the top of the metal surface.

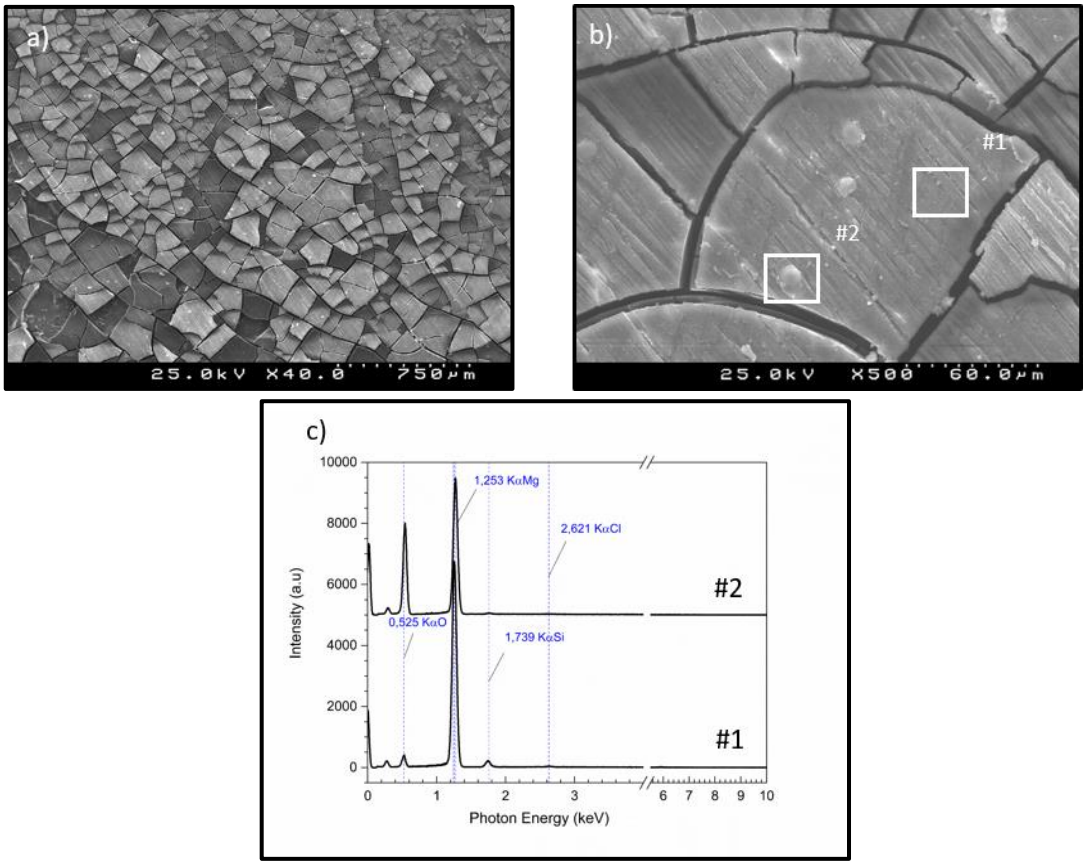

Figure III.44 - SE pictures from corroded surface of HP Mg immersed in a 0.9 wt% NaCl solution and the respective selected EDS areas: a) mud-crack pattern on HP Mg surface, b) Higher magnification of figure III.25.a) and c) EDS spectrum from spots #1 and #2 represented in figure III.25.b).

A higher magnification picture of the matrix shows a nano/micro needle-like structure formed during corrosion, which can be observed in Figure III.45. Those needle particle seems to be relatively homogeneous in size and seems to present nano/micro porosity. They seem to be conventional structures observed in $Mg(OH)_2$ [21].

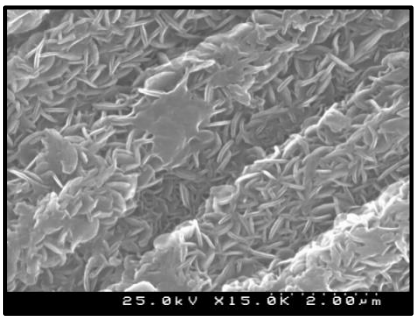

Figure III.45 - High magnification SE picture from corroded matrix of a HP Mg immersed in 0,9wt% NaCl solution.

HP Mg immersed in Ringers solution

The corroded surface of HP Mg, when exposed in Ringer's solution, shows precipitation of flower-like crystals. Those crystals present a relatively homogeneous distribution on the top of the corrosion surface layer at low magnification, depicted in Figure III.46.a). A higher magnification of surface, observed in Figure III.46.b), shows different micro sizes of the flower-like crystals and different arrangement in the position of those crystals. It is possible that the crystal growth occurs vertically and/or horizontally, or maybe they fall when precipitated due to stirring conditions, or another factor can be involved. Spot A, B and C in Figure III.46.b) shows the difference in length size of horizontally deposited crystals appearing in the microstructure with respective sizes of 138, 70 and 41 um. The different sizes of crystals can give the indication of a gradient in ionic concentration occurring near the interface of metal/solution. In Figure III.46.b) it is possible to observe micro cracks and pits appearing in corrosion matrix. The matrix doesn't seem to present crack formation in Figures III.46.c).

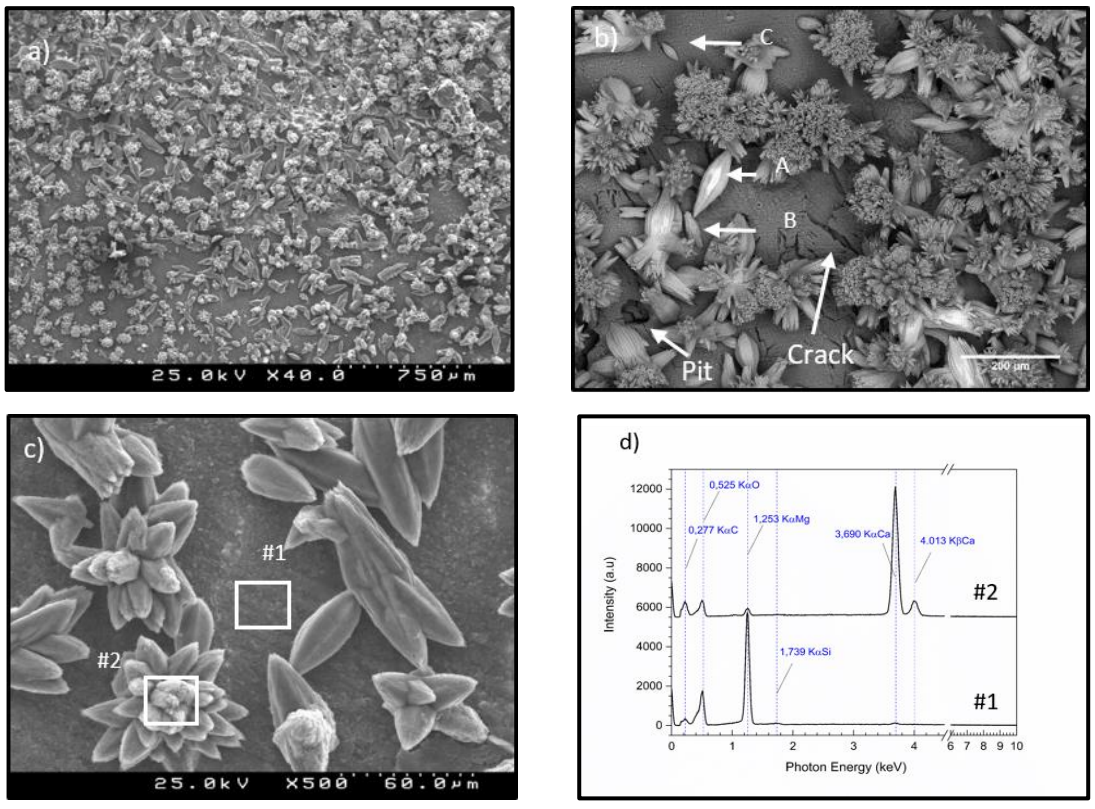

Figure III.46 - SE pictures from corroded surface of a HP Mg in Ringers solution and the respective EDS spectrum: a) overview of the corroded surface with precipitated particles b) Higher magnification of figure III.46.a) and c) EDS spectrum.

EDS selected area represented by #2 in Figure II.46.c), shows in EDS spectrum (Figure III.46.d)) a higher concentration of Ca and a slight increase in C peak when comparing with EDS spectrum #1, and a relatively small concentration of Mg element. By

another hand the matrix seems to present low amount of Ca and an increase presence of Mg and O, which can indicate the presence of Brucite. Those crystals are probably $CaCO_3$ since they exhibit a similar morphology which the ones presented in reference [125].

A higher magnification picture of the corroded matrix (observed in figure III.47) shows a disorganized arrangement between what it seems to be needle/platelet crystals. Stirring conditions maybe can induce some disorientation growth, causing porosity.

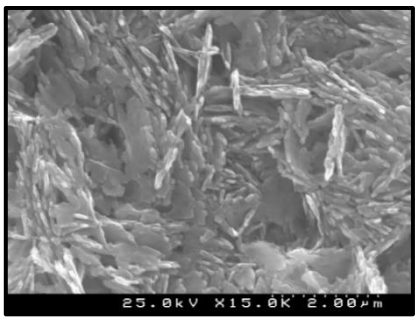

Figure III.47 - High magnification SE picture from corroded matrix of a HP Mg immersed in Ringer's solution.

EDS mapping of surface observed in Figure III.48 clearly shows the distribution of elements previously detected in EDS analysis (Figure III.46.d)).

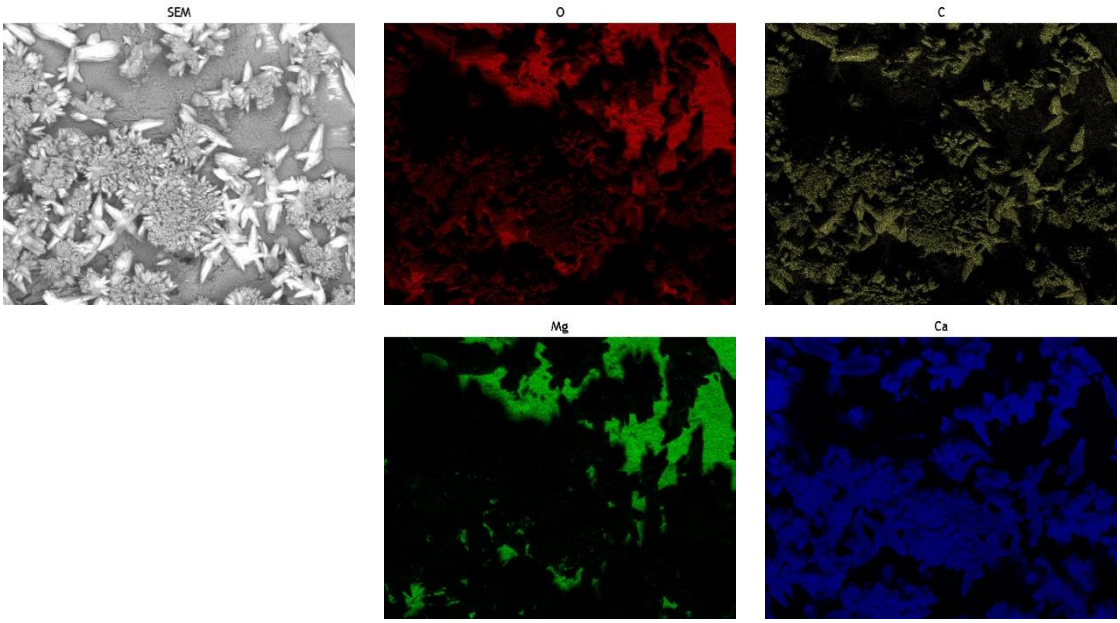

Figure III.48 - EDS mapping showing elemental distribution in corroded surface of a HP Mg immersed in Ringers solution during 316 h, a) SEM picture, b) O element, c) C element, d) Mg element and e) Ca element.

Some disturbance of mapping resolution can appear due to the relieve effect presented by the corroded surface. Nevertheless, it is possible to observe that matrix is

accompanied by Mg and O distribution where Ca seems not to exist neither C. Contrary, the crystals deposited in the top of the corroded matrix appears to be rich in Ca and C elements with a small presence of O and non-Mg element distribution.

HP Mg immersed in PBS solution

Figure III.49 illustrate the SEM morphology of an HP Mg immersed in PBS solution during 336 hours and the respective EDS analysis.

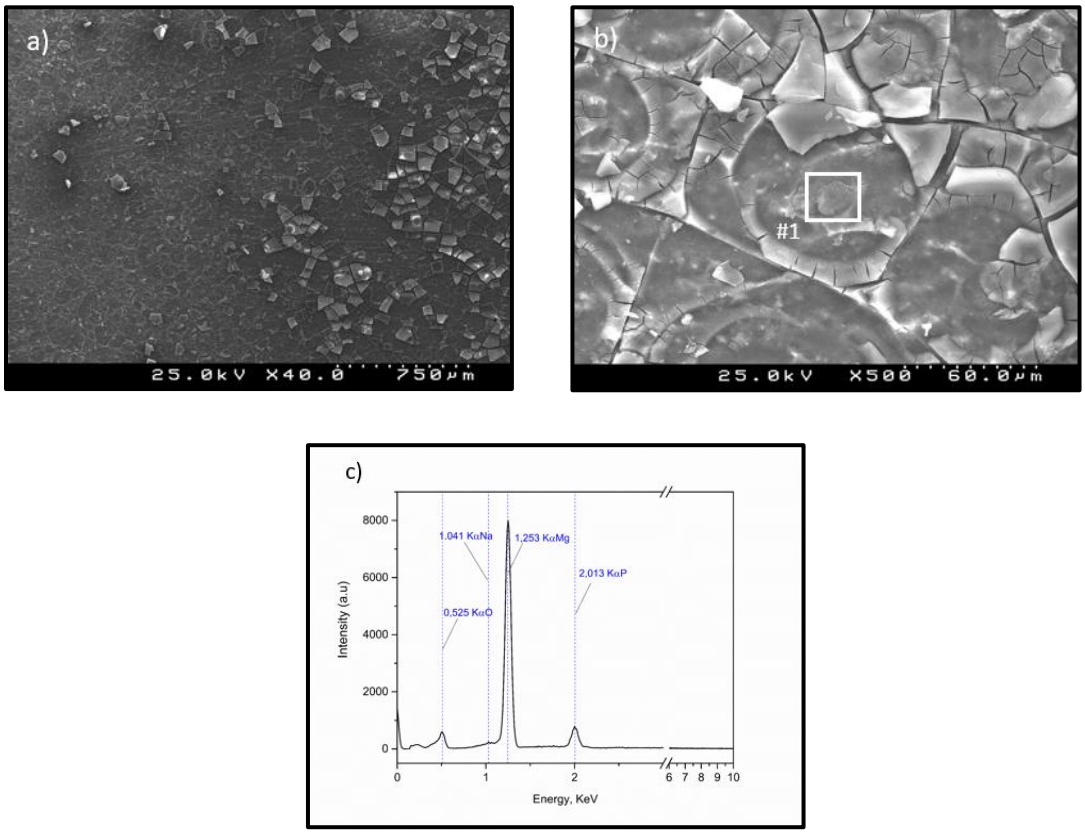

Figure III.49 - SE pictures from corroded surface of a HP Mg in PBS solution and the respective EDS spectrum: a) overview of the corroded surface layer b) Higher magnification corrosion layer c) EDS spectrum from spot #1 depicted in figure III.30.b).

An overview of a typical HP Mg corroded surface in Figure III.49.a) shows a relative intact homogeneous surface layer. If decreased the view field, a higher magnification of Figure III.49.a) is observed in Figure III.49.b), and, what it seems to be, the appearance of superficial micro cracks. A less pronounced mud-crack pattern can be observed, when comparing the corroded surface of HP Mg in NaCl Solution. The patterns like mud can indicate that superficial and interstitial water molecules are adsorbed or connected to minerals, and when dried the surface, OH^- molecules are released. Comparing the mud pattern with the HP Mg pattern immersed in NaCl, this one seems to be more compact indicating probably less interstitial water molecules adsorbed (or the

hydrogen bonds are stronger) since fracture or crack appearance seems to be more superficial.

Selective-area EDS analysis performed in #1 can be observed in Figure III.49.c). The matrix shows a high amount of Mg accompanied by P and O elements. A relative weak Na peak it is observed.

A high magnification in Figure III.50 of the corroded layer shows a relatively dense matrix with. This micrograph is with respect to the corroded metal surface of HP Mg in PBS solution, after 336 hours of immersion.

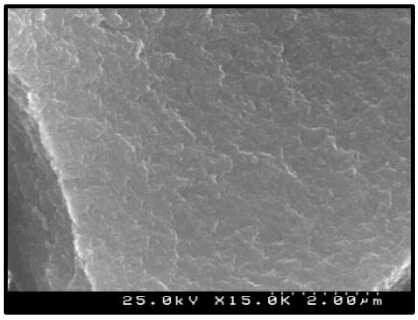

Figure III.50 - High magnification SE picture from corroded matrix of a HP Mg immersed in PBS solution.

III.4.2.2 Morphology of the corroded surface in binary system

The binary system presents what it seems to be a volumetric deposition of corrosion products on the metal surface when exposing to 0.9 wt% NaCl after 24 hours of immersion. Optical microscopy inspection of the corroded surface of binary alloys tells that a similarly corroded layer is precipitated during the 24 hours of immersion. Due to this reason, the followed characterization will be done only to the corroded surface of Mg2Gd alloy.

Mg2Gd immersed in 0.9 wt% NaCl Solution

Figure III.51 highlights corrosion products on the surface of Mg2Gd alloy. As said before similarities in the corroded surface are observed for both Mg5Gd and Mg2Gd alloys. Corrosion layer presents loose particle Islands deposited on a compact corrosion layer. Zone 1 in picture III.51.a) highlight the magnification image present in figure III.51.b). A hole like structure can be observed, and the formation of those holes are likely due to hydrogen liberation during the cathodic reaction. Loose particles seem to be more concentrated near cracks and/or like pits structures, which can be a strong clue that those pits/cracks are releasing H_2 and could increase local pH and so the preferential deposition of $Mg(OH)_2$. A magnification picture shows a needle-like structure deposited in the matrix and loose particles (figure III.51.c)).

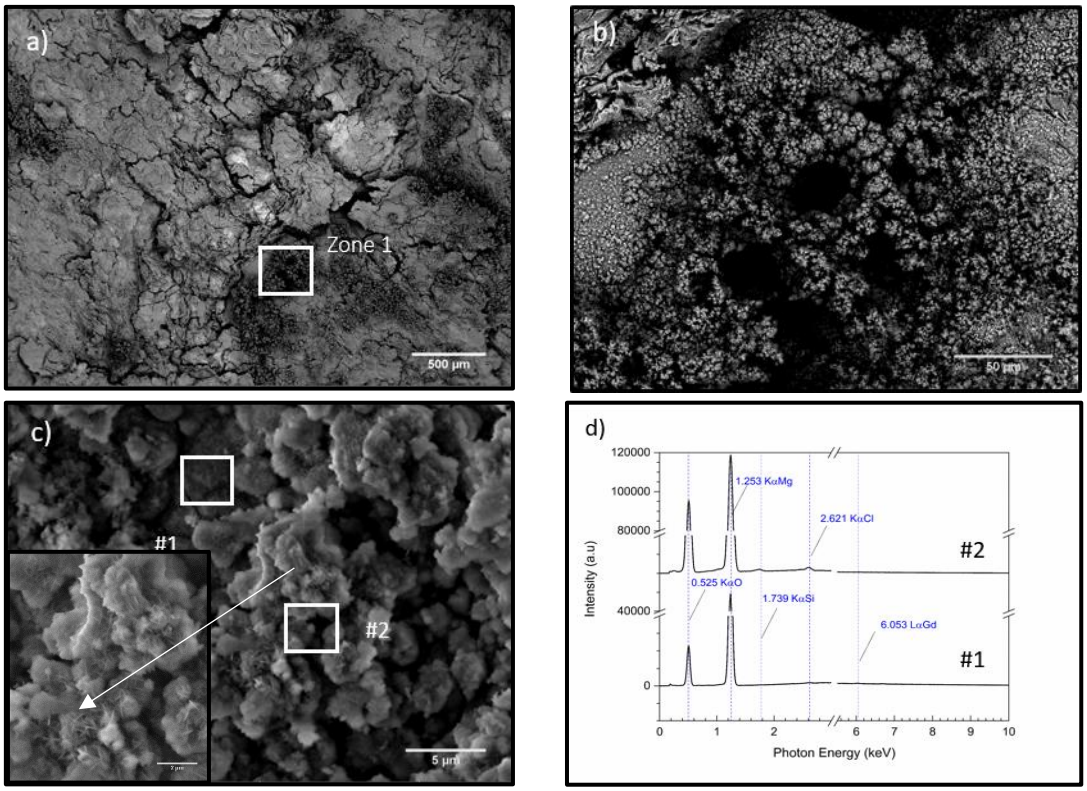

Figure III.51 - SE pictures from corrosion of CP Mg in Ringers solution and EDS spectrum: a) corroded surface with precipitated particles b) Higher magnification of zone I and c) EDS spectrum from zone 1 on figure.

The EDS selected areas represented by #2 and #1 shows sharp peaks of O and Mg, which can corroborate the presence of $Mg(OH)_2$. A small peak of chloride appears in the spectrum with respect to corrosion matrix.

III.4.2.3 Morphology of the corroded surface in Mg2Gd1Mn

Optical microscopy shows a significant corrosion activity in the surface of Mg5Gd1Mn. Since further studies were conducted in Mg2gd1Mn, it will be presented the morphology of corrosion products for this system in the 0.9 wt% NaCl Solution, Ringer's and PBS Solution.

Mg2Gd1Mn immersed in the 0.9 wt% NaCl Solution

A similar morphology of corroded surface between the HP Mg and this system is observed. In Figure III.52.a) a general corrosion layer is observed. The increase in magnification illustrated by Figure III.52.b) shows a crack like mud pattern, with less pronounced (more narrow and less deep) cracks than the initial system stated (HP Mg immersed in the same electrolyte). A similar white round particle is observed, as a like string pattern marked in the mud corrosion layer.

Selected-area EDS #1 and #2 represents the white spherical particle and corroded matrix, respectively. EDS analysis observed in Figure III.52.c) identify as main elements in #2 the O and Mg. By other hand spot #1 shows peak signals of Mn and Gd. Low-intensity signals of Si and Cl can indicate a trace presence of those atoms in corrosion products (corrosion layer). The white particle is probably a $Mg(OH)_2$ particle.

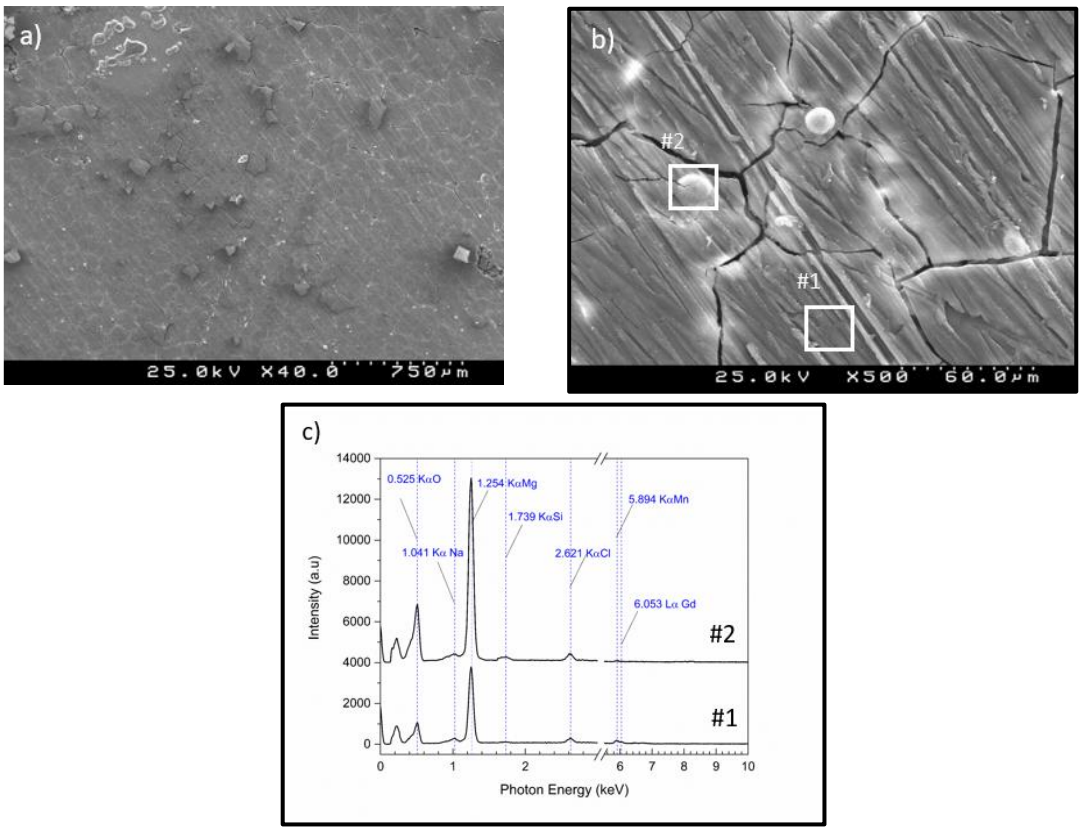

Figure III.52 - SE pictures from corroded surface of Mg2Gd1Mn alloy in a 0.9 wt% NaCl solution and the respective EDS spectrum: a) magnification showing a general corrosion layer b) Higher magnification of figure III.53.a) and c) EDS spectrum of spots#1 (matrix), #2 (white particle).

If highlighted a magnification zone of the corroded matrix, a needle structure similar to the one observed in figure III.45 (HP Mg in NaCl) can be noted, but structure seems to be denser and the needle-like structure more connected, reducing open porosity.

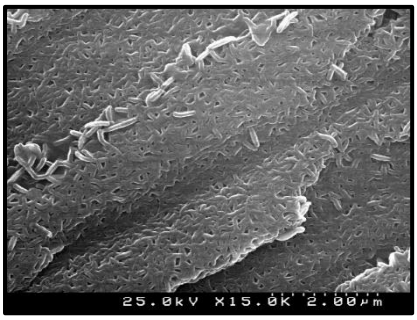

Figure III.53 - A high magnification picture from matrix of Mg2Gd1Mn immersed in NaCl solution.

Mg2Gd1Mn immersed in Ringer's solution

Figure III.54 illustrates the SEM morphologies and the following EDS analysis of Mg2Gd1Mn samples, immersed for 336 hours in a Ringer's solution. A non-uniform corroded layer it appears in Figure III.54.a).

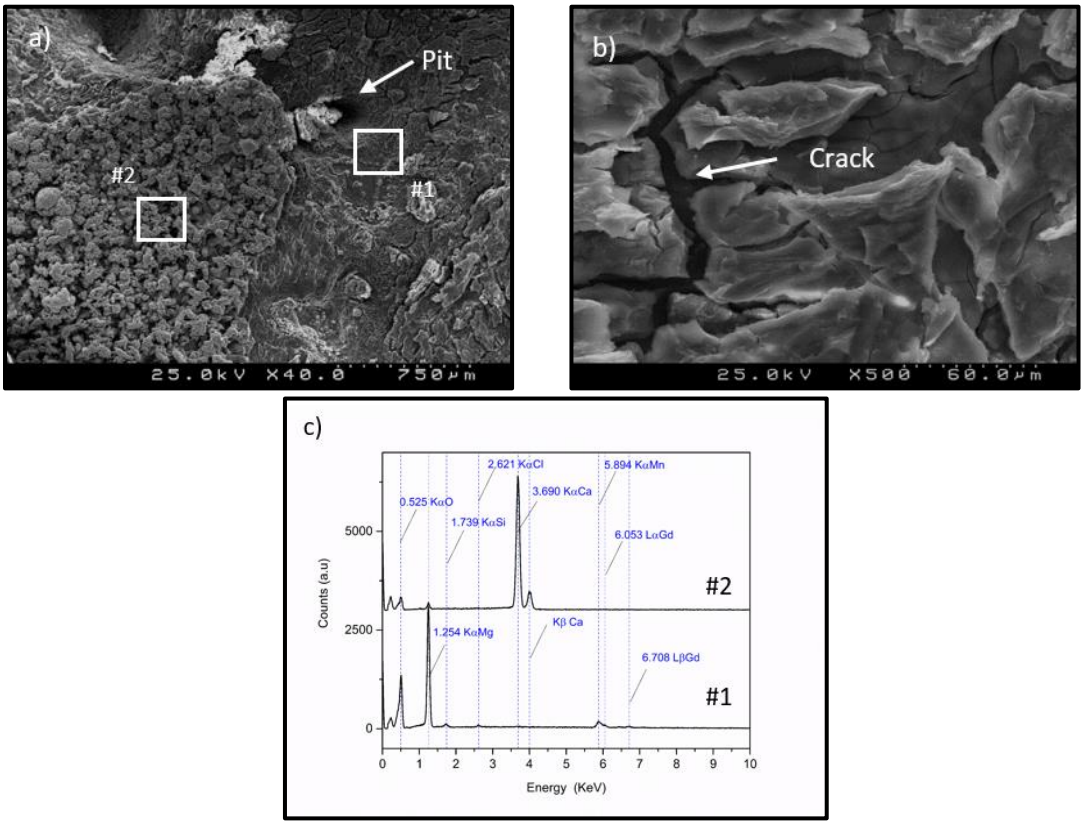

Figure III.54 - SE pictures from corrosion layer of Mg2Gd1Mn in Ringers solution and EDS spectrum: a) typical corroded surface b) Higher magnification of figure III.55.a) and c) EDS spectrum from zone #1 and #2 depicted in figure III.55.a).

In this figure, it is possible to distinguish a compact matrix with some fissures and curling lines maybe because of the existence of a compressed surface. A non-homogeneous

deposition in the overhead of corroded layer surface can be observed. A higher magnification of the matrix in Figure III.54.b), shows the appearance of microcracks with different sizes and with a heterogeneous distribution. A pit-like structure seems to be identified in Figure III.54.a).

Selected-areas EDS are represented by #1 and #2 in Figure III.54.a). Matrix represented by #1 in EDS spectrum (Figure III.54.c)) seems to show a high presence of O and Mg, the presence of Mn and Gd elements and trace signal of Si and Cl, which can be tracked in EDS spectrum (Figure III.54.c)). Low energy levels in spectrum #2 show a slight increase of C peak (not represented in EDS spectrum but is referred to the first peak at low energies) and a reduction in O peak. Mg still appearing and a rapid increase of the peaks intensity of Ca seems to corroborate that Ca crystals are deposited on the top of the corroded surface, as happened with HP Mg in Ringer's solution.

In Figure III.55.a) it is possible to observe a flower-like crystal deposited on top of the corroded matrix. These crystals are mainly based on Ca compounds, appearing bigger in size (larger) than the previous Ca crystals identified in HP Mg immersed in Ringer Solution. By other hand Figure III.55.b) shows a high magnification of matrix. The microstructure seems to present a platelet-like crystals, with a disorganized arrangement and open porosity in between them.

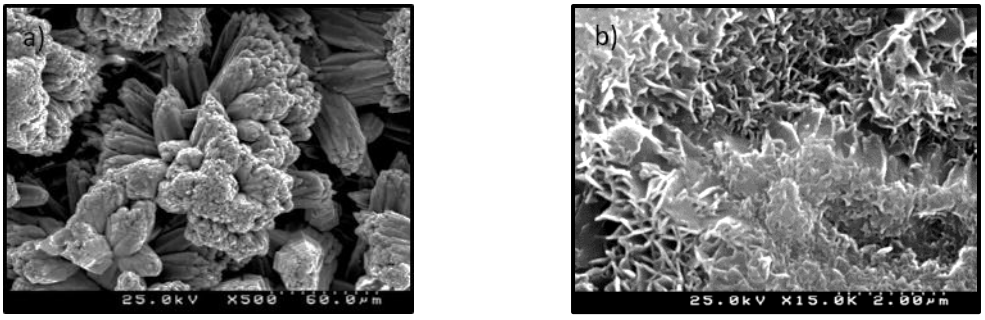

Figure III.55 - SE pictures from corrosion layer of Mg2Gd1Mn in Ringers solution and EDS spectrum: a) flower like crystal structure b) Higher magnification of corroded matrix.

Mg2Gd1Mn immersed in PBS solution

The SE pictures presented in Figure III.56.a) shows a typically corroded surface of Mg2Gd1Mn in PBS solution. One can be noted a mud-cracked like pattern displaying a string type lines marked in mud plateaus. The micro size of cracks (observe Figure 56.b)) appears to be larger relatively to others previous crack size observed, and the surface of mud-crack pattern shows roughness. The respective EDS (Figure III.56.d)) of zone #1 depicted in Figure III.56.b) is presenting high intense peaks of Mg, O and P elements and relatively high intense peaks of Mn and Gd, which are lower in the previous Mg2Gd1Mn systems studies. A higher concentration of those elements in corrosion products can

underline this feature or the formation of a thinner corrosion layer. It is also observed a trace amount of Na element.

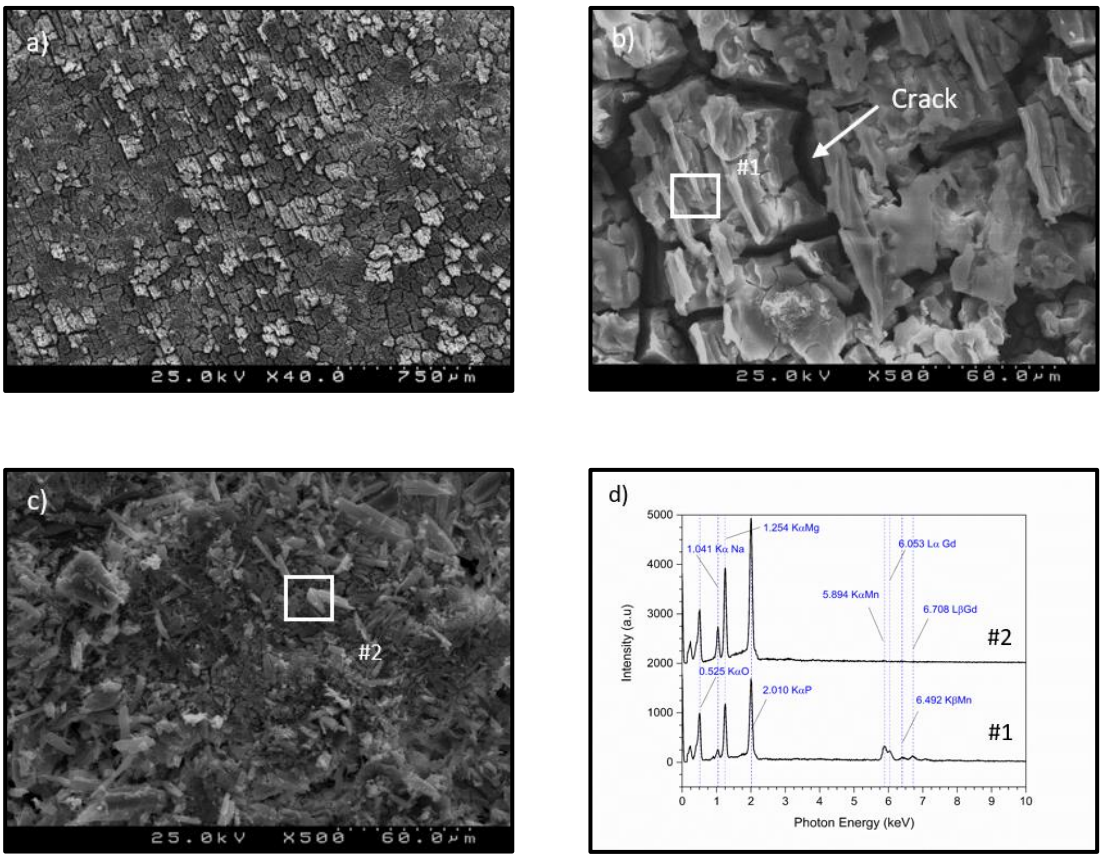

Figure III.56 - SE pictures from corrosion of Mg 2Gd1Mn in PBS solution and EDS spectrum: a) corroded surface with precipitated particles b) Higher magnification of the corrosion layer, c) higher magnification of the corrosion layer with deposition of top crystals and d) EDS spectrum from zone #1 and #2 represented in Figure.56.

Figure III.56.c) depicted a surface deposition of crystals in the corrosion layer. The EDS spectrum shows that spot #2 do not identify Gd and Mn, and present an increase of the Na peak. Those crystals can be richer in Na and with less or none amount of Mn and Gd in their structure.

At higher magnification, the corrosion matrix observed in figure III.57 shows a relative compact formation. Some open voids can be observed and their distribution is non-homogeneous.

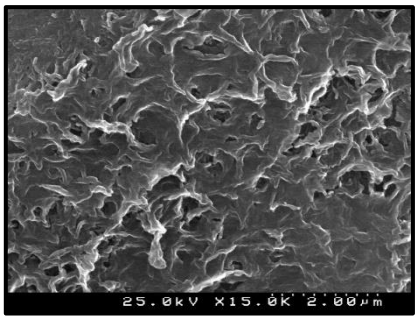

Figure III.57 - High magnification of corroded matrix of Mg2Gd1Mn in PBS solution.

III.4.3 Cross section characterization

SEM observation of cross section allows the visualization of the corroded interface. The EDS maps were very useful to visualize the elemental distribution along corrosion layer, interface, and substrate. At the same time, qualitative measurements using GD-OES allows to observe the variation of the elements intensity with respect to the sputtering time and results in information about the elemental variation with depth. All analysis represented in this subchapter are in respect to EIS samples.

HP Mg immersed in a 0.9 wt% NaCl solution

The HP Mg analysis in a 0.9 % NaCl solution immersed during 216 hours are shown in Figure III.58 a) and b). It is represented in Figure III.58.a) an illustration of the cross-section, where it is possible to identify a relatively thin corrosion products layer, in between the mounting resin and the magnesium substrate. It is observed in this figure that corrosion is preferentially entrenching into the metal substrate (pits formation), leaving behind a deteriorated surface. The thickness of this layer was measured in two places, spot #1 and #2, which are represented in Figure III.60.a). The respective values are 7.2 and 10.2 um, where the last value is slightly significant since it was measured inside at what it seems to be a pit structure. Regarding the SE picture of Figure III.59 a) and 60.b) the structure like pits can be observed. Corrosion propagation does not seem to be uniform since large and narrow pits are forming along the deteriorated metal surface.

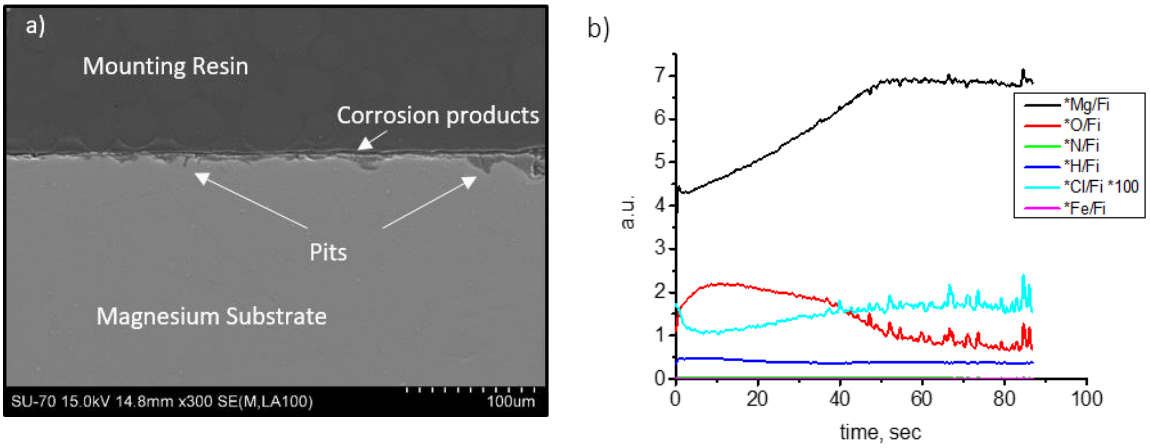

Figure III.58 - Representation of a) Cross section of HP Mg immersed during 216 hours in a 0,9 wt% NaCl solution, b) GD-OES profile of intensity vs sputtering time showing the elemental variation presented in the sample.

GDOES analysis (Figure III.58.b) shows increase of O at the first stages of the sputtering time, corresponding to the corrosion layer. Near interface the concentration of O decreases and Mg increases. It is not perceptible, but a slight increase of H also occurs in the first stages of sputtering time. Cl found higher presence near the interface (however is intensity is magnified by 100x), which can be trapped inside the pits. Is possible a presence of an Oxide layer near to the metal interface and an outside corroded layer of hydroxides.

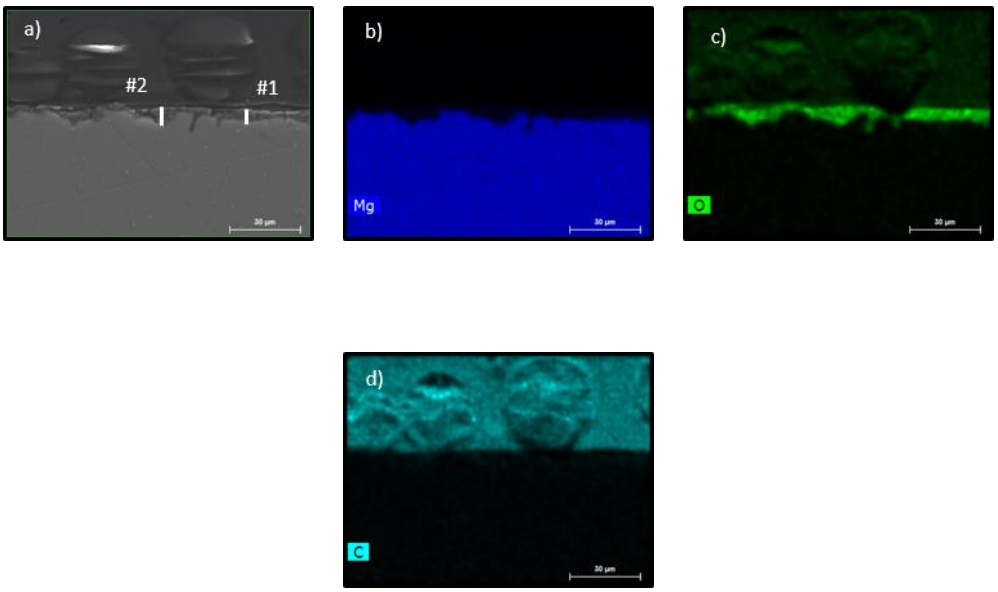

Figure III.59 - EDS mapping illustration of the cross section of HP Mg, immersed during 216 hours in a 0,9% NaCl solution. In a) SE picture; the distribution of elements, a) SE picture b) Magnesium, c) Oxygen and d) Carbon.

The elemental distribution accessed by EDS mapping observed in Figure III.59 confirms the relatively thin layer precipitated during corrosion. By the intensity maps, this

layer seems to be rich in O and with less presence of Mg with respect to the matrix, confirming the presence of a hydroxide/oxide layer. The carbon signal comes from the resin, mounted after dried the sample surface (cracks cannot be observed at those magnifications).

HP Mg immersed in PBS solution

Phosphate buffered saline solution was used, as stated before, in this investigation work and it was studied the corrosion behaviour of HP Mg during 336 hours of immersion. The respective cross section and GD-OES analysis are depicted in Figure III.61. One can see the formation of a corrosion product layer in between the mounting resin and the magnesium substrate. The metal surface degradation seems to be quite uniform when compared with the previous system (HP Mg immersed in a 0.9 wt% NaCl solution). In Figure III.62.a) it is represented the line #1 and #2 which were measured and presented values of 7.3 and 8 um, respectively. Those values represent the thickness of corrosion layer precipitated during corrosion. The GDOES analysis shows (Figure III.60.b)) the presence, at initial sputtering time (at the beginning of the corroded surface), a relatively high intense peak of P accompanied by O and H and further the increased time leads a rapid growth of Mg intensity and decrease of those intensities. This could mean the presence of a very thin corrosion layer, as it can be observed in Figure II.60. The chloride intensity is magnified at it is possible to see the traceable presence of chloride. Some artefact during GDOES experiment could have induced the reducing amount of Mg and a posteriori increase of intensities.

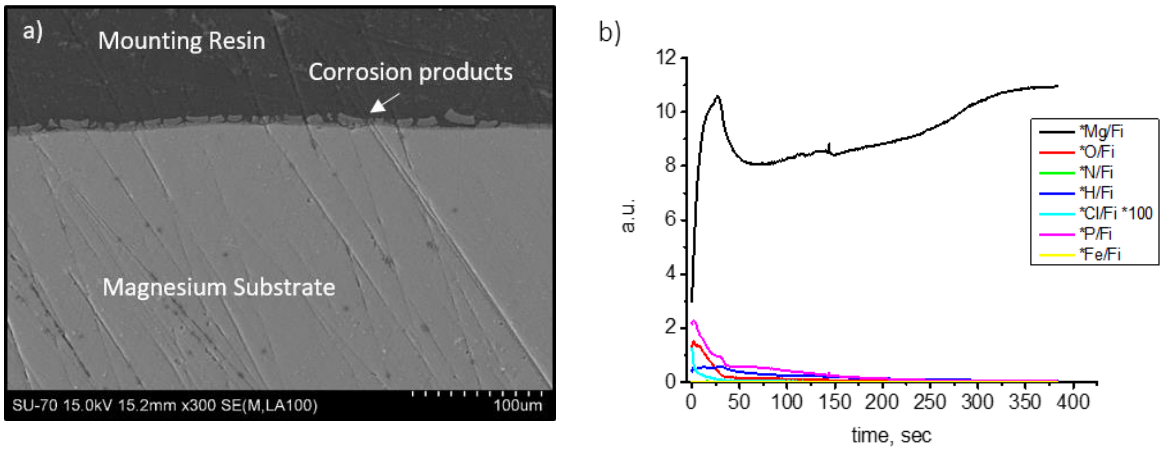

Figure III.60 - Illustration of a) Cross section HP Mg immersed during 336 hours, in a PBS solution, b) GD-OES Intensity vs Sputtering time profile for the different elements presented in this sample.

The EDS maps, which can be observed in Figure III.62, shows an increase intensity signal of oxygen and phosphorus for the corrosion products precipitated during corrosion. By another hand, Magnesium signal is increased in substrate what is expected since the

alloy is a highly pure magnesium. Carbon is the main element present in the mounted resin used for encapsulating the sample, step necessary for metallographic preparation of the sample. During the metallographic preparation, cracks could appear. The cracks are previous to metallographic preparation, maybe when dried the surface after EIS immersion. This can be corroborated because it is possible to observe the presence of carbon into the cracks.

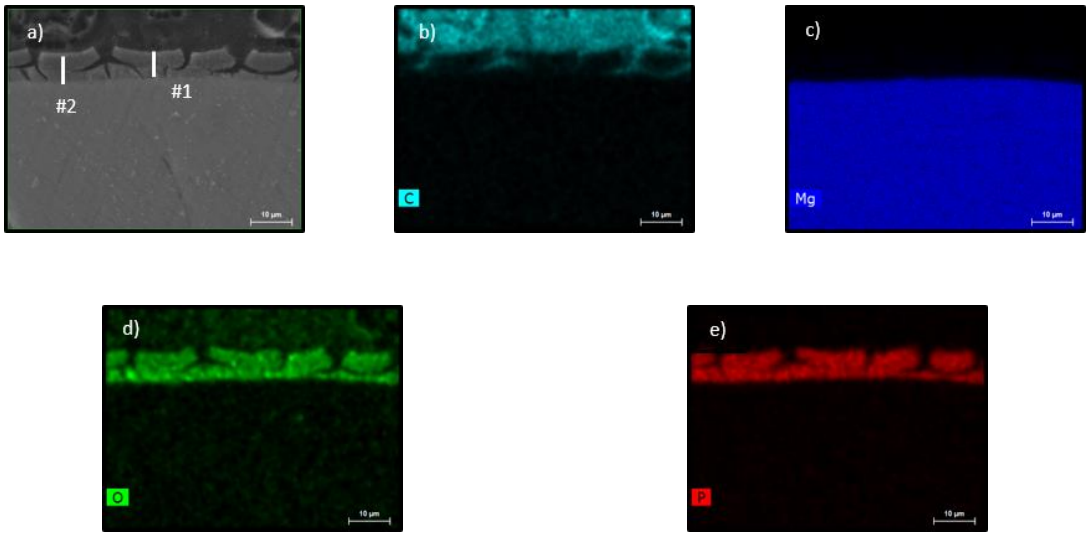

Figure III.61 - EDS mapping illustration of the cross section of HP Mg, immersed during 336 hours in a PBS solution. In a) SE picture; the distribution of elements b) Carbon , c) Magnesium, d) Oxygen and e) Phosphorus.

Mg2Gd1Mn immersed in a 0.9 wt% NaCl solution

The ternary system presents a relatively high thickness of corrosion layer originated by the deposition of corrosion products on the metal surface. An SE picture of the cross section can be observed in the Figure III.63.a) and III.64.a) for the metal alloy exposed during 336 hours into a 0.9 wt% NaCl solution. It was measured the corrosion layer in two different places, represented in Figure III.64.a). Line #1 was a 39 um of length and line #2 60 um, which represents two different values of thickness presented by the layer precipitated during corrosion. The metal surface appears with a severe degradation of the metal surface. This type of morphology degradation is characteristic of micro galvanic coupling, where a relatively strong cathode leads to magnesium dissolution of the matrix. The corrosion the matrix appears with cracks and severely damage due to the metallographic preparation of the surface. It is possible not to difference between in the degradation state of the inner and outer layer. White particles are appearing embedded into the corrosion layer. Contrary to HP Mg GDOES shows increase content of chloride near the interface, in spite is intensity is magnified by a factor of 100X. Similar to HP Mg an

increase of O and the slight increase of H it is noted at the beginning of sputtering time. The further decrease of O and increase of Mg is possibly representing the arrival of the corroded interface. Mn and Gd are present in corrosion layer as in substrate.

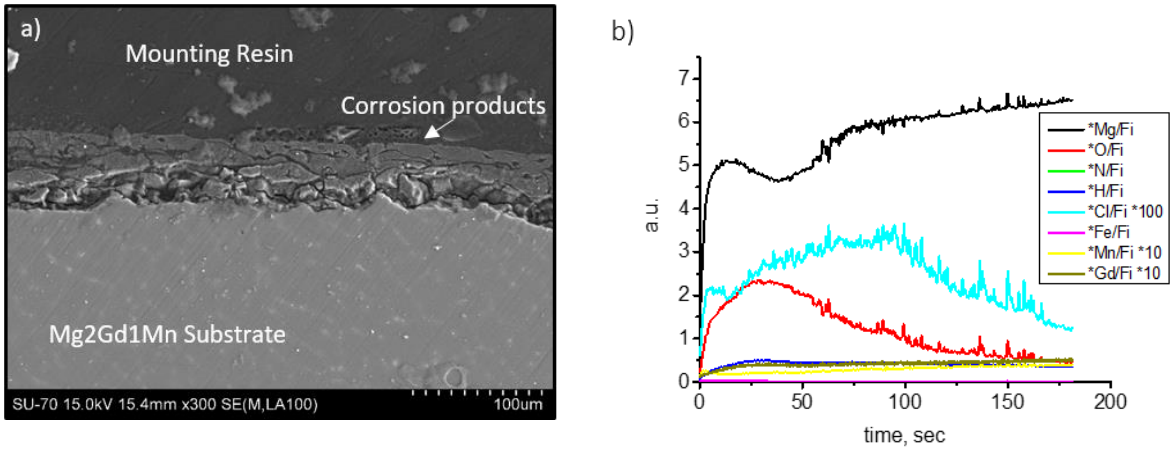

Figure III.62 - Representation of a) Cross section of Mg2Gd1Mn immersed during 336 hours in a 0,9 wt% NaCl solution, b) GD-OES profile of intensity vs sputtering time showing the elemental variation presented in the sample.

Energy dispersive spectroscopy mapping performed in the previous cross-section shows a high-intensity signal of Oxygen (in the corrosion layer), and a low intensity in magnesium, comparatively to the metal substrate.

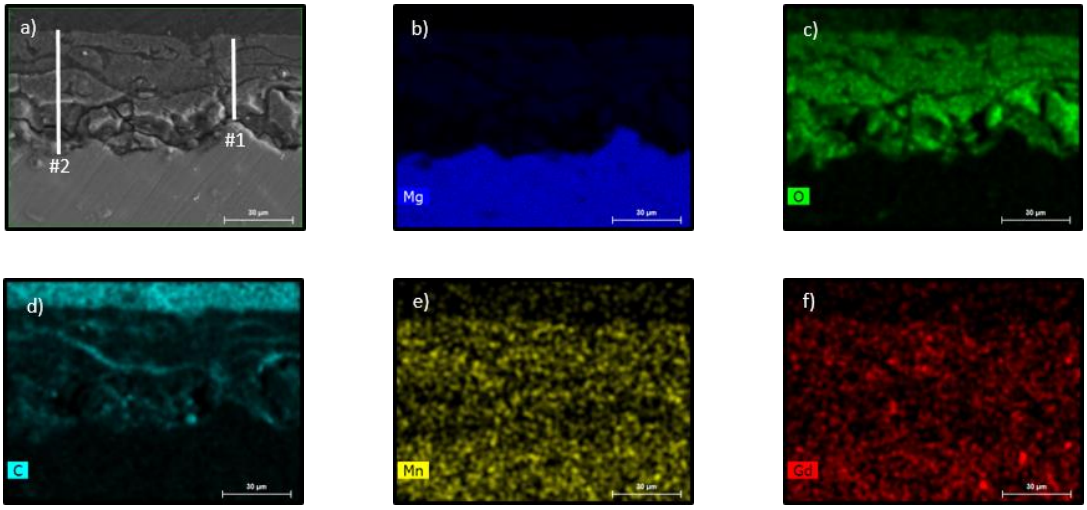

Figure III.63 - EDS mapping illustration of the cross section of g2Gd1Mn, immersed during 336 hours in a 0.9 wt% NaCl solution. In a) SE picture; the distribution of elements, b) Magnesium, c) Oxygen, d) Carbon, e) Manganese and f) Gadolinium.

At the same time, gadolinium and manganese seem to be distributed in corrosion layer. Carbon signal, due to the use of epoxy, can be seen in the cracks which are formed during the dry of the surface (after EIS measurements).

Mg2Gd1Mn immersed in PBS solution

Figure III.65.a) shows a cross section SE picture of the Mg2Gd1Mn immersed during 336 hours in a PBS solution. One can be noted the formation of a corrosion layer in between the mounting resin and Mg2Gd1Mn substrate. It was measured in two locations the length of two lines which represents the thickness of corrosion products deposited on the metal surface. In Figure III.66.a) it is possible to observe line #1 and #2 which have, respectively, lengths of 26.4 and 30 um. In respect to the previous system, the corrosion layer thickness appears to be reduced. Preparation cracks and cracks from possible dehydration of surface due to dried process, after removed the samples from immersion, can be distinguished in Figure III.66.a) and confirmed in EDS mapping (Figure III.66). The interface in between corrosion products and metal substrate seems to be less degraded than the Mg2Gd1Mn immersed in the 0.9 wt% NaCl solution, with both presenting the same time of immersion. A similar behaviour of the metal interface seems to occur when compared the previous electrolyte. However, the degradation is much less pronounced. The GDOES analysis shows a relatively high intensity of P until reaching an increase of MG intensity. The presence of Mn, Gd, Na, O and H also is noted during the corrosion layer. However, some artefact of experiment could explain the low increase of Mg peak until higher values of intensity.

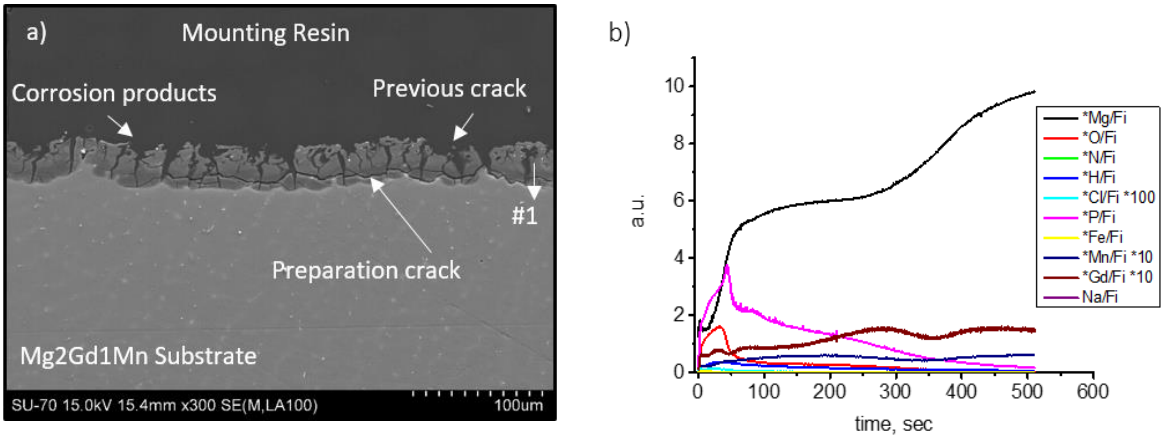

Figure III.64 - Representation of a) Cross section of Mg2Gd1Mn immersed during 336 hours in a PBS solution, b) GD-OES profile of intensity vs sputtering time showing the elemental variation presented in the sample.

The Energy dispersive spectroscopy maps can be observed in Figure III.66. One can be noted that phosphorous and oxygen are present in the identified corrosion layer. Manganese and gadolinium seem to be also distributed into the layer as in the metal matrix, and by other hand magnesium intensity is stronger in metal alloy substrate than in corrosion layer.

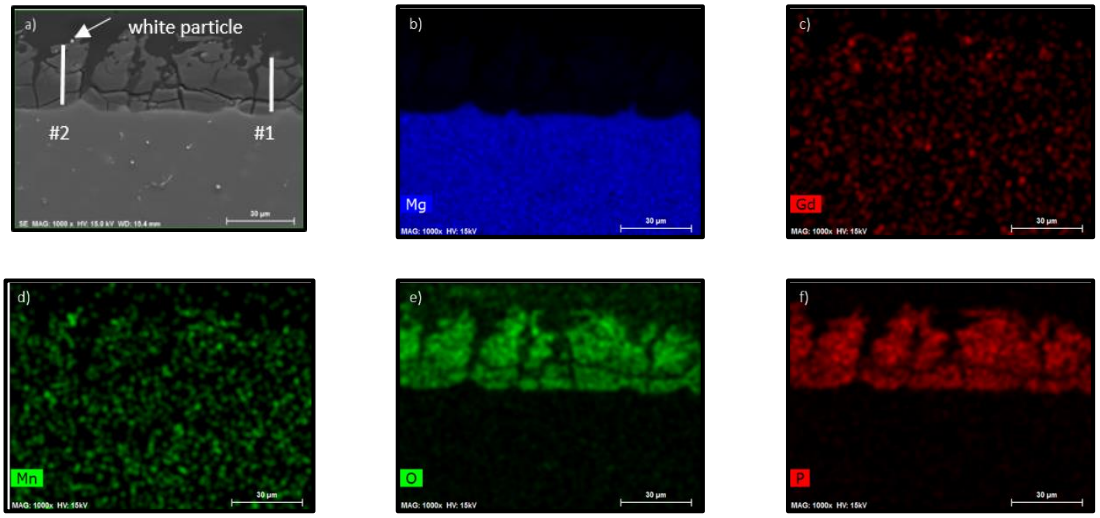

Figure III.65 - EDS mapping showing the elemental distribution along the cross section of Mg2Gd1Mn in PBS solution.

Another feature found in the deposits of corrosion products was the presence of white particles. An increased magnification of spot #1 (which can be observed in figure III.66.a)) shows a cuboid particle, and EDS maps reveal the elemental distribution of those particles (observed in figure III.67).

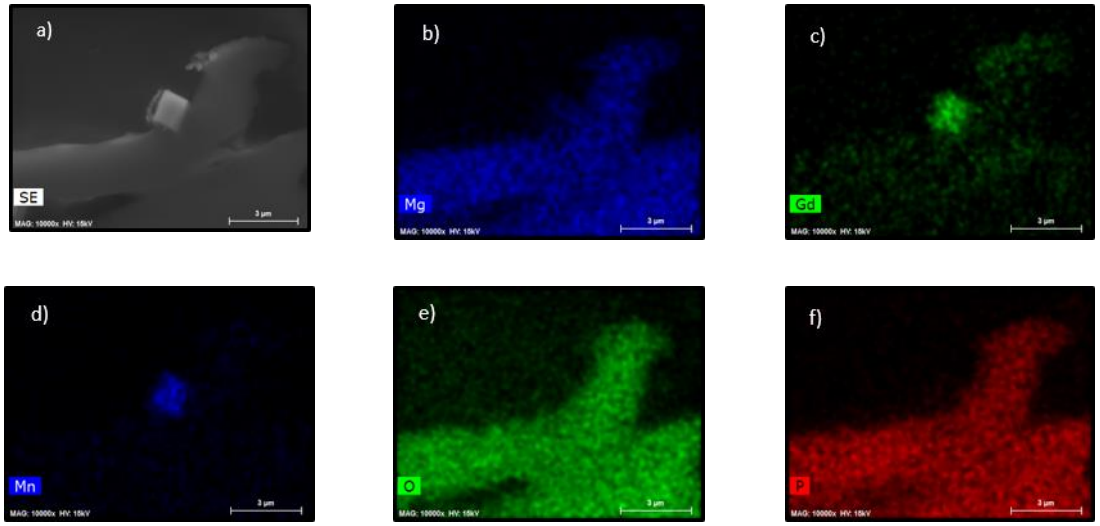

Figure III.66 - Illustration of a) SE micrograph of a as like cuboid intermetallic, EDS mapping of b) Mg, c) Gd, d) Mn, e) O and f) P.

It seems that gadolinium and manganese are appearing into the structure, and by evaluation of the morphology and brightness contrast, it is possible to identify this particle as a probable GdH2 particle, which appears in the microstructure of those alloys.

This can indicate that those particles can work as a strong cathode and are later undermined by the severe corrosion of surrounding matrix. However, AFM/SKPFM in the ternary system shows that those particles have low or non-cathodic activity. It is so possible that they do not participate in corrosion, and a uniform corrosion of matrix could detach those particles. This can explain the as like micro galvanic interface observed in the corroded interface of Mg2Gd1Mn.

Chapter IV – Discussion of Topics

IV.1 Mg-Gd alloys and the unusual high Corrosion Rate

The immersion of binary alloys in a 0.9 wt% NaCl electrolyte, revealed an unusual Corrosion Rate, several orders of magnitude higher than the HP Mg, Mg5Gd1Mn and Mg2Gd1Mn. It exists a tendency between the increase of Gadolinium content in the alloys and the growth of the Corrosion Rate. This corrosion behaviour was not expected since in [112] it was possible to observe a lower Corrosion Rate for binary systems, and which increases with Gd content. Particular results obtained during the performance of different techniques are the following:

- AFM results show Mg5Gd phase with a lower Volta Potential with respect to matrix, before immersion. The segregation zones, which are deplected in gadolinium content in respect to Mg5Gd phase (but enriched in respect to magnesium matrix), show a higher Volta potential in respect to Mg5Gd phase, but slightly lower in respect to Magnesium matrix.

- Hydrogen evolution tests present corrosion rate in the order of 77.96 mm/y for Mg2Gd at 32 hours of immersion in a 0.9 wt% NaCl solution and 169.67 mm/y for Mg5Gd at the same conditions, which are relatively high rates of corrosion;

- EIS measurements clearly show a low impedance modulus in the first 24 hours. The average of |Z| (during 24 hours of immersion) was 245.28 Ohm.cm^2 for Mg2Gd and 104.52 Ohm.cm^2 for Mg5Gd. Mg2Gd system experienced in the first hour of immersion a slight increase in |Z|, further decreasing during all the experiment. Mg5Gd always present a reduction in the impedance modulus.

- The Tafel Extrapolation of polarization curves allowed the estimation of value for I_{corr}. Also in those experiments (at 1 hour of immersion) binary alloys experienced a higher I_{corr}, and consequently high Corrosion Rate.

- Optical and SE observations allowed to visualize a substantial deposition of large, porous corrosion products on the metal surface, in HE and EIS samples.

In agreement with microstructure characterization of binary alloys (section III.1.2.2.1), it is possible to attribute to this corrosion behaviour the presence of Iron impurities. The low solubility of Iron in Magnesium leads to the precipitation of detrimental phases. Those act as strong cathodes which promote micro galvanic activity. Moreover, it was found particles with high content in Silicon. It was presented in Section

I.5.1.3 (Metal as impurities) that the presence of Si can promote the formation and growth of Fe particles and Si was found in all Alloys, mostly located in intermetallics. The exception was found in the Mg5Gd phase which appears cleaner of impurities as the segregation zones and magnesium matrix.

In AFM measurements it was probed a particle which showed a nobler Volta Potential with respect to magnesium matrix. Further immersion revealed active deposition of corrosion products, which could be an indication of cathodic activity. The elemental composition tracked on this particle, after 3 hours of immersion, showed the presence of Si. It is possible that initiation of corrosion is promoted by those micro constituents, which by microstructure characterization and local elemental composition, could be intermetallics of the type Gd_x Si_y Fe_z H_w (in accordance with data presented in Table III.3). Those intermetallics can be located in Mg5Gd phase and magnesium matrix. If the galvanic coupling is occurring between Mg5Gd or segregation zones, Gadolinium will come into solution, and further re-deposition of cathodic particles as Iron could increase further corrosion. Propagation of Corrosion also can occur at those places. It is important to note that Iron was not always found in those square intermetallics. Nonetheless, small amounts could be present and not be tracked by EDS analysis. The responsibility of unusual corrosion rates is pointed to impurities, mainly Fe.

IV.2 Differences and particularities of the corrosion behaviour of Mg-Gd-Mn alloys and HP Mg

Corrosion during short immersion time

Two main corrosion methods of characterization were used in this work such as Electrochemical Impedance Spectroscopy (EIS) and Hydrogen Evolution (HE). Figure IV.1 shows the comparison for each condition between the accumulative value of corrosion rate (CR) (calculated from hydrogen evolution measurements) and the average value of modulus of impedance |Z| (for the same condition), at approximately 24 hours immersion. Low values of corrosion rate are attributed to a less corrosive system. On the contrary high values of |Z| are related with more resistive corrosion systems.

Figure IV.1.a) shows the short immersion time for the 0.9 wt% NaCl solution. One can be noted that HE has lower corrosion rates for Mg2Gd1Mn and higher CR for HP Mg. By other hand EIS measurements shows |Z| lower for Mg5Gd1Mn and higher for HP Mg. The Hydrogen evolution shows, for Mg2Gd1Mn, a similar CR for Ringers and PBS electrolyte in the first 24 hours (with a slightly lower CR for Ringer's electrolyte). The EIS shows lower values of |Z| for PBS solution when comparing with Ringers electrolyte.

The comparison of both methods, at short immersion times, allows to say that a more resistive corrosion system it is observed in the 0.9 wt% NaCl, for Mg2Gd1Mn. The dynamics of impedance also permit the observation that in NaCl electrolyte, the resistance to corrosion is slightly higher.

The HP Mg shows high CR in 0.9 wt% NaCl and Ringer's solutions, though lower CR it is observed in PBS solution. Impedance measurements show that |Z| is similar in Ringers and PBS solutions but higher in the 0.9 wt% NaCl. The relevant results at short immersion time are summarized below.

- It was found that Mg5Gd1Mn presents lower corrosion properties, at least in comparison with Mg2Gd1Mn. Both measurements allow to observe this feature;
- In ternary system, mainly Mg2Gd1Mnn, the pure NaCl Solution present the lower CR and higher |Z| when compared with PBS and Ringers. Ringers Solution offers an increase in protection, at least in comparison with PBS one at very first hours of immersion (observe the increase of slopes in Figure III.28);
- The HP Mg shows different corrosion behaviour when compared with ternary systems. The higher CR is founded in the NaCl solution but an unusual increase of |Z| it is also recorded. The CR is lower for PBS and Ringers, but much lower for PBS than Ringers. Impedance |Z| values are very similar although shows a higher slope of the dynamic impedance in the first hours of immersion;
- The better protection in the first time of immersion conferred by Ringers vs. NaCl (for Mg2Gd1Mn) could be because of the effect of carbonates which in a very early stage could adsorb first at the surface. The less strong buffering effect of those salts also could explain this behaviour.

It is important to refer that it was used static conditions in the Hydrogen Evolution experiments and stirring conditions during EIS measurments. The difference between this two conditions could affect pH of solution and preferential precipitation of compounds, inducing different behaviour in respect to precipitation of corrosion products and the so presenting different corrosion behaviour.

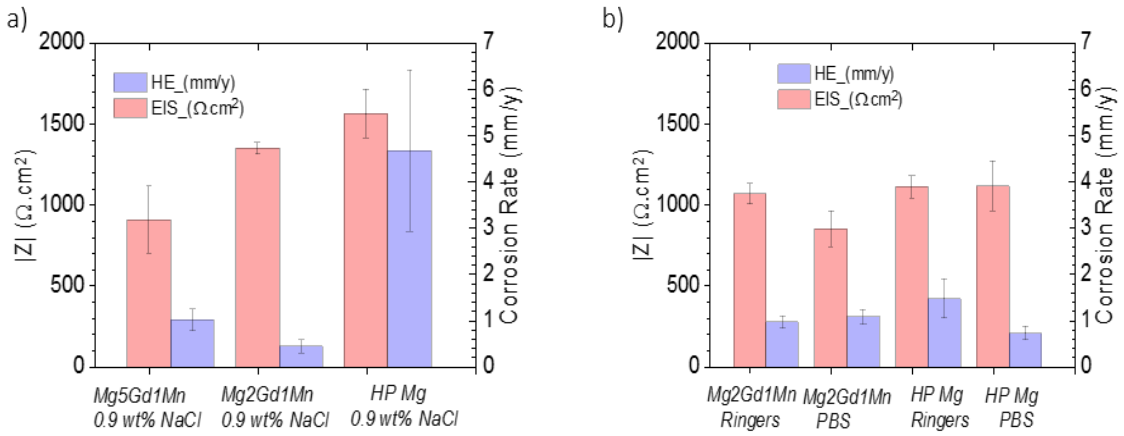

Figure IV.1 - Illustration of average corrosion rate (calculated from HE measurements) and |Z| (calculated form EIS measurements) for different electrolytes used in this work, at short immersion time (first 24 hours). In a) Samples immersed in the 0.9 wt% NaCl solution, b) Samples immersed in the Ringers and PBS solution.

Corrosion during long immersion time

The long immersion time was accounted for more than 24 hours of immersion (Figure IV.2). In the 0.9 wt% NaCl solution and at 216 hours of immersion EIS measurements shows that Mg2Gd1Mn has increased |Z| when comparing with HP Mg. At the same time, the |Z| was lower for Mg5Gd1Mn. Corrosion rate continues high for HP Mg (but a significant decrease in CR was noted compared with short immersion time) when comparing with Mg2Gd1Mn. By another hand both ternary systems seem to experience a slight increase of CR, indicating a possible acceleration in Corrosion. However, it seems not to be significant this small increase in CR and values are higher for Mg5Gd1Mn.

The corrosion behaviour in Ringers and PBS solutions at long immersion times is observed in Figure IV.2.b). The CR is higher in Ringer's than PBS. It is well noted the stability and protection that phosphate corrosion products bring to the metal surface which becomes more passive. A similar but opposite trend could be observed with the evolution of |Z| (Figure IV.2.b)). By another hand, it seems that Mg2Gd1Mn experiences some accelerated corrosion (in the HE measurements) in Ringers and NaCl solution. But this behaviour is not observed in PBS solution. At long immersion time, the HP Mg seems to get better corrosion protection in Ringer and PBS electrolytes in respect to Mg2Gd1Mn. The main features in the Long immersion tests are:

- HP Mg seems to present a better corrosion behaviour in Ringers and PBS solution compared to NaCl, at least regarding the CR measurements;

- Accelerated corrosion seems to occur in ternary systems for NaCl and Ringer's solutions. The Mg2Gd1Mn system shows more significant corrosion in Ringer's solution. In NaCl, the corrosion could be said as intermediate. In PBS solution corrosion was minuscule;

- An important difference between the protection of Ringer's solution compounds in Hydrogen Evolution and EIS measurements was noted. For HP Mg, were a more resistance CR in Ringers is noted but low values of impedance |Z| were recorded (Figure IV.2). Furthermore in the 0.9 wt% NaCl solution |Z| seems to show higher values while HE shows high CR values. The difference between static conditions used in HE experiments and stirring conditions in EIS could explain those effects;

- Stirring conditions are usually used to minimize the diffusion layer thickness, which can help to minimize the concentration polarization. It also uniforms the diffusion of species through the electrolyte (since a small shear stress is applied near the surface). This could reduce the effect of localized corrosion by chloride attack, and it seems that HP Mg and Mg2Gd1Mn present fairly good behaviour of Impedance at short immersion time in the 0.9 wt% NaCl solution (Corrosion rate is very high in the first times of immersion in HP Mg for HE measurements). However the same do not occur in Ringer’s solution. This

could be due to pH effects, and preferential precipitation of certain compounds over others since the Ringer's solution is richer than the NaCl solution in ionic species.

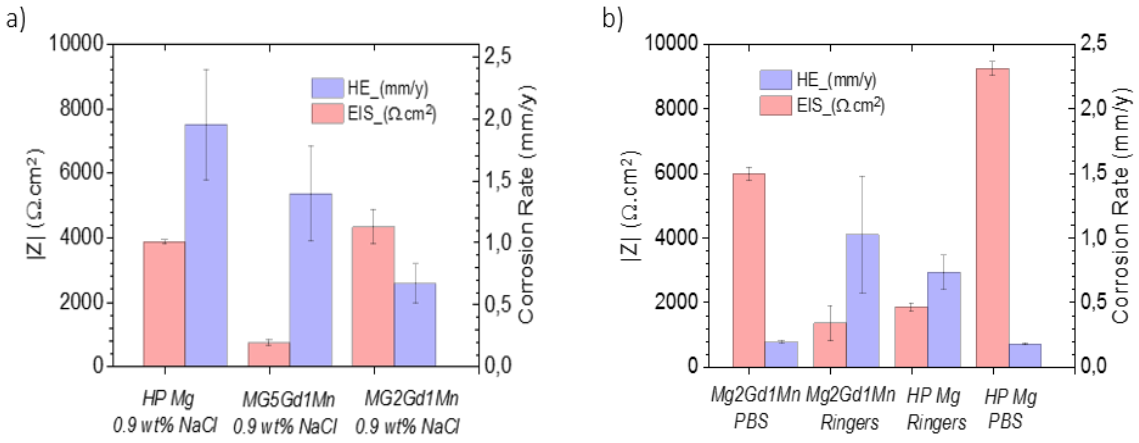

Figure IV.2 - Illustration of average corrosion rate (calculated from HE measurements) and |Z| (calculated form EIS measurements) for different electrolytes used in this work, at long immersion time (216 hours for NaCl electrolyte and 336 hours for Ringers and PBS solution), a) Samples immersed in the 0.9 wt% NaCl solution, b) Samples immersed in the Ringers and PBS solution.

The analysis of short and long immersion time is not trivial and the static and stirring conditions could bring changes in corrosion behaviour evaluated by EIS and HE tests. However in general both EIS and HE methods can give qualitatively conclusions on the corrosion resistance of HP Mg and Mg alloys.

IV.3 Corrosion mechanisms comparison of Mg alloys in different electrolytes

The analysis of the morphology of corrosion product layers, accompanying with GDOES, allows the identification of the presence of Gd and Mn elements in the corrosion layer on the surface of the ternary alloy. It is possible that Mn and Gd are released into solution (which are present in magnesium matrix as soluble elements). The release of Gd and Mn into solution could come from the dissolution of those elements from the magnesium matrix which also dissolves during immersion in corrosive electrolytes. It is also possible that segregation zones and/or Mg(Gd) phases could be dissolving, supporting anodic dissolution. The cuboid intermetallic found embedded in corrosion layer don't seem to dissolve. These intermetallics have Gd and Mn as main elements. It was found too during microstructure characterization that those structures are located near or inside Mg(Gd) phases. AFM and SKPFM measurements showed that no cathodic activity is supported by those particles, at short immersion time (3h) (Figure III.17 and 18).

Elemental composition of those structures was relatively clean of impurities (as Si and Fe by the analysis of microstructural results).

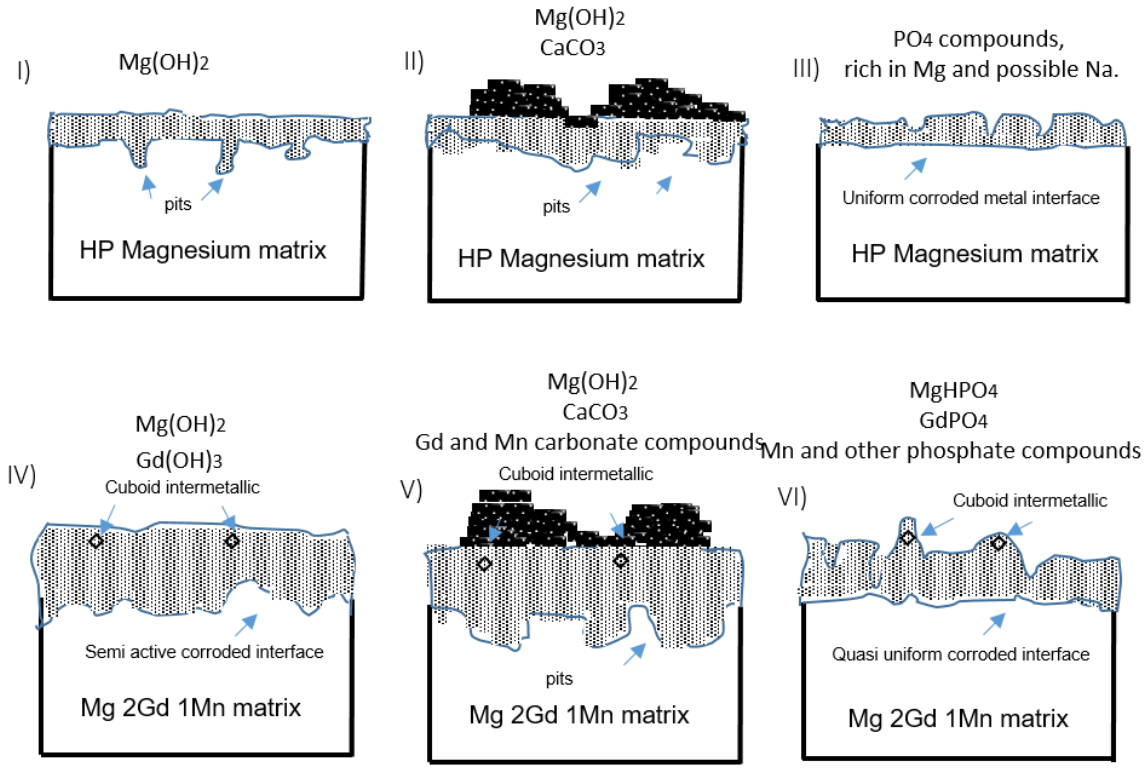

Figure IV.3 - Illustration of corroded interface after long time immersion in the i) HP Mg after in 0.9 wt% NaCl solution, ii) HP Mg in Ringer's iii) HP Mg in PBS iv) Mg2Gd1Mn in 0.9 wt% NaCl solution v) Mg2Gd1Mn in Ringer's Solution VI) Mg2Gd1Mn in PBS solution. On top of each corroded surface it is represented the main possible formation compounds.

Figure IV.3 shows the schematic differences in morphology of the corroded interface of HP Mg and Mg2Gd1Mn alloy. In HP Mg it is possible to observe pit formations, which are usually attributed to the presence of cathodic impurities (mainly iron) and chloride attack. Those pits, however, seems to be small and appear with a deep structure. The immersion in Ringer's solution also shows pit formation, as like occluded or hemispherical pits (section I.4.3) and can origin a higher degraded metal surface. Ringer's also present the particularity that a possible CaCO3 are precipitating on top of corrosion products (with Mg(OH)2 deposited near the metal surface). It is, however, interesting to perform further studies in order to know which structure could be developed first. The first initial protection measured by EIS (short immersion time) seems to be lower in value in Ringers than in NaCl solution (observe figure IV.1). However it is important to refer that those values are average, and the initial values of $|Z|$ are lower in Ringer's solution, and at the end of 24 hours are higher (observe Figure III.28). This could indicate a first formation of CaCO3 and further degradation of the surface by chloride attack could increase anodic

dissolution and so increase local surface pH, according to later deposition. However, those are assumptions, and a proper fitting or analysis of capacitance of EIS spectrums could bring more insights about early and later diffusion mechanisms in the interface metal/solution and later metal/corrosion layer/solution.

By another hand, the PBS brings a more homogeneous corroded interface, without pit formation, which can explain a more resistive behaviour found in EIS and HE measurements. The expected compounds in the PBS corrosion layer are Phosphate compounds.

The corroded interface of Mg2Gd1Mn alloy after immersion in NaCl solution seems to show a semi-active corroded interface. The analysis after immersion in PBS solution shows a much more uniform interface. However a corroded metal interface of the type of micro galvanic corrosion was found in both electrolytes, and more pronounced in the NaCl solution. The cuboid particle found in corrosion products do not dissolve, which is a strong indication that it stays inactive during corrosion of the alloy. It is being undermined at a latter stage of Mg matrix probably released into the corrosion products due to uniform corrosion of magnesium matrix. The other phases such as Mg5Gd seem to be dissolved from the Mg matrix. However, further studies should be performed in order to confirm this observation. The products of dissolution (Gd and Mg) are distributed through the corrosion product layer. This is presented in (Figures III.63 and 66) EDS mapping analysis of cross-sections and in GDOES performed in the Mg2Gd1Mn.

The corrosion layer of HP Mg in NaCl solution shows a lower thickness than Mg2gd1Mn in NaCl solution and a similar thickness comparing with HP Mg in PBS solution. However, the HP Mg were only immersed during 216 hours in the 0.9 wt% NaCl solution. Also, some malfunction during the preparation of cross section could have occurred, affecting the corrosion layer thickness. However, on PBS it is possible to observe a quite difference in thickness, when comparing HP Mg and Mg2Gd1Mn, with lower values for HP Mg, at the same time of immersion. A higher thickness of corrosion products was observed in NaCl solution than PBS solution for Mg2Gd1Mn. The precipitation of alloy elements compounds could explain this difference in thickness.

It was found in the results of morphology the deposition of what it seems to be CaCO3 crystals on the top of a previous corrosion layer (probably Mg(OH)2), presenting a bigger size for Mg2Gd1Mn. Intermediate compounds with alloy elements could explain this feature. Also, the optical inspection of the cross section in Ringer's solution allows the observation of pits. This could be due to a latter attack of chlorides ions and similar mechanisms could occur with HP Mg.

All those observations can be observed in the representative illustration Figure IV.3. The following equations propose a mechanism of corrosion that could explain dissolution behaviour of different elements. The anodic dissolution of Gd and Mg creates the respective ionic (metal cations) species. The species can react with various anionic species present in solution, and these reactions are presented further in the text. It is

important to observe that Mn should not dissolve when attached to Mg since is standard potential does not allow this dissolution. So, Mn should detach as a metal, and the electrochemical reaction should happen further in the solution and it is not taking part of the electrochemical reactions.

Electrochemical reactions:

$Gd\ (s) \rightarrow Gd^{3+} + 3e^-$ (Anodic partial reaction) Reaction (IV.1)

$Mg\ (s) \rightarrow Mg^{2+} + 2e^-$ (Anodic partial reaction) Reaction (IV.2)

$2H_2O + 2e^- \rightarrow H_2 + 2OH^-$ (Cathodic partial reaction) Reaction (IV.3)

It is necessary to describe which chemical reactions occur in different solutions. It is taken into account the concentration of cationic species to be 1 mM for Mg, 0.1 mM for Gd and Mn. The concentration of anionic and Ca^{2+} species corresponds to concentration of the respective salts in Ringers or PBS solutions. The stability of the formation complexes and pH ranges of precipitation were obtained using the Hydra MEDUSA software [126]. For solids, like for aqueous complexes, the *logK*-value for the formation reaction is used and it is inverse to the solubility product, i.e.: $\log K_f = -\log K_{sp}$

Corrosion products precipitation reactions in NaCl solution:

$Mg^{2+} + 2OH^- \rightarrow Mg(OH)_2$ (precipitation pH >10) $pK_{sp} = 10.74$ Reaction (IV.4)

$Gd^{3+} + 3OH^- \rightarrow Gd(OH)_3$ (precipitation pH >6.5) $pK_{sp} = 22.74$ Reaction (IV.5)

$Mn^{2+} + 2OH^- \rightarrow Mn(OH)_2$ (precipitation pH >11) $pK_{sp} = 12.72$ Reaction (IV.6)

Corrosion products precipitation reactions in PBS solution:

$Mg^{2+} + {HPO_4}^{2-} \rightarrow MgHPO_4$ (precipitation pH range 5 to 10) logK = 15.22 Reaction (IV.7)

$Mn^{2+} + {HPO_4}^{2-} \rightarrow MnHPO_4$ (precipitation very stable) logK = 25.29 Reaction (IV.8)

$Gd^{3+} + HPO4^{3-} \rightarrow GdPO_4$ (precipitation very stable) logK = 12.2 Reaction (IV.9)

Corrosion products precipitation reactions in Ringers solution:

$Mg^{2+} + {CO_3}^{2-} \rightarrow MgCO_3$ (precipitation pH range 8 to 11) logK = 2.98 Reaction (IV.10)

$Mn^{2+} + {CO_3}^{2-} \rightarrow MnCO_3$ (precipitation pH range 6.2 to 11.6) logK = 4.9 Reaction (IV.11)

$Gd^{3+} + {CO_3}^{2-} \rightarrow Gd_2(CO_3)_3$ (precipitation pH range 5.5 to 9) logK = 34.7 Reaction (IV.12)

$Ca^{2+} + {CO_3}^{2-} \rightarrow CaCO_3$ (precipitation pH range >7.5) logK = 3.22 Reaction (IV.13)

It was made an assumption of those reactions by consulting Pourbaix Diagram and solubility constant of compounds and MEDUSA software. A higher constant of formation can be understood as the a presence of a more stable compound, a lower solubility product constant (positive pK_{sp}) means that a more stable precipitate is formed.

The difference in corrosion activity of HP Mg and ternary alloys in NaCl, PBS and Ringers solution is explained by the formation of different corrosion products films and the by the different chemical composition of solutions. The presence of porosity is characteristic of Brucite structures ($Mg(OH)_2$) and could be observed in the morphology of corrosion products. This feature allows a more porous corrosion layer, allowing diffusion of corrosive species. Gd and Mn hydroxides can also precipitate (reaction IV.5 and 6) and it is not clear if they offer protective action for the alloy matrix since static and stirring conditions can affect corrosion products formation.

By other hand phosphate compounds could be more dense, acting as a passive barrier protection of metal surface to corrosive species. The formation of phosphate compounds (reactions IV.7, 8 and 9) can explain the protective corrosion effect. The presence of phosphate compounds decreases the rate of corrosion through the formation of a dense corrosion layer with Mg, Gd and Mn alloying elements. Phosphates bring a better inhibition to corrosion in both alloys and at longer times of immersion. This effect is very well observed in Figures IV.2, where Electrochemical and HE measurements show an improvement in corrosion resistance in PBS solution if compared with other electrolytes. However under dynamic conditions of stirring the protective layer seems to suffer occasionally breakdown, as seen in the analysis of EIS spectrums (Figure III.35). It is possible that stirring conditions affect the formation of the corrosion products mentioned and others possible intermediate compounds as Na or K phosphate crystals. Further crystallographic and chemical studies should require attention.

Mn compounds possibly are precipitating as corrosion products, which can be observed in reactions IV.6, 8 e 11. At the potential of Magnesium, Manganese as a metal is at under a stable domain. However, if it occurs the detachment of Mn from magnesium matrix, it can change the state due to lower the potential to values of those where it could

induce oxidation of manganese and so formation of Mn2+. At this state, it is possible for Manganese to precipitate as corrosion product.

In Ringer's solution carbonates can precipitate according to reactions IV.10, 11,12 and 13. It is possible to observe the precipitation of $CaCO_3$ starting to shape deposits on HP Mg surface in Figure III.46. Also, Ca deposits are existing on Mg2Gd1Mn surface, which can be observed in Figure III.55. The precipitation of Ca Carbonate can start at pH of 7.5. This can interfere with the precipitation of $Mg(OH)_2$, which starts at pH 10 (reaction IV.4). During EIS studies, when stirring process decreases pH at the metal surface, it is probable the formation of Ca carbonate compounds and causing some protectiveness to surface at an initial time (Figure III.28 and IV.1). However pitting formation could increase local pH and further deposition of $Mg(OH)_2$ could occur in EIS. In PBS solution $Mg(OH)_2$ precipitation should not occur due to the strong buffered effect presented by PBS solution, which can be observed in pH measurements after immersion in HE samples (Table III.11). A similar trend it is expected in EIS samples.

IV.4 Future Work

Additional lines of investigation could bring a better understanding for the study of biodegradable Magnesium alloys:

- A deeper analysis of the chemistry of corrosion products could reveal more detailed information about corrosion products. FTIR and XPS could be used as characterization techniques, showing information about the chemistry and valence state of elements in corrosion products. The crystallographic structure also can be revealed by further analysis of the diffractograms;

- In order to understand the re-deposition of iron from the impurities and affectation in the spreading of VDP in binary system, Massbauer spectroscopy could be used, identifying the presence of iron and the oxidation state of the same;

- A better understanding of Pit formation and local attack on alloy's surface could bring new insights into the mechanisms of corrosion. For that the corrosion layer could be removed and the metal interface could reveal more about corrosion in the studied alloys;

- Further lines of investigation should address simulated body fluids (SBF) which could bring new insights into how carbonates and phosphates together affect the behavior of corrosion. Also, SBF protein based mediums should be addressed to understand the corrosion behaviour under bio-physiological conditions. Dynamic conditions and/or the use of bioreactors could improve the simulation of Body Fluid conditions. The use of a body temperature (ca 37ºC) also should be addressed;

- In this particular work, it was found difficult to access an exact chemical composition of the alloy by Optical Emission Spectroscopy. Other methods chemical analysis could be performed, in order to get more precise results;

- A deeper view in the local corrosion should be addressed. The use of a set of different localized techniques as Scanning Ion-selective Electrode could reveal more about localized corrosion and pH distribution;

- A deeper characterization of solid-liquid interface of those alloys with the various electrolytes should be addressed. Flow microcapillary plasma mass spectrometer setup can provide local, time-resolved and elemental specific information about corrosion processes. It is possible to use this technique under laminar flows, and have detailed information about chemical stability and dissolution processes occurring at solid – liquid interface. Coupled with EIS measurements it can offer huge improvements in the understanding of mechanisms of corrosion;

- Also, an electrochemical system can be coupled with hydrogen evolution setup in order to correlate the volume of hydrogen evolved and in situ impedance of the sample. This approach may permit the correlation between both data. Data fitting of electrochemical measurements also could be addressed in order to better understand the electrochemical behaviour of systems;

Regarding microstructure:

- A TEM characterization of the different intermetallic found in the microstructure of, especially, ternary system should be addressed in future studies in order to know the influence of those in corrosion;

- A better understanding of the Mg-Gd-Mn phase diagram also could help in the identification of possible intermetallics;

- Heat treatment of ternary alloys could bring more insights on how the microstructure affects corrosion. The heat treatment can remove segregation zones, homogenize the Mg (Gd,Mn) phases and remove another type of intermetallics;

- New metallurgical route processes in the production of alloys could be used. Tixo-casting is an example of a process which could bring improvements in corrosion of the studied alloys;

- In an overall way, the addition of new alloying elements could bring new insights on the corrosion behaviour of those alloys. Elements as Zr, Y and Ca, which are not detrimental to the human body, could be used. It is also important to do a characterization of mechanical properties needed for bio-applications for the alloys in study;

Conclusions

In this master thesis novel magnesium alloys such as Mg-Gd and Mg-Gd-Mn were characterized. Local and corrosion studies in novel biodegradable magnesium alloys were conducted in a 0.9 wt% NaCl, Ringer's and phosphate buffered saline (PBS) solutions.
Microstructural characterization in Mg – Gd systems revealed that the fraction of Mg5Gd phases increases with the increase of Gd content in alloys. Intermetallics with a squared shape morphology also were identified and could be possible types of GdH_2. Elemental composition analysis showed an increase in impurities levels, mainly Si and Fe in intermetallics and in this way a new possible intermetallic could be found of the type Gd-Si-Fe-H.

The addition of Mn in the microstructure seems to change the morphology of some intermetallics. It is possible that the formation of different types of intermetallics it is occurring since elemental analysis showed the presence of big amounts of Mn and Si in white-defined intermetallics. Gd-Mn is a possible intermetallic and in the presence of substantial amount of impurities, it could have the following composition Gd-Mn-Si. Elemental analysis revealed Mn distribution in the Mg5Gd phase and other intermetallics. The possible cuboid shape intermetallics (GdH_2) contain Mn though they appear with fewer amounts of impurities in respect to the binary system.

Atomic force microscopy and SKPFM studies were performed on the binary Mg5Gd and ternary Mg5Gd1Mn systems. This study showed a difference in Volta potential between the intermetallics of type Gd-H and magnesium matrix of high amplitude for Mg5Gd, when compared to the Mg5Gd1Mn. The strong potential difference on intermetallics in Mg5Gd alloy can be attributed to the presence of iron as impurities in the microstructure. The short immersion tests conducted for Mg5Gd alloy showed an increase in topography on top of intermetallics and occurrence of deposition of corrosion products which can corroborate that they act as cathodic sites. On the other hand, in ternary system, this did not occur. It was possible to elucidate the mechanism of corrosion, which appears to be an active micro galvanic coupling in the binary system and a less active or almost inert effect in ternary system, at short immersion times.

Another important result of this work is the difference noted in corrosion behaviour studied by electrochemical impedance spectroscopy (EIS) measurements and hydrogen evolution (HE) tests, in different electrolytes. This effect can be attributed to the various conditions used in each experiment. Immersion tests in EIS were conducted under stirring conditions. HE tests were conducted in a static environment. The local pH on the surface of magnesium alloys can be different at stirring or static conditions. The preferential precipitation of corrosion products can be influenced by those conditions, affecting the

uniformity of corrosion layer formation. Ternary system and HP Magnesium in hydrogen evolution measurements performed in Ringer's solution presented a better corrosion behaviour in comparison with the 0.9 wt% NaCl solution. The hydrogen evolution slowed down when comparing with 0.9 wt% NaCl solution. However, EIS measurements showed a decrease in impedance at low frequencies for both HP Mg and Mg2Gd1Mn in the Ringers electrolyte, when comparing with the 0.9 wt% NaCl solution and the presence of Pitting corrosion could be behind those effects. Also, the formation of pits was observed in the Mg5Gd1Mn alloy immersed in 0.9 wt% NaCl solution.

Microstructural observations and corrosion products morphology allow the identification of different types of corrosion products in the different conditions. In the 0.9 wt% NaCl solution, alloys, and HP Mg were characterized mainly by the appearance of $Mg(OH)_2$. The shape and morphology of corrosion layer are molded by the intrinsic corrosion of each alloy. Highly corrosive Mg-Gd alloys presented abundant and more porous deposits. Ternary and HP Mg alloys showed more compact and dense corrosion layers. Alloying elements (Mn, Gd) were found in the corrosion layers, which is a strong evidence that anodic dissolution brings into solution metal species, in an ionic or metal state. Ringer's solution also showed changes in the morphology of corrosion products, which can be of the type $Mg(OH)_2$ and CaCO3. The PBS brings strong and solid corrosion layer, which can contain phosphates – Mg, Gd phosphates and $Mg(OH)_2$.

The formation conditions of different corrosion products were theoretically evaluated. Several chemical processes were addressed which can contribute to the formation of a corrosion product layer. The following compounds may be formed during Mg alloys corrosion: $Gd(OH)_3$, $GdPO_4$, $Gd_2(CO_3)_3$, $MgHPO_4$, $MgCO_3$ and some others. However to prove the appearance of those compounds further work should be done to get a better chemical identification of those compounds on alloys surface.

The corrosion rate is highly decreased in a phosphate buffered saline solution since corrosion studies show higher impedance modulus and low volume of hydrogen evolution. This displays the strong effect that phosphates bring to the protective nature of the corrosion product layer. It is well noted that besides the strong buffering effect of phosphate buffered saline solution, the precipitation of phosphate compounds will bring a better protective behaviour. In PBS solution and at 15 days of immersion the CR was, for HP Mg and Mg2Gd1Mn, respectively, 0.171 and 0.180 mm/year. This could be a good indication for the use of those materials as biodegradable biomaterials.

References

[1] J. R. Davis, “Overview of Biomaterials”, *Mater. Med. devices*, p. 315, 2003.

[2] A. Yoruc Binnaz Hazar and B. Sener Cem, “Biomaterials", *A Roadmap Biomed. Eng. Milestones*, pp. 67–114, 2012.

[3] C. M. Boutry, H. Chandrahalim, P. Streit, M. Schinhammer, a. C. Hanzi, and C. Hierold, “Towards biodegradable wireless implants”, *Philos. Trans. R. Soc. A Math. Phys. Eng. Sci.*, vol. 370, pp. 2418–2432, 2012.

[4] B. Basu, D. Kati, A. Kumar, " ADVANCED BIOMATERIALS Fundamentals, Processing and Applications", *The American Ceramic Society, Wiley*, 2009.

[5] C. J. Kirkpatrick, D.W. Grainger, D. W. Hutmacher, K. E. Healy, P. Ducheyne, "Comprehensive Biomaterials", *Elsevier, 1st Edition*, 2011.

[6] A. . Fallis, “Granta CES 2009 EDUPACK Chap 2”, *J. Chem. Inf. Model.*, vol. 53, no. 9, pp. 1689–1699, 2013.

[7] K. Horie, M. Barón, R. B. Fox, J. He, M. Hess, J. Kahovec, T. Kitayama, P. Kubisa, E. Maréchal, W. Mormann, R. F. T. Stepto, D. Tabak, J. Vohlídal, E. S. Wilks and W. J. Work “Definitions of terms relating to reactions of polymers and to functional polymeric materials (IUPAC Recommendations 2003)”, *Pure Appl. Chem.*, vol.2 76, no. 4, pp. 889–906, 2004.

[8] N. T. Kirkland and N. Birbilis, "Magnesium Biomaterials: Design, Testing, and Best Practice", *Springer*, 2014.

[9] L. E. Claes, “Mechanical characterization of biodegradable implants”, *Clin. Mater.*, vol. 10, no. 1–2, pp. 41–46, 1992.

[10] F. Witte, N. Hort, C. Vogt, S. Cohen, K. U. Kainer, R. Willumeit, F. Feyerabend, “Degradable biomaterials based on magnesium corrosion”, *Curr. Opin. Solid State Mater. Sci.*, vol. 12, no. 5–6, pp. 63–72, 2008.

[11] Cambridge University Engineering Department, “Materials data book”, *Mater. Courses*, pp. 1–41, 2003.

[12] M. P. Staiger, A. M. Pietak, J. Huadmai, and G. Dias, “Magnesium and its alloys as orthopedic biomaterials: A review”, *Biomaterials*, vol. 27, no. 9, pp. 1728–1734, 2006.

[13] S. González, E. Pellicer, S. Suriñach, M. D. Baró, and J. Sort, “Biodegradation and Mechanical Integrity of Magnesium and Magnesium Alloys Suitable for Implants”, *Biodegradation - Engineering and Technology, Dr. Rolando Chamy (Ed.), InTech*, 2013.

[14] S. O. Adeosun, G. I. Lawal, and O. P. Gbenebor, “Characteristics of Biodegradable Implants”, *J. Miner. Mater. Charact. Eng.*, vol. 2, no. 2, pp. 88–106, 2014.

[15] H. Nishida and Y. Tokiwa, “Effects of higher-order structure of Poly(3-hydrolxybutyrate) on biodegradation. ll Effects of crystal structure on microbial degradation.”, *J. Environ. Polym. Degrad.*, vol. 1, no. 1, pp. 65–80, 1993.

[16] Q. Zhang, X. G. Wang, P. Cao and W. Gao, “Degradation Behavior of a Biodegradable Fe-Mn Alloy Produced by Powder Sintering”, *Int. J. Mod. Phys. Conf. Ser.*, vol. 6, pp. 774–779, 2012.

[17] D. Vojtech, J. Kubasek, J. Capek and I. Pospisilova, “Magnesium , Zinc and Iron Alloys for Medical Applications in Biodegradable Implants”, *Metal*, 2014.

[18] N. T. Kirkland, "Magnesium Biomaterials - Past, Present and Future", *Corrosion Engineering, Science and Technology, 47(5), pp.322-328,* 2012

[19] N. I. T. C. Socity, "Nace Basic Corrosion", *National Association of Corrosion Engineers, 2nd Edition,* 1971.

[20] Mário G.S. Ferreira, "*Corrosão de Materiais"*, Universidade de Aveiro, 2001.

[21] M. P. Brady, G. Rother, L. M. Anovitz, K. C. Littrell, K. A. Unocic, H. H. Elsentriecy, G. L. Song, J. K. Thomson, N. C. Gallego and B. Davis, “Film Breakdown and Nano-Porous Mg (OH)$_2$ Formation from Corrosion of Magnesium Alloys in Salt Solutions”, *vol. 162, no. 4, pp. 140–149,* 2015.

[22] G. L. Song, "Corrosion of Magnesium Alloys", *Woodhead publishing in materials,* 2011.

[23] H. Altun and S. Sen, “Studies on the influence of chloride ion concentration and pH on the corrosion and electrochemical behaviour of AZ63 magnesium alloy”, *Mater. Des.*, vol. 25, no. 7, pp. 637–643, 2004.

[24] D. Landolt, "Corrosion and surface chemistry of metals", *EPFL Press, 1st Edition,* 2007.

[25] P. Marcus, "Corrosion Mechanisms in Theory and Practice*", Marcel Dekker Inc., 2nd Edition,* 2011.

[26] R. Baboian, R. S. Treseder, "Nace Corrosion Engineer's Reference Book", *Nace International, 3rd Edition, p. 452,* 2002.

[27] R. Winston Revie and H. H. Uhlig, "Corrosion and Corrosion Control: An introduction to corrosion science and engineering", Wiley Interscience, 4rd Edition, 2008.

[28] M. Pourbaix, "Atlas of electrochemical equilibria in aqueous solutions", *National Association of Corrosion Engineers*, 1974.

[29] E. E. Stansbury and R.A. Buchanan, "Fundamentals of Eletrochemical Corrosion", *ASM International, 2000.*

[30] William D. Callister Jr. and David G. Rethwisch, "Materials Science and Engineering: An Introduction", *John Wiley and Sons, 8th Edition.*

[31] B. Guang, L. Song, and A. Atrens, "Corrosion Mechanisms of Magnesium Alloys", *Advanced Engineering Materials, vol. 2648, pp. 10–33,* 1999.

[32] G. Song, "Galvanic corrosion of magnesium alloy AZ91D in contact with an aluminium alloy , steel and zinc", *Corrosion science, vol. 46, pp. 955–977,* 2004.

[33] N. N. Aung and W. Zhou, "Effect of grain size and twins on corrosion behaviour of AZ31B magnesium alloy", *Corros. Sci., vol. 52, no. 2, pp. 589–594,* 2010.

[34] C. R. Mccall, M. A. Hill, and R. S. Lillard, "Crystallographic pitting in magnesium single crystals", *Corrosion Engineering, Science and Technology, vol. 40, no. 4, pp. 337–344,* 2005.

[35] N. Perez, "Electrochemistry and Corrosion Science", *Kluwer Academic Publishers, no. 1, pp. 1–5,* 2014.

[36] E. Ghali, W. Dietzel, and K. U. Kainer, "General and localized corrosion of magnesium alloys: A critical review", *J. Mater. Eng. Perform., vol. 22, no. 10, pp. 2875–2891,* 2013.

[37] G. Song, A. Atrens, D. Stjohn, J. Nairn, and Y. Li, "The electrochemical corrosion of pure magnesium in 1 N NaCl," *Corros. Sci., vol. 39, no. 5, pp. 855–875,* 1997.

[38] R. Tunold, H. Holtan, M. B. H. Berge, A. Lasson, and R. Steen-Hansen, "The corrosion of magnesium in aqueous solution containing chloride ions," *Corros. Sci., vol. 17, no. 4, pp. 353–365,* 1977.

[39] A. Pardo, M. C. Merino, A. E. Coy, R. Arrabal, F. Viejo, and E. Matykina, "Corrosion behaviour of magnesium/aluminium alloys in 3.5 wt.% NaCl," *Corros. Sci., vol. 50, no. 3, pp. 823–834,* 2008.

[40] O. Fruhwirth, G. W. Herzog, I. Hollerer, and A. Rachetti, "Dissolution and hydration kinetics of MgO," *Surf. Technol., vol. 24, no. 3, pp. 301–317,* 1985.

[41] G. G. Perrault, “The potential-pH diagram of the magnesium - water system ”, *Eletroanalytical Chemistry and Interface Electrochemistry, vol. 51, pp. 107–119*, 1974.

[42] D. Persaud-Sharma and A. McGoron, “Biodegradable Magnesium Alloys: A Review of Material Development and Applications”, *J. Biomim. Biomater. Tissue Eng., vol. 12, pp. 25–39*, 2012.

[43] G. L. Makar, “Corrosion Studies of Rapidly Solidified Magnesium Alloys”, *J. Electrochem. Soc., vol. 137, no. 2, pp. 414–421*, 1990.

[44] G. Song, A. Atrens, D. Stjohn, J. Nairn and Y. Li, "The eletrochemical corrosion of pure magnesium in 1N NaCl", *Corrosion Science, vol. 39, no. 5*, 1997.

[45] D. Hoche, C. Blawert, S.V. Lamaka, N. Scharnaql, C. Mendis, M.L. Zheludkevich, "The effect of iron re-deposition on the corrosion of impurity containing magnesium", *Phys. Chem. Chem. Phys., vol. 18, 1279-1291*, 2016.

[46] C. Hoog, N. Birbilis, and Y. Estrin, “Corrosion of pure Mg as a function of grain size and processing route”, *Adv. Eng. Mater., vol. 10, no. 6, pp. 579–582*, 2008.

[47] A. E. Coy, F. Viejo, P. Skeldon and G. E. Thompson, “Susceptibility of rare-earth-magnesium alloys to micro-galvanic corrosion,” *Corros. Sci., vol. 52, no. 12, pp. 3896–3906*, 2010.

[48] R. Arrabal, A. Pardo, M. C. Merino, K. Paucar and M. Mohedano, “Influence of Gd on the Corrosion Behavior of AM50 and AZ91D Magnesium Alloys”, *Corrosion, vol. 9312, no. May, pp. 398–410*, 2012.

[49] M. C. Merino, K. Paucar, P. Casaju, M. Mohedano, R. Arrabal and E. Matykina, “Salt spray corrosion behaviour of new Mg – Al alloys containing Nd or Gd”, *Corrosion Engineering, Science and Technology vol. 48, no. 3, pp. 183–194*, 2013.

[50] F. Andreatta, I. Apachitei, A. A. Kodentsov, J. Dzwonczyk and J. Duszczyk, “Volta potential of second phase particles in extruded AZ80 magnesium alloy”, *Electrochimica Acta, vol. 51, pp. 3551–3557*, 2006.

[51] I. Apachitei and J. Duszczyk, “Microgalvanic activity of an Mg – Al – Ca-based alloy studied by scanning Kelvin probe force microscopy”, *Scripta Materialia, vol. 57, pp. 1012–1015*, 2007.

[52] A. D. Südholz, N. T. Kirkland, R. G. Buchheit, and N. Birbilis, “Electrochemical Properties of Intermetallic Phases”, *Electrochemical and Solid-State Letters, vol. 14*, 2011.

[53] G. Ben-hamu, D. Eliezer, G. Ben-hamu, D. Eliezer, and K. S. Shin, “The role of Si and Ca on new wrought Mg – Zn – Mn based alloy”, *Materials Science and Engineering A, 447, pages 35–43*, 2007.

[54] A. J. López, C. Taltavull, B. Torres, E. Otero, and J. Rams, “Characterization of the Corrosion Behavior of a Mg Alloy in Chloride Solution”, *Corrosion, vol. 69, no. 5, pp. 497–508,* 2013.

[55] M. Alvarez-Lopez, M. D. Pereda, J. A. D. Valle, M. F. Lorenzo, M. C. Garcia-Alonso, O. A. Ruano, M. L. Escudero, “Corrosion behaviour of AZ31 magnesium alloy with different grain sizes in simulated biological fluids”, *Acta Biomaterialia*, vol. 6, no. 5, pp. 1763–1771, 2010.

[56] N. N. Aung and W. Zhou, “Effect of heat treatment on corrosion and electrochemical behaviour of AZ91D magnesium alloy”, *J. Appl. Electrochem.*, vol. 32, no. 12, pp. 1397–1401, 2002.

[57] J. D. Hanawalt, C. E. Nelson and J. A. Peloubert,“Corrosion Studies of Magnesium and Its Alloys”, *Metals Technology*, 1941.

[58] G. Song, "Chapter 1 - Corrosion behavior and prevention strategies for magnesium (Mg) alloys", *Woodhead Publishing Limited*, 2010.

[59] M. Bugnet, A. Kula, M. Niewczas and G. A. Botton, “Segregation and clustering of solutes at grain boundaries in Mg – rare earth solid solutions”, *Acta Materialia vol 79, 66-73,* 2014.

[60] L. Yang *et al.*, “Effect of traces of silicon on the formation of Fe-rich particles in pure magnesium and the corrosion susceptibility of magnesium,” *J. Alloys Compd.*, vol. 619, pp. 396–400, 2015.

[61] G. L. Song,"Corrosion of Magnesium Alloys", *Woodhead Publishing in Materials,* 2011.

[62] B. A. Shaw, “Corrosion Resistance of Magnesium Alloys”, *ASM Internacional, vol. 13*, 2003.

[63] X. Li, A. Scherf, M. Heilmaier, and F. Stein, “The Al-Rich Part of the Fe-Al Phase Diagram,” *J. Phase Equilibria Diffus., vol. 37, no. 2, pp. 162–173,* 2016.

[64] T. S. N. Sankara Narayanan, II-Song Park and Min-Ho Lee, " SurfaceModification of Magnesium and it's Alloys for Biomedical Applications , Volume 1", *Woodhead Publishing Series in Biomaterials*, 2015.

[65] S. S. Pathak, S. K. Mendon, M. D. Blanton, and J. W. Rawlins, “Magnesium-Based Sacrificial Anode Cathodic Protection Coatings (Mg-Rich Primers) for Aluminum Alloys”, *Metals, pp. 353–376*, 2012.

[66] J. O. M. Bockris and A. K. N. Reddy, *Modern Electrochemistry*, vol. 1, no. 5. 1974.

[67] S. S. et All, "Corrosion failure analysis and metallography", *American Society for Metals: Columbus*, 1986.

[68] D. P. Sharma, A. McGoron ,"Biodegradable Magnesium Alloys: A Review of Material Development and Applications", *J. Biomim Biomater Tissue Eng.*, 2012.

[69] A. Atrens, G. Song, F. Cao, Z. Shi, and P. K. Bowen, "ScienceDirect Advances in Mg corrosion and research suggestions", *J. Magnes. Alloy.*, vol. 1, no. 3, pp. 177–200, 2013.

[70] T. J. Warner, N. A. Thorne, G. Nussbaum, and W. M. Stobbs, "A cross-sectional TEM study of corrosion initiation in rapidly solidified Mg-based ribbons", *Surf. Interface Anal.*, vol. 19, no. 1–12, pp. 386–392, 1992.

[71] D. S. Gandel, "The effect of Mn and Zr additions on Fe impurities and the corrosion performance of Mg",*University of Monash,* 2013.

[72] R. Zeng, W. Dietzel, F. Witte, N. Hort, and C. Blawert, "Progress and challenge for magnesium alloys as biomaterials", *Adv. Eng. Mater., vol. 10, no. 8, pp. 3–14,* 2008.

[73] Y. Song, E. H. Han, D. Shan, C. D. Yim, and B. S. You, "The effect of Zn concentration on the corrosion behavior of Mg-xZn alloys", *Corros. Sci., vol. 65, pp. 322–330,* 2012.

[74] R. Civitelli and K. Ziambaras, "Calcium and phosphate homeostasis: concerted interplay of new regulators.", *J. Endocrinol. Invest., vol. 34, no. 7 Suppl, pp. 3–7,* 2011.

[75] H. Matsuno, A. Yokoyama, F. Watari, M. Uo, and T. Kawasaki, "Biocompatibility and osteogenesis of refractory metal implants, titanium, hafnium, niobium, tantalum and rhenium", *Biomaterials, vol. 22, no. 11, pp. 1253–1262,* 2001.

[76] J. Mercer, W. and Hillis, "The Critical Contaminant Limits and Salt Water Corrosion Performance of Magnesium AE42 Alloy", *SAE Tech. Pap. 920073*, 1992.

[77] M. Liu *et al.*, "Calculated phase diagrams and the corrosion of die-cast Mg-Al alloys", *Corros. Sci., vol. 51, no. 3, pp. 602–619,* 2009.

[78] J. W. Chang *et al.*, "Comparison of the corrosion behaviour in 5% NaCl solution of Mg alloys NZ30K and AZ91D", *J. Appl. Electrochem., vol. 38, no. 2, pp. 207–214,* 2008.

[79] F. Feyerabend *et al.*, "Evaluation of short-term effects of rare earth and other elements used in magnesium alloys on primary cells and cell lines", *Acta Biomater., vol. 6, no. 5, pp. 1834–1842,* 2010.

[80] L. L. Rokhlin, "The Regularities in the Mg-Rich Parts of the Phase Diagrams, Phase Transformations and Mechanical Properties of Magnesium Alloys With Individual Rare Earth Metals", *archives of metallurgy and materials,* 2007.

[81] L. L. Rokhlin, "Magnesium Alloys Containing Rare Earth Metals: Structure and Properties", *Taylor & Francis*, 2003.

[82] H. Okamoto, "Gd-Mg (Gadolinium-Magnesium)," *J. Phase Equilibria*, vol. 14, no. 4, pp. 534–535, 1993.

[83] J. F. Nie and M. Gibson, "On the unexpected formation of rare earth hydrides in magnesium – rare earth casting alloys", *Scripta Materialia*, 2014.

[84] F. A. N. Zhang, B. Hu, H. Xu, S. Liu, and T. A. O. Zhou, "Experimental Investigation and Thermodynamic Calculation of the Phase Equilibria in the Mg-Gd-Mn Ternary System," *Metall. Mater. Trans.* A, vol. 46, no. 10, pp. 4804–4811, 2015.

[85] Y. Huang, L. Yang, S. You, W. Gan, K. Ulrich, and N. Hort, "Unexpected formation of hydrides in heavy rare earth containing magnesium alloys," *J. Magnes. Alloy., vol. 4, no. 3, pp. 173–180*, 2016.

[86] A. Krause *et al.*, "Degradation behaviour and mechanical properties of magnesium implants in rabbit tibiae," *J. Mater. Sci., vol. 45, no. 3, pp. 624–632*, 2010.

[87] S. Zhang *et al.*, "Research on an Mg-Zn alloy as a degradable biomaterial," *Acta Biomater., vol. 6, no. 2, pp. 626–640*, 2010.

[88] E. Zhang, L. Xu, G. Yu, F. Pan, and K. Yang, "In vivo evaluation of biodegradable magnesium alloy bone implant in the first 6 months implantation.," *J. Biomed. Mater. Res. A, vol. 90, no. 3, pp. 882–893*, 2009.

[89] Patrick Peeters, "Preliminary Results After Application of Absorbable Metal Stents in Patients With Critical Limb Ischemia", *J. Endovasc. Ther., vol. 12*, 2005.

[90] H. Hermawan, D. Dubé, and D. Mantovani, "Developments in metallic biodegradable stents", *Acta Biomater.*, vol. 6, no. 5, pp. 1693–1697, 2010.

[91] Yufeng Zheng, "Magnesium alloys as degradable biomaterials", *CRC Press*, 2015.

[92] P. Pérez *et al.*, "Corrosion behaviour of Mg-Zn-Y-Mischmetal alloys in phosphate buffer saline solution", *Corros. Sci., vol. 69, pp. 226–235*, 2013.

[93] I. M. Pohrelyuk, V. M. Fedirko, O. V. Tkachuk, and R. V. Proskurnyak, "Corrosion resistance of Ti-6Al-4V alloy with nitride coatings in Ringer's solution", *Corros. Sci., vol. 66, pp. 392–398*, 2013.

[94] A. M. Fekry and M. A. Ameer, "Electrochemistry and Impedance Studies on Titanium and Magnesium Alloys in Ringer ' s Solution", *Int. J. Electrochem. Sci., vol. 6, pp. 1342–1354*, 2011.

[95] D. Gopi, J. Indira, L. Kavitha, and J. M. F. Ferreira, “Hydroxyapatite coating on selectively passivated and sensitively polymer-protected surgical grade stainless steel”, *J. Appl. Electrochem., vol. 43, no. 3, pp. 331–345,* 2013.

[96] C. Schille *et al.*, “Corrosion of experimental magnesium alloys in blood and PBS: A gravimetric and microscopic evaluation”, *Mater. Sci. Eng. B Solid-State Mater. Adv. Technol., vol. 176, no. 20, pp. 1797–1801,* 2011.

[97] M. I. Jamesh, G. Wu, Y. Zhao, D. R. McKenzie, M. M. M. Bilek, and P. K. Chu, “Electrochemical corrosion behavior of biodegradable Mg-Y-RE and Mg-Zn-Zr alloys in Ringer’s solution and simulated body fluid”, *Corros. Sci., vol. 91, pp. 160–184,* 2015.

[98] S. A. Salman, K. Kuroda, and M. Okido, “Preparation and characterization of hydroxyapatite coating on AZ31 Mg alloy for implant applications”, *Bioinorg. Chem. Appl.*, 2013.

[99] G. Vander Voort, “Metallography of Magnesium and its Alloys”, *Nature*, vol. 156, no. 3969, pp. 614–614, 1945.

[100] R. G. Kelly, J. R. Scully, D. W. Shoesmith, and R. G. Buchheit, "Electrochemical Techniques in Corrosion Science and Engineering", *Marcel Dekker, Inc,* 2003.

[101] Z. Shi, M. Liu, and A. Atrens, “Measurement of the corrosion rate of magnesium alloys using Tafel extrapolation”, *Corros. Sci., vol. 52, no. 2, pp. 579–588,* 2010.

[102] Z. Shi and A. Atrens, “An innovative specimen configuration for the study of Mg corrosion”, *Corros. Sci., vol. 53, no. 1, pp. 226–246,* 2011.

[103] C. M. A. Brett, A. N. A. Maria, and O. Brett, “Principles , Methods , and Applications”, *Oxford University Press,* 1993.

[104] B. D. Cullity, “Elements of X- Ray Diffraction", *Addison - Wesley Publishing Company*, 1956.

[106] D. Brandon and W. D. Kaplan, "Microstructural Characterization of Materials", *John Wiley & Sons, 2nd*, 2008.

[107] S. W. Hughes, “Measuring liquid density using Archimedes’ principle”, *Phys. Educ., vol. 41, no. 5, pp. 445–447,* 2006.

[108] G.W. Padua and Q. Wang, "Nanotechnology Research Methods for Foods and Bioproducts", *John Wiley & Sons,* 2012.

[109] J. I. Goldstein, D. E. Newbury, C. E. Lyman, and D. C. Joy, "Scanning Electron Microscopy and X-Ray Microanalysis. A text for Biologists, Materials Scientists and Geologists ", *Plenum Press, London and New York, 2nd Edition*, 1992.

[110] J. Garratt-Reed and D. C. Bell, "Energy-dispersive X-ray analysis in the electron microscope", *Taylor & Francis e-Library*, 2005.

[111] A. Srinivasan, C. Blawert, Y. Huang, C. L. Mendis, K. U. Kainer and N. Hort, "Corrosion behavior of Mg–Gd–Zn based alloys in aqueous NaCl solution," *J. Magnes. Alloy., vol. 2, no. 3, pp. 245–256*, 2014.

[112] N. Hort, C Blawert et al.., "Magnesium alloys as implant materials-Principles of property design for Mg-RE alloys," *Acta Biomater., vol. 6, no. 5, pp. 1714–1725*, 2010.

[113] C. Liu *et al.*, "Biodegradable Mg-Cu alloys with enhanced osteogenesis, angiogenesis, and long-lasting antibacterial effects," *Sci. Rep., vol. 6, no. May, p. 27374*, 2016.

[114] Z. Shi, A. Prasad, and A. Atrens, "Plug-In Specimens for Measurement of the Corrosion Rate of Mg Alloys," *vol. 64, no. 6, pp. 657–663*, 2012.

[115] Kiryl Yasakau " Active corrosion protection of AA2024 by sol-gel coatings with corrosion inhibitors", *Universidade de Aveiro*, 2011.

[116] E. G. Hshler, E. Board, J. Hamilton and H. L. Paul, "Solid Surface Physics", *Springer-Verlag Berlin Heidelberg New York* 1979.

[117] R. Hausbrand, M. Stratmann and M. Rohwerder, "The Physical Meaning of Electrode Potentials at Metal Surfaces and Polymer / Metal Interfaces : Consequences for Delamination", *Journal of The Electrochemical Society*, 2008.

[118] K. Shimizu, H. Habazaki, P. Skeldon, G. E. Thompson, and D. M. Layers, "Radiofrequency GDOES : a powerful technique for depth profiling analysis of thin films," *Surf. Interface Analysis, pp. 564–574, vol. 35*, 2003.

[119] P. Marcus and F. Mansfeld,"Analytical Methods in Corrosion Science and Engineering", *Taylor and Francis*, 2006.

[120] J. R. D. E. Laeter, H. Hidaka, H. S. Peiser, K. J. R. Rosman, and P. D. P. Taylor, "Atomic weights of the elements : Review 2000 (IUPAC Technical Report)", *Pure Appl. Chem., Vol. 75, No. 6, pp. 683–800*, 2003.

[121] Maria del R. S. Campos, " The Role of Intermetallic Phases In the Corrosion of Magnesium-Rare Earth Alloys", *Technischen Universität Hamburg-Harburg,* 2016.

[122] S. H. Davis "Cambridge Monograph of Mechanics, Theory of Solidification", *Cambridge University Press,* 2003.

[123] J. Campbell, "Complete Casting Handbook Metal Casting Processes and Design", *Butterworth-Heinemann,* 2011.

[124] E. E. Underwood, "Quantitative Stereology for Microstructural Analysis", *Microstructural Analysis Tools and Techniques, Plenum Press, New York,* 1973.

[125] L. Yang, "Room temperature synthesis of flower-like CaCO3 architectures" *The Royal Society of Chemistry,* 2013.

[126] Ignasi Puigdomenech, *Hydra/Medusa Chemical Equilibrium Database and Plotting Software* (2004) KTH Royal Institute of Technology.